Analyzing Multiphase Flow in Membrane Electrode Assembly Using a Mixed Wettability Mathematical Model

by

Jie Zhou

A thesis submitted in partial fulfillment of the requirements for the degree of

Doctor of Philosophy

Department of Mechanical Engineering
University of Alberta

Abstract

Improving fuel cell performance at high current density is critical for reducing stack size, cost and weight in automobile applications. A major source of performance losses at high current density is the accumulation of liquid water in the electrode which blocks reactant transport. Studying water management in proton exchange membrane fuel cell (PEMFC) is, therefore, critical in achieving the full potential of PEMFC.

In this work, a novel multi-dimensional, non-isothermal, two-phase fuel cell model is present to study water management in a membrane electrode assembly (MEA). The porous electrode microstructural details are accounted for using a mixed wettability pore size distribution (PSD) model. The PSD model is used to predict two-phase related transport properties, such as saturation and relative permeability, based on the porous layer's microstructure and wettability.

The proposed model has been used to study: (a) the effect of catalyst layer microstructure and wettability on fuel cell performance; (b) the role of the micro-porous layer (MPL); and (c) a new electrode architecture, i.e., the electrode coated membrane (ECM).

Simulation results indicate that, when liquid water is present, reactant transport in the catalyst layer is the key factor limiting fuel cell performance.

As shown by the model, improved water management in the catalyst layer can be achieved with: (a) a large hydrophobic contact angle; (b) a moderate hydrophilic volume fraction; and (c) a large PSD and small pores in the hydrophilic phase.

The study on the MPL shows that, under fully humidified conditions, the reasons for the improved water management, after introducing an MPL in a fuel cell, are: (a) increased temperature, and (b) low saturation in the MPL. The increased temperature in the electrode results in enhanced evaporation and higher back-diffusion from the cathode to the anode, thereby, alleviates water accumulation. Since the MPL is mainly hydrophobic, water does not accumulate in its interior, thereby, creating in-plane transport pathways for the reactant.

Finally, an inkjet printed electrode coated membrane (ECM) with ionomer based carbon MPL is studied. The ECM demonstrates better performance than the conventional MPL under dry conditions. However, under wet conditions, water accumulation is a problem for ECMs leading to reduced performance. The proposed model shows that, under wet conditions, better performance can be achieved for ECMs with: (a) thin MPL; (b) a high electrical conductivity; (c) a low MPL thermal conductivity; (d) a high porosity; (e) a moderate amount of hydrophilic percentage; and (f) a large PSD.

In summary, this work presents a novel multi-dimensional, non-isothermal, two-phase fuel cell model that accounts for microstructural details by means of a mixed wettability PSD model. This model provides an ideal framework to study the microstructure effect of porous layers on water management. Knowing the microstructure effect, this work paves the way for designing porous

layer microstructure with desired fuel cell performance.

Keywords: Two-phase model, water management, membrane electrode assembly, wettability, pore size distribution, microstructure.

Preface

Parts of chapter 2 of this thesis have been published in the journal article as J. Zhou, A. Putz, and M. Secanell. "A Mixed Wettability Pore Size Distribution Based Mathematical Model for Analyzing Two-Phase Flow in Porous Electrodes I. Mathematical Model". *Journal of the Electrochemical Society*, 2017, Volume. 164, pp. 530-539. I was responsible for literature review, model development and implementation, data analysis and manuscript writing. A. Putz was the industrial collaborator with our laboratory who provided industrial and technical perspectives in writing the manuscript. M. Secanell was the supervisory author and contributed with the concept formation, insightful guidance in validating the model and ideas of stabilizing the model, manuscript composition and editing.

Parts of chapter 3 of this thesis have been published in the journal article as J. Zhou, D. Stanier, A. Putz, and M. Secanell. "A Mixed Wettability Pore Size Distribution Based Mathematical Model for Analyzing Two-Phase Flow in Porous Electrodes: II. Model Validation and Analysis of Micro-Structural Parameters". *Journal of the Electrochemical Society*, 2017, Volume. 164, pp. 540-556. I was responsible for literature review, parametric study, part of PEMFC electrode fabrication and testing, data analysis and manuscript writing. A. Putz was the industrial collaborator with our laboratory who provided industrial and technical perspectives in writing the manuscript. D. Stanier helped with the electrode fabrication and testing. M. Secanell was the supervisory author and contributed with the concept formation, insightful guidance in validating the model and ideas of stabilizing the model, manuscript composition and editing.

Parts of chapter 4 of this thesis have been published in the journal article as J. Zhou, S. Shukla, A. Putz, and M. Secanell, "Analysis of the role of the microporous layer in improving polymer electrolyte fuel cell performance," Electrochimica Acta, 268C: 366-382, 2018. I was responsible for literature review, numerical study, part of the inkjet printed electrode fabrication and testing, data analysis and manuscript writing. S. Shukla helped with the fabrication and testing of electrodes. A. Putz was the industrial collaborator with our laboratory who provided industrial and technical perspectives in writing the manuscript. M. Secanell was the supervisory author and main contributor with the concept formation, manuscript composition and editing.

To my family

Acknowledgements

I would like to thank my supervisor, Dr. Marc Secanell, for providing me the opportunity to pursue cutting edge fuel cell research under his guidance. Over the years, he has been a constant source of inspiration and motivation for me and I have gained valuable lessons about conducting research and life in general from him. His ability to bring out the best in everyone has helped me gain a scientific mindset and raise the bar on the quality of my work. Had it not been for his guidance and support, I doubt that this thesis would have ever been written.

I thank Dr. Andreas Putz who supervised me during my graduate program internship at AFCC. His wonderful teachings on colloidal science motivated me to work in the area of fuel cell modelling and simulation.

I acknowledge the financial support from Natural Sciences and Engineering Research Council of Canada (NSERC), Canadian Foundation for Innovation (CFI), Modeling Research for Polymer Electrolyte Fuel Cell (CARPE-FC), and the University of Alberta for this research.

I would like to thank my colleagues and friends at the ESDLab and the University of Alberta for helping me out on a number of occasions. Specifically, I would like to thank Dave and Shantanu for their help in conducting some of the experiments, Alex and Mayank for insightful ideas and discussions about the fuel cell operation, Chad for demonstrating his cooking skills by the occasional treats and Aslan, Kaylin, Madhur, Julia, David and others for their companionship.

Saving the best for the last, I would like to thank my parents for their support at all time. Without their emotional support, it would have been very difficult for me to stay far away from home for such a long time. I would also like to thank Yuying who has always been supportive during the long working hours and believed in me all the time.

Table of Contents

List of Tables

List of Figures

Nomenclature

English Letters

$\bar{H}_i$	Specific enthalpy of species i
$\dot{N}_i$	Water flux in phase i
$\boldsymbol{u}_g$	velocity of gas mixture
c_g	Total gas mixture concentration
D_T^{eff}	Thermo-osmosis diffusion coefficient
D_λ^{eff}	Sorbed water diffusion coefficient
$D_{i,j}^{\text{eff}}$	Effective diffusivity of species i in j
D_λ^{eff}	Effective diffusion coefficient in ionomer
EW	Equivalent weight of the ionomer
F	Faraday constant
i	Volumetric current density
j	Current density
k^{eff}	Effective thermal conductivity
k_{sat}	Absolute permeability
$k_{g,HI}$	Gas permeability in hydrophilic network
$k_{g,HO}$	Gas permeability in hydrophobic network
k_g	Gas permeability
k_l	Liquid permeability

k_{rg} Relative gas permeability

M_{H_2O} Water molar mass

n_d Electroosmosis coefficient

p_c Capillary pressure

p_g Pressure of gas mixture

p_l Pressure of liquid water

r_c Critical pore radius

S Saturation

S_i Source term for species i

T Temperature

u_g Velocity of gas mixture

x_{H2O} Water vapor molar fraction

x_{O2} Oxygen molar fraction

N_i Total molar flux of species i

Abbreviations

CCM Catalyst coated membrane

CL Catalyst layer

ECM Electrode coated membrane

GDL Gas diffusion layer

IP Intrusion porosimetry

MEA Membrane electrode assembly

MPL Micro-porous layer

MSP Method of Standard Porosimetry

PCI Phase change induced

PEMFC Proton exchange membrane fuel cell

Greek Letters

β	Normalized water flux
γ	Surface tension
λ	Sorbed water content
λ_{PSD}	Interconnectivity of bundle rejoined capillaries
μ_i	Dynamic viscosity of species i
ϕ_m	Electrolyte potential
ϕ_s	Electrical potential
ρ_i	Density of species i
σ_m^{eff}	Effective ionic conductivity
σ_s^{eff}	Effective electronic conductivity
θ	Contact angle
ε_o	Porosity

Chapter 1

Introduction

1.1 Motivation

The recent Paris Agreement [10] demonstrates the determination of mankind to substantially reduce greenhouse gas emissions. Phasing out the existing fossil fuel technologies such as coal power plants and the internal combustion engine is paramount to achieving this goal. Fuel cell technology is one of the alternative forms of automobile propulsion systems to replace internal combustion engines. Hydrogen fuel cells are energy delivery devices that convert the chemical energy from hydrogen into electricity while producing only water. As compared to a traditional gas engine, fuel cells can reach high energy efficiency with low operational noise.

Water generated by fuel cells is one of the key factors affecting fuel cell performance and durability, especially under cold conditions [11–14]. This is because the accumulated water in the electrodes hinders reactant transport and reduces the catalyst efficiency. Improving water management is paramount to optimize proton exchange membrane fuel cells (PEMFCs) performance and reduce the amount of required expensive catalyst, especially when the cell is operating at high relative humidity.

Efforts have been made over the past decade to understand the multiphase flow transport in PEMFCs porous media [15–17]. However, a multidimensional, non-isothermal, multiphase membrane electrode assembly (MEA) model that accounts for the micro-structural information of the electrode was not available in the fuel cell scientific community. This thesis therefore, aims

at looking critically at multiphase transport in PEMFC by developing a comprehensive numerical model that fills the above literature gap. The model will then be used to guide fuel cell porous transport and catalyst layer design in order to enhance the water management in PEMFC.

1.2 Proton Exchange Membrane Fuel Cell (PEMFC) Background

Fuel cells are environmental-friendly energy conversion devices which convert the chemical energy in a fuel to electricity. In PEMFCs, the electricity is generated by electrochemically reacting hydrogen (fuel) with the oxygen and producing water as the only by-product. A basic schematic of a PEMFC that includes the species transports is shown in Figure 1.1. The schematic shows

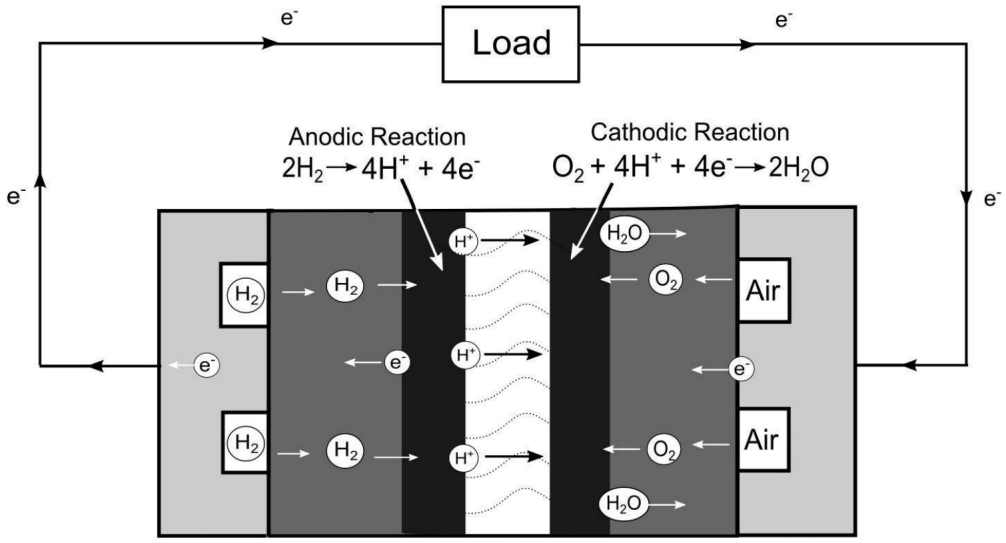

Figure 1.1 – Schematic of a PEMFC and its basic operation. Reprinted with permission [2].

that PEMFCs contain two electrodes which are separated by an ionic conductive and electrical non-conductive polymer electrolyte membrane (PEM). The PEM leads to the separation of the electrons and protons by allowing the protons to pass through and forcing the electrons to travel through the external circuit. The electrical power can then be used by an external load. To avoid direct combustion between hydrogen and oxygen, the PEM is de-

signed to prevent gas permeation. Like other battery devices, the electrodes are the places where oxidation and reduction reactions occur. The reactant is supplied from the gas channel, and the electrons are collected by the bipolar plates. For them to reach the electrochemical reactive side, they need to travel through the gas diffusion layers (GDL) and the micro-porous layers (MPL). One of the purposes of having GDLs and MPLs is to protect the thinner and electrochemically reactive catalyst layer (CL).

At the anode, the hydrogen oxidation reaction (HOR) takes place and the half-cell reaction is given as,

$$2H_2 \rightleftharpoons 4H^+ + 4e^- \tag{1.1}$$

where the input reactant is hydrogen (H_2) and the protons (H^+) and electrons (e^-) are released from the reaction. The protons can be transported by the electrolyte which exists in the CLs and PEM. Thus, the motion of the generated protons is to go through the PEM to reach the cathodic CL. Carbon black in CL, MPL and GDL is the medium allowing electrons to travel. When electrons travel through the external circuit, they can provide usable electricity.

The produced electrons and protons at the anode meet again at the cathodic CL and react with the oxygen gas. The electrochemical reaction taking place at the cathode is the oxygen reduction reaction (ORR) which can be expressed as,

$$O_2 + 4H^+ + 4e^- \rightleftharpoons 2H_2O \tag{1.2}$$

where the liquid water is the final product of the reaction. The performance of PEMFCs is commonly limited by the sluggish ORR since reaction kinetics are very slow. To speed up the process, a catalyst, usually platinum, is used.

The overall electrochemical reaction in the PEMFC can be written as,

$$O_2 + 2H_2 \rightleftharpoons 2H_2O \tag{1.3}$$

To demonstrate the electrochemical performance of a PEMFC, polarization curves are considered the simplest representation and are commonly reported

in the fuel cell scientific community. The performance of a PEMFC can be represented by its current density, in A/cm^2, at a given voltage. The unit of current density is normalized over the area of the testing cell and this allows the comparison of cell performance in different scales.

Figure 1.2 shows a typical polarization curve of a fuel cell. A polarization curve can be divided into three regions that represent the three main irreversible loss mechanisms in a fuel cell, i.e., kinetic, ohmic, and mass transport losses. Kinetic losses are due to the necessity to overcome the electrochemical

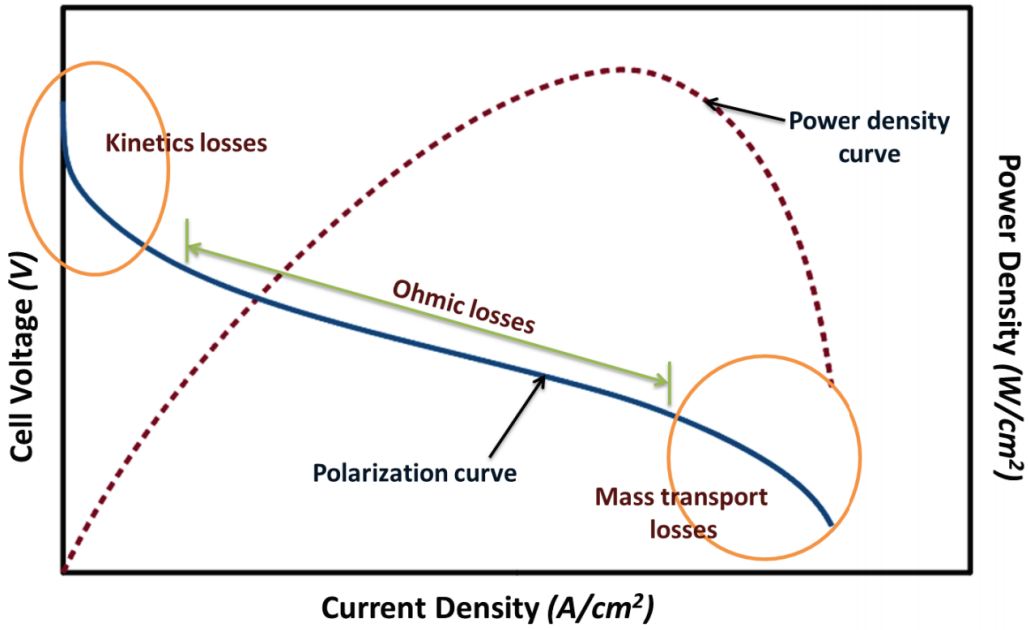

Figure 1.2 – A typical polarization curve to represent fuel cell performance. Reprinted with permission [3].

activation barrier of cathodic oxygen reduction and anodic hydrogen oxidation reactions. Ohmic losses which start to become important at intermediate current densities, are the result of the proton transport losses in the electrolyte phase and electron transport losses in the solid phase. At high current density, mass transport losses are also important. The cause of mass transport losses can be attributed to insufficient reactant supply at the catalyst known as starvation. The reduced reactant concentration is due to the large amount of water production at high current density resulting in liquid water accumu-

lation which blocks the reactant pathway.

1.2.1 Fuel Cell Fabrication

The membrane assembly electrode (MEA) includes five main components: GDL, MPL, CL, PEM and bipolar plate. The functionality of GDL and MPL are very similar, providing the reactant transport pathway in their void space, allowing electrons to travel to the reactive side and ejecting the produced liquid water and heat to the gas channel. Generally, the GDL is fabricated from a carbon cloth or carbon paper coated with polytetrafluoroethylene (PTFE) which is used to assist water management in PEMFC. The MPL is a composite of carbon black mixed with PTFE. To manufacture MPL, spraying and doctor blading onto the GDL have been used [18, 19].

Anode and cathode CLs and PEM are the heart of the MEA. A variety of CL fabrication techniques have been developed during the past few decades such as spraying, screen-painting, doctor blade method, sputtering and inkjet printing. In the context of the thesis, the primary focus is on doctor blade and inkjet printing methods because of the equipment availability and high reproducibility. Among the methods, doctor blade method is considered suitable for MEA mass production [20] with reasonable precision in catalyst loading. Inkjet printing, introduced in 2007 [21], aims at achieving very accurate catalyst loading with insignificant transfer losses and high control of Nafion and catalyst distribution in CL due to its drop-on-demand capabilities [22].

MEAs might contain diffusion electrodes, where the CL is applied to the MPL, or catalyst coated membranes. The latter is usually preferred because less catalyst lost to the MPL [23]. Catalyst coated membrane fabrication can be achieved using two methods, decal-transfer and direct membrane coating depending on the substrate used [20, 24, 25]. In the decal-transfer method, the CL is first deposited onto the substrate, usually a Teflon film and then transferred onto the membrane by hot-pressing. There is no additional CL transfer involved for catalyst-coated membrane method. Using decal-transfer can avoid membrane swelling as well as catalyst penetrating into the diffusion layer which reduces the activity [23]. The method is suitable for mass

production due to its simplicity, reproducibility and reasonable catalyst loading precision. Direct membrane deposition method offers higher performance against decal-transfer method in general [26]; as the catalyst is dispersed directly onto the membrane, the interfacial contact between membrane and CL has been enhanced.

The most commonly used membrane material for PEMFC is perfluorosulfonic acid (PFSA). It consists of two parts [27]: (i) ionic clusters, which contain perfluorovinyl ether groups terminated with sulfonate groups, and (ii) a polytetrafluoroethylene (PTFE, a.k.a. DuPont's Teflon$^{\mathbf{TM}}$) backbone.

The main functions of the bipolar plate are to distribute the gas reactant and collect the current. Thus, the material of the bipolar plate needs to be electrically conductive such as carbon and graphite. The gas channel which are the small grooves on the surface of the bipolar plate is created by engraving or milling during the manufacturing. Generally, the MEA model does not include the bipolar plate since its effects are secondary.

1.2.2 Fuel Cell Testing

PEMFC electrochemical performance is of importance to validate numerical models. Fuel cell performance is usually characterized by obtaining polarization curves in a fuel cell testing station, such as Scribner 850e. After cell assembly, the first step is to precondition the cell. The polarization curve can then be recorded in two modes, i.e., galvanostatic and potentiostatic. Under galvanostatic mode, the current is held constant over time and the voltage is allowed to vary whereas in the potentiostatic mode, the voltage is held constant. Other electrochemical techniques such as cyclic voltametry and chronoamperometry can also be used to estimate the active area.

The majority of numerical model validation, especially for two-phase flow models, relied on experimental data in literature [11, 28–31] with little knowledge of the stoichiometry or flow rate in the channel, channel configuration and time of recording the data (it takes time to reach steady state). Fuel cell operating conditions can strongly affect the fuel cell performance. The channel reactant distribution effects are usually neglected in two-dimensional

fuel cell models, thus determining the right fuel cell operating conditions that can achieve reactant uniformity in the channel is important [32]. To validate a steady state two-dimensional multiphase MEA model, several conditions need to be satisfied:

1. high and constant stoichiometry in the flow channel to provide uniform reactant distribution and remove produced liquid water,
2. parallel channel configuration to avoid convective flow under the land area of the bipolar plate,
3. operating the cell with a sufficient time to make sure steady state is achieved,
4. minimal hydrogen or oxygen cross-over.

1.3 Literature Review

Experimental studies have highlighted several possible ways to enhance the fuel cell performance by modifying the porous layer to avoid complete flooding of the electrode:

1. Diffusion media micro-structure modifications:
   (a) Inserting an MPL in between the CL and the GDL to increase the water evaporation [1, 33, 34],
   (b) Adding macro-cracks by milling holes in the MPL [35–37],
   (c) Creating hydrophilic pathways in diffusion media for water passage [38–40].
2. Optimal layer composition design:
   (a) Varying the PTFE content, pore size distribution (PSD) and thermal properties in GDL and MPL [41–43],
   (b) Morphological CL control by adding pore former in the ink used for fabrication [44–46].

3. Novel electrode architectures:

   (a) Functionally graded electrodes [47–49],

   (b) Patterned electrodes [22, 50–55].

It can be concluded from the above experimental studies that the microstructures and wettability of the porous layer are of paramount importance to MEA water management, and as a result, overall fuel cell performance and cost. However, conducting experiments can be time consuming, expensive, and most importantly, the transport phenomena inside the cell cannot be well understood as current visualization tools are not yet feasible to look at the water inside the CL.

Numerical models can resolve the above issues. With the advancements in computational power and parallel algorithms, running simulations is much faster than conducting experiments. Further, different fuel cell designs can be studied using the numerical model by performing simulations with varying parameters. Last but not least, as the governing equations in the numerical models are physics based, the transport phenomena can be studied.

1.3.1 Two-Phase Models

Developing a two-phase model that accounts for: a) varying micro-structures, b) multi-dimensionality, and c) phase change effects, is critical to understand the effect of the micro-structural modifications on water management and provide guidance in optimal layer micro-structure design.

The difficulty in modeling two-phase flow in PEMFCs lies mostly in striking a balance between the computational cost and the complexity of the multi-physics problem. This is because the electrochemical reactions, especially oxygen reduction reaction (ORR), are strongly coupled with energy, gas species and liquid water transport. Numerical approaches to study two-phase transport in fuel cells include: a) volume-averaged models [4, 12–14, 28, 30, 56–59], b) pore network models (PNM) [60, 61], and c) micro-scale (full morphology) models [62–64].

Volume-averaged models are based on the assumption that there exists a representative elementary volume (REV) in the porous medium by assuming the material is homogeneous. REV is the volume over which an estimation can be made that will yield an averaged property representative of the whole material.

PNMs are based on network diagrams that use idealized geometries, i.e., pores and throats, to represent the complex micro-structure of a porous media. In PNMs, the physical processes are solved locally at each pore.

Micro-scale models use imaging data such as x-ray computed tomography (X-CT) or focus ion beam scanning-electron microscopy (FIB-SEM), to reconstruct the microstructural information of the porous layer. As compared to the PNM, more geometrical details are included in the micro-scale models. The transport physics in the micro-scale model are solved at the pore-level.

Given the length scales in each layer, PNMs and micro-scale models might be better choices to study two-phase flow in the GDL while volume-averaged models are suitable in the MPL and CL. In the GDL, the layer thickness is 150-400 μm and the pore size is between 5-60 μm. Due to the size of the pores, a REV for the GDL might be of the same size or even larger than the GDL thickness; thereby, a volume-average model should not be used [65]. The use of a REV for the GDL can, however, be justified in two-dimensions, through the channel model, on the basis of averaging along the channel. Conventional CLs and MPLs thicknesses are 5-15 μm and 40-80 μm, respectively. CLs contain pores that are 5-210 nm, with most pores in the range of 20-80 nm [62, 66–68], and MPLs contain pores that are smaller than 1 μm [69]. Given the pore size and layer thickness, there are hundreds of pores across any CL and MPL, therefore, an REV is likely to exist. In this case, volume-averaged models are appropriate and effective properties, such as effective thermal conductivity, effective diffusivity and effective permeability, are likely well approximated by using statistical theory of heterogeneous media.

Volume-averaged Models - The first approach (saturation-based model) proposed involved the solution of a saturation equation obtained by replac-

ing liquid pressure by saturation in Darcy's law [12–14, 28, 56]. The main issue with the saturation-based model is that the driving force for liquid water should be liquid pressure instead of saturation. Another concern of using saturation-based models is that, in most cases, a continuous function is used to approximate the saturation variable even though, saturation is likely to be discontinuous at the interface between porous layers, e.g., at MPL-GDL interface, due to the different wettabilities and pore sizes. Also, the approach is usually limited to fully humidified conditions as the specification of a finite saturation at the GDL/channel boundary implies that some liquid water should already be present in the channel. Even if a value of zero saturation is used, liquid water can flow from the channel to the MEA.

The Levertt J-function is commonly used to relate saturation with capillary pressure. However, the Leverett J-function is an empirically measured curve that is difficult to be related directly to a porous media's microstructure. Thus, it is difficult to optimize the structure of the porous layers using Leverett J-functions.

The first saturation based two-phase model was presented by He et al. [70]. Since the model only accounts for the cathodic side, a constant liquid water flux is imposed at the membrane/cathode CL interface to account for electroosmosis. Depending on the choice of constant water flux, it might over or underpredict the membrane water transport. The result of the model highlighted evaporation as a critical mechanism for water removal in the fuel cell. Thermal effects on evaporation are, however, not included in the model which might result in an underprediction on the amount of water removed by evaporation.

Siegel et al. [14] proposed a saturation based model that accounted for the full MEA domain including the gas channel. The model showed the highest saturation appeared in the cathode CL close to the channel inlet. However, no flux boundary condition for liquid water is imposed at the channel outlet which forces liquid water leaving at the channel inlet. Since the bipolar plate was not considered in their model, the electrical potential was not included in their model.

Nam et al. [28] introduced a network model for species diffusion into the two-phase model. With the network model, the effects of fiber diameter and porosity on cell performance were examined. To overcome the deficiency of the saturation based model, a jump in saturation was applied to the interface between CL and GDL. However, due to the complexity of the network model, their two-phase model was implemented in 1D and the effect of channel could not be studied.

More saturation-based models were proposed since then to study the two-phase transport in the PEMFC with higher dimensions [71, 72] or introducing interface boundary conditions between MPL and CL [13, 56, 73]. To sum up, the main concern of using the saturation-based models is that, in most cases, a continuous function is used to approximate the saturation variable even though saturation is likely to be discontinuous at the interface between porous layers, e.g., at MPL-GDL and MPL-CL interfaces, due to the different wettabilities and pore sizes. Also, the approach is usually limited to fully humidified conditions as the specification of a finite saturation at the GDL/channel boundary implies that some liquid water should already be present in the channel. Even if a value of zero saturation is used, liquid water can flow from the channel to the MEA.

The multi-phase mixture models, usually referred to M^2 models, have also been developed [32, 74–76]. The momentum equations solved in the M^2 models are based on Navier-Stokes equations. As the M^2 models cannot be used to study the phase change effect, the applications of the model are very narrow [77]. Therefore, M^2 models are not considered suitable for studying the phase change induced flow which is an important phenomena in PEMFC [78].

The third approach, namely the capillary-based approach or two-equation approach, involves solving mass and momentum equations for gas and liquid phases independently and then relating the capillary pressure, i.e., the difference between the gas and liquid pressure to saturation using a closure equation based on micro-structural information such as a PSD [29–31, 58]. The use of gas and liquid pressure results in continuous solution variables even at the interface between layers with different wettabilities which resolves the underlying

issue in the saturation based model [12, 14, 28].

The first capillary-based two-phase fuel cell model, to the author's knowledge, was proposed by Weber and Newman where a 1D, isothermal, two-phase model was introduced [31]. The micro-structural information was included in the model by means of a mathematical PSD model. The advantages of using the PSD model is that the two-phase related transport properties can be estimated using the micro-structural information, i.e., PSD, instead of determined by ex-situ characterization. The model demonstrated the saturation jump between different porous layers, and by performing parametric studies, the effect of hydrophobic fraction in the GDL was studied. The contribution of the model was significant to the fuel cell scientific community; however, as the model was implemented in 1D, the channel and land effects were not studied, and due to the isothermal assumption, the effect of temperature was also not studied.

The model developed by Weber et al. [31] was later improved to include the thermal effect and liquid water transport in the membrane [78]. The improved model was used to study the role of the MPL on water management in fuel cells and with the model, they concluded that the effect of MPL is to force water transport from the cathode to anode via the membrane. With the thermal effect included, the model suggested the heat-pipe effect in fuel cells was important to improve the reaction kinetics and mass transport.

A cathode CL model was proposed by Eikerling [30] to look critically into the micro-structural effect on cathode CL water management. The PSD in the model was characterized into two categories: a) primary pores (3-10 nm) which favors large reaction and evaporation, and b) secondary pores (10-40 nm), which are open for reactant transport. However, the effects of adjacent layers, i.e., membrane, GDL or MPL, on mass transport were not included in the model.

In Eikerling's model [30], the single wettability assumption was used and the CL was treated as completely hydrophilic. Mulone et al. [58] and Mateo et al. [4] further improved Eikerling's model [30] by introducing a mixed wettability PSD model. The necessity of the mixed wettability was demonstrated

by correctly predicting the capillary pressure vs. saturation curve. The model suggested that, under partially saturated conditions, the small hydrophobic pores are available for reactant transport whereas others pores are filled with liquid water.

Mateo [4] also implemented a mixed wettability PSD model by assuming homogeneous hydrophilic and hydrophobic networks co-existed in the CL. The PSD model however, was not integrated into a two-phase MEA model.

Due to the complexity of the PSD models, the above models are in one dimension. Higher dimensional capillary-based models without PSD models have been developed by many researchers [11, 79, 80], but not with a PSD micro-structural model. The main advantage of using higher dimensional models is that the channel and landing effect on the liquid water distribution can be studied. The saturation distribution in the MEA shown by Zenyuk et al. [11] clearly demonstrated that the liquid water accumulated under the landing area.

Overall, a multi-dimensional, non-isothermal, capillary-based model relating gas and liquid pressure to saturation by means of a flexible, mixed wettability PSD has yet to be developed. The advantages of capillary-based over the saturation-based models are:

1. The physical driving forces, liquid and gas pressure, are solved for, as solution variables.

2. The saturation jump due to differences in wettability and pore sizes between porous layers can be studied.

3. Optimized wettability and layer micro-structures can be studied by introducing a PSD model.

4. Gas convection effects can also be studied.

Pore-Network Models - One well-known deficiency of the MEA volume-averaged model is the suitability of REV assumption in the GDL. The REV is violated when the local diameter of the carbon fiber exceeds the size of the

REV. Another drawback of the volume-averaged model is the lack of consideration of discrete water clusters due to the use of continuum equations. The above problems can be solved using PNMs.

In PNM, the pore space is partitioned into a collection of pore bodies connected through pore throats which act as local resistances. This allows the model to account for pore-level physics and pore space geometry explicitly. Inhomogeneous morphology as well as wettability of the porous material are also accounted by assigning different pore sizes and contact angles. Based on imaging data, the actual geometry can be reconstructed. The advantage of PNM is that it can capture capillary fingering effects observed experimentally. In addition, since the formulations are defined in the pore scale, the effective properties are computed directly based on structure as an outcome instead of an input as in volume-averaged models.

PNMs can be used to simulate capillary flow, thermal transport and gas transport on a pore scale. Because the PNM accounts for many micro-structure details, it allows for the use of simplified governing equations, however, its computational expense is high [80]. Zenyuk et al. [80] proposed the combination of a pore-level model for the GDL and a volume-averaged model for PEM and CL to study capillary transport in MEA. The advantages of the coupled model is that the pore network can be used to capture the water transport through the GDLs with inhomogeneous morphology, and the volume-averaged model can be used to model the transport in CL and MPL and electrochemical reactions with a better computational efficiency.

Micro-scale Models - Advancements in imaging techniques, such as X-CT, FIB-SEM and scanning transmission x-ray microscopy (STXM), have made the visualization of the micro-structure of fuel cell porous layers with higher resolution feasible. Numerical tools have been developed to convert the imaging data into a reconstructed computational domain and to mesh the images to perform numerical simulations. Micro-scale models take advantage of the reconstructed mesh and simulate transport phenomena either using a continuum approach (direct numerical simulation, DNS) or the Lattice Boltzmann

method (LBM). The difference between the two is that to use DNS, the continuum equation has to hold, whereas LBM originates from fluid molecular description and incorporates physical terms with particle interactions.

With the increase in computational power, more attention has been paid to micro-scale models [62] during the last decade. This is because micro-scale models have the potential to provide a comprehensive understanding of porous layer transport phenomena from a morphological point of view. A main advantage of micro-scale models against volume-averaged model is that the transport properties are obtained at the pore-level rather than using effective coefficients. For modeling multiphase flow, capillary fingering can be well captured by micro-scale models [81, 82]. However, the downsides of micro-scale models include: a) high computational cost, and b) difficulty handling coupled physics.

Overall, volume-averaged approach that accounts for micro-structural information using a PSD model to study the multiphase flow in PEMFC was selected. The proposed approach has the following advantages over PNMs and micro-scale models,

1. It can be used to predict the cell performance at the MEA level instead of providing only local information.

2. It can incorporate critical transport processes, such as thermal transport and phage change.

3. The model has less computational cost than PNMs and micro-scale models.

4. It can incorporate some micro-structural information via a mixed wettability PSD model.

1.3.2 Porous Media Characterization

The PSD is an integral part of the numerical model that is proposed in this thesis. A PSD is a simple but useful representation of the porous layer microstructure. Methods that are currently available to estimate the PSD in the

fuel cell literature include: a) intrusion porosimetry (IP), b) method of standard porosimetry (MSP), and c) nitrogen adsorption. The detailed methodologies are discussed below.

Intrusion Porosimetry (IP) - IP is an analytical technique that can be used to determine pore diameter, total pore volume, and bulk and absolute densities of a porous material. The working fluid is pressurized into the porous material gradually until the desired pressure is reached. As the shape of the pore is assumed cylindrical and the porous material is assumed to be made of a bundle of rejoined irregular capillaries, Young-Laplace equation is used to relate the invading pressure to pore radius as follows,

$$p_c = p_{wetting} - p_{non-wetting} = \frac{2\gamma cos(\theta)}{r} \tag{1.4}$$

where p_c is the capillary pressure which is the pressure difference between wetting fluid (working fluid) and non-wetting fluid (gas phase, close to zero since the system is evacuated prior to the intrusion porosimetry), γ is surface tension, θ is the contact angle for working fluid to porous material, and r is the pore radius.

Since mercury is non-wetting to the majority of materials, the overall PSD in a porous material can be studied using mercury as the working fluid. The porous layer used in fuel cell applications are known for the co-existence of hydrophilic and hydrophobic networks to liquid water [83, 84]. Mercury is capable of estimating the total PSD. To distinguish the two networks, water IP can be used to represent the hydrophobic PSD since the liquid water is pressurized only into the hydrophobic phase. The hydrophilic phase can be obtained by subtracting water IP from mercury IP.

When the sample is being pressurized, there is a risk of deforming the pore geometry, especially when the pressure is high. This leads to an overestimation of the large pore volume fraction. Also, there are pores that might not be easily accessible such as closed pores or hydrophilic pores that are surrounded by hydrophobic pores. This can lead to an underprediction of the pore size.

Method of Standard Porosimetry (MSP) - MSP is based on capillary equilibrium. Two partially saturated samples are prepared, i.e., the standard sample with known capillary pressure vs. saturation curve and the sample to be measured. The samples are then put in contact until the capillary equilibrium state is reached, i.e., two samples share the same capillary pressure [85]. Saturation in the standard sample is determined using the current sample weight divided by the fully saturated sample weight. Since the capillary pressure vs. saturation curve for the standard sample is known, the capillary pressure can be obtained. After obtaining the capillary pressure for both samples, pore radius is calculated based on the Young-Laplace equation. A new data point is achieved by allowing slow evaporation of the working fluid. In this way, the PSD can be determined.

The choice of working fluid in MSP is to let it enter the sample freely as the opposite of IP. Octane is used for measuring the overall PSD in MSP since it is wetting to most of the materials used in fuel cell applications. To obtain the hydrophilic portion of the porous layer, water is considered the working fluid.

One drawback of the MSP is that hydrophilic pores surrounded by the hydrophobic walls might be inaccessible when water is used as the working fluid. This leads to an overestimation of the hydrophobic pores in the measured material. Another problem with MSP is that when the tested sample is merged to the working fluid, it might expand in water or other working fluid which results in unrealistic volume predictions.

Nitrogen Adsorption - Nitrogen adsorption is often the choice of estimating specific surface area and with Brunauer-Emmett-Teller (BET) equation, the PSD in the porous material is determined. The BET equation is based on Langmuir theory of monolayer gas adsorption on a solid surface. From Kelvin equation, the pore radius prior to capillary condensation can be calculated based on the gas partial pressure. The actual pore radius is then obtained using the Barrett, Joyner and Halenda (BJH) method which accounts for the condensed film thickness of the adsorbate molecules [66].

The advantage of using nitrogen adsorption is that it can access much smaller pores as compared to IP [66]. However, nitrogen adsorption isotherms indicate that the biggest pore size that can be measured is around 100 nm which is much smaller than the pore size in MPLs and GDLs. In addition, nitrogen adsorption is unable to assess the wettability of the porous material.

Overall, the pore size in GDLs and MPLs are usually greater than 100 nm, therefore nitrogen adsorption is not applicable. MSP provides several advantages over IP such as, accounting for the variation in contact angle, and using constant compression pressure. However, MSP cannot correctly measure the hydrophilic pore volume for materials that swell [86]. Due to equipment availability, and the fact that it can be used in desired pore range, water IP and mercury IP are selected to characterize the hydrophobic and overall PSDs in GDL, MPL and CL in this thesis.

1.3.3 Effect of Multi-Phase Flow on Membrane Electrode Assemblies

Depending on the function of each MEA component, the effect of multiphase flow changes. For instance, the CL needs to retain sufficient water vapor to hydrate the electrolyte, whereas in the GDL, there is no need as the electrolyte phase does not exist. Therefore, understanding the effect of multiphase flow on each porous layer is important to improve fuel cell performance. In this way, the most critical layer to water management in the fuel cell can be identified and its micro-structure optimization can be done more efficiently.

Catalyst Layer - Substantial improvement in MEA performance and cost reduction have been achieved by modifying the microstructure and wettability of the CL in terms of improving the catalyst utilization under partially saturated conditions [22, 30, 44–47, 47, 47–55, 87].

Numerical studies on the CL in fuel cell literature focused mostly on parameter optimization such as CL thickness, porosity, Nafion content and platinum loading [11, 48, 87, 88] due to the lack of ability of accounting for the microstructural details. For example, Zenyuk et al.[11] found that for CLs less than

5 μm, performance loss due to water accumulation under startup conditions is significant. However, micro-structural effects such as PSD and wettability on water management were not presented in their study. The model used to study CL microstructure was introduced by Eikerling in [30] where the effect of wetting state in CL on electrochemical reaction was studied. However, the cathode CL in the model was considered hydrophilic and the effect of hydrophobic pores was not analyzed. With the two-phase model proposed in this thesis, the effects of phase change induced flow, and CL microstructure such as PSD and wettability, can be studied.

New electrode architectures were introduced in fuel cell literature to improve the catalyst utilization. Examples are functionality graded electrodes [47–49], patterned electrodes/PEM [22, 50–55], and nano-structured thin-film (NSTF) electrodes [89, 90]. Koh et al. [54] reported a remarkable performance increase (59% increase in current density under fully humidified condition) with a micropatterned PEM with a width $\times$ gap dimension of 3×5 μm. A similar performance increase was also observed by Zhou et al. [51] with patterned PEM. The line patterned PEM introduced by Bea et al. [53] showed a maximum 30% increase in current density with 1 μm pattern space, however, with a smaller pattern space of 70 nm, the performance decreases. The above researchers [51, 53, 54] have attributed the improved performance to the increased electrochemical active area and a better reactant transport. However, the exact physical details in MEA remain unknown. Thereby, numerical models are of importance to gain a better understanding of the physical changes with the new electrode architectures. As compared to the experiments, numerical models also provide a strong flexibility in simulating varying electrode architectures as well as reducing the overall material cost.

Micro-porous Layer - The use of an MPL in fuel cells is known to improve fuel cell performance, especially under wet conditions, for instance, Owejan et al. [1] observed a $20 - 30\%$ increase in performance under fully humidified conditions after adding the MPL, and Karan et al. [91] showed that having an MPL enhanced the stability of the polarization curves. Additional research has

shown the effects of MPL composition modification and PTFE treatment on performance [41, 92, 93]. However, the reason for the improved performance is still under debate. Proposed explanations for the improved performance are: i) forcing water towards the anode [94–97], ii) increasing the rate of water removal from the cathode CL to the channel [28, 74, 98, 99], and iii) removing the water in vapor form by increasing the temperature in the electrodes and also preventing condensed water at the GDL from entering the CL [1, 33, 100].

By studying a one-dimensional isothermal two-phase model, Weber and Newman [94] proposed that more water was being transported from cathode to anode once an MPL is inserted. The model predicted that since the MPL requires a higher capillary pressure to breakthrough compared to the GDL, the membrane liquid permeation flux from cathode to anode would increase. Baghalha et al. [95] observed the same water movement in numerical simulations when the PEM is more water-permeable than the MPL. By visualizing liquid water distribution in the gas channel, however, Spernjak et al. [96] observed more water at the anode gas channel when the fuel cell was operating at low current densities than at higher current densities. This contradicts the numerical predictions that at a higher current density, more water should be transported from cathode to anode due to increased liquid pressure in the cathode. Further, two MPLs with two drastically different breakthrough pressures were tested by Owejan et al. [1]. The experimental results showed that the performance is independent of MPL breakthrough pressure. The above experimental evidence highlights that it is unlikely that the MPL has an impact on membrane liquid permeation.

Another hypothesis is that the MPL helps to enhance the back-diffusion in the PEM due to a better vapor retention. This was shown by examining the electrochemical performance with varying MPLs [97]. However, the water flux measurements conducted by Karan et al. [91] and Atiyeh et al. [101] showed that adding an MPL at the cathode neither enhanced back-diffusion nor increased cathode water removal from the CL to the GDL.

Numerical models employed by Nam and Kaviany [28, 98] and Passaogullari and Wang [74, 99] showed that adding the MPL leads to an increase of the

cathode liquid water removal rate by alleviating the water accumulation at the MPL/CL interface. They both attributed the reduced saturation in the CL to the small pore size in the MPL. However, both studies were based on a cathode membrane electrolyte assembly (MEA) model that did not account for the membrane water transport.

By utilizing neutron radiography and numerical simulation, Weber and Hickner [100] concluded that water is being removed from the electrodes due to phase change induced (PCI) flow. Water evaporates in the CL and is transported in vapor form through the electrode. It then condenses away from the electrodes, along a temperature gradient from CL to GDL. Based on experimental observations from ex situ diffusive vapor flux and liquid permeation flux measurements as well as in situ electrochemical performance with varying MPLs, Owejan et al. [1] also hypothesized that PCI flow would be important. He also hypothesized that the MPL prevents the condensed water in the GDL from entering forming a liquid film at the GDL/CL interface, creating an in-plane diffusive path for reactant transport. These studies show that the thermal conductivity of the MPL has a great impact on improving cell performance.

More recently, in situ heat and water flux measurements conducted by Thomas et al. [33] showed that by inserting the MPL between CL and GDL, the temperature of the CL increased by at least 1° C at high current density when the MPL is introduced. The measured electrode temperature leads to a higher evaporation which facilitates the diffusive transport of the water vapor by creating a higher concentration gradient. The challenge remains in developing a numerical model coupling all the physical processes that are affected by the addition of the MPL in order to assess their importance. This requires a robust numerical model which accounts for gas and liquid convection, thermal effects, phase change, can operate under dry and wet conditions and contains the micro-structural information of the porous layer and its wettability. The two-phase model developed in this thesis is suitable for studying the functionality of the MPL.

1.4 Contributions of This Work

This thesis aims at developing a multi-dimensional, non-isothermal, two-phase model model that contains a mixed wettability PSD model capable of relating micro-structural information to transport properties in each fuel cell component. The model will then be validated with experimental data from both our laboratory and literature and used to better understand the effect of different components on fuel cell operation at high current density. The contributions of the thesis to the fuel cell scientific community are as follows,

1. developing and validating a novel, open source, non-isothermal two-phase flow model that accounts for micro-structural information [59],
2. illustrating the effects of CL microstructure and wettability on fuel cell performance [102],
3. analyzing the role of the MPL [103],
4. designing a novel electrode architecture, i.e., the electrode coated membrane.

The model developed in this thesis is a critical building block toward the development of a three dimensional transit unit cell model for fuel cells.

1.5 Structure of the Thesis

The thesis is organized into six chapters. Chapter 1 introduced the motivation of studying multi-phase flow in PEMFC, the background of basic fuel cell operations, fuel cell components and fuel cell testings. A literature review was provided to show the need of a multi-dimensional, non-isothermal, two-phase model that accounts for micro-structural effects and the studies that can be carried out using the model. Chapter 2 describes the MEA mathematical model, the numerical PSD closure equations, solution strategy and data post-processing. Chapter 3 outlines the experimental methods used for measuring the PSD, fabrication of catalyst coated membranes (CCMs), and the fuel cell

hardware and testing configurations, and input parameters. The proposed two-phase model is then validated against the experimental data measured in our laboratory and imaging data reported in literature. Parametric studies for CL and GDL hydrophobic contact angle, hydrophilic volume fraction and pore radius are performed by utilizing the model to highlight possible opportunities for improved structural design of porous media. Chapter 4 discusses the long debate in fuel cell literature regarding the role of the MPL. Parametric studies have been performed on MPL thermal conductivity, thickness and structural properties to show the actual critical role of evaporation on water removal and provide guidance on optimal MPL design. Chapter 5 illustrates the applicability of the model to the development of novel electrode architectures such as electrode coated membrane. Finally, Chapter 6 presents the final conclusions of this thesis and provides guidance in possible further researches in multi-phase transport in fuel cell modelling.

Chapter 2

Membrane Electrode Assembly Model

A multi-dimensional, non-isothermal, two-phase membrane electrode assembly (MEA) numerical model is developed where the micro-structure of the porous layers is characterized by a mixed wettability pore size distribution (PSD). The PSD model is used to predict local water saturation based on gas and liquid pressure, and can be used to study the effect of varying pore size and wettability. The PSD model predicts capillary pressure vs. saturation, saturation vs. relative liquid permeability and many other curves based on PSDs from several GDLs obtained using mercury intrusion porosimetry. The MEA model accounts for gas transport via convection, molecular and Knudsen diffusion, liquid water transport, sorbed water transport by back-diffusion, electro- and thermo-osmosis, and heat generation and transport. Multi-step kinetic models are used to predict anode and cathode electrochemical reactions. Local transport losses are accounted for using a local transport resistance.

2.1 Pore Size Distribution Model

The bundle of rejoined capillaries idealization is commonly used, in conjunction with a PSD [4, 30, 31], to estimate the transport properties in porous material under dry and wet conditions. The PSD model used in this thesis, proposed

Parts of this chapter have been published:
J. Zhou et al., A Mixed Wettability Pore Size Distribution Based Mathematical Model for Analyzing Two-phase Flow in Porous Electrodes I: Mathematical Model. *Journal of the Electrochemical Socieity* 164(6): F530-F539, 2017

by Mateo and Secanell [4], accounts for the porous media mixed wettability by means of different PSDs. It overcomes the shortcomings of previous PSD models, such as those proposed by Weber [31] and Eikerling [30], where either the individual hydrophilic and hydrophobic PSD cannot be studied unless two networks are uniformly distributed over the same pore size or single wettability was assumed.

In the PSD model [4, 30, 31], the Young-Laplace equation is used to relate capillary pressure, calculated using Darcy's law, to pore radius,

$$p_c = \frac{2\gamma cos(\theta)}{r_c} \tag{2.1}$$

where γ is the surface tension, θ is the contact angle, r_c is the critical pore radius and p_c is the capillary pressure. The capillary pressure is

$$p_c = p_{nonwetting} - p_{wetting} \tag{2.2}$$

where $p_{nonwetting}$ is the pressure in the non-wetting phase, and $p_{wetting}$ is the pressure in the wetting phase. In fuel cell applications, liquid water and the gas mixture are the non-wetting and wetting phases, respectively. Closure equations are then used to relate the critical pore radius at a given capillary pressure and the PSD to saturation, absolute permeability, relative gas/liquid permeability, liquid-gas interfacial surface and Knudsen radius.

2.1.1 Model Description

The PSD model is based on three main assumptions,

1. independent hydrophilic and hydrophobic pore networks,
2. pores are of cylindrical shape,
3. wetting fluid has access to all pores.

Figure 2.1 shows an idealized diagram of the partially saturated, sliced and randomly reconstructed array of capillaries. The diagram shows that the pores are connected through the space between the slices, i.e., the wetting fluid

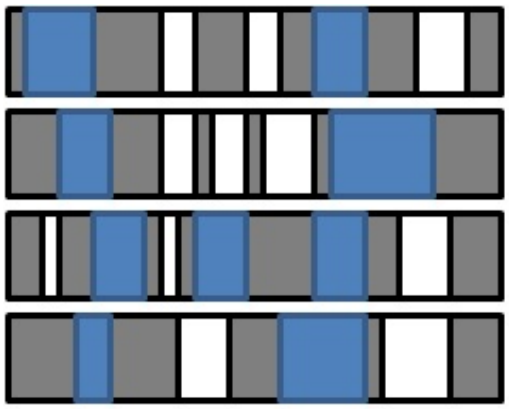

Figure 2.1 – Diagram of illustrating a partially saturated porous media, reprinted with permission [4].

has access to all pores. When estimating the transport parameters such as absolute permeability, the connectivity of the pores needs to be considered. This is accounted in the model by introducing a parameter λ_{PSD} which will be discussed in the later section. Based on the Young-Laplace equation (2.1), the smaller hydrophilic pores are filled first, followed by the bigger hydrophilic pores, the larger hydrophobic pores and finally smaller hydrophobic pores.

A summation of log-normal distributions is used to approximate the PSD. The PSD can be divided into a collection of log-normal distributions over the pore sizes representing the hydrophilic and hydrophobic pore networks, respectively. The initial form of the mixed wettability PSD model is:

$$\frac{dX}{dr} = \frac{1}{V_T}\frac{dV(r)}{dr} = \frac{1}{V_T}\left[\frac{dV_{\mathrm{HI}}}{dr} + \frac{dV_{\mathrm{HO}}}{dr}\right] \tag{2.3}$$

where V_T is the total pore volume and $dV(r)/dr$ is the differential accumulated pore volume with respect to a change in pore radius dr. $X(r)_{HI}$ is the normalized volume of hydrophilic pores per total pore volume. The expanded PSD model takes the form:

$$\frac{dX}{dr} = \left\{ F_{\mathrm{HI}} \sum_{k=1}^{N} \left[\frac{f_{\mathrm{HI},k}}{r\, s_{\mathrm{HI},k}\sqrt{2\pi}} E_{\mathrm{HI},k} \right] + F_{\mathrm{HO}} \sum_{k=1}^{M} \left[\frac{f_{\mathrm{HO},k}}{r\, s_{\mathrm{HO},k}\sqrt{2\pi}} E_{\mathrm{HO},k} \right] \right\} \tag{2.4}$$

where $E_{\mathrm{HI},k}$ and $E_{\mathrm{HO},k}$ are:

$$E_{\mathrm{HI},k} = \exp\left(- \left[\frac{\ln(r) - \ln(r_{\mathrm{HI},k})}{s_{\mathrm{HI},k}\sqrt{2}} \right]^2 \right) \tag{2.5}$$

$$E_{\mathrm{HO},k} = \exp\left(-\left[\frac{\ln(r) - \ln(r_{\mathrm{HO},k})}{s_{\mathrm{HO},k}\sqrt{2}}\right]^2\right) \tag{2.6}$$

F_{HI} *and* F_{HO} are the volume fractions of the hydrophilic and the hydrophobic pores, respectively; $f_{i,k}$ is the partial contribution of sub-distribution functions from mode k in either the hydrophilic or the hydrophobic pore network (referred here with index i); $r_{i,k}$ is the characteristic pore radius of sub-distribution functions from mode k; and $s_{i,k}$ is the standard deviation. The parameters to define the overall PSD (hydrophilic and hydrophobic) are f_k, r_k and s_k. In the hydrophilic or hydrophobic phase, r_k and s_k remain the same as $r_{i,k}$ and $s_{i,k}$, respectively. In terms of f_k, it accounts for the contributions from both phases as,

$$\begin{aligned} f_k =& F_{\mathrm{HI}} f_{\mathrm{HI},k} + F_{\mathrm{HO}} f_{\mathrm{HO},k} \\ s.t. \quad & \sum_k f_{HI,k} = 1 \\ & \sum_k f_{HO,k} = 1 \end{aligned} \tag{2.7}$$

2.1.2 Experimental Measurement

Mercury Intrusion Porosimetry - Mercury intrusion porosimetry is commonly adopted by the fuel cell scientific community to characterize the pore size distribution and porosity of porous materials [104, 105]. In this thesis, this is accomplished using a PoreMaster 33 from Quantachrome. To perform a test, the sample is loaded into a penetrometer, which consists a glass capillary stem connected to the pressure chamber, a sample cup as the head, and a cell contact assembly for sealing. The penetrometer is sealed and placed into the low pressure station for evacuation and low pressure test. Since mercury is highly hydrophobic for most porous materials and it has very low vapor pressure, it will intrude different pores at varying pressure and the gas pressure can be assumed to be zero such that liquid pressure is the same as the capillary pressure. Therefore, the mercury is used as the working fluid. Young-Laplace equation (2.1) is used to relate capillary pressure to pore size by assuming

a constant surface tension (480 mN/m) and contact angle (140°) at room temperature during the test. This assumption is reasonable as the change in temperature during the experiments is small. After evacuation, the mercury automatically fills the penetrometer's cup and capillary stem. During the low-pressure test, nitrogen gas is used to pressurize the mercury and mercury intrudes into the sample pores starting from the biggest. The pressure range is from 0.004 psi to 54 psi. After the low pressure test, samples are transferred to the high pressure testing station where hydraulic oil (Quantachrome, 01098) is used to further increase the pressure to 33,000 psi.

The instrument automatically collects the pressure data and absolute volume intruded. An example of the raw data for SGL 24BA is shown in Figure 2.2.

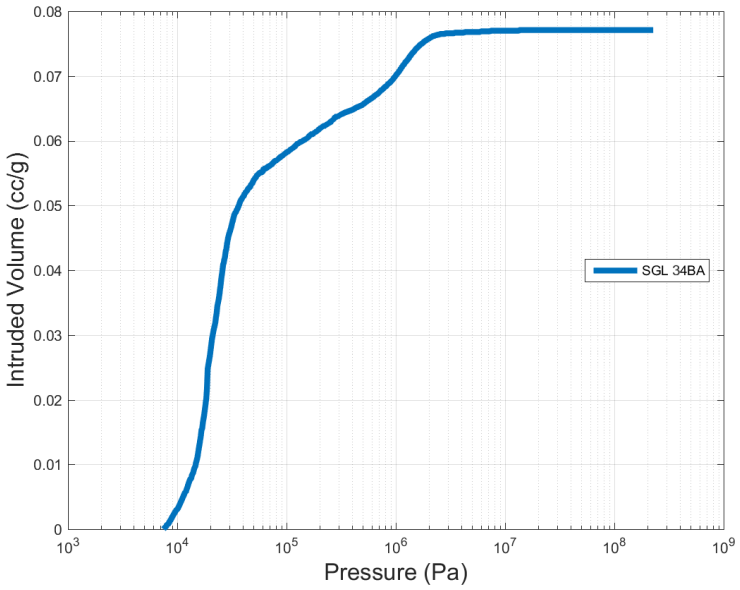

Figure 2.2 – Raw data, capillary pressure vs. intruded volume for SGL 34BA.

The raw data is processed to obtain the PSD. The intruded volume is normalized with total intruded volume and the change of the normalized volume with respect to the change of pore radius is used to define the PSD,

$$\frac{dX}{dr} = \frac{1}{V_T}\frac{dV}{dr} = \frac{1}{V_T}\left[\frac{V_{n+1} - V_n}{r_{n+1} - r_n}\right] \tag{2.8}$$

where V_T is the total intruded volume, V_n is accumulated intruded volume at experimental step n and r_n is the corresponding pore radius, dV is the increment of intruded volume at each step, and dr is the increment of pore radius. In order to highlight the pore radius, the PoreMaster 33 reports the PSD in logarithmic scale as,

$$\frac{dX}{d(ln(r))} = r\frac{dX}{dr} \tag{2.9}$$

Figure 2.3 shows an example of PSD for SGL 34BA.

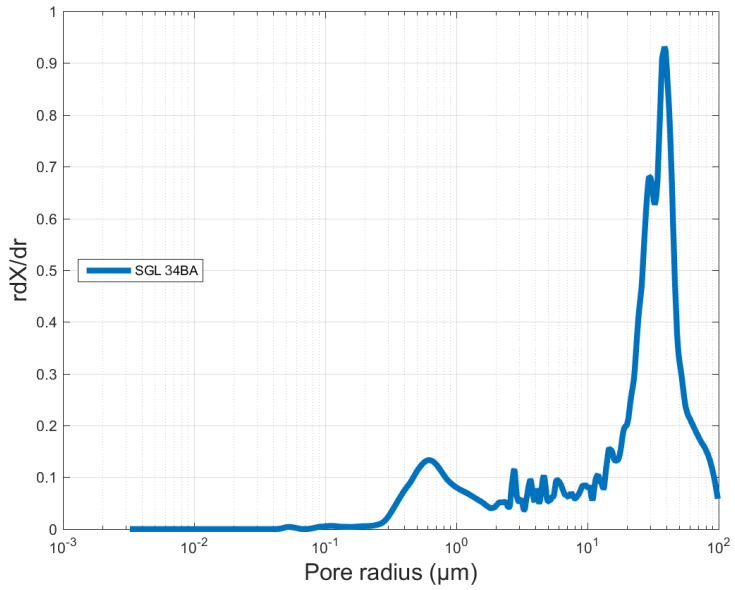

Figure 2.3 – PSD for SGL 34BA.

The hydrophobic phase of the porous material should be characterized by water intrusion porosimetry, however, due to the difficulties in removing the air bubbles in the porosimetry, in-house water intrusion porosimetry cannot be performed.

A typical experimental procedure for obtaining the PSD of a GDL is presented. Before the experiment, the porous samples are dried in an oven at 80°C for about 5 hours to remove the irreducible saturation and humidity. Six GDL samples are then cut into strips of size 2 cm by 0.8 cm, and weighted with and without the penetrometer before putting them in the low pressure station. The penetrometer is then evacuated up to an absolute pressure of

0.004 psi, and then, further evacuated for 30 minutes. The cell is then filled with mercury and slowly pressurized to a maximum pressure of 44 psi at the low pressure station. The weight of the penetrometer filled with mercury is recorded and then it is transferred to the high pressure station. Before putting it into the high pressure station, a tiny amount of mercury is exchanged with hydraulic oil at the end of the cell stem. At the high pressure station, the mercury is further pressurized to a maximum pressure of 33000 psi. The intruded volume of mercury at each pressure is recorded. The Young-Laplace equation is used to estimate the PSD from the cumulative pore volume curve. The machine pore diameter range is between 950 μm and 6.4 nm

2.1.3 Fitting Procedure to Obtain a Pore Size Distribution

The experimentally obtained PSD data is in discrete form. Parameters described in Eq. (2.4) to define the log-normal distributions need to be obtained. This is achieved by solving the following least-square minimization problem,

$$\begin{aligned} \text{Minimize} \quad & \sum_{i=1}^{Np} \left[\frac{\Delta X_i}{\Delta r_i} - \sum_k \left(\frac{F_H \, f_{H,k}}{r_i \, s_{H,k} \sqrt{2\pi}} E_{H,k,i} \right) \right]^2 \\ s.t. \quad & 0 \leq f_k \leq 1 \\ & 0 < s_k \leq 5 \\ & 0 < r_k \leq 1 \times 10^{-3} \\ & \sum_k f_k = 1 \end{aligned} \tag{2.10}$$

where

$$E_{H,k,i} = \exp\left(- \left[\frac{\ln(r_i) - \ln(r_{H,k})}{s_{H,k}\sqrt{2}} \right]^2 \right) \tag{2.11}$$

The term $\Delta X_i / \Delta r_i$ represents the experimentally measured increment of normalized pore volume which can be expressed in the form of $\Delta X_i = X_i - X_{i-1}$,

when i equals to one, the term X_{i-1} is zero. The term Δr_i is the increment of pore radius. H represents hydrophilic or hydrophobic phase.

The upper bound for s_k is determined practically during the fitting process and higher than 5 makes the distribution too wide to represent a realistic PSD. As the pores in GDL, MPL and CL are smaller than 1 mm, r_k is bounded from 0 to 1 mm. The range of f_k is from 0 to 1 since the PSD is a normalized function which represents the cumulative volume over total volume of a porous layer, no weight distribution f_k can be greater than 1. The sum of the multiple weight distributions should be unity.

Attempts were made in Matlab to solve the least-square fitting problem using the solver LSQNONLIN, however, since it is a gradient-based solver, convergence is an issue due to the local optimal solutions. Improvements are made with LibreOffice using Differential Evolution and Particle Swarm Optimization (DEPS) evolutionary solver. DEPS consists of two independent algorithms, Differential Evolution and Particle Swarm Optimization and they are complementary to each other in that they even out each other's shortcomings. The detailed explanation for DEPS can be found in [106]. With the DEPS solver, a good fitting is achieved.

To fit the PSD shown in Figure 2.3, two modes are required in the PSD model as two distinguishable peaks are observed. By solving the least-square problem, overall PSD parameters are obtained as shown in Table 2.1. Figure 2.4

Table 2.1 – PSD parameters for SGL 34BA

Parameter		Value
		SGL 34BA
PSD properties		
Characteristic pore radius (μm)	r_1	36.00
	r_2	18.00
Characteristic pore widths	s_1	0.3
	s_2	2.2
Characteristic pore fraction	f_1	0.56
	f_2	0.44

(a) shows the experimental data and numerical fitting with two separate mode, and Figure 2.4 (b) shows the overall PSD.

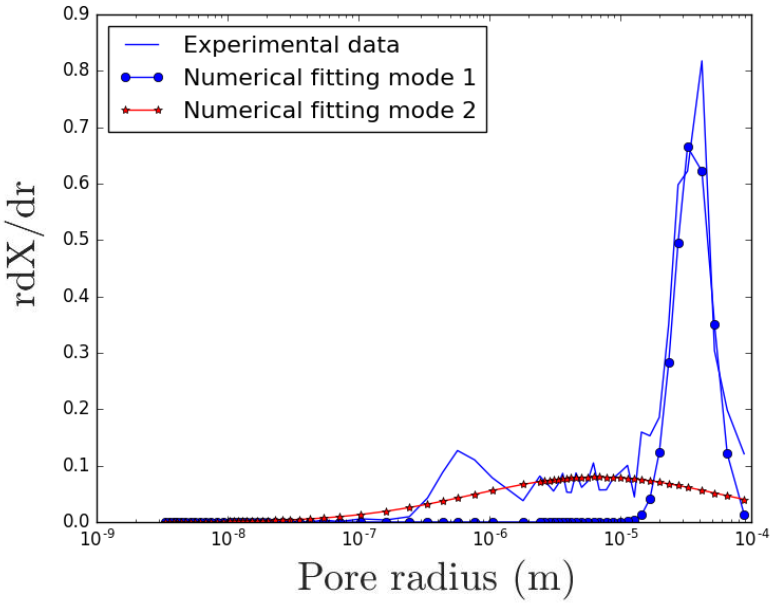

(a)

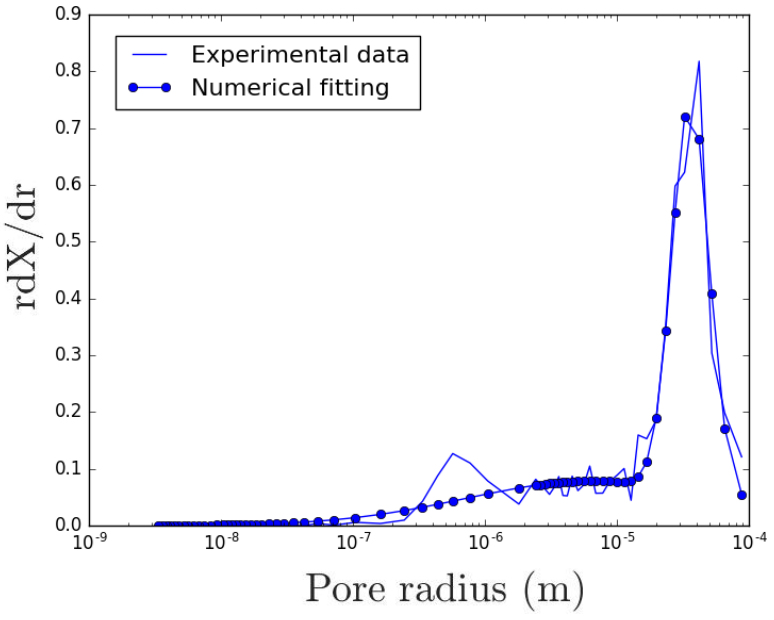

(b)

Figure 2.4 – Numerically fitted PSD: (a) mode one and mode two, separately, and (b) overall PSD.

2.1.4 Saturation

When the liquid water is present in the porous layer, saturation can be used to quantify the amount of liquid water and can be represented as,

$$S = \frac{V_l}{V_{pore}} \tag{2.12}$$

where V_l is the volume occupied by liquid water in the pore space and V_{pore} is the total pore volume. In the PSD model, saturation is estimated by integrating the contributions from all pores in the porous media as follows:

$$S = S_{\mathrm{HI}} + S_{\mathrm{HO}} = \int_0^{r_{\mathrm{HI}}} \frac{dX(r)_{\mathrm{HI}}}{dr}\, dr + \int_{r_{\mathrm{HO}}}^{\infty} \frac{dX(r)_{\mathrm{HO}}}{dr}\, dr \tag{2.13}$$

for the hydrophilic phase, the limits of integration start from zero pore radius to effective critical pore radius r_{HI} as small pores will be filled first. For the hydrophobic phase, the integration limits begin from effective pore radius r_{HO} to a pore radius of infinity as the large pores in the hydrophobic phase will be filled first.

Solving the integral above analytically, an explicit equation for saturation is obtained [4]:

$$\begin{aligned} S = F_{\mathrm{HI}} \sum_k \frac{f_{\mathrm{HI},r,k}}{2} \left[1 + \mathrm{erf}\left(\frac{\ln(r_{c,\mathrm{HI}}) - \ln(r_{\mathrm{HI},k})}{s_{\mathrm{HI},k}\sqrt{2}}\right)\right] \\ + F_{\mathrm{HO}} \sum_k \frac{f_{\mathrm{HO},k}}{2} \left[1 - \mathrm{erf}\left(\frac{\ln(r_{c,\mathrm{HO}}) - \ln(r_{\mathrm{HO},k})}{s_{\mathrm{HO},k}\sqrt{2}}\right)\right] \end{aligned} \tag{2.14}$$

2.1.5 Permeability

Absolute permeability: In porous materials, permeability is a measure of the material's resistance to fluid transport, i.e., a material with high permeability offers very little resistance to fluid flow. Its value is affected by material's porosity, shape of the pores, and connectivity of the pores. In the PSD model, the mean velocity of a cylindrical pore is estimated using Darcy's law. Combining Darcy's law with the solutions for Newtonian viscous flow through a circular cross section pipe (Poiseuille flow), the absolute permeability in a circular capillary can be estimated as [107],

$$k = \frac{r^2}{8} \tag{2.15}$$

where r is the capillary radius. The overall absolute permeability is calculated by integrating the contributions from all pores in the layer:

$$k_{\text{sat}} = \left[\frac{\varepsilon_o}{\lambda_{\text{PSD}}}\right]^2 \int_0^\infty \frac{r^2}{8}\frac{dX}{dr}dr \tag{2.16}$$

where ε_o is the porosity and λ_{PSD} represents the interconnectivity of the pores. The term in front of the integral represents the probability of finding two interconnected pores. Combining equation (2.4) with the previous equation, (2.16), and solving the integrals, the absolute permeability in a fully saturated porous medium is [107]:

$$k_{\text{sat}} = \frac{1}{8}\left[\frac{\varepsilon_o}{\lambda_{\text{PSD}}}\right]^2 \sum_k r_k^2 f_k \, \exp\left(-2\, s_k^2\right) \tag{2.17}$$

Relative liquid permeability: The relative liquid permeability is determined as the ratio between the effective liquid permeability and the absolute permeability as follows [107]:

$$k_{rl} = \frac{1}{8k_{sat}}\left[\frac{\varepsilon_o\, S}{\lambda_{\text{PSD}}}\right]^2 \left[\int_0^{r_{\text{HI}}} r^2 \frac{dX(r)_{\text{HI}}}{dr}dr + \int_{r_{\text{HO}}}^\infty r^2 \frac{dX(r)_{\text{HO}}}{dr}dr\right] \tag{2.18}$$

where all terms except k_{sat} account for the contributions of a partially saturated layer from both hydrophilic and hydrophobic pores.

The analytical form to get hydrophilic and hydrophobic contributions can be found in Appendix A.1.

Relative gas permeability: The relative gas permeability, defined as the ratio of gas permeability and absolute permeability, is estimated using [107]:

$$k_{rg} = \frac{1}{8k_{\text{sat}}}\left[\frac{\varepsilon_o\,(1-S)}{\lambda_{\text{PSD}}}\right]^2 \left[\int_{r_{\text{HI}}}^\infty r^2 \frac{dX(r)_{\text{HI}}}{dr}dr + \int_0^{r_{\text{HO}}} r^2 \frac{dX(r)_{\text{HO}}}{dr}dr\right] \tag{2.19}$$

The integrals in equation (2.19) can be solved analytically resulting in the final expressions provided in Appendix A.2.

2.1.6 Liquid-Gas Interfacial Surface Area

To account for the possibility of having a common area for liquid and gas between filled and empty capillaries, a probability density function is defined:

$$\mathrm{P}_b = \frac{a(r)_c}{a_{max}}\left(1 - \frac{a(r)_c}{a_{\max}}\right) \tag{2.20}$$

where $a(r)_c$ is the liquid invaded cross-section area per unit volume of cylindrical pores and a_{max} is the total cross-section area per unit volume which is estimated as:

$$a_{\max} = \sum_k \frac{f_k \exp\left(\frac{s_k^2}{2}\right)}{4\, r_k} \tag{2.21}$$

The probability function forces the liquid-gas interfacial surface area to be zero either when the layer is fully dry or fully wet, whereas when the layer is partially saturated, there exists a maximum value for the interfacial surface area.

The cross sectional area per unit volume is determined by taking the ratio between the cross-section area (πr^2) of the pore and its volume ($\pi r^2 L$):

$$a(r)_c = \frac{a(r)}{V_T} = \int_0^{r_{\mathrm{HI}}} \frac{1}{L}\frac{dX_{\mathrm{HI}}}{dr}dr + \int_{r_{\mathrm{HO}}}^{\infty} \frac{1}{L}\frac{dX_{\mathrm{HO}}}{dr}dr \tag{2.22}$$

where V_T is the total pore volume and L is the length of the cylindrical pores which is estimated as $4r$ as proposed in [30] due to a lack of experimental data.

The interfacial surface area expressions for hydrophilic and hydrophobic pores can be found in Appendix A.3. The overall expression for the interfacial surface area per unit volume is:

$$a_v(r) = \mathrm{P}_b \cdot a_{\max} \tag{2.23}$$

2.1.7 Average Knudsen Radius

The average capillary radius is estimated by taking the ratio between pore volume ($\pi r^2 L$) and the lateral area surface ($2\pi r L$), and multiplying by two to get the radius [4]:

$$r_{\mathrm{Kn}} = 2\frac{V(r)}{a_{\mathrm{wall}}(r)} = 2\frac{\displaystyle\int_{r_{\mathrm{HI}}}^{\infty} \frac{1}{V_T}\frac{dV_{\mathrm{HI}}(r_{\mathrm{HI}})}{dr}dr + \int_0^{r_{\mathrm{HO}}} \frac{1}{V_T}\frac{dV_{\mathrm{HO}}(r_{\mathrm{HO}})}{dr}dr}{\displaystyle\int_{r_{\mathrm{HI}}}^{\infty} \frac{1}{V_T}\frac{da_{\mathrm{wall,HI}}(r_{c,\mathrm{HI}})}{dr}dr + \int_0^{r_{\mathrm{HO}}} \frac{1}{V_T}\frac{da_{\mathrm{wall,HO}}(r_{\mathrm{HO}})}{dr}dr} \tag{2.24}$$

where the lateral area per unit volume is given by:

$$a_{\mathrm{wall}} = \int_0^{\infty} \frac{a_{\mathrm{Lateral}}}{V_T} = \int_0^{r_{\mathrm{HI}}} \frac{2}{r}\frac{dX(r)_{\mathrm{HI}}}{dr}\,dr + \int_{r_{\mathrm{HO}}}^{\infty} \frac{2}{r}\frac{dX(r)_{\mathrm{HO}}}{dr}\,dr \tag{2.25}$$

The radius calculated for Knudsen diffusion accounts for the collision between gas molecules and pore walls. Therefore, the limits of the integral over the pores are switched to estimate the volume of gas pores. The detailed integral expressions are in Appendix A.4.

2.1.8 PSD Model Validation

2.1.8.1 Gas diffusion layer

Figure 2.5 shows the experimentally measured (the average of three sets of data) and numerically fitted PSDs for SGL 34BA and Toray 090 (20% PTFE). The method of least squares and equation (2.3) are used to fit the experimental data in a LibreOffice spreadsheet. It can be seen from Figure 2.5 that the numerical fittings agree with the experimental PSDs in both cases. The pores in SGL 34BA (see Figure 2.5 (a)) are centered at 14.2 μm and 34.0 μm, respectively. It has a wider pore size range as compared to Toray 090 which is characterized by two modes centered at 18.0 μm and 23.0 μm (see Figure 2.5 (b)). The percentage of hydrophilic pores assigned to each GDL is obtained by fitting the residual liquid saturation. Although the residual saturation cannot be interpreted as evidence of hydrophilic pores, because residual saturation might also be due to pore geometry and connectivity, it is used in the model to represent the hydrophilic pores because it accounts for the liquid water that cannot be easily removed from the porous material. The smaller PSD mode is assigned to the hydrophilic phase as shown in Figure 2.5.

The capillary pressure vs. saturation relationships obtained from the PSD model are compared against the experimental data of several GDLs in Figure 2.6. First, to validate the PSD implementation, the experimentally measured capillary pressure-saturation relationship for SGL 10AA is reproduced using the parameters reported by Weber et al. [84]. With the correct implementation, the capillary pressure-saturation relationship for SGL 34BA is then compared to the experimental data of SGL 10AA and SGL 10BA reported by Gostick et al. [83]. The numerically predicted capillary pressure-saturation relationship for Toray 090 is also compared to the experimental data reported

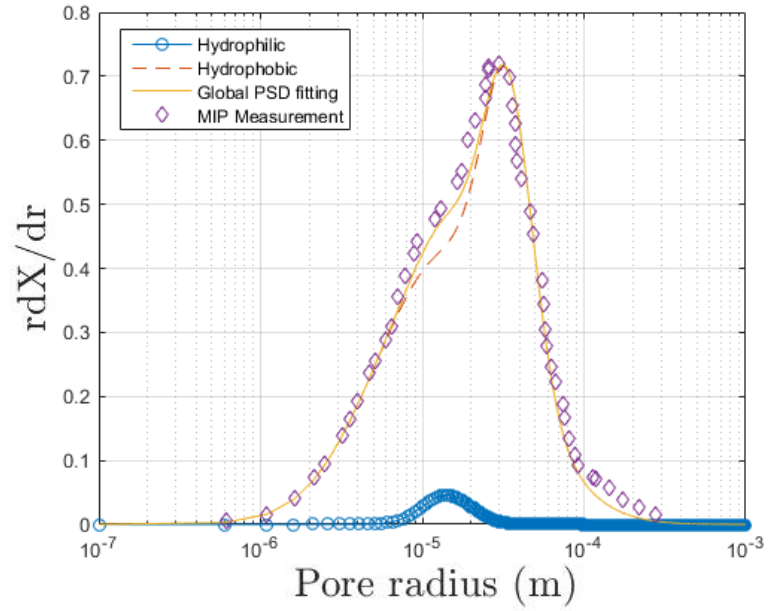

(a)

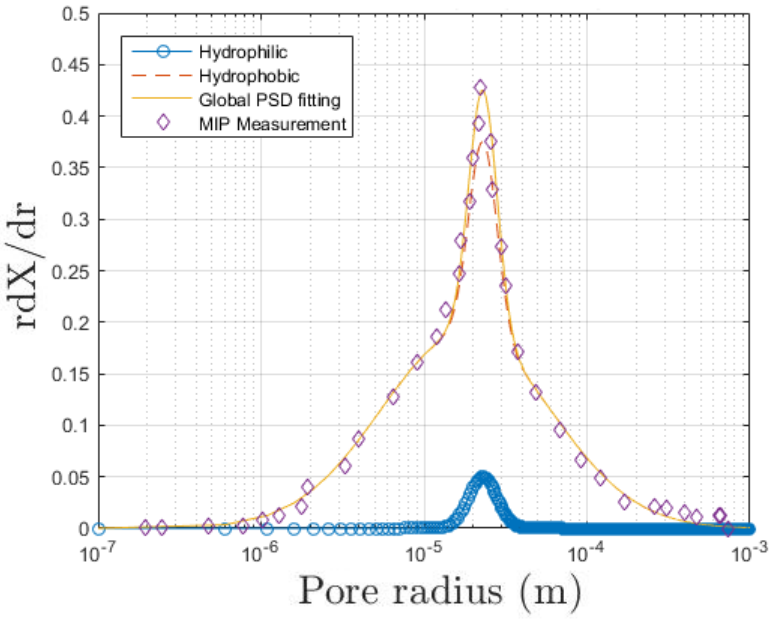

(b)

Figure 2.5 – Experimentally measured and numerically fitted PSDs for: (a) SGL 34BA and (b) Toray 090.

by Gostick et al. [83] and Fairweather et al. [108] in Figure 2.6 (b). The predicted values for SGL 34BA and Toray 090 are within the values reported for the same type of GDLs in [83, 108]. The model can provide reasonable

results. It is known that the capillary pressure vs. saturation relationship shows hysteresis [83, 108]. Only the imbibition (water filling into the porous material) is used in this thesis because it is assumed that water enters the layer following an imbibition process but is usually removed by evaporation instead of drainage (water removing from porous material by injecting gas) in an operating fuel cell.

The measurements of GDL relative permeability have not received much attention during the past decades. It is only recently that the relative liquid water permeability was measured by Hussaini et al. [109], Luo et al. [110] and Koido et al. [111]. Alternatively, numerical models such as the PSD model developed in this thesis or pore network model [60] can be used to estimate the relative permeability.

The relative liquid permeability predicted by the Toray 090 and SGL 34BA PSD models are shown in Figure 2.7. The values are between the simulation results reported by Luo et al. [110] and Koido et al. [111]. The difference in results is because Luo et al. [110] used a pore network model and Koido et al. [111] used the lattice Boltzmann method. The absolute permeabilities of the two GDLs have been matched with literature reported values [112, 113] by setting the interconnectivity factor λ_{PSD} in the PSD model to be 1.26 and 2.00 for SGL 34BA and Toray 090, respectively.

The GDL absolute permeabilities have been reported in various studies [112, 114–121]. It has been shown that the absolute permeability depends on many factors such as level of compression, type of carbon black, percentage of PTFE content and PSD. The typical GDL permeability falls mostly within the range of 10^{-12} to 10^{-10} m^2.

Figure 2.8 shows the PSD model predicted saturation vs. liquid-gas interfacial surface area for SGL 34BA and Toray 090. It can be seen from the figure that Toray 090 has larger liquid-gas interfacial surface area as compared to SGL 34BA at high saturation. This is because the overall pores size is smaller in Toray 090 resulting in higher opportunities for liquid water filled pores to connect with gas filled pores.

As the pores in the GDL are in μm (see Figure 2.5), the molecular diffusion

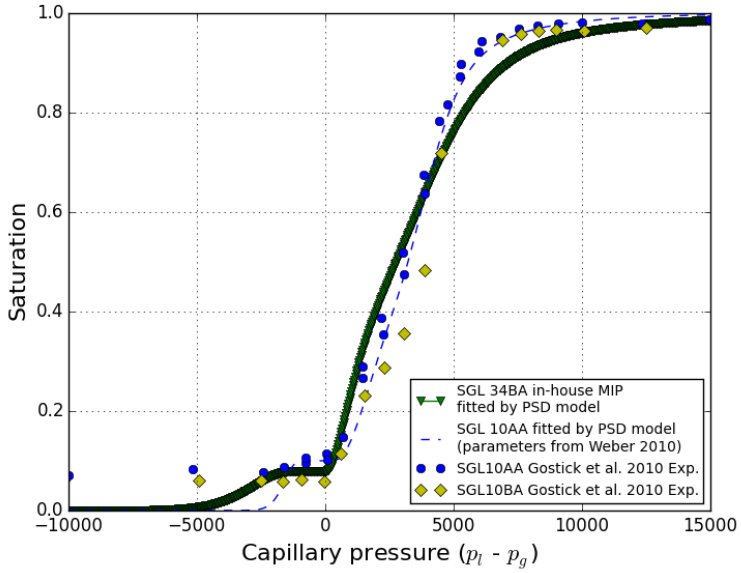

(a)

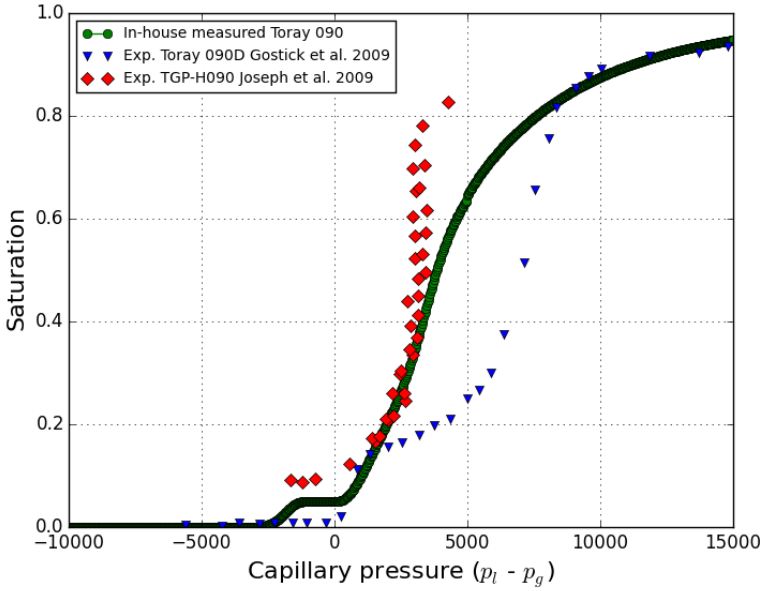

(b)

Figure 2.6 – The validation of the capillary pressure vs. saturation curves for (a) SGL 34BA and (b) Toray 090: experimental data (points) and model predictions (point lines).

is dominant. To estimate the effective diffusivity in the GDL, the partially-saturated carbon fiber diffusion layer model proposed by Garcia-Salaberri et

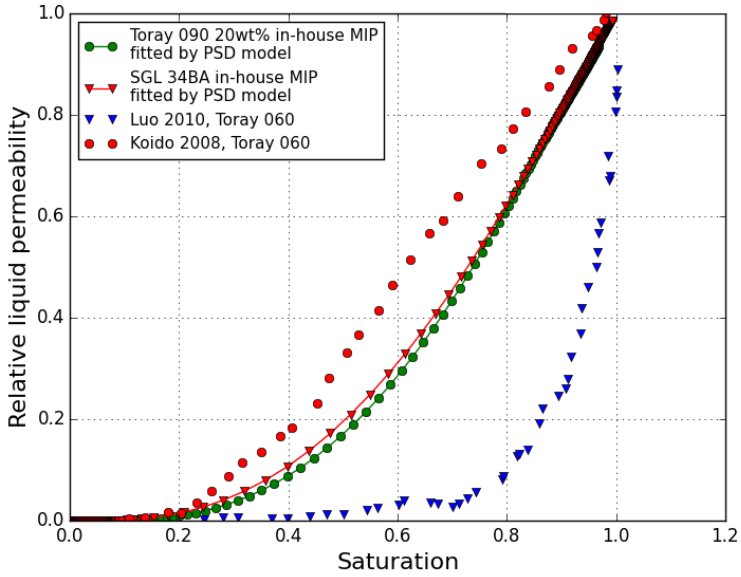

Figure 2.7 – Saturation-relative liquid permeability relationship for SGL 34BA and Toray 090 as compared to literature, literature data (points) and model predictions (point lines).

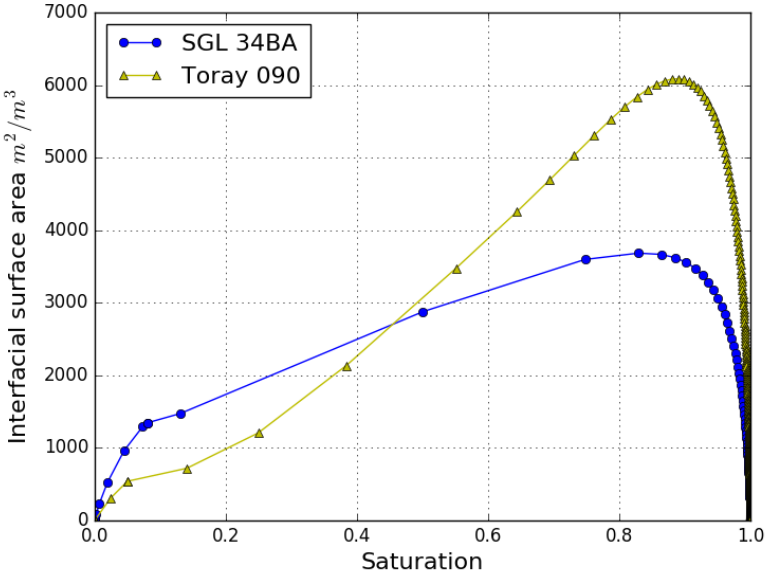

Figure 2.8 – Saturation vs. liquid-gas interfacial surface area for SGL 34BA and Toray 090.

al. [122] is used for both in-plane and through-plane directions. The effective

gas diffusivity is:

$$D_g^{\text{eff}} = \frac{\epsilon D_i}{\tau}(1-s)^n \tag{2.26}$$

where ϵ is the porosity, τ is the tortuosity, s is the local saturation and n is the exponent which characterizes the impact of liquid water saturation on diffusive gas transport, i.e., n is 3.5 in the through-plane direction and n is 2.5 in the in-plane direction.

The bundle of capillaries idealization appears to provide reasonable agreements with the experimental data as shown in Figure 2.6. The connectivity between the pores is accounted for only when estimating the absolute permeability using λ_{PSD} in equation (2.16). The λ_{PSD} reflects interconnection between randomly rejoined capillaries and is determined by fitting the experimentally measured absolute permeability. In estimating the rest of the parameters, i.e., liquid-gas interfacial surface area and average Knudsen radius, information about connectivity is lost in the PSD model as compared to a pore network [60] or micro-scale simulation [62]. The pore geometry, which might be also important, is idealized in all cases (including in micro-structures when a morphological image opening depth is used [60]). Discrepancies between experimental data and PSD model predictions in Figure 2.6 and 2.7 might be due to the lack of consideration of the above features in the PSD model.

2.1.8.2 Catalyst layer

Figure 2.9 (a) shows the CL PSD fitting, with the parameters in Table 2.2, against the experimental MIP data.

The percentage of hydrophilic pores used in the PSD model is assumed to be 25% since the capillary pressure-saturation relationship for doctor blade CL has not been reported in the literature. The doctor blade CL is a CL fabricated by spreading the ink over a substrate using a doctor blade. A parametric study on hydrophilic volume fraction in CL is provided in the next chapter. To validate the ability of the model to reproduce capillary pressure-saturation relationships, the experimental data reported by LaManna et al. [5] was reproduced (see Figure 2.9 (c)) using the PSD in Figure 2.9 (b) (provided

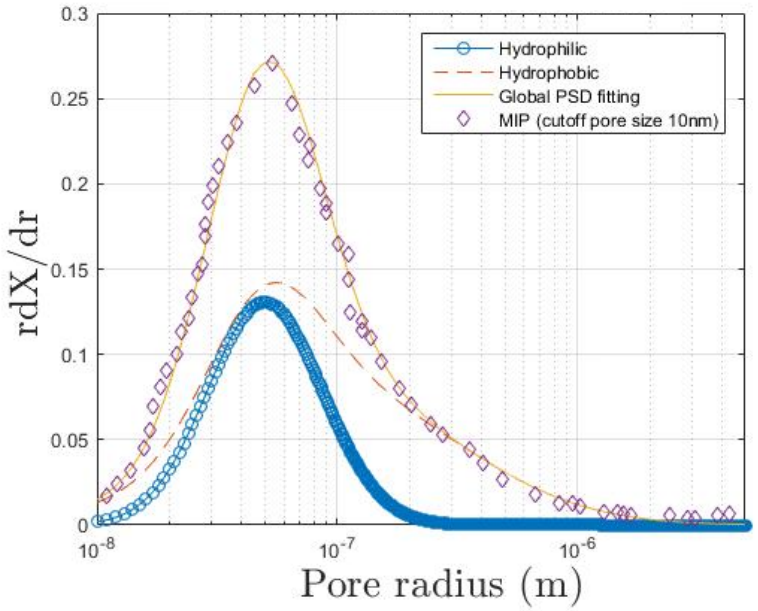

(a)

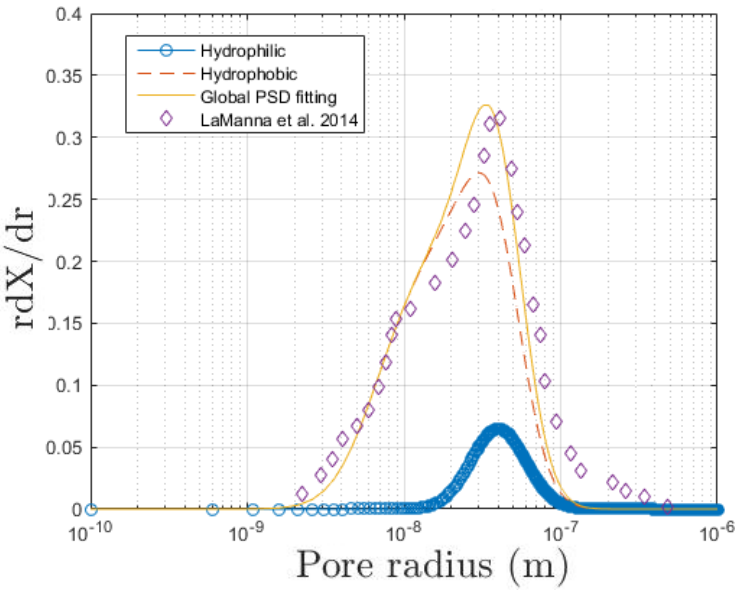

(b)

Figure 2.9 – (a) Experimentally measured PSD using MIP for Doctor blade CL and its fitting, (b) the PSD reported by LaManna et al. [5] and its fitting.

by LaManna et al. [5]). Figure 2.10 also compares the capillary pressure vs. saturation relationships between a doctor blade CL and the CL reported

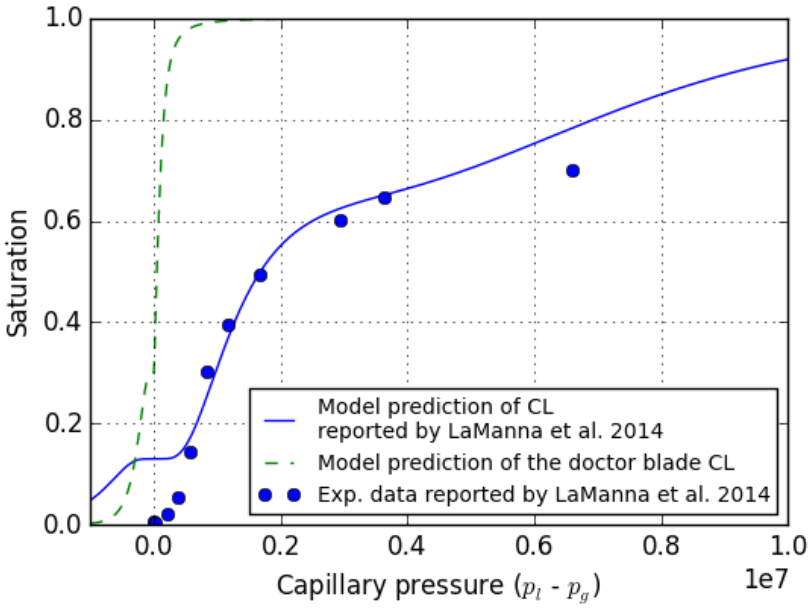

Figure 2.10 – Capillary pressure-saturation relationships of the model predictions and the experimental data [5].

by LaManna et al. [5]. The original data reported by LaManna et al. [5] are multiplied by cos(99°) in order to account for the assumed contact angle for water in this thesis. The assumed contact angle of 99° is reported by Zawodzinski et al. [124]. The two are remarkably different likely because the CL structures are very different. The pores in the doctor blade CL are centered at 50 nm and 100 nm respectively, with the smaller pores assumed to be in the hydrophilic phase. Whereas, the majority of pores in the CL reported by LaManna et al. [5] are less than 50 nm. Therefore, the difference in capillary pressure-saturation relationship between the two CLs is due to the different PSDs with higher capillary pressure required to invade the smaller hydrophobic pores in the CL reported by LaManna et al. [5].

The saturation vs. relative liquid permeability and vs. interfacial surface area of the CL are shown in Figure 2.11. As compared to the GDLs, a similar increase of relative liquid permeability with saturation is observed. The CL interfacial surface area is about two orders of magnitude higher than the GDL due to the smaller PSD in CL.

Inside the pore space of the CL, the length scale of the capillary radius is

Table 2.2 – Input parameters for GDL and CL

Parameter		Value		
		Toray 090 (20%$PTFE$)	SGL 34BA (5%$PTFE$)	CL
PSD properties				
Characteristic pore radius (μm)	r_1	23.00	14.20	0.05
	r_2	18.00	34.00	0.10
Characteristic pore widths	s_1	0.20	0.35	0.55
	s_2	1.20	1.00	1.20
Characteristic pore fraction	$f_{HI,1}$	1.00	1.00	1.00
	$f_{HI,2}$	0.00	0.00	0.00
	$f_{HO,1}$	0.20	0.39	0.29
	$f_{HO,2}$	0.80	0.61	0.71
Hydrophilic volume fraction (%)	F_{HI}	5 [83]	8[83]	25
Porosity	ε	0.69 (MIP)	0.74 (MIP)	0.42
Thickness (cm)	δ	2.70×10^{-2} [112]	2.60×10^{-2} [112]	5.02×10^{-4} (SEM)
Absolute permeability (m^2)	k_{abs}	6.66×10^{-12} [112]	1.88×10^{-11} [113]	1.00×10^{-18} [30]
Contact angle (hydrophilic) (°)	θ_{HI}	70 [83]	70 [83]	84 [66]
Contact angle (hydrophobic) (°)	θ_{HO}	130 [108]	122 [104]	93 [123]

comparable to the mean free path of the diffusion particles and Knudsen diffusion is important. The Knudsen diffusion coefficient of species i is estimated as:

$$D_i^K = \frac{2\, r_{\mathrm{Kn}}}{3} \sqrt{\frac{8\, R_g\, T}{\pi\, M_i}} \tag{2.27}$$

where M_i is the molar mass of species i, T is the temperature and R_g is the gas constant. The effects of molecular and Knudsen diffusivity are combined using the Bosanquet equation [125]:

$$D_i = \left[\frac{1}{D_{ij}} + \frac{1}{D_i^K} \right]^{-1} \tag{2.28}$$

where D_{ij} is the binary molecular diffusion coefficient.

The effective diffusivity of the CL is estimated using percolation theory [126]:

$$D_g^{\mathrm{eff}} = D_i (1-s)^{\gamma} \left(\frac{\epsilon_V^{cl} - \epsilon_{th}}{1 - \epsilon_{th}} \right)^{\mu} \theta(\epsilon_V (1-s) - \epsilon_{th}) \tag{2.29}$$

where ϵ_V^{cl} is the volume fraction of void space in CL, γ is the exponent which accounts for the loss of mass transport due to liquid water, ϵ_{th} and μ are constants that depend on the orientation of the components in CL and the function $\theta(\epsilon_V(1-s) - \epsilon_{th})$ is the Heaviside unit step function. In this thesis, μ is 2.0 based on [127], γ is assumed to be the same as μ, and ϵ_{th} is 0.25 as it provides good agreement with the experimental data reported by Yu et al. [6] as shown in Figure 2.12. Figure 2.12 shows the predicted value using the expression in the thesis for the CL under study ($r_{\mathrm{Kn}} = 100$ nm) as well

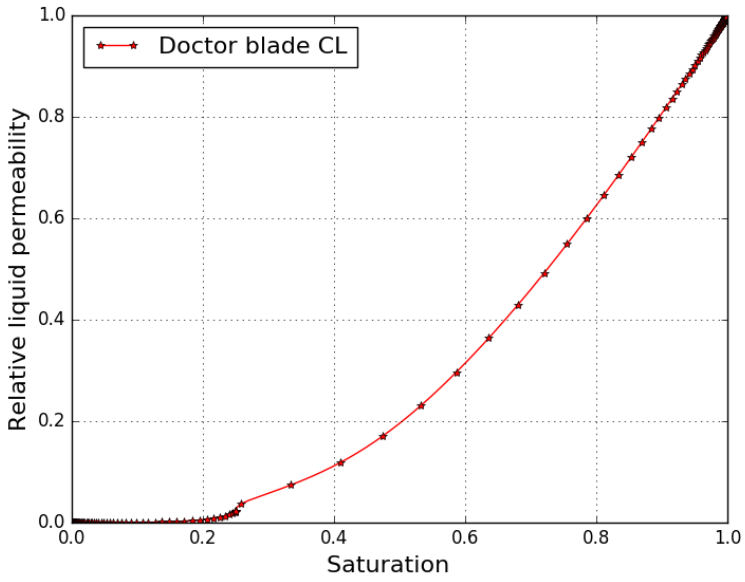

(a)

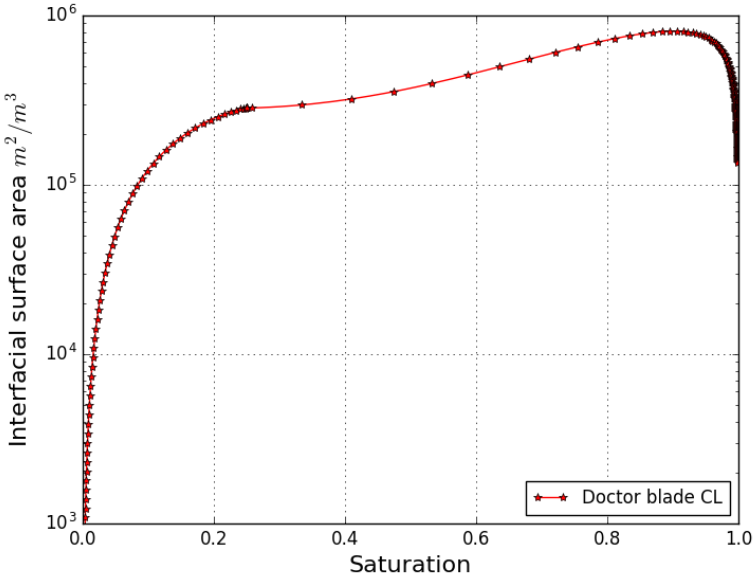

(b)

Figure 2.11 – Numerically predicted: (a) saturation vs. relative liquid permeability, and (b) saturation vs. interfacial surface area for doctor blade CL.

as smaller Knudsen radii. The smaller Knudsen radii in Figure 2.12 indicate that when the average Knudsen radius is reduced under saturated conditions,

the effective oxygen diffusivity might be strongly influenced by the Knudsen effect. The Pt/V_G and Pt/V_A in the figure are Pt nanoparticles supported by different carbon particles, i.e., graphitized Vulcan (V_G) and amorphous Vulcan (V_A), respectively. The symbols in the experimental data represents the standard deviation.

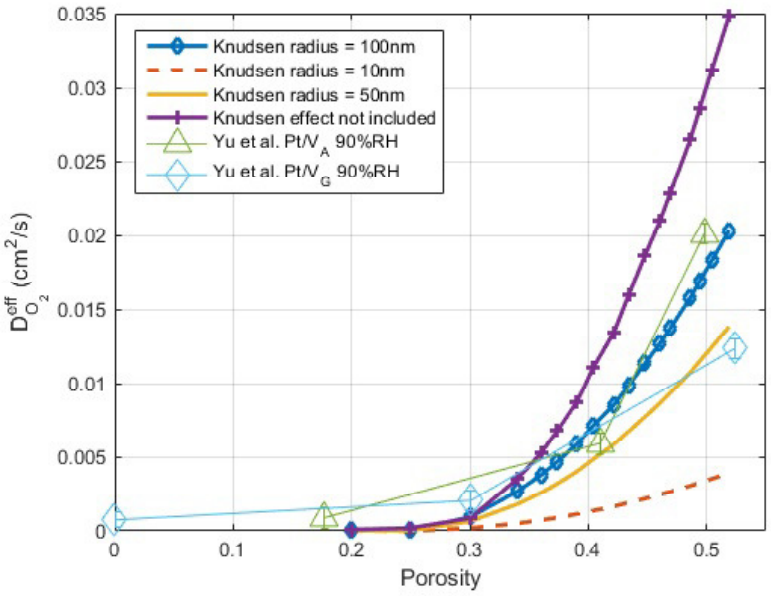

Figure 2.12 – Curve fit of effective oxygen diffusivity to Yu et al. [6] experimentally observed data at 80 ° C and 101 kPa.

2.2 Membrane Electrode Assembly Model

The development of a non-isothermal, two-phase membrane electrode assembly (MEA) model is an extension of the previous work by Secanell [127], Dobson [128], Moore [129] and Bhaiya [130]. The computational domain is a across-the-channel unit as shown in Figure 2.13. Seven layers are included in the model, anode GDL, MPL and CL, membrane, and cathode GDL, MPL and CL.

2.2.1 Assumptions

The mathematical model used to study two-phase flow in PEMFC is subject to the following assumptions:

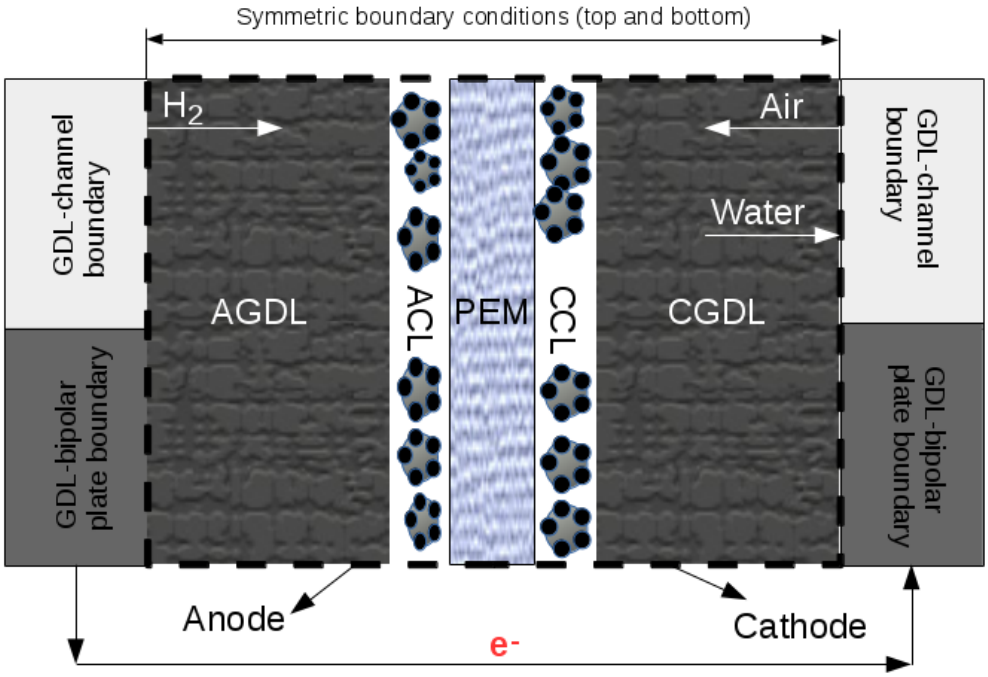

Figure 2.13 – Computational Domain of MEA model.

1. The fuel cell operates at steady state.

2. Liquid water movement is dominated by capillary forces (see 2.2.8).

3. Hydrophilic and hydrophobic pore-networks are homogeneous in the diffusion medium.

4. The liquid water and gas mixture are considered incompressible and Newtonian fluid in the laminar regime in the porous media.

5. The phase change in the pore-network is driven by the gradient between partial pressure of water vapor and saturation water vapor pressure.

6. Membrane is impermeable to liquid water and gas species.

7. The oxygen reduction reaction (ORR) is characterized by the double trap kinetic model described in [131].

8. The hydrogen oxidation reaction (HOR) is characterized by the dual path kinetic model described in [132].

2.2.2 Mixture Transport

The mass conservation equation used to describe the gas mixture transport in the fuel cell is [133],

$$\frac{\partial \rho}{\partial t} + \nabla \cdot (\rho \boldsymbol{u}_g) = S \tag{2.30}$$

where ρ is the density of the mixture, t is time, $\boldsymbol{u}_g$ is the flow velocity, and S is a source term that combines the consumption and/or production of all the species.

The momentum conservation equation for the mixture is usually assumed to be given by the incompressible Navier-Stokes equation which can be expressed as,

$$\frac{\partial \boldsymbol{u}_g}{\partial t} + (\boldsymbol{u}_g \cdot \nabla)\boldsymbol{u}_g - \nu \nabla^2 \boldsymbol{u}_g = -\nabla w + \mathbf{g} \tag{2.31}$$

where ν is the kinematic viscosity, w is the specific thermodynamic work, i.e., internal source term, which is in the form of $\frac{p}{\rho_0}$, where p is the pressure and ρ_0 is the uniform density, and $\mathbf{g}$ is the external source term which is gravity in this case.

Based on the assumptions, the mass conservation equation used to describe each individual gas species can be simplified to,

$$\nabla \cdot \mathbf{N}_i = S_i \tag{2.32}$$

where $\mathbf{N}_i$ is the molar flux of species i, and S_i is the source term.

The previous model implementation only considers the diffusive molar flux [127, 130]; the convective flux due to gas mixture transport has been introduced in the proposed model. The total molar flux including the convective molar flux is,

$$\mathbf{N}_i = \mathbf{J}_i + c_i \boldsymbol{u}_g \tag{2.33}$$

where $\mathbf{J}_i$ is the diffusive flux modeled by Fick's first law, for example, in the cathode, water vapor and oxygen are assumed to be infinitely dilute in nitrogen, the diffusive flux in the cathode are given as,

$$\mathbf{J}_{O2} = -c_g D^{\text{eff}}_{O2,N2} \nabla x_{O2}, \tag{2.34}$$

$$\mathbf{J}_{H2O} = -c_g D^{\text{eff}}_{H2O,N2} \nabla x_{H2O} \tag{2.35}$$

where c_g is the total molar concentration, $D^{\text{eff}}_{i,N2}$ is the effective diffusion coefficient between gas species i and nitrogen, and x_i is the molar fraction of gas species.

The $\boldsymbol{u}_g$ is velocity of the gas mixture in cm/s which is an addition to the previous model implementation [127, 130], Darcy's law is used to model gas mixture transport in the porous media,

$$\boldsymbol{u}_g = \frac{k_g(p_c)}{\mu_g} \nabla p_g \tag{2.36}$$

where ρ_g is the gas mixture density, $k_g(p_c)$ is the effective gas permeability which is a function of capillary pressure, μ_g is the dynamic viscosity, and p_g is the gas mixture pressure which is an additional solution variable introduced in the two-phase model. With the mass conversation equation (2.32), the governing equation for gas mixture transport is,

$$-\nabla \cdot \left(\frac{\rho_g k_g(p_c)}{\mu_g} \nabla p_g \right) = S_{\text{gas}} \tag{2.37}$$

where S_{gas} will be discussed in the later section 2.2.8.

As p_g is solved as the solution variable, the coupling between p_g and c_g needs to be considered. The ideal gas law is used to relate the p_g to c_g;

$$c_g(p_g) = \frac{p_g}{RT} \tag{2.38}$$

note that T is also the solution variable in the model. The density ρ_g is assumed constant by assuming incompressible flow. The molecular diffusion coefficient is also a function of p_g as it is computed using ChapmanEnskog theory [134].

Combining mass conservation equation (2.32) with (2.33), the governing equation for each gas species transport in the cathode can then be written as,

$$\nabla \cdot \left(c_g(p_g)\ D^{\text{eff}}_{H_2O(vapor),N_2} \nabla x_{H_2O(vapor)} \right) - \nabla \cdot (c_g(p_g) x_{H2O} \boldsymbol{u}_g) \ = \ S_{H2O} \tag{2.39}$$

$$\nabla \cdot \left(c_g(p_g)\ D^{\text{eff}}_{O_2,N_2} \nabla x_{O_2} \right) - \nabla \cdot (c_g(p_g) x_{O_2} \boldsymbol{u}_g) \ = \ S_{O_2} \tag{2.40}$$

Table 2.3 – Source terms for oxygen and water transport equations due to the electrochemical reactions.

Parameters	GDL,MPL	CCL	ACL	PEM
S_{O_2}	0	$-\frac{i}{4F}$	0	0
S_w	0	$\frac{i}{2F}$	0	0

assuming there is no gas species cross-over through the PEM, molar fraction of nitrogen can then be obtained as $1 - x_{H2O} - x_{O2}$ in the cathode.

For the anode, the water vapor is assumed infinitely dilute in hydrogen. The governing equation can be expressed as,

$$\nabla \cdot \left(c_g(p_g)\ D^{\text{eff}}_{H_2O(vapor),H_2} \nabla x_{H_2O(vapor)}\right) - \nabla \cdot (c_g(p_g) x_{H2O} \boldsymbol{u}_g) \ = \ S_{H2O} \quad (2.41)$$

The source terms due to electrochemical reaction are summarized in Table 2.3 and the source terms due to water sorption and phase change are discussed in later sections. The term i represents the volumetric current density in Table 2.3.

2.2.3 Charge Transport

The conservation equations for charge species transport can be expressed as,

$$\nabla \cdot \mathbf{j}_i = S_i \quad (2.42)$$

where $\mathbf{j}_i$ is the current density of species i and S_i is the source/sink term due to electrochemical reaction which will be discussed in section 2.2.6.

Ohm's law is used to model the transport of protons and electrons,

$$\mathbf{j}_p = -\sigma_m^{\text{eff}} \nabla \phi_m, \quad (2.43)$$

$$\mathbf{j}_e = -\sigma_s^{\text{eff}} \nabla \phi_s, \quad (2.44)$$

where $\mathbf{j}_p$ and $\mathbf{j}_e$ are the protonic and electronic current densities, respectively. They are equal to each other in absolute value but have the opposite sign, i.e., $j_e = -j_p$, and σ_i^{eff} is the effective conductivity for each species.

Combining equation (2.42) with (2.43) and (2.44), the transport equations for protons and electrons are determined,

$$\nabla \cdot (\sigma_m^{\text{eff}} \nabla \phi_m) = S_{H+} \quad (2.45)$$

$$\nabla \cdot (\sigma_s^{\text{eff}} \nabla \phi_s) = S_{e-} \tag{2.46}$$

Note that the transport of the protons only takes place in the layers that contain the electrolyte, i.e., anode CL, cathode CL and PEM and electron transport does not take place in PEM. The source terms due to the electrochemical reactions (ORR and HOR) are,

$$S_{\text{H}^+} = \begin{cases} i & \text{in cathode CL} \\ -i & \text{in anode CL} \\ 0 & \text{everywhere else} \end{cases} \tag{2.47}$$

and

$$S_{\text{e}^-} = \begin{cases} -i & \text{in cathode CL} \\ i & \text{in anode CL} \\ 0 & \text{everywhere else} \end{cases} \tag{2.48}$$

2.2.4 Water Transport in the Electrolyte

Water transport in the electrolyte is considered in sorbed form and the driving forces are electro-osmotic drag, back diffusion and thermo-osmosis. The electro-osmotic drag is proportional to the proton flux,

$$\mathbf{N}_{\lambda,\text{drag}} = -n_d \frac{\sigma_m^{\text{eff}}}{F} \nabla \phi_m \tag{2.49}$$

where n_d is the electroosmosis coefficient which is defined as the average number of water molecules per proton dragged through the PEM based on the potential gradient, σ_m^{eff} and ϕ_m are the effective protonic conductivity and the electrolyte potential, and F is the Faraday constant.

The sorbed water flux due to back diffusion is defined as [59, 127, 135]

$$\mathbf{N}_{\lambda,\text{diffusion}} = -\frac{\rho_{\text{dry}}}{EW} D_\lambda^{\text{eff}} \nabla \lambda \tag{2.50}$$

where ρ_{dry} is the density of dry Nafion$^{\mathbf{TM}}$ membrane, EW is the equivalent weight of membrane which is defined as the ratio of the weight of dry polymer electrolyte in grams to number of moles of SO_3^-, D_λ^{eff} is the effective back diffusion coefficient which is a bulk property in the PEM and an effective

value in the CLs, the sorbed water content is represented in terms of λ, which is the ratio of the number of moles of water to the number of moles of SO_3^- in the electrolyte.

The sorbed water transport is also driven by temperature gradients as observed by several researchers [136, 137]. The effect of thermo-osmosis can be expressed as,

$$\mathbf{N}_{\lambda,\text{thermo-osmosis}} = -\frac{D_T^{\text{eff}}}{M_{H_2O}}\nabla T \tag{2.51}$$

where D_T^{eff} is the effective thermo-osmotic diffusion coefficient and the M_{H_2O} molar mass of water.

The total sorbed water flux in the electrolyte can be summarized as,

$$\begin{aligned}\mathbf{N}_\lambda =& \mathbf{N}_{\lambda,\text{drag}} + \mathbf{N}_{\lambda,\text{diffusion}} + \mathbf{N}_{\lambda,\text{thermo-osmosis}} \\ =& -n_d\frac{\sigma_m^{\text{eff}}}{F}\nabla\phi_m - \frac{\rho_{\text{dry}}}{EW}D_\lambda^{\text{eff}}\nabla\lambda - \frac{D_T^{\text{eff}}}{M_{H_2O}}\nabla T\end{aligned} \tag{2.52}$$

where bulk transport properties are used in the PEM and effective values are used in CLs. Overall, the mass conservation equation for sorbed water in the electrolyte is,

$$-\nabla\cdot\left(n_d\frac{\sigma_m^{\text{eff}}}{F}\nabla\phi_m + \frac{\rho_{\text{dry}}}{EW}D_\lambda^{\text{eff}}\nabla\lambda + \frac{D_T^{\text{eff}}}{M_{H_2O}}\nabla T\right) = S_\lambda \tag{2.53}$$

The source term, S_λ, is given by,

$$S_\lambda = \begin{cases} k_t\frac{\rho_{dry}}{EW}(\lambda_{eq}-\lambda) & \text{in CLs,} \\ 0 & \text{everywhere else,}\end{cases} \tag{2.54}$$

where k_t is a time constant; in steady state simulations, the value of k_t is 100 [127], and λ_{eq} is determined by the sorption isotherm [138] at equilibrium. λ_{eq} is a function of the equivalent weight, water vapor molar fraction, and temperature [139]. Since water sorption/desorption affects water vapor transport, S_λ should be included in equation (2.41). Note that the water sorption/desorption from/to liquid water is not accounted for in the model.

2.2.5 Thermal Transport

The thermal transport equation is detailed in the previous work of Bhaiya [135]. The general energy conservation equation is,

$$\frac{\varepsilon_v \partial(\rho_g \hat{h}_g)}{\partial t} + \nabla \cdot \left(\varepsilon_v \rho_g \hat{h}_g \boldsymbol{u}_g\right) = \nabla \cdot \left(\kappa^{\text{eff}} \nabla T\right) - \nabla \cdot \left(\sum \bar{H}_i \mathbf{N}_i\right) + \hat{S}_{\text{heat}} - \dot{W}_{\text{electrical}} \tag{2.55}$$

where ε_v is the layer porosity, $\hat{h}_g$ is the mass specific enthalpy of the gas, $\boldsymbol{v}_g$ is the interstitial velocity of the gas mixture, the interstitial velocity is the gas velocity passing through the porous layer in the flow direction, κ^{eff} is the effective thermal conductivity, $\bar{H}_i$ is the molar specific enthalpy of species i, $\mathbf{N}_i$ is the molar flux, and $\hat{S}_{heat}$ and $\dot{W}$ are volumetric rates of heat production and work done by the system, respectively.

For each fuel cell component the form of the above expression varies. For example, at the cathode CL, for a steady-state case the equations above can be simplified and expanded to the following form,

$$\begin{aligned} &\nabla \cdot \left(k^{\text{eff}} \nabla T\right) + D^{\text{eff}}_{O_2,N_2} c \nabla x_{O_2} \cdot (\nabla \bar{H}_{O_2} - \nabla \bar{H}_{N_2}) \\ &+ D^{\text{eff}}_{H_2O,N_2} c \nabla x_{H_2O} \cdot (\nabla \bar{H}_{H_2O} - \nabla \bar{H}_{N_2}) - \mathbf{N}_\lambda \cdot \nabla \bar{H}_\lambda - \mathbf{N}_l \cdot \nabla \bar{H}_l + \hat{S}_{\text{heat}} = 0. \end{aligned} \tag{2.56}$$

where the source term $\hat{S}_{\text{heat}}$ includes the following:

1. The irreversible heat generation (efficiency losses) due to activation overpotential:

$$S_{\text{irrev,ORR}} = -i\eta = -i\left(\phi_s - \phi_m - E_{\text{ORR}}\right) \tag{2.57}$$

   where η is the overpotential, as η is negative for a cathodic reaction, a negative sign is placed in the formula, E_{ORR} is the equilibrium potential derived from the Nernst equation [129, 140].

2. Reversible heat generation in the cathode catalyst layer due to ORR is:

$$S_{\text{rev,ORR}} = \frac{i}{2F}\left(-T\Delta\bar{S}_{\text{ORR}}\right) = \frac{i}{2F}\left(-T f_{\text{ORR}} \Delta\bar{S}_{\text{overall}}\right) \tag{2.58}$$

   where $\bar{S}_{\text{overall}}$ is the overall entropy change per mole of fuel (H_2). Since the entropy of the half-cell reaction cannot be explicitly obtained, a

factor f_{ORR}, is introduced to account for the fraction of reversible heat produced in the ORR.

3. Heat source term due to phase change:

$$S_{\text{phase,CL}} = M_{H2O} S_{H2O(\text{evap/cond})} \hat{L}_{\text{water}} \tag{2.59}$$

where $\hat{L}_{\text{water}}$ is the specific latent heat of vaporization/condensation of water, which is a function of temperature and is reported in [141].

4. The electronic and protonic Ohmic heating (irreversible):

$$S_{\text{ohmic,CL}} = \sigma_m^{\text{eff}} \left(\nabla\phi_m \cdot \nabla\phi_m\right) + \sigma_s^{\text{eff}} \left(\nabla\phi_s \cdot \nabla\phi_s\right) \tag{2.60}$$

5. Heat source term due to water vapor sorption/desorption in the ionomer

$$S_{\text{sorption,CL}} = \frac{k_t \rho_{\text{dry}}}{EW} \left(\lambda_{eq} - \lambda\right) \bar{H}_{\text{sorption}} \tag{2.61}$$

where $\bar{H}_{\text{sorption}}$ is the heat release due to molar enthalpy change which corresponds to water vapor sorption.

2.2.6 Electrochemical Reaction

The term i in the earlier sections is the current produced per unit volume of catalyst layer and it can be described in the most general form by the Butler-Volmer equation [142]. For the sluggish ORR where higher overpotential is needed for reaction to occur, Butler-Volmer equation can be simplified to Tafel equation. Butler-Volmer and Tafel kinetics are only valid for single electron transfer and multi-step reactions with a unique rate determining step. However, it has been shown experimentally that the rate determining step for HOR [132, 143, 144] and ORR [145–147] changes with the overpotential. Thus, the dual-path model for HOR [132] and double trap kinetic model for ORR [131] are proposed and implemented in OpenFCST to accurately predict the reaction rates.

Wang et al. [148] developed dual-path kinetic model for computing HOR current density; the equation implemented is,

$$j_{\text{HOR}} = j_{0T} \left[\frac{c_{H_2}}{c_{H_2}^{\text{ref}}} - \frac{c_{H_2}^0}{c_{H_2}^{\text{ref}}} e^{\frac{-2F\eta}{\gamma_{\text{ads}} RT}}\right] + j_{0H} \left[\frac{c_{H_2}}{c_{H_2}^{\text{ref}}} e^{\frac{F\eta}{2RT}} - \frac{c_{H_2}^0}{c_{H_2}^{\text{ref}}} e^{\frac{-F\eta}{\gamma_{\text{ads}} RT}} e^{\frac{-F\eta}{2RT}}\right] \tag{2.62}$$

where c_{H_2} is the concentration of hydrogen at the Pt surface, $c^0_{H_2}$ is the equilibrium concentration of hydrogen at the Pt surface, $c^{\text{ref}}_{H_2}$ is the saturation concentration of H_2 under 1 atm pressure, γ_i is the reaction order with respect to species i, and j_{0T} and j_{0H} are the exchange current densities for the Tafel and Heyrovsky reactions, respectively. A detailed derivation of equation (2.62) can be found in reference [148].

The double trap model is used for the ORR and the detailed implementation can be found in [131]. The expression to compute ORR current density is,

$$j_{\text{ORR}} = j^* \left[e^{-\frac{\Delta G^*_{\text{RD}}}{kT}} \theta_{\text{Pt-OH}} - e^{-\frac{\Delta G^*_{\text{RD}}}{kT}} \psi \right] \tag{2.63}$$

where j^* is a reference prefactor for the ORR reaction which is set to 1,000 A/cm^2 in [129, 149] and Pt-OH is the coverage of the intermediate steps which can be found in [129, 131], ΔG^*_i are the potential dependent free energies of activation of the ith step and these free energies are given in [131], and ψ is the fraction of active platinum sites available, which is related to the coverage of intermediate species using the following equation,

$$\psi = 1 - \theta_{\text{Pt-O}} - \theta_{\text{Pt-OH}} \tag{2.64}$$

2.2.7 Local Transport Resistance in Catalyst Layer

The micro-structural features of the CL have been reported in the range of $50-150$ nm [150]. Similar particle size is observed for common carbon particles used as catalyst support such as Vulcan XC-72R, and Ketjen black [151]. Evidence has shown that platinum is likely to exist on the outer surface of the carbon support [152]. One way to model the CL microstructure is to assume an individual platinum covered carbon support particle surrounded by a thin ionomer film. This idealized structure, namely Ionomer Covered Catalyst Particle (ICCP), is shown in Figure 2.14 and it is implemented in the OpenFCST [153].

In the ICCP model, oxygen is assumed to first dissolve into the ionomer film, and then diffuse through the ionomer film to reach the surface of the platinum covered carbon particle. The reactions takes place at the ionomer/-

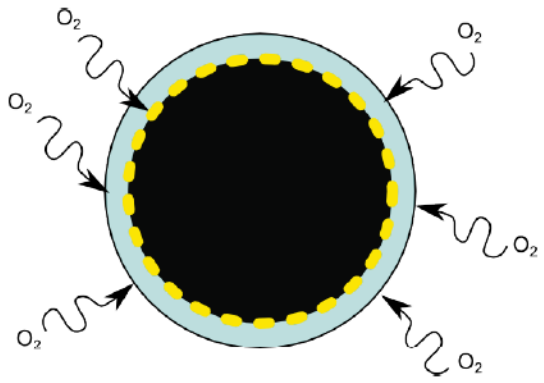

Figure 2.14 – Diagram of ICCP. The assumed structure is a spherical carbon particle with an even distribution of platinum on the exterior carbon surface, surrounded by a thin ionomer film, with permission [7].

carbon interface as the carbon particle surface is covered by platinum. The local transport resistances occur at: (a) gas/ionomer interface and (b) diffusive pathway from gas/ionomer interface to ionomer/carbon interface inside the ionomer. At the reaction site, the volumetric current density for each ICCP is determined by the oxygen concentration at the ionomer/carbon interface as,

$$i_{agg} = \frac{j(c_{O_2,f|c}) \cdot A_s}{V} = \frac{j(c_{O_2,f|c}) \cdot A_s}{\frac{4}{3}\pi r_{agg}^3} \tag{2.65}$$

where $j(c_{O_2,\,f|c})$ is the current per unit surface of platinum, calculated using a kinetic model with the oxygen concentration at the ionomer film/carbon interface $c_{O_2,\,f|c}$, and A_s is the total active platinum surface area,

$$A_s = \frac{A_v}{1-\epsilon_V} V = \frac{A_v}{1-\epsilon_V} \frac{4}{3} \pi r_{agg}^3 \tag{2.66}$$

where A_v is the area of platinum per unit volume of catalyst layer, ϵ_V is the catalyst layer porosity and r_{agg} is the ICCP inner radius.

In order to obtain the oxygen concentration at the ionomer/carbon interface, the transport losses due to the gas/ionomer interface and diffusive transport in the ionomer need to be modeled. The loss at gas/ionomer interface is modeled by assuming finite oxygen dissolution kinetics, e.g., [154],

$$N_{O_2} = -k_{O_2}(c_{O_2,\,g|f} - c^{eq}_{O_2,\,g|f}) \tag{2.67}$$

where k_{O_2} is the dissolution rate, and $c^{eq}_{O_2,\,g|f}$, the equilibrium oxygen concentration, is obtained using Henry's law from the gas phase oxygen partial

pressure.

The diffusive flux of oxygen in the ionomer is described using Fick's law. Assuming spherical symmetry,

$$N_{O_2} = -D_{O_2,N}\frac{dc_{O_2}}{dr} \tag{2.68}$$

At steady state the total consumption of oxygen must be equal to the total flux passing through the spherical surface,

$$R_{O_2} = -N_{O_2} \cdot 4\pi r^2 \tag{2.69}$$

where the total oxygen consumption due to the electrochemical reaction is,

$$R_{O_2} = \frac{j(c_{O_2,\,f|c}) \cdot A_s}{4F} \tag{2.70}$$

Combining the equations above, and integrating across the thickness of the ionomer thin film, the oxygen concentration at the ionomer/carbon interface is obtained,

$$c_{O_2,\,f|c} = c_{O_2,\,g|f} - \frac{\delta_{agg}}{r_{agg}(r_{agg}+\delta_{agg})}\frac{j(c_{O_2,\,f|c}) \cdot A_s}{16F\pi D_{O_2,N}} \tag{2.71}$$

At steady state, the total flux of oxygen through the gas/ionomer interface is equal to the rate of consumption,

$$\frac{j(c_{O_2,\,f|c}) \cdot A_s}{4F} = N_{O_2}(r_{agg}+\delta_{agg})4\pi(r_{agg}+\delta_{agg})^2 \tag{2.72}$$

Combining equations (2.67) and (2.72),

$$c_{O_2,\,g|f} = c^{eq}_{O_2,\,g|f} - \frac{j(c_{O_2,\,f|c}) \cdot A_s}{16F \cdot \pi(r_{agg}+\delta_{agg})^2 k_o} \tag{2.73}$$

Equation (2.73) can be substituted in equation (2.71). As the current density term $j(c_{O_2,\,f|c})$ is an implicit expression, equation (2.71) is nonlinear. This requires a nonlinear solver, in this case, Newton's method is used to solve the equation iteratively until a final residual of 10^{-15} is reached.

2.2.8 Two-phase Transport

The two-phase transport is an addition to the previously developed model in OpenFCST [7]. Most mathematical models in the literature assume that capillary pressure is the driving force for pore filling in porous media, an assumption that is justified based on non-dimensional analysis that shows that surface tension effects are orders of magnitude larger than gravitational, inertial and viscous effects. To validate this assumption, Bond [155, 156], Bo, Weber [156], We, and Capillary [157], Ca, are calculated below.

In the porous media, the Bond number can be represented as

$$\mathrm{Bo} = \frac{(\rho_l - \rho_g)\, g d_{pore}^2}{\gamma} \tag{2.74}$$

where ρ_l is the liquid water density, ρ_g is the gas mixture density, g is the acceleration due to gravity and d_{pore} is the pore diameter. ρ_l is of the order of 10^3 kg m^{-3}, ρ_g is of the order of 1 kg m^{-3}, g is of the order of 10^1 m s^{-2} and d_{pore} is the characteristic length for flow in the porous media for example, d_{pore} in GDL is of the order of 10^{-5} m [4, 117]. Therefore, Bo $\sim 10^{-3} << 1$ in the GDL and, therefore, capillary forces dominate. This would also apply to MPLs and CLs since the pore sizes are smaller.

The Weber number can be expressed as

$$\mathrm{We} = \frac{\rho_l u_l^2 d_{pore}}{\gamma} \tag{2.75}$$

where u_l is the interstitial liquid water velocity. u_l is of the order of 10^{-5} m s^{-1} [156]. Therefore, We $\sim 10^{-10} << 1$, the inertial effect is negligible compared to capillary effects.

Lastly, the Capillary number, Ca, is evaluated [157]:

$$\mathrm{Ca} = \frac{u_g \mu_g}{\gamma} \tag{2.76}$$

where u_g is a characteristic gas velocity, μ_g is the viscosity of the surrounding gas (mixture) phase and γ is the surface tension between the liquid and the gas phase at fuel cell operating conditions. $\boldsymbol{u}_g$ is of the order of 10^{-4} m s^{-1} [31], μ_g is of the order of 10^{-5} kg m^{-1} s^{-1} and γ is of the order of 10^{-2} N m^{-1}. This gives Ca $\sim 10^{-7} << 1$; thus the viscous drag is negligible.

Table 2.4 – Estimated dimensionless numbers for an operating PEMFC.

Dimensionless	Physical meaning	GDL	CL
Characteristic length		10 μm	0.1 μm
Bond	Gravitational force to surface tension	10^{-3}	10^{-7}
Weber	Inertial force to surface tension	10^{-10}	10^{-12}
Capillary	Viscous force to surface tension	10^{-7}	10^{-7}

All dimensionless numbers for GDL and CL are summarized in Table 2.4 and it clearly shows that surface tension effects are at least three orders of magnitude larger than any of the other effects discussed above.

Darcy's law is used to model the liquid water and gas mixture transport (2.37) in the MEA as the Reynolds number in the porous media for gas and liquid phase is smaller than one. The liquid water pressure is solved as solution variable and the governing equation for liquid water transport in the MEA is,

$$-\nabla \cdot \left(\frac{\rho_l k_l(p_c)}{\mu_l} \nabla p_l \right) = S_{\text{liquid}} \tag{2.77}$$

where ρ_l is the interstitial density of liquid water, k_l is the effective permeability, and μ_l is the dynamic viscosity. The capillary pressure p_c is computed based on the solutions of p_l and p_g as follows,

$$p_c = p_l - p_g \tag{2.78}$$

The source terms for liquid and gas pressure due to phase change, electrochemical reaction, and membrane water transport are,

$$S_{\text{gas}} = \begin{cases} -M_{H2O} S_{H2O(\text{evap/cond})} & \text{in GDL and MPL,} \\ -M_{H2O} S_{H2O(\text{evap/cond})} + \dfrac{i}{4F} M_{O2} + S_\lambda M_{H2O} & \text{in cathode CL,} \\ -M_{H2O} S_{H2O(\text{evap/cond})} + \dfrac{i}{2F} M_{H2} + S_\lambda M_{H2O} & \text{in anode CL,} \\ 0 & \text{PEM.} \end{cases} \tag{2.79}$$

$$S_{\text{liquid}} = \begin{cases} M_{H2O} S_{H2O(\text{evap/cond})} & \text{in GDL and MPL,} \\ M_{H2O} S_{H2O(\text{evap/cond})} - \dfrac{i}{2F} M_{H2O} & \text{in cathode CL,} \\ M_{H2O} S_{H2O(\text{evap/cond})} & \text{in anode CL,} \\ 0 & \text{PEM.} \end{cases} \tag{2.80}$$

where the source term for condensation and evaporation is described by,

$$S_{H_2O(\text{evap/cond})} = k_{e/c} a_{lv} \left(\frac{p_v - p_{\text{sat}}(p_c, T)}{p_{\text{sat}}(p_c, T)} \right) \tag{2.81}$$

where $k_{e/c}$ is the aerial evaporation or condensation rate constant, a_{lv} is the liquid-gas interfacial surface area per unit volume, and p_v is the vapor pressure. When water vapor pressure is higher than the saturation vapor pressure, condensation takes place, otherwise, evaporation will happen. The effective saturation vapor pressure in a capillary, $p_{\text{sat}}(p_c, T)$, is determined by considering the Kelvin effect as follows,

$$p_{\text{sat}}(p_c, T) = p_{\text{sat}} \exp \left(\frac{p_c M_{H2O}}{RT \rho_l} \right) \tag{2.82}$$

where p_{sat} is the uncorrected saturated vapor pressure of water.

2.2.9 Governing equations

The equations for gas mixture pressure and liquid pressure are added to the system of governing equations previously implemented in OpenFCST [7]. Overall, the model solves: oxygen and water vapor molar fractions, liquid and gas mixture pressure (introduced in this thesis), protonic and electronic potentials, sorbed water in the ionomer phase, and temperature, as the solution variables. The governing equations are as follows,

$$
\begin{aligned}
&\nabla \cdot \left(c_g(p_g)\ D^{\text{eff}}_{O_2,N_2} \nabla x_{O_2}\right) - \nabla \cdot (c_g(p_g) x_{O_2} \boldsymbol{u}_g) && = S_{O_2}\ , \\
&\nabla \cdot \left(c_g(p_g)\ D^{\text{eff}}_{H_2O(vapor),N_2 \text{ or } H_2} \nabla x_{H_2O(vapor)}\right) - \nabla \cdot (c_g(p_g) x_{H2O} \boldsymbol{u}_g) && = S_w\ , \\
&\nabla \cdot \left(\frac{\rho_g k_g(p_c)}{\mu_g} \nabla p_g\right) && = S_{gas}\ , \\
&\nabla \cdot \left(\frac{\rho_l k_l(p_c)}{\mu_l} \nabla p_l\right) && = S_{liquid}\ , \\
&\nabla \cdot \left(\sigma_m^{\text{eff}} \nabla \phi_m\right) && = S_{H^+}\ , \\
&\nabla \cdot \left(\sigma_s^{\text{eff}} \nabla \phi_s\right) && = S_{e^-}\ , \\
&\nabla \cdot \left(n_d \frac{\sigma_m^{\text{eff}}}{F} \nabla \phi_m + \frac{\rho_{dry}}{EW} D_\lambda^{\text{eff}} \nabla \lambda + \frac{D_T^{\text{eff}}}{M_{H_2O}} \nabla T\right) && = S_\lambda\ , \\
&\nabla \cdot \left(k^{\text{eff}} \nabla T\right) + \nabla \cdot \left(\sum \bar{H}_i \mathbf{N}_i\right) && = S_T.
\end{aligned}
\tag{2.83}
$$

where $c_g(p_g)$ is the total gas mixture concentration, x_i is the molar fraction of species i, $D^{\text{eff}}_{i,j}$ is the effective diffusivity of species i in j (based on molecular and Knudsen diffusivity), $\boldsymbol{u}_g$ is the gas velocity calculated based on Darcy's law ($k_g \nabla p_g / \mu_g$), k_g and k_l are the gas and liquid permeabilities, respectively, ρ_i and μ_i represents the density and dynamic viscosity of the species i, σ_m^{eff} and σ_s^{eff} are the effective ionic and electronic conductivities, respectively, D_λ^{eff} and D_T^{eff} are the sorbed water and thermo-osmosis diffusion coefficients in the membrane, respectively, $\mathbf{N}_i$ is the total flux, i.e., the sum of convective and diffusive fluxes of species i ($\mathbf{N}_i = c_g(p_g) x_i \boldsymbol{u}_g - c_g(p_g) D^{\text{eff}}_{i,j} \nabla x_i$), and $\bar{H}_i$ is the specific enthalpy of species i. The source terms are summarized in Tables 2.5 and 2.6.

Table 2.5 – Source terms in GDL, MPL and PEM

Parameters	GDL,MPL	PEM
S_{O2}	0	0
S_w	$S_{H2O(\text{evap/cond})}$	0
S_{gas}	-$M_{H2O} S_{H2O(\text{evap/cond})}$	0
S_{liquid}	$M_{H2O} S_{H2O(\text{evap/cond})}$	0
S_{H^+}	0	0
S_{e^-}	0	0
S_λ	0	0
S_T	$H_{lv} S_{H2O(\text{evap/cond})} - \sigma_s^{\text{eff}}(\overrightarrow{\nabla}\phi_s \cdot \overrightarrow{\nabla}\phi_s)$	$-\sigma_m^{\text{eff}}(\overrightarrow{\nabla}\phi_m \cdot \overrightarrow{\nabla}\phi_m)$

Table 2.6 – Source terms in CLs

Parameters	CCL	ACL
S_{O2}	$\frac{i}{4F}$	0
S_w	$S_{H2O(\text{evap/cond})} - S_\lambda$	$S_{H2O(\text{evap/cond})} - S_\lambda$
S_{gas}	$-M_{H2O}S_{H2O(\text{evap/cond})} + \frac{i}{4F} + S_\lambda M_{H2O}$	$-M_{H2O}S_{H2O(\text{evap/cond})} + \frac{i}{2F} + S_\lambda M_{H2O}$
S_{liquid}	$M_{H2O}S_{H2O(\text{evap/cond})} - \frac{i}{2F}M_{H2O}$	$M_{H2O}S_{H2O(\text{evap/cond})}$
S_{H^+}	i	$-i$
S_{e^-}	$-i$	i
S_λ	$-k_\lambda \frac{\rho_{dry}}{EW}(\lambda_{eq} - \lambda)$	$-k_\lambda \frac{\rho_{dry}}{EW}(\lambda_{eq} - \lambda)$
S_T	$H_{lv}S_{H2O(\text{evap/cond})} + i(\phi_s - \phi_m - E_{ORR}) + \frac{i}{2F}(Tf_{ORR}\Delta\overline{S}_{\text{overall}})$ $-\sigma_m^{\text{eff}}(\vec{\nabla}\phi_m \cdot \vec{\nabla}\phi_m) - \sigma_s^{\text{eff}}(\vec{\nabla}\phi_s \cdot \vec{\nabla}\phi_s) - k_\lambda \frac{\rho_{dry}}{EW}(\lambda_{eq} - \lambda)\bar{H}_{\text{sorption}}$	$H_{lv}S_{H2O(\text{evap/cond})} - i(\phi_s - \phi_m - E_{HOR}) + \frac{i}{2F}(T(1 - f_{ORR})\Delta\overline{S}_{\text{overall}})$ $-\sigma_m^{\text{eff}}(\vec{\nabla}\phi_m \cdot \vec{\nabla}\phi_m) - \sigma_s^{\text{eff}}(\vec{\nabla}\phi_s \cdot \vec{\nabla}\phi_s) - k_\lambda \frac{\rho_{dry}}{EW}(\lambda_{eq} - \lambda)\bar{H}_{\text{sorption}}$

2.2.10 Boundary Conditions

Boundary conditions for the model include Dirichlet conditions (fixed boundary condition) for molar fractions and gas pressure at the channel-GDL interface; Dirichlet boundary conditions at GDL-land interface for electrical potential and temperature; and no flux conditions everywhere else in the domain. Since the simulations are performed by specifying a cell voltage, these simulations are equivalent to operating the cell in potentiostatic mode. Note that a Neumann boundary condition for the current density could be used to simulate galvanostatic mode; however, this boundary condition leads to numerical instabilities.

The selection of appropriate boundary conditions for liquid pressure at the GDL-channel interface is critical to any two-phase flow model. Zero flux [14, 29, 158] and fixed saturation values are usually imposed as boundary conditions [111]. These boundary conditions are either forcing all water to be vaporized in the MEA or imposing the existence of liquid water at the GDL-channel boundary. Their applicability is, therefore, limited and a more general boundary condition should be developed. An example of a more appropriate boundary condition is the one recently proposed by Zenyuk et al. [11] where a step function is used. After reaching the breakthrough pressure, the liquid pressure however, is considered to be constant in this method. A dynamic boundary condition which relates liquid pressure to liquid water flux might be a more realistic choice and is implemented in this thesis. If the capillary pressure is below a given threshold value, i.e., a breakthrough pressure, a zero liquid water flux is imposed. Once the capillary pressure reaches a given

breakthrough pressure, 2000 Pa in this thesis based on [83], a flux proportional to the liquid pressure is applied, i.e.,

$$\rho_l \boldsymbol{u}_l \cdot \mathbf{n} = -\left(\frac{\rho_l k_l}{\mu_l}\nabla p_l\right)\cdot \mathbf{n} = k\left(\frac{p_l - p_{l,\text{channel}}}{p_0}\right) g(p_l) \tag{2.84}$$

where

$$g(p_l) = \left[\frac{\tanh((p_l - p_{\text{l,channel}})/p_0) + 1}{2}\right]\theta(p_c - p_{\text{BT}}) \ , \tag{2.85}$$

k is the unknown proportionally constant that controls the flux of water as a function of the liquid pressure, p_{BT} is the liquid breakthrough pressure, and $\theta(p_c - p_{\text{BT}})$ is a step function, i.e., it is set to be zero until $p_l > p_{\text{BT}}$ is satisfied in the Newton solver loop and not modified further in order to maintain numerical stability. Its validity is confirmed during post-processing by making sure that the liquid water flux remains positive. By performing a parametric study on k, a value of 10^{-6} kg/(m$^2 \cdot s$) is selected. In order to prevent negative liquid water flux entering from the boundary once the step function is set to be one, a hyperbolic tangent function $\tanh((p_l - p_{l,\text{channel}})/p_0)$ is used. $p_{l,\text{channel}}$ is the liquid pressure at the channel-GDL interface and it is set to be atmospheric pressure considering the droplet volume is large enough so that Laplace pressure is negligible, and p_0 is a non-dimensional factor which is set to be 1 Pa in this case. No liquid flux boundary conditions are applied at the PEM/CL and GDL/land interfaces and at symmetric boundaries, i.e., upper and lower faces in Figure 2.13.

2.3 Solution Strategy

2.3.1 Linearization and Weak Formulation

The non-linear system of equations (2.83) is solved using Newton's method. A solution is obtained using Newton's method by sequential linearization of the nonlinear problem [127]. The linearized second order partial differential equations are then discretized using the Galerkin weighted residuals method. An example is shown below to demonstrate how the equations have been linearized. At steady state, equations (2.37) and (2.77) can be written in

the form,

$$\nabla \cdot (\mathbf{A}(p)\nabla p) = f(p) \tag{2.86}$$

where $\mathbf{A}$ is a second order tensor that might depend on the solution variable, $f(p)$ is the nonlinear source term that depends on all unknown variables. The residual, R, is defined as,

$$\mathrm{R} = \nabla \cdot (\mathbf{A}(p)\nabla p) - f(p) \tag{2.87}$$

The problem is solved iteratively by providing an increment of δp to the current solution p^n. The solution is then updated after this iteration, p^{n+1}=δp + p^n, where the increment δp will eventually approach zero.

In order to solve the nonlinear equation, a linearization of the partial differential equation needs to be obtained first. The term on the left hand side (LHS) can be approximated as follows using directional derivatives of functional analysis [127, 159],

$$\nabla\cdot(\mathbf{A}(p^{n+1})\nabla p^{n+1}) \approx \nabla\cdot\mathbf{A}(p^n)\nabla(p^n)+\frac{\partial \mathbf{A}(p)}{\partial p_k}|_{p=p^n}\delta p_k \nabla p^n+\mathbf{A}(p^n)\nabla\delta p \tag{2.88}$$

The source term on the left hand side (LHS) in equation 2.86 can be approximated in a similar way,

$$f(p^{n+1}) \approx f(p^n) + \frac{\partial f(p)}{\partial p_k} \; |_{p=p^n} \; \delta p_k \tag{2.89}$$

where $\dfrac{\partial}{\partial p_k}$ represents the derivative with respect to solution variable k.

Once the problem has been linearized, the finite element method, namely Galerkin method, is used to obtain the weak form of the equation that is then implemented in OpenFCST [7]. A test function u is multiplied on both sides of the equation and the equation is integrated over the computational domain,

$$\begin{aligned} &\int_\Omega u\nabla \cdot [\mathbf{A}(p^n)\nabla(p^n) + \frac{\partial \mathbf{A}(p)}{\partial p_k}|_{p=p^n}\delta p_k \nabla p^n + \mathbf{A}(p^n)\nabla\delta p]d\Omega \\ &= \int_\Omega u(f(p^n) + \frac{\partial f(p)}{\partial p_k} \; |_{p=p^n} \; \delta p_k)d\Omega \end{aligned} \tag{2.90}$$

The equation can be rearranged using integration by parts as follows,

$$s(\nabla \cdot \mathbf{v}) = \nabla \cdot s\mathbf{v} - \nabla s \cdot \mathbf{v} \tag{2.91}$$

where s is a scalar and $\mathbf{v}$ is a vector. The RHS can be written as,

$$\int_\Omega \nabla \cdot u[\mathbf{A}(p^n)\nabla(p^n) + \frac{\partial \mathbf{A}(p)}{\partial p_k}|_{p=p^n}\delta p_k \nabla p^n + \mathbf{A}(p^n)\nabla\delta p]d\Omega \tag{2.92}$$

$$-\int_\Omega \nabla u \cdot [\mathbf{A}(p^n)\nabla(p^n) + \frac{\partial \mathbf{A}(p)}{\partial p_k}|_{p=p^n}\delta p_k \nabla p^n + \mathbf{A}(p^n)\nabla\delta p]d\Omega \tag{2.93}$$

The divergence theorem is then used on equation 2.92,

$$\int_\Omega (\nabla \cdot \mathbf{v})d\Omega = \int_{\partial\Omega} (\mathbf{n} \cdot \mathbf{v})d\partial\Omega \tag{2.94}$$

which becomes a surface integral,

$$\int_{\partial\Omega} \mathbf{n} \cdot u[\mathbf{A}(p^n)\nabla(p^{n+1}) + \frac{\partial \mathbf{A}(p)}{\partial p_k}|_{p=p^n}\delta p_k \nabla p^n]d\partial\Omega \tag{2.95}$$

where $\mathbf{A}(p^n)\nabla(p^{n+1})$ contains $\mathbf{A}(p^n)\nabla(p^n)$ and $\mathbf{A}(p^n)\nabla\delta p$. At this stage, the equation (2.92) and (2.93) can be expressed as,

$$\begin{aligned}
&-\int_\Omega \nabla u \cdot [\mathbf{A}(p^n)\nabla(p^n) + \frac{\partial \mathbf{A}(p)}{\partial p_k}|_{p=p^n}\delta p_k \nabla p^n + \mathbf{A}(p^n)\nabla\delta p]d\Omega \\
&+\int_{\partial\Omega} \mathbf{n} \cdot u[\mathbf{A}(p^n)\nabla(p^{n+1}) + \frac{\partial \mathbf{A}(p)}{\partial p_k}|_{p=p^n}\delta p_k \nabla p^n]d\partial\Omega \\
&=\int_\Omega u(f(p^n) + \frac{\partial f(p)}{\partial p_k}\ |_{p=p^n}\ \delta p_k)d\Omega
\end{aligned} \tag{2.96}$$

Rearranging all the terms with respect to the solution variable δp, the stiffness matrix can be represented as,

$$\begin{aligned}
&-\int_\Omega \nabla u \cdot [\frac{\partial \mathbf{A}(p)}{\partial p_k}|_{p=p^n}\delta p_k \nabla p^n + \mathbf{A}(p^n)\nabla\delta p]d\Omega \\
&+\int_{\partial\Omega} \mathbf{n} \cdot u[\frac{\partial \mathbf{A}(p)}{\partial p_k}|_{p=p^n}\delta p_k \nabla p^n]d\partial\Omega \\
&-\int_\Omega u\frac{\partial f(p)}{\partial p_k}\ |_{p=p^n}\ \delta p_k d\Omega
\end{aligned} \tag{2.97}$$

The force vector is,

$$\int_\Omega \nabla u \cdot [\mathbf{A}(p^n)\nabla(p^n)]d\Omega - \int_{\partial\Omega} \mathbf{n} \cdot u[\mathbf{A}(p^n)\nabla(p^{n+1})]d\partial\Omega + \int_\Omega u(f(p^n))d\Omega \tag{2.98}$$

2.3.2 Solution Methodology

The governing equations were implemented in the open source fuel cell simulation software OpenFCST [7]. Second order Lagrange elements provided by the deal.II libraries [160] are used to approximate all solution variables. The system matrix and the force vector are evaluated using Gaussian quadrature rule. The resulting non-symmetric matrix is solved using the multi-frontal parallel distributed solver (MUMPS) [161].

The initial mesh contains 12,775 degrees of freedom. The mesh is adaptively refined once using the error estimator by Kelly et al. [162] in deal.II by dividing the 30% of the cells with the largest errors into four cells in order to minimize the local errors.

The convergence criterion for the Newton solver is that the normalized L2-norm of the residual is smaller than 10^{-8}, i.e., $(1/\sqrt{N})\sqrt{\sum_{i=1}^{N}(\mathrm{R}_i)^2}$ where N is the number of degrees of freedom and R_i is the residual at each degree of freedom defined in equation (2.87).

The solutions are grid-independent as the difference of integrated quantities, e.g., total current density and water flux at the boundary, at each cell voltage between the current mesh and a systematically refined mesh is within 0.1% difference.

The overall running time to achieve a complete polarization curve with 20,832 degrees of freedom with 4 processors in parallel is between 8.37 and 651.83 minutes, depending on convergence rate. Convergence is challenging in the regions where the cell transitions from dry (only water vapor leaving the MEA) to wet (liquid water leaving the MEA).

2.3.3 Post Processing

New post-processing routines were implemented in OpenFCST [7] to evaluate velocity vectors and volumetric and surface integrals over the computational domain based on the solutions vapor and liquid. Water fluxes are computed at post-processing by solving the following boundary integrals:

$$\dot{N}_{\mathrm{wv}} = \int_A c_g D_{H2O(\mathrm{vapor}),N2} \nabla x_w \cdot \mathbf{n} dA \tag{2.99}$$

$$\dot{N}_{\text{wl}} = -\int_A \frac{\rho_l k_l}{\mu_l} \nabla p_l \cdot \mathbf{n} dA \tag{2.100}$$

The computed water fluxes are also used to confirm that the conservation equation is satisfied globally. The evaporated or condensed water in the cathode electrodes, current density and heat generated are computed by integrating the volumetric source terms in equations (2.80) and (2.79) over the cathode CL, e.g.,

$$\dot{N}_{\text{evap}} = \frac{1}{V_{\text{CL}}} \int_{V_{\text{CL}}} M_{\text{H2O}} S_{\text{H2O(evap)}} dV_{\text{CL}} \tag{2.101}$$

The cell resistance which is usually measured either by current interrupt or high frequency impedance analysis can also be estimated in the post-processing routine [87]. Using the calculated heat dissipated in the GDL, MPL and CL due to electronic transport and heat dissipated in the PEM due to protonic transport, for example, the dissipated power due to protonic transport in the membrane is calculated using the following equation,

$$\dot{Q}_{H^+} = \triangle V_{H^+} \cdot i = \nabla \phi_m \cdot (\sigma_m^{\text{eff}} \nabla \phi_m) \tag{2.102}$$

Likewise, the dissipated power in the CLs, MPLs, and GDLs, due to electronic transport is,

$$\dot{Q}_{e^-} = \triangle V_{e^-} \cdot i = \nabla \phi_s \cdot (\sigma_s^{\text{eff}} \nabla \phi_s) \tag{2.103}$$

The overall cell resistance is estimated as [87],

$$R = \frac{(\dot{Q}_{e^-} + \dot{Q}_{H^+})}{i^2} A_{\text{active}} \tag{2.104}$$

where $\dot{Q}_{disp}$ is the total heat dissipation, i is the current density and A_{active} is the experimental active area. The model predicted cell resistance is likely lower than the actual cell resistance since contact resistances are not accounted for.

2.4 Conclusion

A multi-dimensional, non-isothermal and two-phase membrane electrode assembly model is developed in the open-source fuel cell simulation package

OpenFCST [7]. In order to develop the model, the following models were implemented in the OpenFCST framework, i.e., PSD model, liquid and gas transport, gas convection and phase change effect. The developed MEA model takes into account gas transport by molecular and Knudsen diffusion, liquid transport by hydraulic permeation and phase change, membrane water transport by back-diffusion, thermo-osmosis, electro-osmosis drag and heat generation and transport. Double trap and dual path kinetic models are used to predict cathode and anode electrochemical reactions. Local transport losses are accounted for using a local transport resistance as discussed in [87, 153]. A dynamic boundary condition at the gas diffusion layer (GDL)/gas channel interface is implemented allowing the model to study both dry and wet conditions as well as the transition between states.

In order to relate layer micro-structural information to water accumulation, a PSD model, obtained by MIP, is used. The PSD model is used to predict local water saturation based on gas and liquid pressures, and can be used to study the effect of varying pore size and wettability. The micro-structural PSD model is validated by comparing the capillary pressure-saturation and saturation-relative liquid permeability relationships to literature data.

Chapter 3

Two-phase Model Validation and Porous Layer Microstructure Optimization

Several two-phase, non-isothermal membrane electrode assembly (MEA) models have been developed over the past decades [11–14, 44]. A promising approach to include micro-structural details in MEA models has been the recent development of pore size distribution (PSD) based mathematical models for analyzing two-phase flow in porous electrodes models [4, 30, 31, 58, 163]. In all previous work, however, the PSD model was either not integrated in a complete MEA model [4, 30, 58] or was integrated only in a one-dimensional model [31, 84]. As a result, detailed validation of the numerical models has seldom been performed, and it has been mainly based on its capability to reproduce polarization curves [11, 12, 31]. A two-dimensional model is required in order to study the validity of the water distribution in channel and land regions. The effect of reactant depletion along the channel can be studied using three-dimensional models; however, extending the model into three-dimensional will greatly increase the model complexity which might lead to convergence issues. Also, the reactant depletion along the channel can be resolved by maintaining high flow rate in channel. Thus, a two-dimensional model is sufficient to study

Parts of this chapter have been published:
J. Zhou et al., A Mixed Wettability Pore Size Distribution Based Mathematical Model for Analyzing Two-phase Flow in Porous Electrodes II. Model Validation and Analysis of Micro-Structural Parameters. *Journal of the Electrochemical Socieity* 164(6): F540-F556, 2017

the two-phase transport in MEA.

In the previous chapter, a mixed wettability pore size distribution based mathematical model has been introduced for analyzing two-phase flow in porous electrodes. The pore size distribution and membrane electrode assembly models were validated by comparison to experimental polarization curves from literature data. The model, however, was not validated in terms of its ability to accurately estimate cell performance and cell resistance under both hot/dry and cold/wet conditions, two-dimensional water distributions, and liquid and water vapor fluxes. The goal of this chapter is to further validate and analyze the results of the developed model for varying operating conditions, and GDL and CL structures.

3.1 Two-phase Model Validation

In this chapter, the model developed in the previous chapter is used to study hot and dry, hot and wet, and cold and wet conditions. The gas mixture transport is not included for the results in this chapter to reduce the model complexity. It has been accounted in Chapters 4 and 5. Results show that, under dry conditions, the model is equivalent to a single phase model and all water leaves the MEA in vapor form. Under wet conditions, the model is capable of predicting the regions of water accumulation which have been observed experimentally by many researchers [8, 9, 164, 165]. Model validation is performed by comparing the model predictions to experimental polarization curves and membrane resistance values for different GDLs operating at various conditions in our laboratory. The numerically predicted water distributions are compared with neutron and x-ray radiography data in the literature [8, 9].

3.1.1 Catalyst Layer Fabrication and Characterization

CCMs were prepared in-house using the doctor blade method. The catalyst ink was prepared with 46.7 wt% Pt on carbon (Tanaka, TEC10EA50E), and equal amounts of propylene glycol (PG) (Sigma Aldrich) and cooled isopropyl alcohol (IPA) (Sigma Aldrich) by weight. After bath sonicating the ink for

30 minutes at 30 °C, Nafion solution (Ion Power LQ1105 1100EW 5wt%) was added in order to achieve a Nafion loading of 30 wt%. Sonication continued for another 30 minutes, followed by probe sonication for 15 minutes, and bath sonication for a final 30 minutes.

The ink was deposited on a PTFE substrate using a pipette. A doctor blade at a height of 6 mils was then drawn across the substrate at approximately 25.4 mm/s using an automatic film applicator (BYK Gardner 2121). Once the layer was dry, it was decal-transferred onto a NRE-211 membrane by applying a temperature of 120 °C and a pressure of 1.92 MPa for 5 minutes. Platinum loading was determined by weighing the Teflon sheet before and after decaling.

3.1.2 Membrane Electrode Assembly Testing

All tests were performed with a Scribner 850e test station with the conditions listed in Table 3.1. After conditioning the cell, the platinum active area was determined using cyclic voltammetry (CV) at 30°C. Fuel cell testing hardware with parallel channel plates and a test area of 5 cm^2 was used. Three MEAs were tested for each GDL type to ensure the results were repeatable. In hot/dry and hot/wet cases, each data in the polarization curve was obtained at a flow rate of 0.2 slpm and 0.4 slpm in anode and cathode, respectively, while operating the cell at a constant current density in steps of 0.02 A/cm^2 for one minute.

Table 3.1 – Experimental validation parameters

Parameters	Hot/dry	Hot/wet	Cold/wet
GDL type	SGL 34BA/Toray 090	SGL 34BA/Toray 090	SGL 34BA/Toray 090
CL fabrication method	doctor blade	doctor blade	doctor blade
Anode flow rate (slpm)	0.20	0.20	1.00
Cathode flow rate (slpm)	0.40	0.40	3.00
Temperature (K)	353.15	353.15	333.15
Channel type	Parallel	Parallel	Parallel
RH both cathode and anode (%)	50	90	90
Anode and cathode pressure (atm)	ambient	ambient	ambient
Active area (m^2_{Pt}/g_{Pt})	35.19 ± 5.02	35.19 ± 5.02	35.19 ± 5.02
Platinum loading (mg_{Pt}/cm^2)	0.2 ± 0.05	0.2 ± 0.05	0.2 ± 0.05

For the cold/wet case, high fluctuations in cell voltage over time were observed at low flow rates and high current densities as shown in Figure 3.1. In the figure, the variation of cell voltage vs. time for three different MEAs

is plotted by holding the current density at 0.5 A/cm^2 (near limiting current) for one hour and varying the cathode flow rate from 4 slpm to 0.4 slpm. The high fluctuations in Figure 3.1 at a flow rate of 0.4 slpm are likely due to water accumulation in the gas channel. With increasing flow rate, the cell voltage and its stability increase. As the flow rate continues to grow, the reason for the variability in performance may be due to water accumulation in the MEA since the variability disappears once an MPL is introduced as observed in our experiments (see Figure 4.7 in Chapter 4) as well as by Atiyeh et al. [166]. The cathode channel flow rate used for the cold/wet case is, therefore, set to 3 slpm because the cell voltage is more stable. The anode flow rate is set to 1 slpm. In order to make sure the cell is operating at steady-state, the current was recorded after a 20 minute hold.

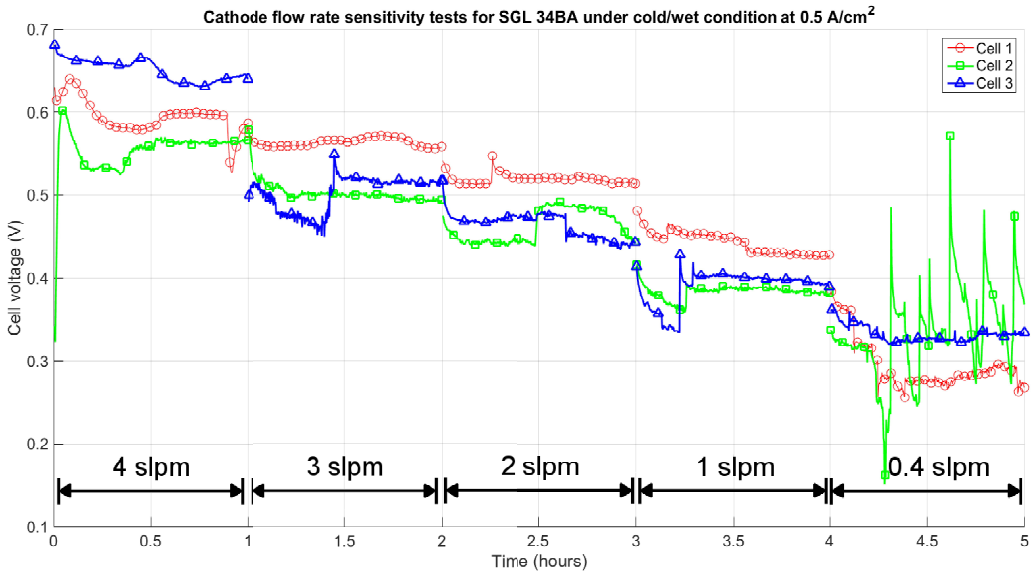

Figure 3.1 – Variations of cell voltage vs. time at various cathode channel flow rates for three MEAs at a constant current density at 0.5 A/cm^2 under cold/wet condition.

3.1.3 Input Parameters

The MEA parameters, such as computational geometry, kinetic parameters and transport properties, are set such that they reflect the PEFC configuration. Channel and current collector width are 1.0 mm. Table 2.2 shows PSD GDL

and CL baseline parameters in the simulations. The porosity and PSD of Toray 090 GDL (20%PTFE) and SGL 34BA were measured in-house using mercury intrusion porosimetry (MIP). The experimental data for Toray 090 are in agreement with a previous publication [112]. The volume fractions of hydrophilic pores in the GDLs are estimated by manually fitting the capillary-saturation curves in the literature [83].

The CL PSD is measured using MIP and the thickness is measured using scanning electron microscopy (SEM). The CL porosity is estimated by subtracting electrolyte and solid phase volume fractions from one. The external CL contact angle has been measured in references [123, 167, 168]. However, a direct measurement of the CL internal contact angle has not been reported. In this study, the hydrophobic contact angle used in the CL is 93° and it is an average of the values (92° and 94°) reported by Yu et al. [123]. The contact angle assigned to the hydrophilic pore-network is 84° by considering the contact angle of Ketjen Black carbons reported by Soboleva et al. [66]. All electrochemical parameters for CLs are obtained from the experiments discussed in the MEA fabrication and testing sections.

The thermal related parameters, i.e., GDLs, CLs and PEM thermal conductivity as well as all PEM transport properties used in the model, are from the previous OpenFCST non-isothermal MEA model validation study reported by Bhaiya et al. [3]. The double trap and dual path kinetic parameters used in the model are given in Moore et al. [131] and Wang et al. [169], respectively. The micro-scale ICCP model parameters used in the simulation were reported by Secanell et al. [87], in particular the local resistance rate constants are 0.1 and 0.001 cm/s in anode and cathode, respectively for 80°C and 50% RH, and 60°C. For 80°C and 90% RH the values are 0.1 and 0.005 cm/s. In order to obtain the value for local resistance rate constant at 80°C and 50% RH and 80°C and 90% RH, simulations for CLs with varying Pt loading were performed using multiple local resistance rate values until the slope of the total oxygen resistance vs. the roughness factor (i.e., the product of Pt loading and electrochemical active surface area) for the model and the experiments in reference [170] were similar. The values of the local resistance rate that provided the

best fit for the two relative humidities are then used in the study.

All input parameters in the model are the same for all simulations except evaporation and condensation rates which are considered to be temperature dependent, and the local resistance constant used in the ICCP model [87] at 80°C and 90% RH. At 80°C, 50% RH and 90% RH cases, an evaporation rate of $2 \cdot 10^{-3}$ mol/(cm$^2 \cdot$ s) is used as it allows most water to be evaporated, as observed experimentally. At 60°C and 40°C, a value of $2 \cdot 10^{-4}$ mol/(cm$^2 \cdot$ s) is used in order to take into account experimental evidence reported by Zenyuk et al. [171] showing a decrease in evaporation rate with temperature. At 80°C, a condensation rate of $2 \cdot 10^{-3}$ mol/(cm$^2 \cdot$ s) is used as smaller values result in an RH greater than one. At 60°C and 40°C, the condensation rate constant used is $2 \cdot 10^{-2}$ mol/(cm$^2 \cdot$ s).

3.1.4 Model Validation with Electrochemical Performance

Experimental data and numerical model predictions are compared for the MEA with the doctor blade CCM and the SGL 34BA at a variety of operating conditions (see Table 3.1). Figure 3.2 (a), (c) and (e) show the polarization curves for SGL 34BA obtained from simulations and experiments. The corresponding cell resistances are shown in (b), (d) and (f). The cell resistances are computed experimentally by current interrupt [172] and numerically by calculating the electronic heat loss in GDLs and the protonic heat dissipation in the membrane as discussed in [87]. The error bars represent the standard deviation of the averaged forward sweep of three different cells. Figure 3.2 (e) shows the polarization curves for the three cells obtained experimentally by holding each data point for 20 minutes. Experimental and numerical results are in reasonable agreement at all conditions. In order to understand the importance of water movement in determining the water distribution, both water vapor and liquid water fluxes at the anode and cathode boundaries, and the water transported by the membrane due to electro-osmotic drag, back diffusion and thermal-osmosis are studied. The PCI flow in the cathode CL and GDL is also examined quantitatively. All the water fluxes and PCI flow in the MEA are shown in Figure 3.3. The normalized water flux reported in the plots is

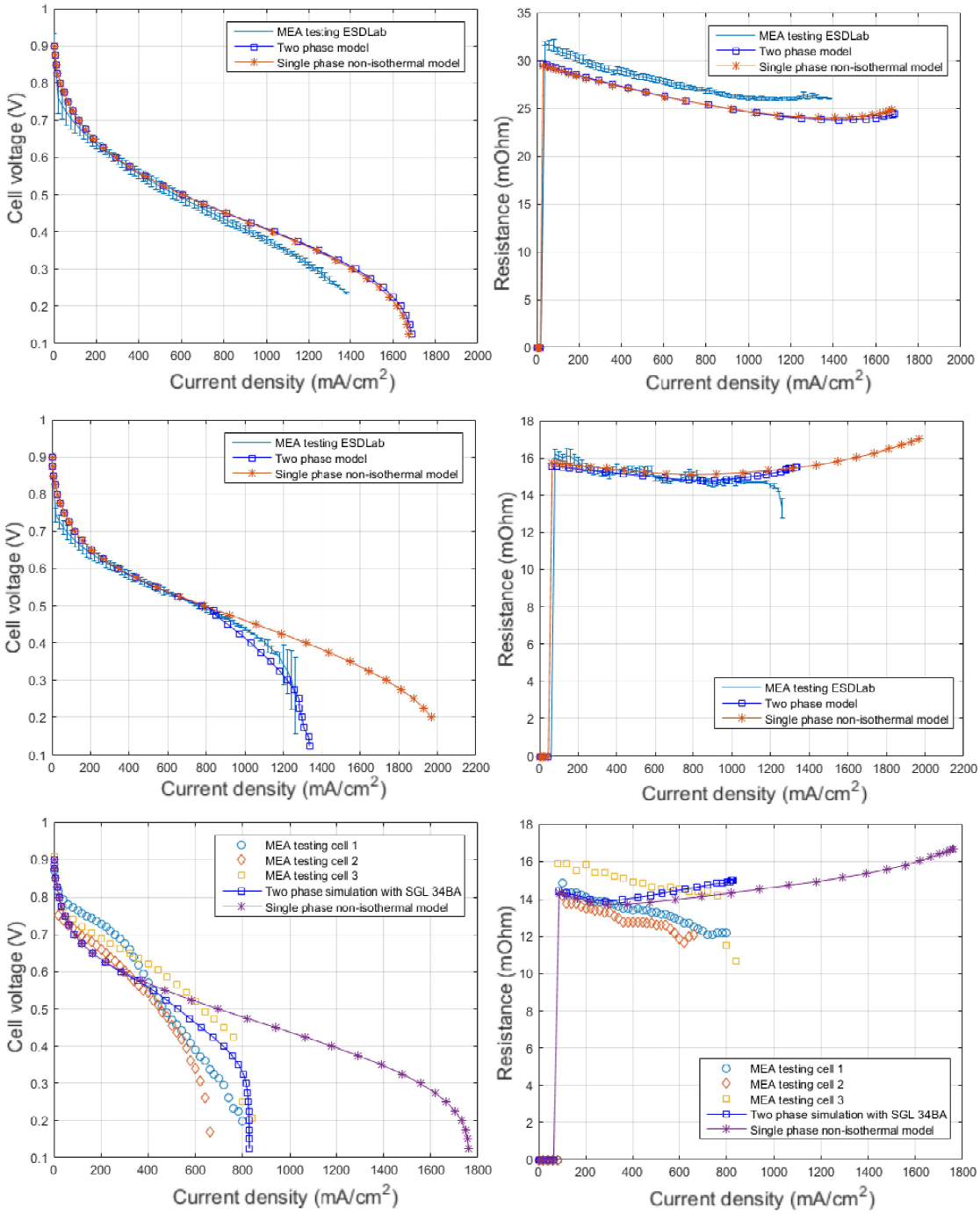

Figure 3.2 – Experimental validation of polarization curves using two-phase model at: (a) 80°C and 50% RH, (c) 80°C and 90% RH, (e) 60°C and 90% RH for SGL 34BA, and the corresponding cell resistance at: (b) 80°C and 50% RH, (d) 80°C and 90% RH, (f) 60°C and 90% RH.

defined as,

$$\beta = \frac{2F}{j}\frac{N_{\mathrm{H2O}}}{M_{\mathrm{H2O}}} \tag{3.1}$$

where N_{H2O} is the water flux evaluated at the boundary in g/(cm$^2 \cdot$ s), F is Faraday's constant, j is the current density and M_{H2O} is the water molar mass. The positive values in Figure 3.3 (a) represent a flux leaving the MEA. In Figure 3.3 (b), a positive value represents that the water evaporates. The boundary condition guarantees liquid water will not enter the MEA. A negative liquid water flux is only observed on one occasion because of the instability of the change in the boundary condition when the capillary pressure reaches the breakthrough pressure. As the temperature decreases, the majority of water leaving the cathode boundary changes from vapor to liquid phase.

3.1.4.1 Hot/dry case

In the hot/dry case, Figure 3.2 (a) shows single-phase and two-phase models exhibit the same polarization curves. The distributions of saturation in the MEA and the cathode CL at current density 1.5 A/cm^2 are shown in Figure 3.4 (a) and (b). Zero saturation is observed everywhere except at the cathode CL. In this case, the existence of a hydrophilic network in the CL is of importance in order to provide a minimal liquid-gas interface required for vaporization. Vaporization is possible because the gas in the cathode CL is not saturated as shown in Figure 3.4 (c). The saturation distribution explains why single-phase and two-phase flow models show similar results in Figure 3.2 (a).

The water fluxes and the amount of PCI flow in the cathode are shown in Figure 3.3 (a) and (b). Figure 3.3 (a) shows that the amount of water produced by the electrochemical reaction plus the water entering the anode is equal to the total water vapor flux leaving the system, and the flux of liquid water is found to be zero at all current densities. At low relative humidity and high temperature, therefore, complete evaporation takes place inside the cathode CL as shown in Figure 3.3 (b) and liquid water movement is prevented due to the low liquid relative permeability at low saturation. Comparing anode and cathode water vapor flow rates in Figure 3.3 (a), the movement of water from

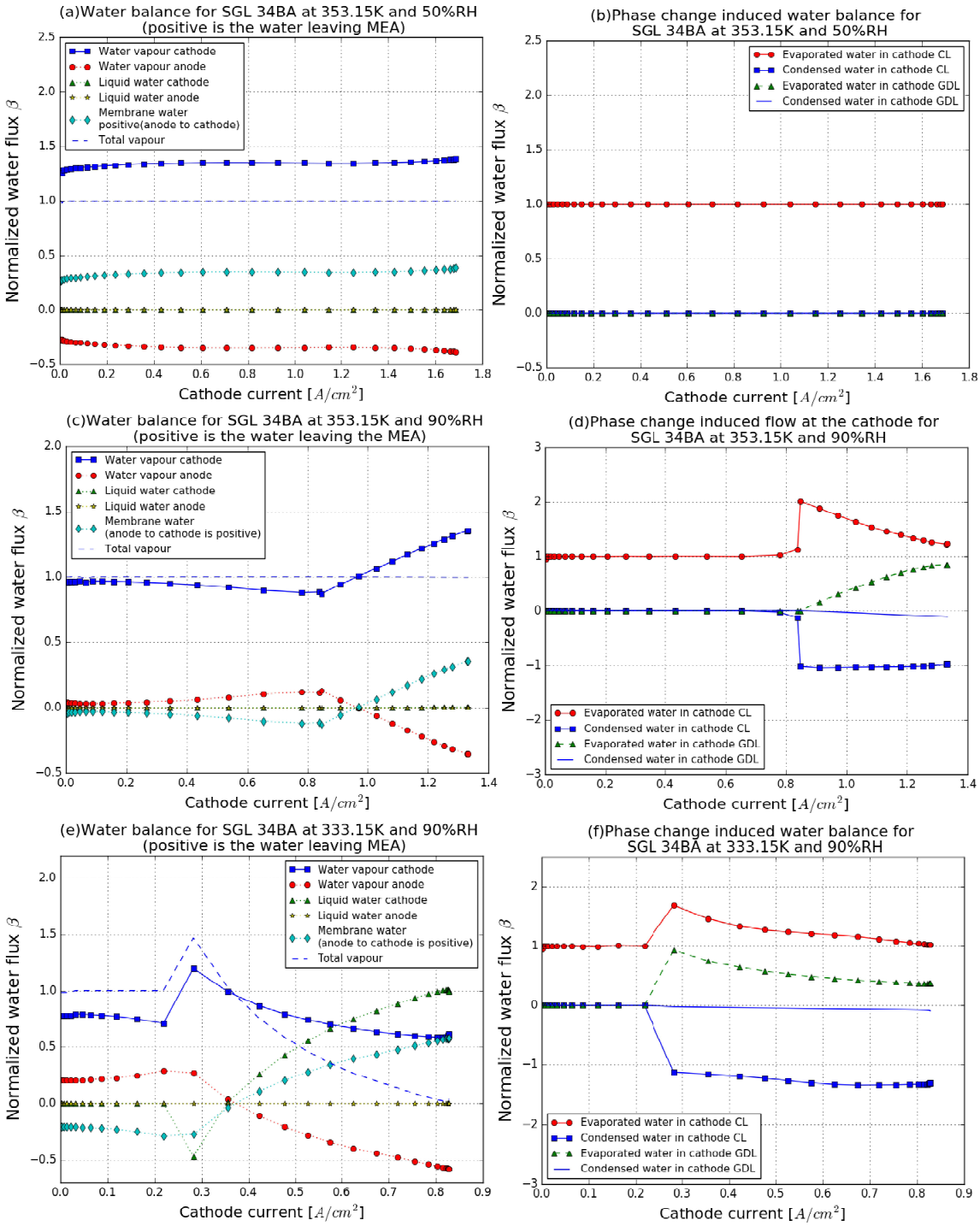

Figure 3.3 – Water flux plots for SGL 34BA at: (a) 80°C and 50% RH, (c) 80°C and 90% RH, (e) 60°C and 90% RH, phase change induced water plots for SGL 34BA at: (b) 80°C and 50% RH, (d) 80°C and 90% RH, (f) 60°C and 90% RH at the cathode.

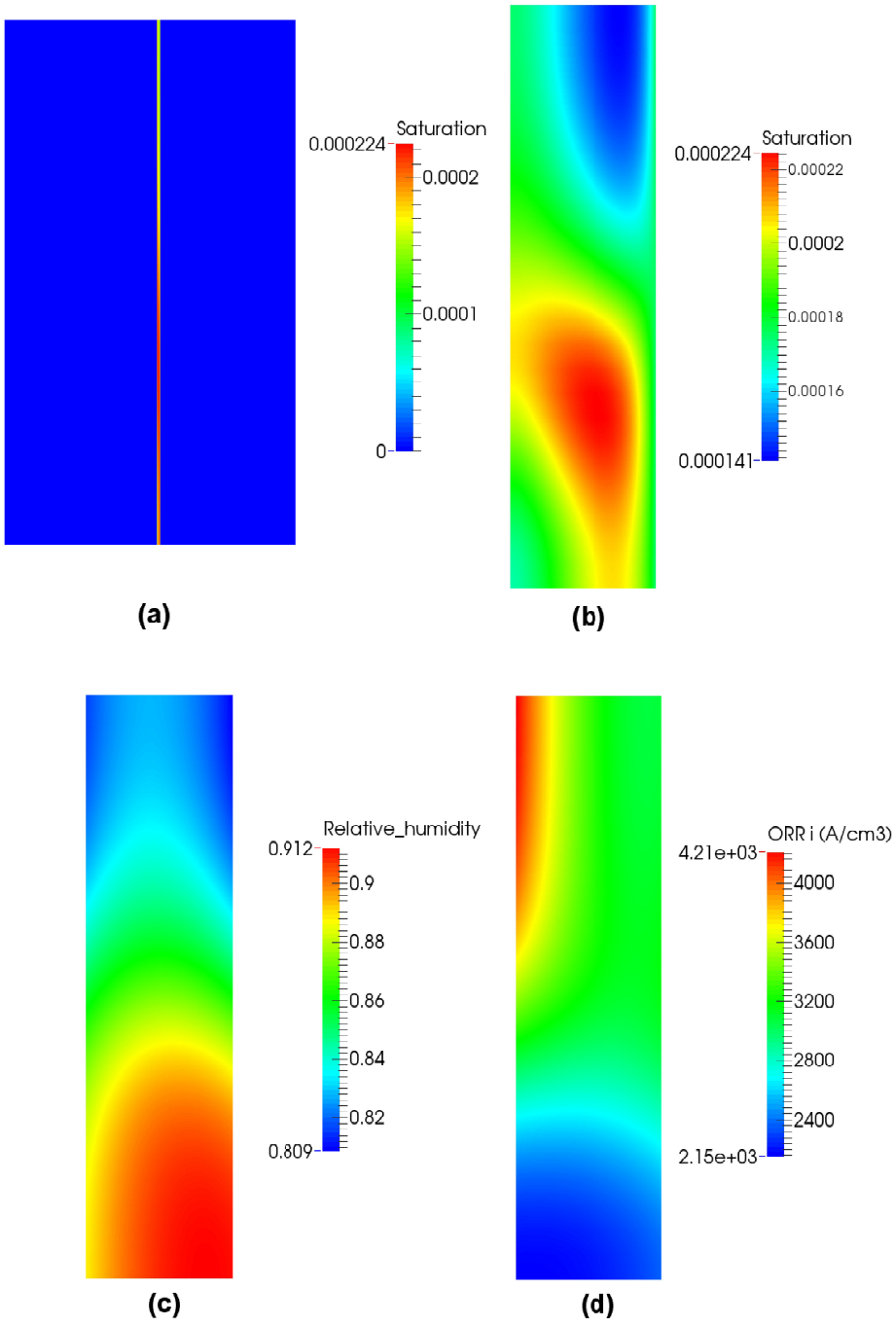

Figure 3.4 – Distribution of: (a) saturation in the MEA, (b) saturation in the cathode CL, (c) relative humidity in the cathode CL, and (d) volumetric oxygen reduction reaction (ORR) current density in the cathode CL for SGL 34BA under hot/dry condition at 1.5A/cm^2.

anode to cathode is shown to be governed by the electro-osmotic drag.

3.1.4.2 Hot/wet case

In the hot/wet case, the difference in performance between the single-phase and two-phase models is significant at high current density because of water accumulation. Figure 3.5 shows the saturation distribution in the MEA and the saturation, volumetric current density and membrane water content distributions in the cathode CL at 1.0 A/cm^2 where the performance is limited by the blockage of liquid water. In the MEA, the majority of liquid water is observed in the cathode CL and a discontinuity in water saturation is clearly observed at the CL/GDL interface. The discontinuous saturation between the cathode CL and GDL is a result of different wettabilities. As compared to the hot/dry case (see Figure 3.4 (d)), the rate of the reaction is more concentrated close to the cathode CL/GDL interface due to the additional diffusive transport losses caused by the presence of liquid water. The increased water saturation can be explained by the volumetric evaporated/condensed water in the CL.

The distributions of relative humidity, volumetric evaporation and condensation, and interfacial surface area in the cathode CL are shown in Figure 3.6 at the same current density. The majority of the CL is oversaturated as shown in Figure 3.6 (a) indicating that the movement of liquid water in the CL is governed by capillary flow. Sorbed water in the ionomer moves from the inner CL to the CL/GDL interface due to increased electro-osmotic drag at 1.0 A/cm^2 (see Figure 3.5 (c)). Since the middle of the CL is oversaturated (see Figure 3.6 (a)), the membrane water near the GDL/CL interface is desorbed into vapor and then condensed as shown in Figure 3.6 (c). The condensed water at the CL/GDL interface is then transported back to the inner CL due to a saturation gradient (see Figure 3.5 (b)). At the PEM/CL interface, water is evaporated and the water vapor is sorbed back into the ionomer. The end result is a circulation loop with membrane water moving from PEM/CL to the GDL/CL interface and liquid water moving back from GDL/CL interface to the PEM/CL interface. Due to the Kelvin effect, the relative humidity required for water vapor to condense in hydrophobic pores is

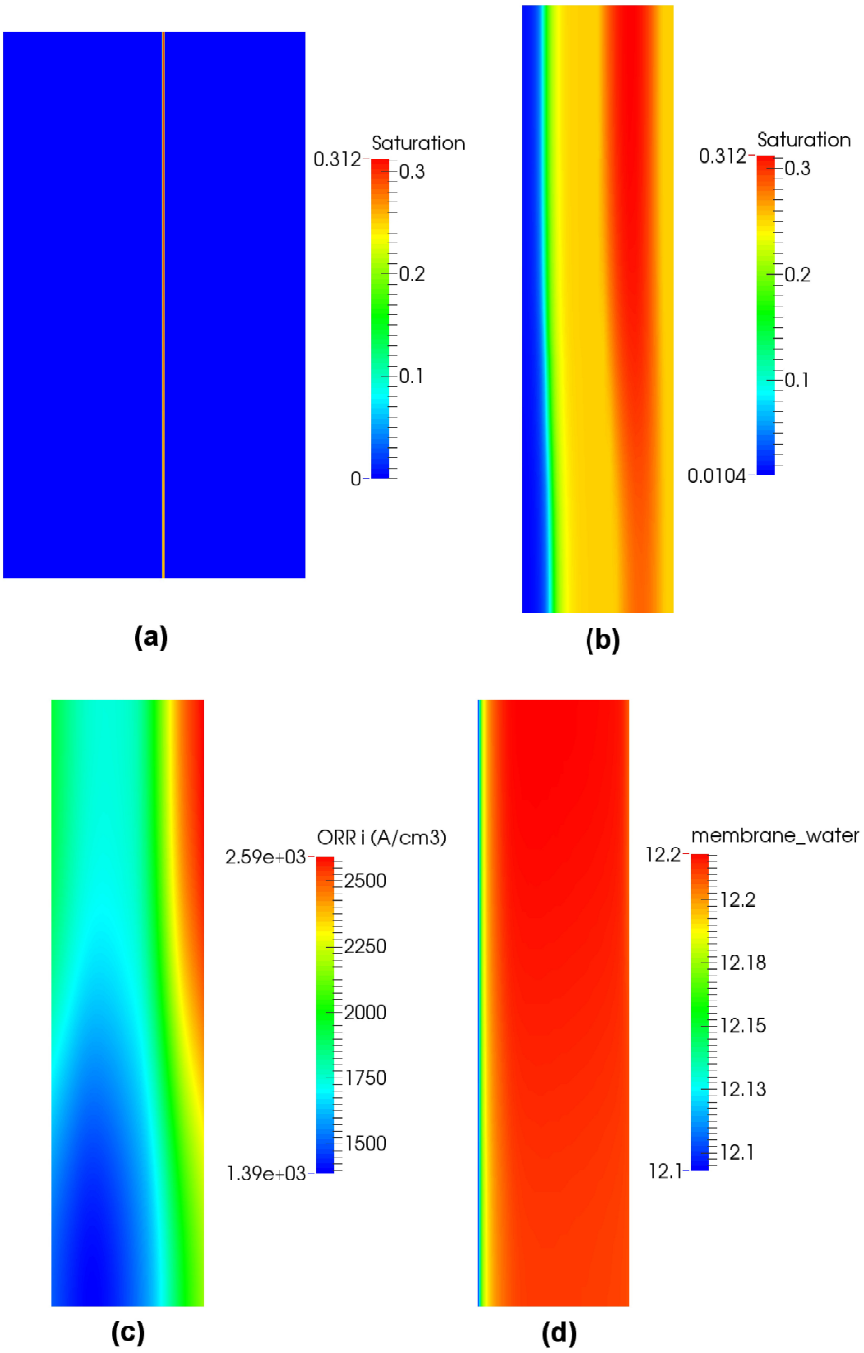

Figure 3.5 – Distribution of: (a) saturation in the MEA and (b) saturation in the cathode CL, (c) volumetric ORR current density and (d) membrane water content in the cathode CL, at current density 1.0 A/cm^2 under hot/wet condition.

higher than 100%. This results in a relatively small volumetric condensation

distribution in the CL as shown in Figure 3.6 (c). The high evaporation rate observed in Figure 3.6 (b) at the cathode GDL/CL interface is due to the fast diffusive water transport at the GDL side and the high interfacial surface area available for phase change (see Figure 3.6 (d)).

Figures 3.3 (c) and (d) show the water movement in the MEA and the amount of PCI flow at the cathode. As compared to the hot/dry case, the saturation increases greatly in the cathode CL at high current densities (see Figure 3.5 (a) and Figure 3.4 (b)), whereas the liquid water flux is still zero at all current densities. The zero flux of liquid water can be explained by the evaporation zone observed at the GDL/CL interface (see Figure 3.6 (b)) which changes all water from liquid to vapor form. The water vapor flux from cathode to anode observed in Figure 3.3 (c) suggests that the water transport in the membrane is governed by back diffusion at low current densities. This can be explained by the relative humidity gradient between the anode and cathode. With the increase in current density, the relative humidity in the cathode continues to grow creating a larger driving force for back diffusion until the cathode electrode is fully saturated at about 1.0 A/cm^2. Back diffusion then reaches its maximum while water transport due to the electro-osmotic drag continues to grow resulting in water movement from anode to cathode (see Figure 3.3 (c)). As the majority of the cathode CL is oversaturated at high current densities (see Figure 3.6 (a)), the water transported by the membrane is first evaporated from the ionomer, then condensed in the middle region of CL and finally evaporated at the GDL/CL interface.

3.1.4.3 Cold/wet case

The difference in performance between single-phase and two-phase models is substantial when the temperature is reduced from 80°C to 60°C as shown in Figure 3.2 (e). In this case, liquid water accumulation is clearly limiting the MEA performance. Figure 3.7 shows the saturation distribution in the MEA and CL, volumetric ORR current density and membrane water content in the cathode CL at current density 0.7 A/cm^2 where the performance of the fuel cell has severely decreased in comparison to the single-phase model prediction.

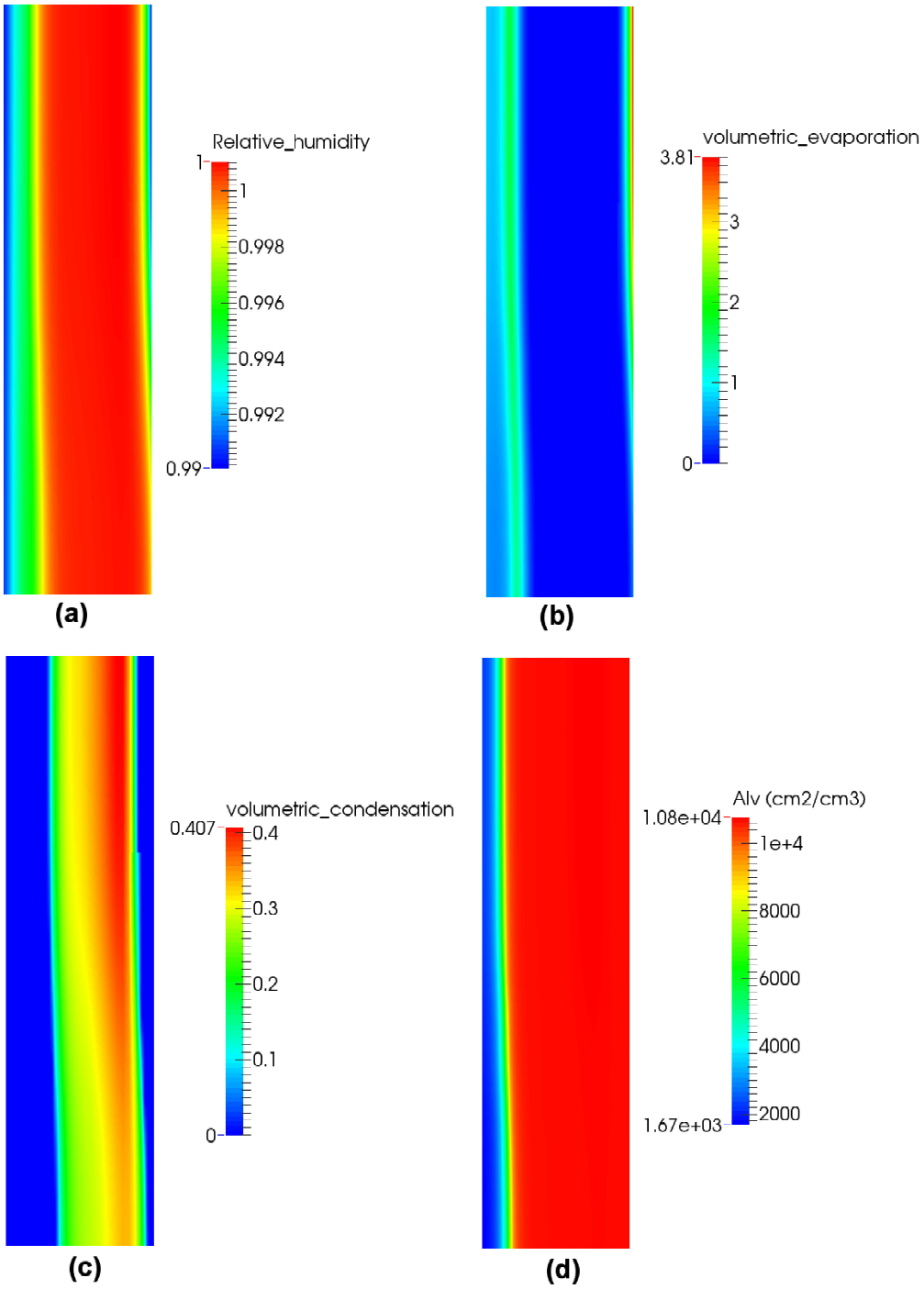

Figure 3.6 – Distribution of: (a) relative humidity, (b) volumetric evaporation, (c) volumetric condensation, and (d) interfacial surface area in the cathode CL at current density 1.0 A/cm^2 under hot/wet condition.

The overall liquid water saturation increases in both cathode CL and GDL as compared to the hot/wet case (see Figure 3.5 (a)) with water accumulation

clearly visible in the GDL. This can be explained by both reduced evaporation rate and saturated vapor pressure with decreasing the temperature leading to more condensation in the cathode (see Figure 3.3 (f)). As a result of the higher saturation, the majority of the electrochemical reaction is concentrated at the GDL/CL interface highlighting that the transport of reactant has been severely obstructed by liquid water in the cathode CL. At the CL/membrane side, the cathode CL is less active. The membrane water content is uniform in the cathode CL and it is lower than in the hot/wet case due to the dependence of the sorption isotherm on temperature.

The water movement under wet/cold condition is studied by plotting the water fluxes in the MEA and the amount of evaporated/condensed water at the cathode, see Figure 3.3 (e) and (f). At low temperature and high current densities, the majority of water transported to the cathode boundary is in liquid form, because most of the cathode CL is oversaturated and the liquid water evaporation is insignificant. As compared to the hot/wet case, where the cathode water vapor increases with the current density, the cathode vapor flux shows a gradual decrease once the liquid water starts to leave at the cathode boundary. Figure 3.3 (f) shows that the evaporated water in the cathode CL decreases with increasing current density whereas the condensed water remains approximately constant at moderate current densities. The amount of water evaporated in CL decreases at high current densities due to the increase in membrane water transport from anode to cathode (see Figure 3.3 (e) and (f)). Figures 3.3 (e) and (f) show that, when current density is over 0.3 A/cm^2, the water vapor leaving the cathode boundary is close to the liquid water evaporated in the cathode GDL. This highlights that, even when the cathode CL is fully saturated, water can still be evacuated via GDL-channel boundary in the vapor form due to the evaporation in the GDL.

3.1.5 Model Validation with Imaging Data

In situ liquid water visualization measurements without MPL have been reported by Deevanhxay et al. [8] and Lee et al. [9] for fuel cells operating at 28°C, 60% RH and a flow rate of 0.1 slpm, and 60°C, 100% RH and a flow

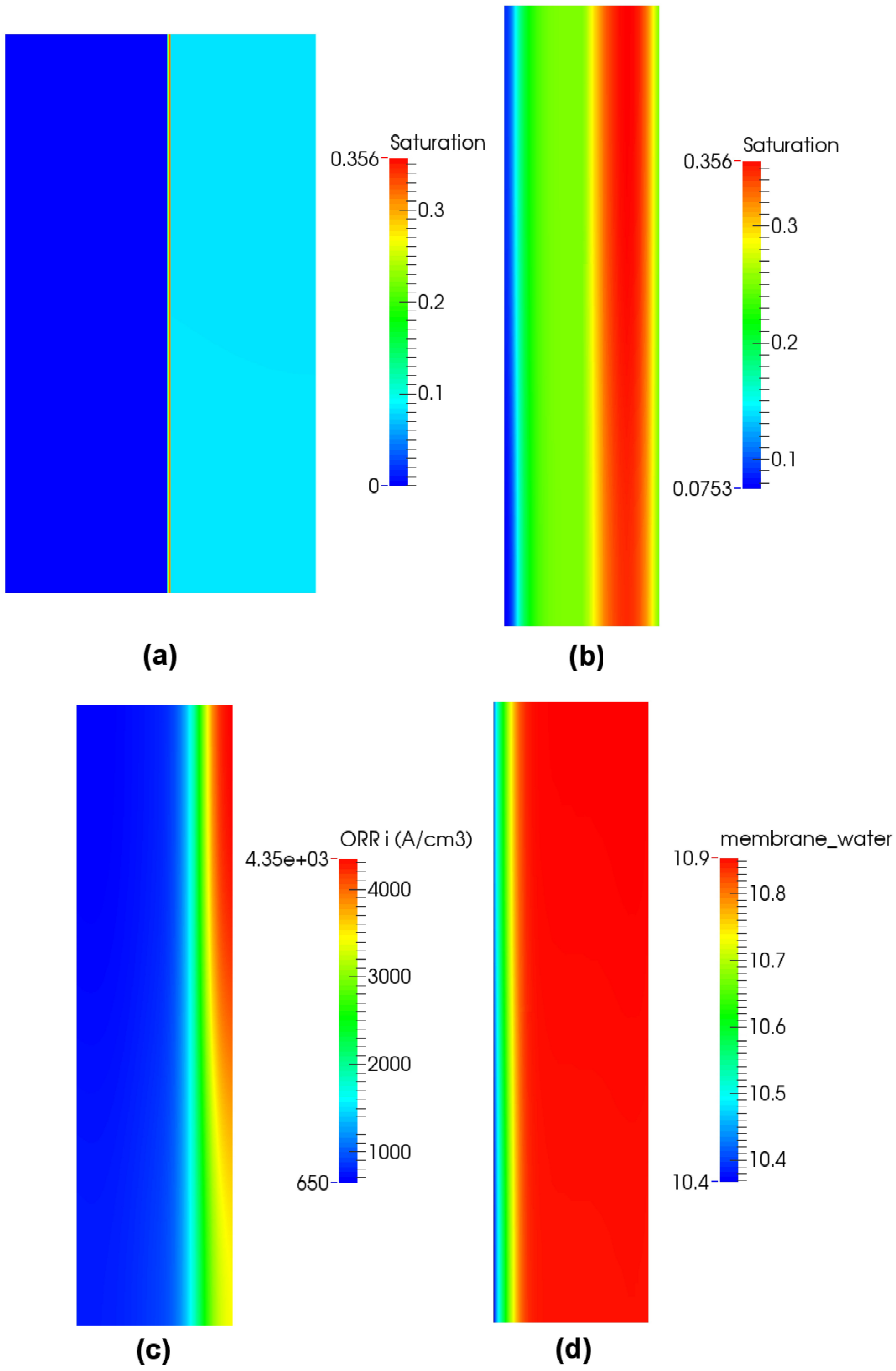

Figure 3.7 – Distribution of: (a) saturation in the MEA, (b) saturation in the cathode CL, (c) volumetric ORR current density and (d) membrane water content in the cathode CL at current density 0.7 A/cm^2 under cold/wet condition.

rate of 1 slpm, respectively. The data reported by Deevanhxay et al. [8] has a spatial resolution of 1.5 μm, and a pixel resolution of 4.7 μm for the data

reported by Lee et al. [9]. In order to compare the water distribution between the two-phase model predictions and imaging data, simulations are performed using the same configurations reported in the experiments [8, 9].

The width of channel and rib used is 0.1 mm. The membrane (NRE-211) and the GDL (SGL 34BA) properties in the simulation are modified to correspond to the configurations in the experiment, i.e., thickness of membrane has been adjusted to 50 μm and the GDL thickness and porosity are 190 μm and 0.8, respectively. The rest of the parameters remained the same. The operating conditions are 28°C, 60% RH and one atmosphere. The numerical saturation distribution in the cathode and the cathode CL are shown in Figures 3.8 (a) and (b) at a current density 0.5 A/cm^2. It can be seen that the majority of the liquid water is concentrated at the CL/GDL interface, and the cathode CL saturation decreases from the GDL to membrane side. These agree with the experimental observations [8]. Figure 3.8 (c) shows the saturation distributions in the cathode CL under the rib, channel and rib/channel interface predicted by the numerical model and the imaging data taken 480 and 600 seconds after operating the cell. The liquid water concentration (cm^3/(g·carbon)) reported by Deevanhxay et al. [8] is converted to liquid water saturation by first subtracting the OCV water concentration (0.22 cm^3/(g $\cdot$ carbon)), multiplying the result by the carbon density (1.9 g/cm^3) reported in [170], and finally multiplying by the ratio between solid phase (the carbon black only) and void phase. The soft X-ray data [8] in Figure 3.8 (b) shows a continuous decrease of water saturation from the GDL to the membrane side, whereas a slight increase in saturation is observed near the GDL side from the numerical prediction. The reason for this discrepancy might be because of imperfect GDL/CL interface which the model does not account for.

With the CL parameters (0.35 mg/cm^2 platinum loading) reported by Lee et al. [9], a simulation is conducted with a channel and rib width of 0.2 mm. A TGP-H-060 GDL with a thickness of 130 μm and the same PSD configuration as the Toray 090 reported in this paper is used in the simulation. To compensate the microstructural changes in the GDL due to the 85% compression reported by Lee et al. [9], both the porosity and the pore radius are reduced

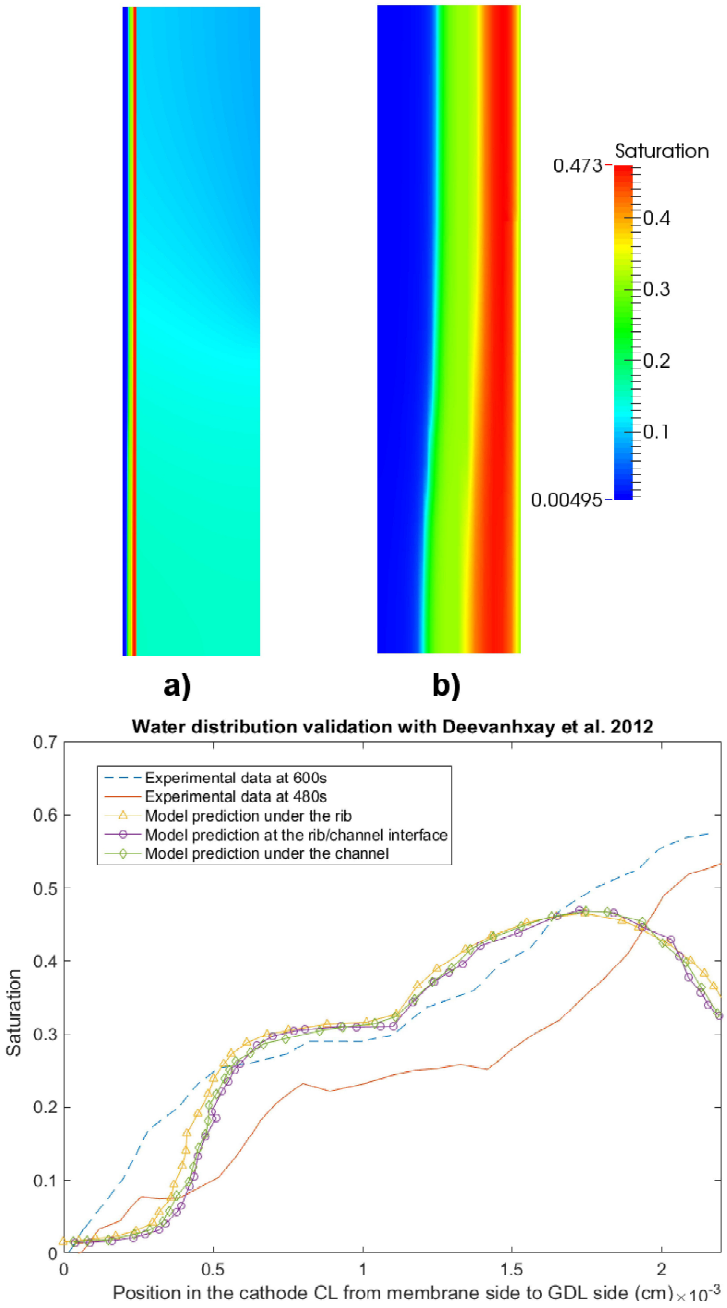

Figure 3.8 – Validation of water profile with soft X-ray radiography data reported by Deevanhxay et al. [8], saturation distributions (a) in cathode and (b) in cathode CL, and (c) through plane saturation plots in cathode CL under the rib at current density 0.5 A/cm^2.

by 15% in the simulation accordingly. The operating conditions used are 60°C, 100% RH and one atmosphere, the rest of the parameters remain the same as

in the previous validation section. Figure 3.9 (a) shows the saturation distribution in the cathode at current density 0.5 A/cm^2. Liquid water accumulation is observed at the region close to the cathode CL/GDL interface in agreement with the experimental observation [9].

Figure 3.9 (b) shows the comparison of the water content at through-plane direction between experimental data and numerical predictions. The water thickness (cm) reported by Lee et al. [9] is converted to liquid water saturation by dividing by the length of active area along the beam path (0.8 cm) and porosity (0.7) of the GDL. An increase of water saturation from the channel side to the GDL/CL interface is observed both experimentally and numerically. The proposed two-phase model predicts a sharper saturation gradient at the region close to GDL/CL interface whereas the experimentally observed gradient [9] was much smoother than the numerical prediction (see Figure 3.9 (b)). The difference in saturation plots between model prediction and experimental observation might be due to the compression in the GDL which potentially changes the microstructure of the porous media among many other reasons.

3.1.6 Analysis of Different Gas Diffusion Layer

Figure 3.10 shows the experimental and numerical iR-free polarization curves for a fuel cell with the same MEA as in previous results but with a Toray 090 (20%PTFE) GDL. The contact resistance in the cells using Toray 090 were found to be high as compared to the cells with the SGL 34BA. GDL conductivity is high for both and the same MEA is used in both cases, so it is assumed contact resistances are responsible for the discrepancy which the model does not account for. iR-free curves are thus used in this section. The experimental results agree with the two-phase model predictions at all conditions highlighting that the two-phase model is able to predict the change in the MEA performance with different types of GDLs. Numerical results for SGL 34BA are also shown to highlight the differences between the two GDLs.

Cell performance decreases for the Toray 090 (20%PTFE) as compared to the SGL 34BA, especially in the mass transport region at high temperature. Figure 3.11 shows a comparison of the oxygen molar fraction distributions be-

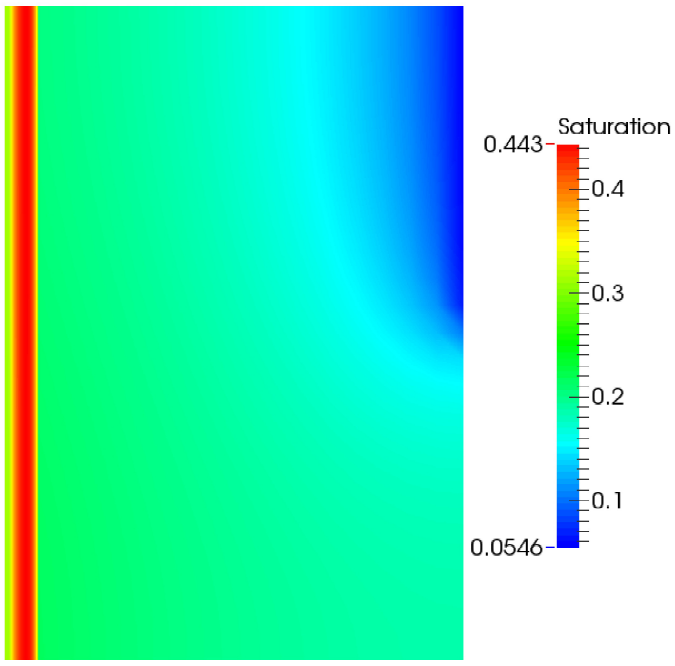

(a)

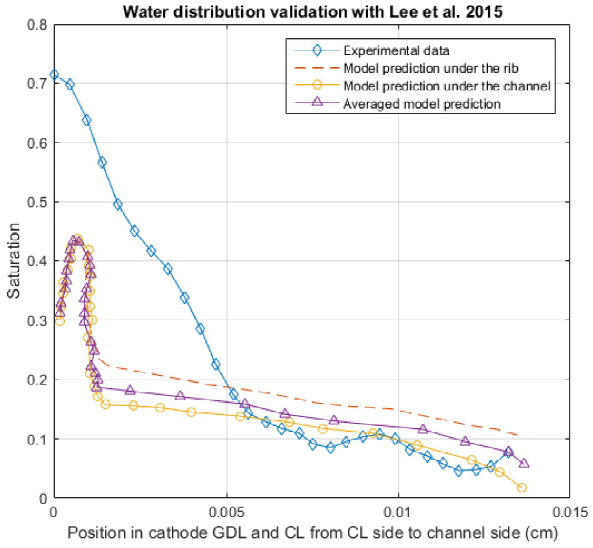

(b)

Figure 3.9 – Comparison of water profile to synchrotron radiographic imaging data reported by Lee et al. [9], (a) saturation distribution of the cathode and (b) the cathode CL, and (c) through plane saturation distribution of numerical data vs. imaging data at current density 0.5 A/cm^2.

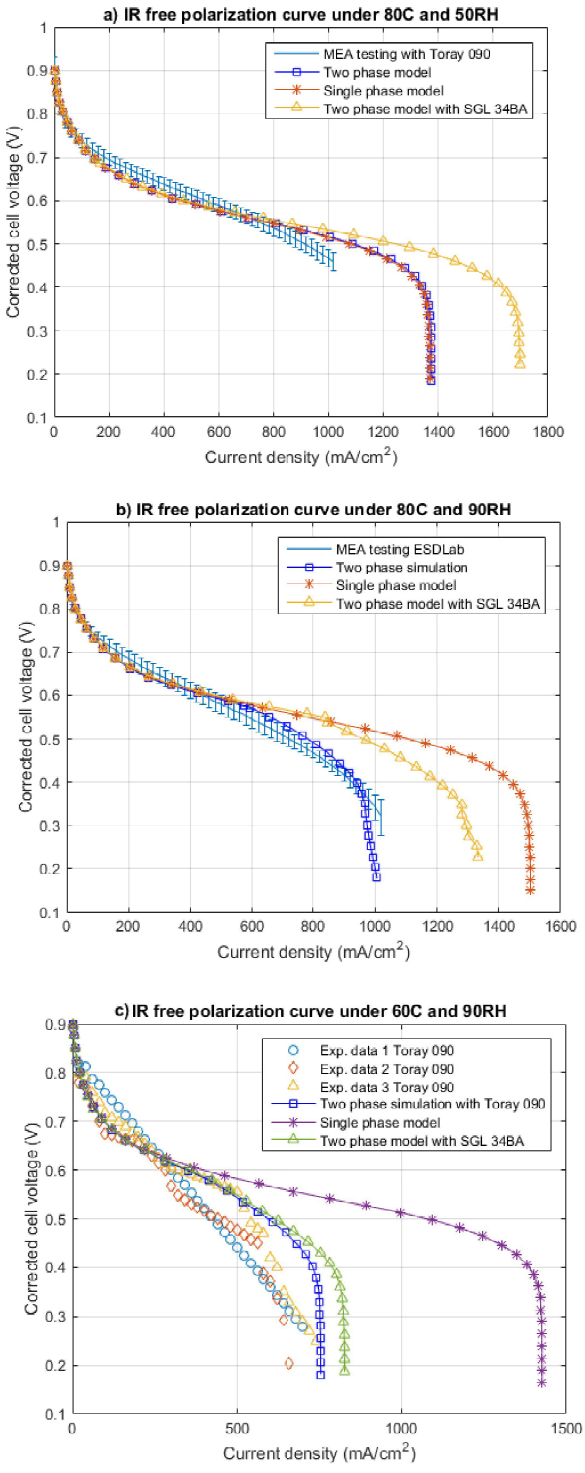

Figure 3.10 – Experimental validation of iR free polarization curves using two-phase model at: (a) 80°C and 50% RH, (b) 80°C and 90% RH, and (c) 60°C and 90% RH for Toray 090 20%PTFE.

tween SGL 34BA and Toray 090 in the cathode CL in the single-phase and two-phase region, respectively. The reduced MEA performance for Toray 090 in the single-phase region is due to the lower porosity, which results in a lower reactant concentration in the CLs as shown in Figure 3.11 (a) and (b). The difference in the overall performance between the two GDLs decreases in the two-phase region, especially in the cold/wet case (see Figure 3.10 (c)). This can be attributed to water accumulation in the cathode CL which blocks the reactant transport (see Figure 3.11 (c) and (d)) and deactivates the ORR reaction at the inner region. The difference in limiting current density between two GDLs in the cold/wet case can be explained by the GDL water management.

Figures 3.12 (a) and (b) show the capillary pressure profiles in the cathode GDLs for SGL 34BA and Toray 090 (20%PTFE), under cold/wet conditions at current density 0.6 A/cm^2, where the performance is severely limited due to water accumulation. The capillary pressure distributions are significantly different for the two GDLs. As SGL 34BA has a wider PSD [163] than Toray 090, the PSD centered at 34.0 μm results in a higher effective liquid permeability as shown in Figure 3.12 (c) which can be used to explain the previous capillary pressure distributions. An increase in effective liquid permeability is clearly observed in SGL 34BA when the capillary pressure is greater than zero. Whereas in Toray 090, only when the capillary pressure is above 2000 Pa, the growth of the effective liquid permeability starts to be visible. Therefore, the capillary pressure required to transport the same amount of liquid water in SGL 34BA is less than in Toray 090 which leads to a decrease in capillary pressure. As a result of the 14.2 μm pores in SGL 34BA, a higher interfacial surface area at low saturation range is observed as compared to the Toray 090, see Figure 3.13 (a). Therefore, the amount of liquid water evaporated in SGL 34BA is higher than Toray 090 (see Figure 3.3 (f) and 3.13 (b)), which further reduces the capillary pressure in the cathode GDL.

The distributions of saturation for SGL 34BA and Toray 090 shown in Figure 3.14 (a) and (b) are the results of the capillary pressure distributions and the relationships between capillary pressure and saturation [163]. Due to the more anisotropic capillary pressure distribution in Toray 090, a greater change

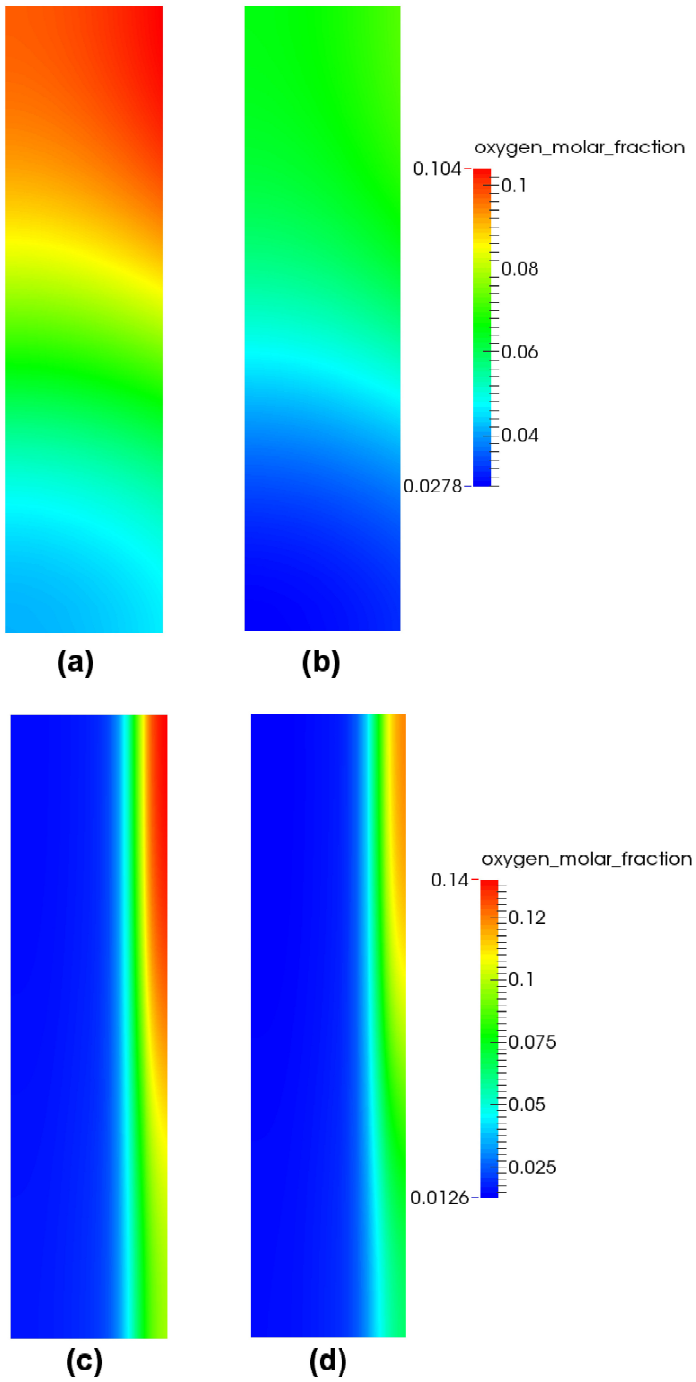

Figure 3.11 – Distributions of oxygen molar fraction in the cathode CL for: (a) SGL 34BA and (b) Toray 090 in the hot/dry case at 1.3 A/cm^2, (c) SGL 34BA and (d) Toray 090 in the cold/wet case at 0.6 A/cm^2.

in saturation between the channel and the rib regions is observed in Figure 3.14 (b) as compared to SGL 34BA. The oxygen molar fraction distributions

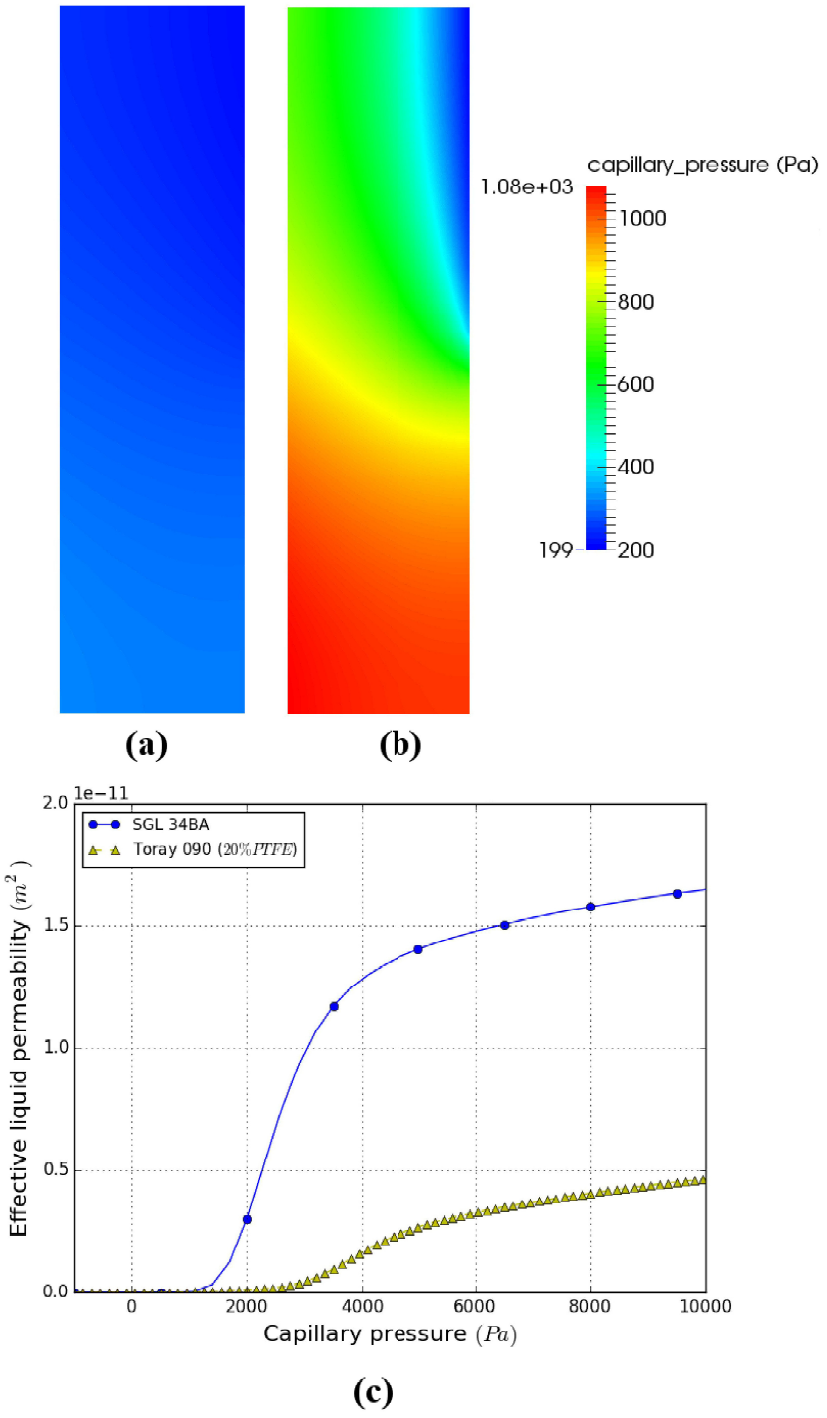

Figure 3.12 – Distributions of capillary pressure for (a) SGL 34BA and (b) Toray 090, (c) capillary pressure-effective liquid permeability relationships and under the cold/wet condition at 0.6 A/cm^2.

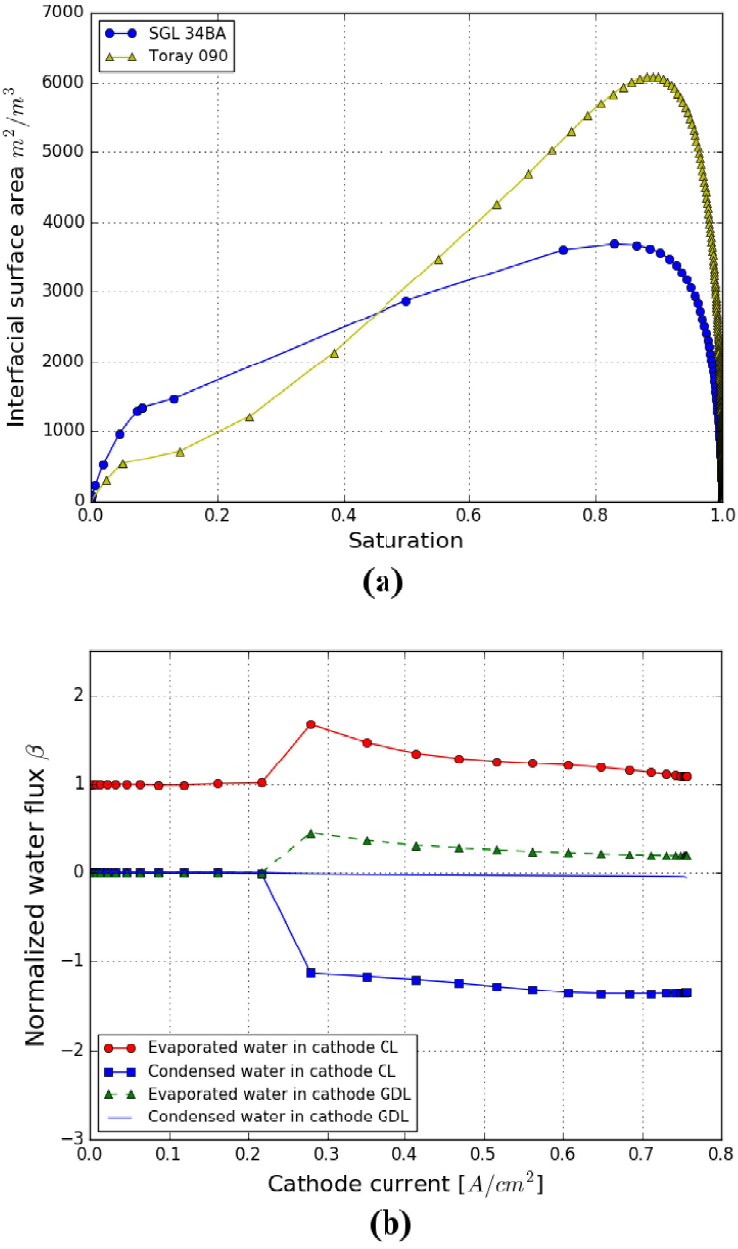

Figure 3.13 – Distributions of (a) saturation-interfacial surface area relationships for two GDLs, (b) the PCI flow for Toray 090 in the cathode under the cold/wet condition at 0.6 A/cm^2.

for two GDLs are plotted in Figure 3.14 (c) and (d). As compared to the SGL 34BA, a decrease in oxygen molar fraction under the rib is clearly observed in Toray 090 (see Figure 3.14 (d)) due to the more anisotropic saturation distribution.

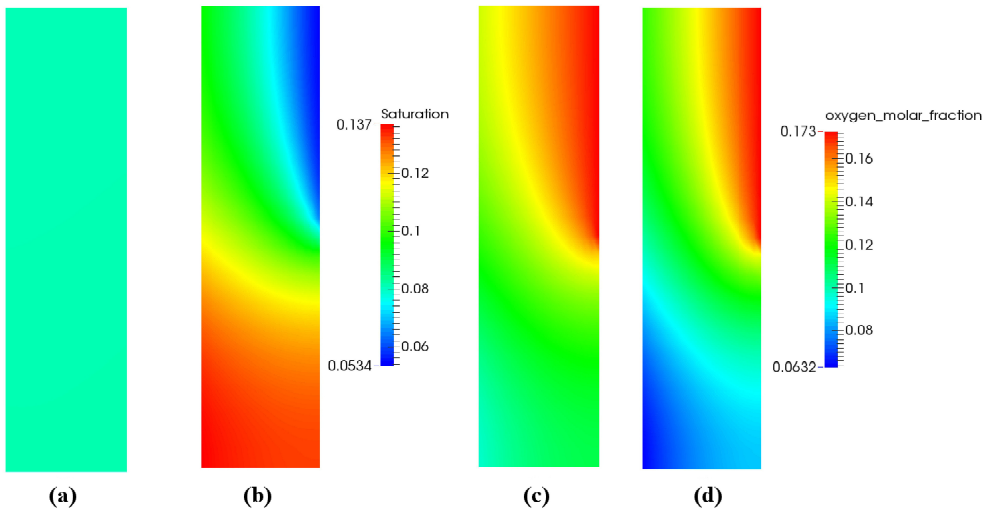

Figure 3.14 – Distributions of saturation for (a) SGL 34BA and (b) Toray 090, and oxygen molar fraction for (c) SGL 34BA and (d) Toray 090 in the cathode GDLs under the cold/wet condition at 0.6 A/cm^2.

3.1.7 Analysis of Membrane Water Transport

In situ water flux measurements have been reported by Thomas et al. [33], Atiyeh et al. [166], and Adachi et al. [173]. In order to compare the water flux measured by Thomas et al. [33], a simulation is configured with the same parameters reported by Thomas et al. [33], i.e., a 30 μm thick membrane, a 0.2 mg$_{\text{Pt}}$ cm^{-2} anode and a 0.6 mg$_{\text{Pt}}$ cm^{-2} cathode, each 10 μm thick, and an SGL 25BA GDL. The RH used in all cases is 100% and three sets of operating temperatures, i.e., 57.5°C cathode and 62.5 °C anode, 62.5°C cathode and 57.5 °C anode, and 60.0°C at both sides, are used in the simulations to explore the effect of temperature on membrane water transport.

To understand the effect of membrane diffusion coefficient on water transport, three sets of the diffusion coefficient expressions, i.e., Motupally et al. [174], Fuller [175] and Nguyen et al. [176], are studied. Figure 3.15 (a) shows the comparisons between three diffusion coefficients and the experimental data of Thomas et al. [33] with no additional temperature gradient imposed between anode and cathode. A good agreement is observed between Fuller's [175] prediction and the experimental data [33], whereas both Motupally et al.'s [174] and Nguyen et al.'s [176] predict a higher water flux leaving the cath-

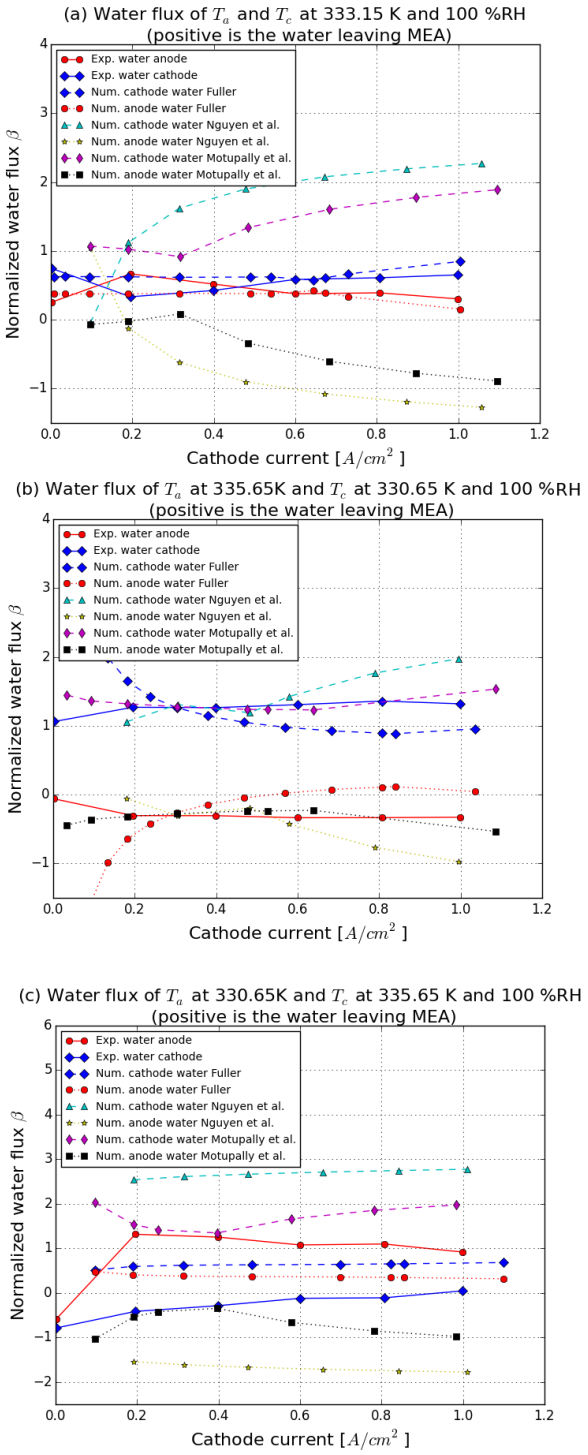

Figure 3.15 – Membrane water transport analysis at 100% RH: (a)60°C at both sides, (b) 57.5°C cathode and 62.5 °C anode and (c) 62.5°C cathode and 57.5 °C anode.

ode. Both Motupally et al. [174] and Nguyen et al. [176] estimated a lower

diffusion coefficient. By performing a parametric study on electro-osmotic drag (EOD) coefficient, 1.0, which has been used in all cases, shows a better agreement with the experimental data (see Figure 3.15 (a)). Similar values have also been reported by Adachi et al. [173].

With a higher temperature at the anode, all three diffusion coefficient expressions agree with the experimental measurements [33] (see Figure 3.15 (b)). In the opposite case, i.e., hotter cathode, in Figure 3.15 (c), the experimental data shows water entering the cathode, whereas all numerical results predict a positive water flux being evacuated from the cathode. The discrepancies in the water flux might be due to several reasons: (i) water diffusion, electro-osmotic drag, and thermo-osmosis transport coefficients might not be appropriate for the type of membrane used in the study by Thomas et al. [33] (membrane type not reported), and (ii) liquid water permeation and its thermal behavior in the membrane are not accounted for in the model.

3.1.8 Analysis of Cell Temperature

The effect of temperature on water management at 90%RH was carried out by examining the electrochemical performance and liquid water flux at the cathode boundary as shown in Figure 3.16. The oxygen and water vapor partial pressure at the cathode boundary are shown in Table 3.2. The cell performance shows a gradual improvement with temperature until the temperature reaches 90°C. This is in agreement with experimental observation in [177]. As shown in Figure 3.16 (b), there is no liquid water evacuated at the cathode boundary in both 80°C and 90°C cases. Thus, improvement in performance from 50°C to 80°C is due to improved water rejection, while the reduced performance at 90°C is due to oxygen dilution due to the high water partial pressure.

Table 3.2 – Partial pressure of oxygen and water vapor at the cathode boundary and saturated vapor pressure with varying cell temperature

Parameters	50°C	60°C	70°C	80°C	90°C
Oxygen (Pa)	18948	17529	15300	12260	8410
Water vapor pressure (Pa)	10956	17401	27430	41975	62523

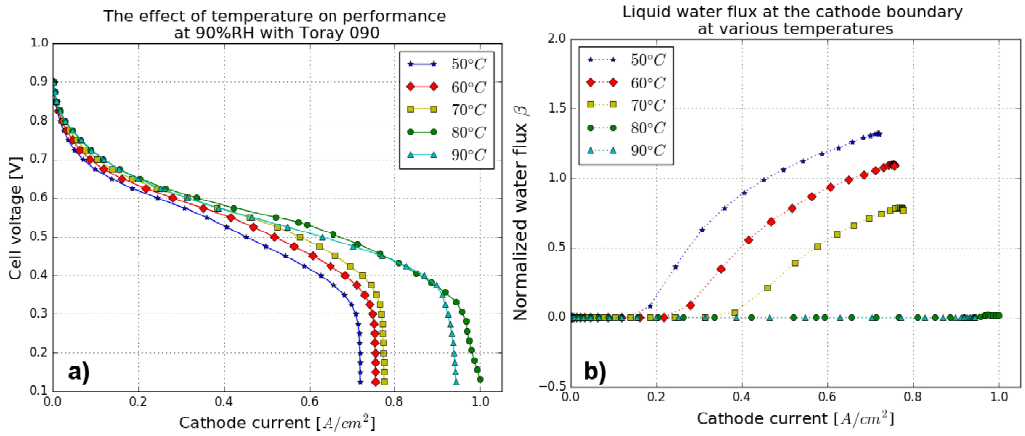

Figure 3.16 – Temperature analysis: (a) MEA performance and (b) liquid water flux at the cathode boundary.

3.2 Effect of Porous Layer Wettability and Microstructure on Water Management

The impact of CL and GDL hydrophilic volume fraction, hydrophobic contact angle and pore size distribution on performance are studied.

3.2.1 Analysis of Catalyst Layer Microstructure

In order to study the impact of the CL hydrophobic contact angle, percentage of hydrophilic pores and PSD on performance, the two-phase model with Toray 090 above is used as a base case for performing the parametric studies. Since the two-phase flow effects are highest at 60°C and 90% RH, these operating conditions are used.

3.2.1.1 Performance Study of CL Hydrophobic Contact Angle

CL wettability is difficult to measure experimentally and is a major source of uncertainty in the model. The impact of CL contact angle is, therefore, assessed by performing a parametric study with various hydrophobic contact angles, i.e., 92°, baseline case (93°), 96°, 100°, and 110°. Figure 3.17 (a) shows the performance variation with the above CL contact angles. An increase in the MEA performance at high current densities is observed with an increase in CL contact angle. The change in performance can be attributed to the

variations of the capillary pressure-saturation relationships for the above CL contact angles (see Figure 3.17 (b)).

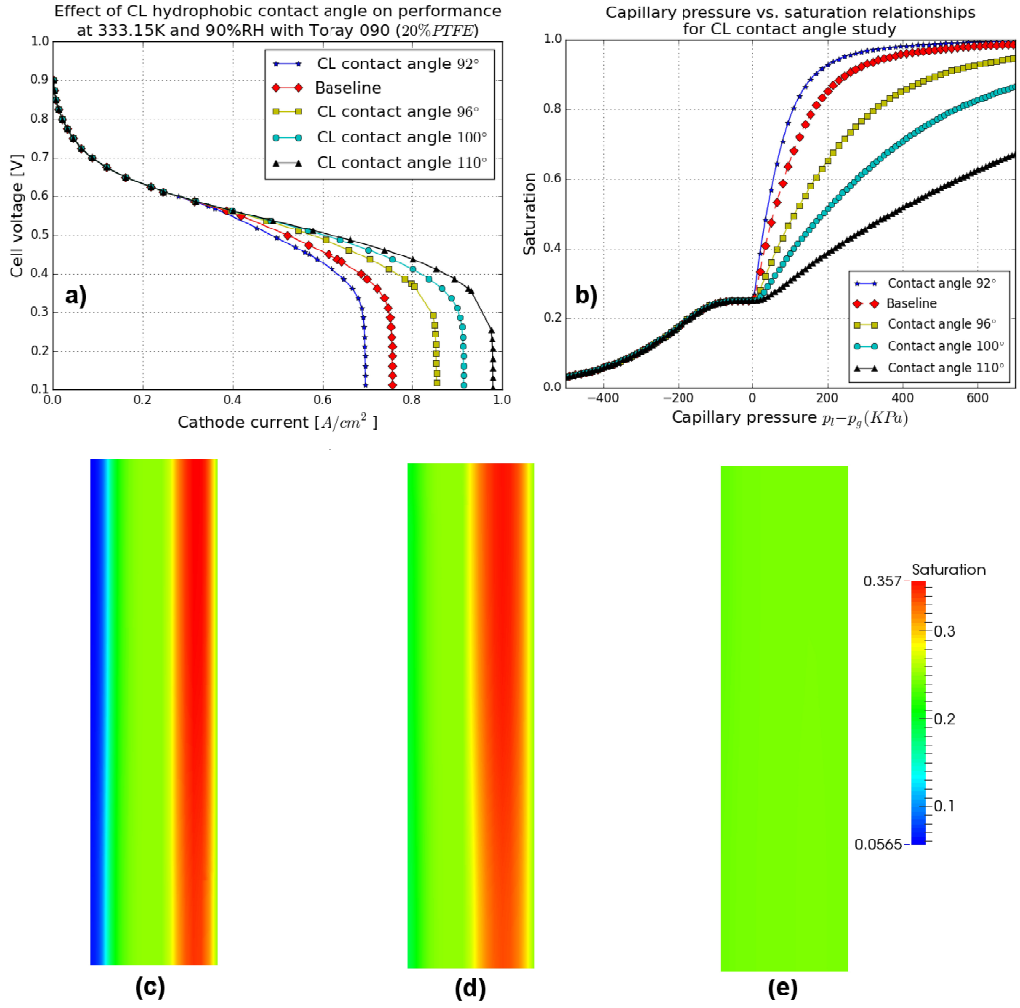

Figure 3.17 – CL contact angle study: (a) the MEA performance, (b) capillary pressure-saturation relationships, distributions of saturation in the cathode CL at contact angle: (c) 92°, (d) baseline, and (e) 110° at 0.6 A/cm^2.

Based on the Young-Laplace equation, an increase of the contact angle will result in a higher capillary pressure required to invade the same pore as shown in Figure 3.17 (b). The distributions of saturation with three contact angles, 92°, 93° and 110° in the cathode CL at a current density 0.6 A/cm^2 are shown in Figure 3.17 (c), (d) and (e). With a higher contact angle, a lower saturation distribution is observed. A lower contact angle in the CL allows the layer to retain more liquid water and, therefore, an increase in contact angle

is beneficial.

3.2.1.2 Performance Study of CL Hydrophilic Volume Fraction

In order to assess the impact of CL hydrophilic volume fraction, simulations are performed by varying the CL hydrophilic volume fraction, i.e., 0.10, 0.20, 0.25 (baseline), and 0.35, while the other parameters in the PSD model are kept the same. The value of 0.35 corresponds to the case where the volume fraction of hydrophobic pores is near the necessary volume fraction for percolation. Figure 3.18 (a) shows the cell performance for all cases. The CL with a hydrophilic volume fraction of 20% shows the highest performance.

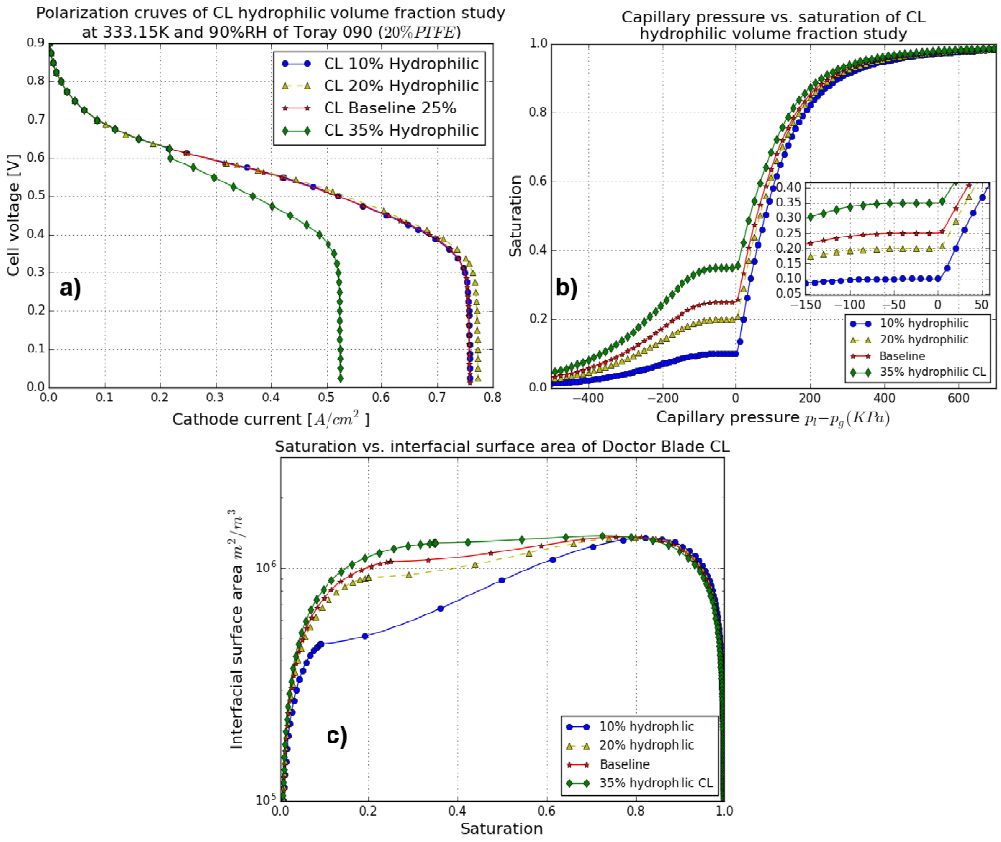

Figure 3.18 – CL hydrophilic percentage study: (a) the MEA performance, (b) capillary pressure-saturation relationships, and (c) saturation-interfacial surface area relationships.

Figure 3.19 shows saturation and volumetric electrochemical rate distributions in the cathode CL for the various CL hydrophilic percentages presented

above at 0.5 A/cm^2. The highest saturation region is near the GDL/CL interface for all cases. The lowest liquid water accumulation in the CL/membrane region is observed for the 20% hydrophilic percentage CL. CLs with hydrophilic volume fractions higher than 20% result in increased liquid water accumulation because lower capillary pressure is required to invade the pores as highlighted by the capillary pressure-saturation curve in Figure 3.18 (b). On the other hand, the CL with less than 20% hydrophilic volume fraction has a lower interfacial surface area (see Figure 3.18) which results in higher liquid water accumulation in order to exhaust the same amount of water in vapor phase.

3.2.1.3 Performance Study of CL Pore Size Distribution

In order to evaluate the impact of CL pore size distribution on overall performance, a parametric study is performed by varying CL PSD as follows: i) increase the overall pore size in the CL by 50%; ii) reduce the pore size by 20%; and iii) increase the pore size by 50% and assign the bigger pores to the hydrophilic phase. The PSDs and the effects of CL PSD on performance are shown in Figure 3.20 (a) and (b). The results in Figure 3.20 (b) indicate that a CL with larger pores will exhibit better performance. Also, it is preferred that the hydrophilic phase contains the smaller pores.

The reason for the increased performance can be explained by the saturation-effective liquid permeability plot in Figure 3.20 (c). To mitigate the flooding, a larger CL PSD is required as it increases the effective liquid permeability which leads to better liquid water rejection. With the same CL PSDs, the hydrophilic phase with smaller PSD mode shows an improvement in performance, because it requires less capillary pressure to be invaded.

3.2.2 Analysis of Gas Diffusion Layer Microstructure

The effects of GDL contact angle, percentage of hydrophilic pores and PSD for Toray 090 are studied using the two-phase model. The cold/wet case is considered to have the highest two-phase flow impact; thus the simulations are run under this condition.

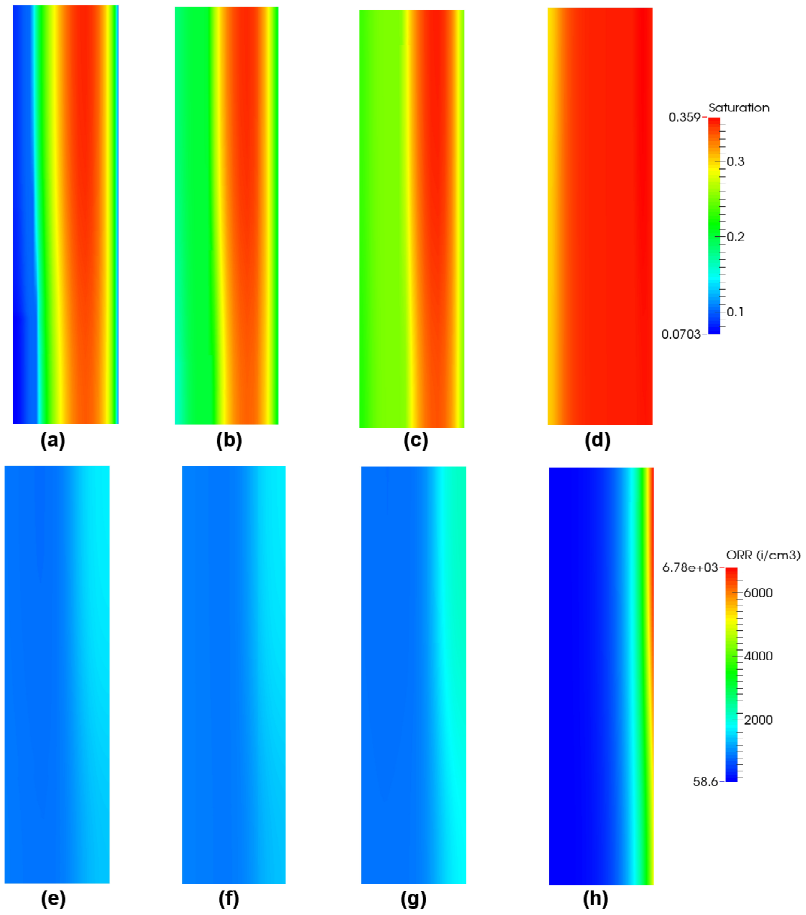

Figure 3.19 – CL hydrophilic percentage study: distribution of saturation in the cathode CL, (a) 10% hydrophilic, (b) 20% hydrophilic, (c) baseline 25% hydrophilic, and (d) 35% hydrophilic, and distribution of volumectric ORR, (e) 10% hydrophilic, (f) 20% hydrophilic, (g) baseline 25% hydrophilic, and (h) 35% hydrophilic at current density $0.5 A/cm^2$.

3.2.2.1 Performance Study of GDL Hydrophobic Contact Angle

In order to understand the impacts of GDL hydrophobic contact angle on the MEA performance, simulations are run at various hydrophobic contact angles, i.e., 95°, 110°, 120°and baseline (130°). Figure 3.21 (a) shows the MEA performance with the above GDL contact angles. As compared to the CL contact angle study, GDL contact angles do not have a major influence on MEA performance.

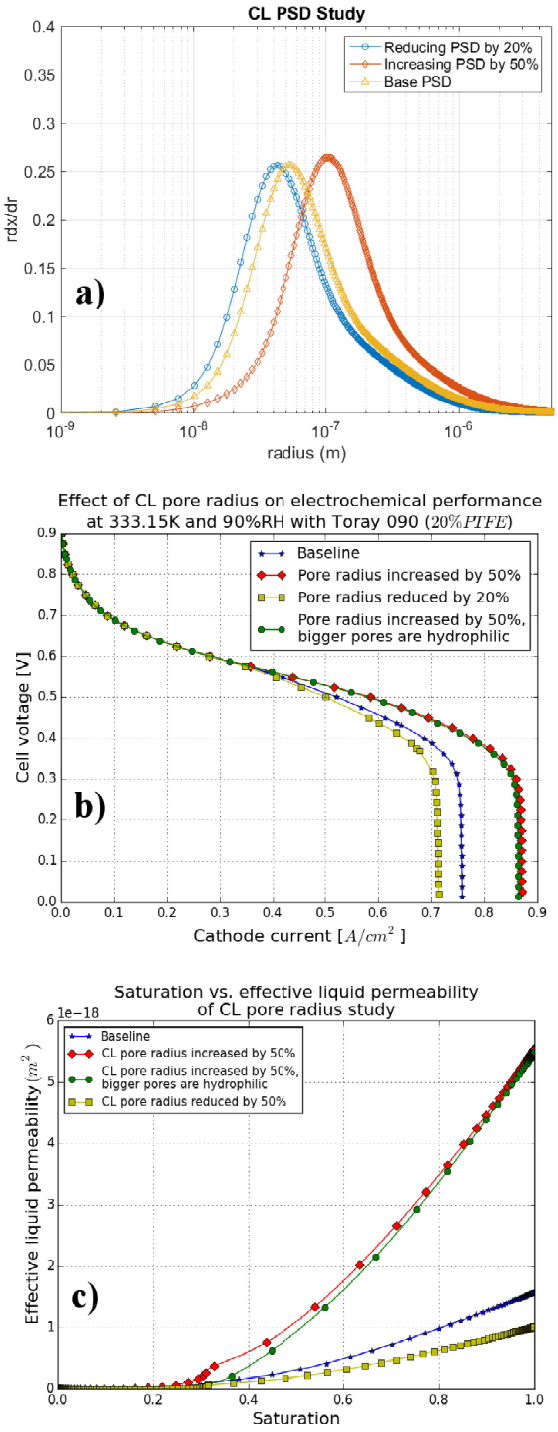

Figure 3.20 – CL pore size distribution study: (a) the PSDs, (b) the MEA performance, and (c) saturation vs. effective liquid permeability.

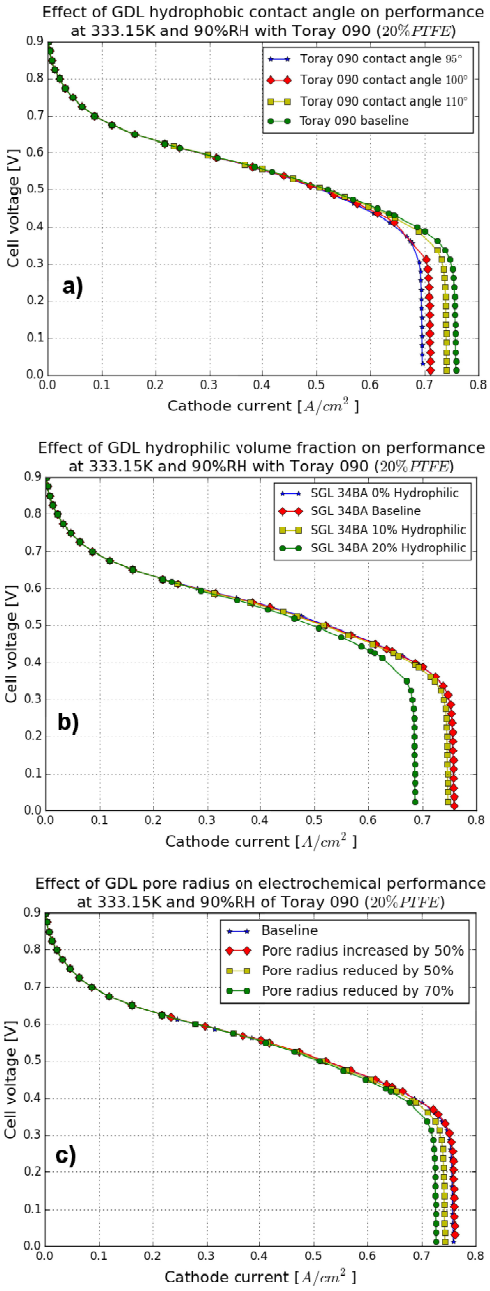

Figure 3.21 – Polarization curves: (a) GDL contact angle study, (b) GDL hydrophilic volume fraction study, and (c) GDL pore radius study.

3.2.2.2 Performance Study of GDL Hydrophilic Volume Fraction

To study GDL hydrophilic volume fraction, simulations are performed by varying the GDL hydrophilic percentages, i.e., 0%, baseline (5%), 10% and 20%. The performances with the above GDL hydrophilic volume fractions are shown

in Figure 3.21 (b). In comparison to the CL hydrophilic volume fraction study, the impact of GDL hydrophilic volume fraction on MEA performance is again small. No major difference in performance is observed among 0%, baseline case, and 10% GDL hydrophilic percentage. A reduction in performance is only observed at high current densities for 20% GDL hydrophilic percentage.

3.2.2.3 Performance Study of GDL Pore Size Distribution

To study how the GDL PSD affects performance, simulations are run for four cases: i) the baseline case; ii) the pore size increased by 50%; iii) the pore size reduced by 50%; and, iv) the pore size reduced by 70%. The sensitivity of this model to this parameter is small. Only a small decrease in performance with reduced GDL pore radius is observed in Figure 3.21 (c). Further, there is no significant increase in performance with increasing GDL pore radius.

3.3 Conclusion

A multi-dimensional, non-isothermal, two-phase flow model developed in the open-source fuel cell simulation package OpenFCST [7] in the previous chapter is validated by comparing numerical predictions against experimental data under various operating conditions, imaging data at low temperatures and water fluxes.

Under hot/dry condition, two-phase model predictions coincide with single-phase model results because the MEA contains minimal amounts of water. In the hot/wet case, reduced performance at high current densities is observed due to water accumulation in the cathode CL even though the liquid water flux at the cathode boundary is zero at all current densities, highlighting that water is ejected in vapor form at the temperature of 80°C. In the cold/wet case, the performance decreases due to the partial flooding of the GDL and the formation of a thin water film in the cathode CL, which prevents oxygen from penetrating into the CL. The liquid water is also shown to leave the cathode boundary as evaporation is not enough to remove all water produced due to the reduced temperature.

Simulation results were compared to literature X-ray and water flux observations. The model saturation profiles in GDL and CL are in agreement with experiments. Water fluxes are also in agreement when the diffusion coefficient proposed by Fuller et al. [175] and an EOD of one is used except for the case where cathode temperature is higher than the anode. These results give us confidence in the proposed model.

Simulation at varying temperature are preformed. Results suggest that operating at high temperatures helps to mitigate flooding at high relative humidity. However, by increasing the temperature, the inlet reactant concentration decreases which prevents further improvement in performance at 90°C. Thus, at atmospheric pressure, 80°C appears to be the optimal temperature to effectively evaporate all liquid water in the MEA and provide sufficient reactant to improve the fuel cell performance.

The PSD-based MEA model is used to study the effect of micro-structural changes in porous media, such as changes in PSD, hydrophilic volume fraction and contact angle, on fuel cell performance. Two GDLs, i.e., SGL 34BA and Toray 090 (20%PTFE), with different PSDs, contact angles and hydrophilic volume fractions are studied using the two-phase model. The model predictions are in agreement with experimental results with SGL 34BA showing better performance than Toray 090 for all cases. The improved performance is due to larger porosity, permeability (bigger pores), contact angle and interfacial surface area (smaller pores in hydrophilic phase) for the SGL 34BA.

Parametric studies to analyze fuel cell performance sensitivity to changes in CL and GDL hydrophilic volume fraction, hydrophobic contact angle and PSD showed that the MEA performance is more sensitive to changes in CL microstructure than GDL. An electrode microstructure with a large hydrophobic contact angle, relative low hydrophilic volume fraction, and larger pore radius appears to give optimal results.

Chapter 4

Analysis of the Role of the Microporous Layer

A multi-dimensional, non-isothermal, two-phase numerical model is used to understand the role of the microporous layer (MPL) in improving polymer electrolyte fuel cell (PEFC) performance. The model is validated under varying operating conditions against experimental data from conventional PEFCs in literature and low loading electrodes measured in-house with and without an MPL. Under dry conditions, the MPL is found to have a minimal effect on cell performance, except for improving ohmic transport and performance stability. Under wet conditions, results show that the MPL increases the temperature in the catalyst coated membrane, thereby enhancing evaporation in the cathode and creating a larger sorbed water gradient across the membrane which results in improved water vapor transport out of the cathode and increased diffusion from cathode to anode, respectively. A mild improvement in performance is also observed due to improved in-plane diffusion once an MPL is introduced under wet condition as a result of the smaller pore size and hydrophobic nature of the MPL. A parametric study suggests that GDL and MPL thermal conductivity are the most critical parameters to improve fuel cell performance followed by thickness and hydrophilic percentage. Other microstructural parameters appear to have minimal effect. Optimal thermal conductivity and hydrophilic percentage are required to achieve optimal fuel

Parts of this chapter have been published:
J. Zhou et al., Analysis of the Role of the Microporous Layer in Improving Polymer Electrolyte Fuel Cell Performance. *ElectroChimica Acta*

cell performance under fully humidified conditions.

4.1 Numerical parameters

GDL and MPL pore size distributions (PSDs) were measured in our laboratory using mercury intrusion porosimetry (MIP) as described in [59]. Since the SIGRACET (SGL) 24BC contains a GDL and an MPL, in order to acquire the MPL PSD, the SGL 24BA PSD was subtracted from the SGL 24BC PSD. The PSD of the inkjet printed CL is estimated numerically from a focused ion beam-scanning electron microscope (FIB-SEM) data set using a sphere fitting algorithm as described in [62]. Three distinguishable peaks are observed with experimental MPL and CL PSDs, thus, three modes are used in the PSD model to fit them. The PSDs for GDL, MPL and CL are shown in Figure 4.1.

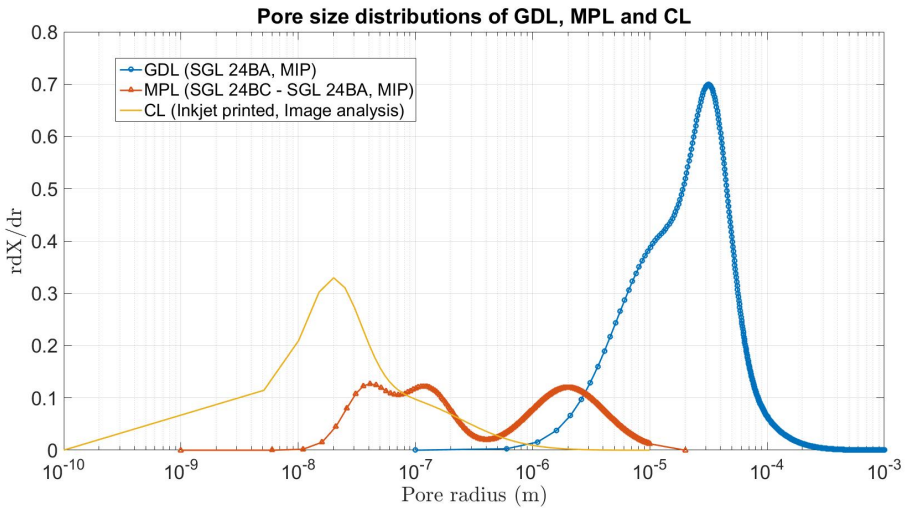

Figure 4.1 – Pore size distributions of GDL, MPL and CL.

The parameters used to validate the conventional fuel cells in [1] and the in-house low loading electrodes are discussed. For the in-house fabricated electrodes, most of the parameters are either estimated based on fabrication parameters or acquired using the characterization tools available in our laboratory, such as SEM, MIP, image reconstruction, and cyclic voltammetry. For the conventional electrodes, the parameters are either kept the same or modified based on the information provided in [1] as discussed below. All sim-

ulation parameters are kept constant during the simulations but the operating conditions.

All GDL parameters for SGL 24BA are those reported in [59] for an SGL 34BA, except for the thickness and porosity which are adjusted to the values provided by the manufacturer for an SGL 24BA, i.e., 190 μm and 74%, respectively. The GDL thermal conductivity is estimated based on the equation reported in [178]. For the Mitsubishi Rayon Co. (MRC) 105 and Toray TGP-H-060 GDLs used in [1], the parameters are shown in Table 4.4. The GDLs through-plane thermal conductivities used are, 0.003 W/(cm $\cdot$ K) for Mitsubishi Rayon Co. (MRC) 105 and 0.014 W/(cm $\cdot$ K) for Toray TGP-H-060 as reported by Owejan et al. [1]. The rest of the GDL parameters used in the simulation are based on X-ray tomography data reported by Zenyuk et al. [179].

MPL parameters are given in Tables 4.1 and 4.4 for the low loading and conventional MEAs simulated, respectively. A direct measurement of the MPL thermal conductivity by Burheim et al. [180] showed that their MPL had a thermal conductivity of 0.0008 ± 0.0003 W/(cm $\cdot$ K) and the contact resistance between the GDL and the MPL was negligible. In this study, an MPL thermal conductivity of 0.0008 W/(cm $\cdot$ K) is, therefore, used for SGL 24 BC. For Mitsubishi Rayon Co. (MRC) 105 and Toray TGP-H-060, the thermal conductivity of MPL is estimated to be 0.0005 W/(cm $\cdot$ K) based on simulation results.

The MPL could be completely hydrophobic due to the PTFE treatment. However, a fully hydrophobic MPL in the model leads to numerical instability as the MPL relative liquid permeability is nearly zero which results in unrealistic high hydraulic resistance. Therefore, a 1% hydrophilic pore network is assumed. The reason for allocating 50% bigger pores (2 μm) in hydrophilic phase is also for lowering the hydraulic resistance.

Table 4.2 provides the low loading CL parameters determined based on fabrication parameters and electrochemical characterization. The active area is measured using the hydrogen adsorption peak from cyclic voltammetry (CV) at a temperature of 30°C with anode and cathode fed with fully hu-

Table 4.1 – MPL input parameters

MPL Parameters		
Porosity		0.62 [181]
Thickness (μm)		45.0 [182]
Thermal conductivity (W/(cm $\cdot$ K))		0.0008 [180]
Electrical conductivity, through plane (S/cm)		10.5 [182]
Electrical conductivity, in plane (S/cm)		272.78 [182]
Contact angle (water) in hydrophilic phase		84°[66]
Contact angle (water) in hydrophobic phase		110°[84]
Absolute permeability (m^2)		1.39e-13 [119]
MPL PSD characterization		
Hydrophilic volume fraction (%)		1
PSD interconnectivity λ_{PSD}		1.0
Characteristic pore radius (μm)	r_1	0.072
	r_2	0.125
	r_3	2.000
Characteristic pore widths	s_1	0.35
	s_2	0.5
	s_3	0.9
Characteristic pore fraction	$f_{HI,1}$	0.50
	$f_{HI,2}$	0.00
	$f_{HI,3}$	0.50
	$f_{HO,1}$	0.45
	$f_{HO,2}$	0.10
	$f_{HO,3}$	0.45

midified hydrogen and nitrogen, respectively. A CL thermal conductivity of 0.0027 W/(cm $\cdot$ K) is used based on the data reported by Khandelwal and Mench [183] which states that it is in the range of 0.0027 ± 0.0005 W/(cm $\cdot$ K). The carbon black used in our laboratory is XC-72 which has a contact angle of about 79° as reported in [66] and density of 1.69 g/cm^3 [184]. The hydrophilic percentage in the CL is determined by looking at the saturation level at zero capillary pressure for the 10 μm CL reported in [185]. The contact angles are estimated by fitting the slopes in the capillary pressure vs. saturation curve reported in the same reference. For the conventional CL experiments, Owejan et al. [1] used MEA 5510 from W. L. Gore Associates with catalyst loadings of 0.4 $\text{mg}_{\text{Pt}}/\text{cm}^2$ at both anode and cathode. The thickness of the CL is assumed to be 10 μm and the platinum active area is 70 m^2/g based on

the values reported previously by Owejan et al. [186]. The parameters that have been modified to simulate conventional electrodes instead of low loading electrodes are provided in Table 4.4. The choice of using a higher absolute gas permeability as compared to absolute liquid permeability in the CL is to account for slip flow of gas at pore walls which enhances gas flow when the pore sizes approach to the mean free path [187].

Table 4.2 – Inkjet printed CL input parameters

CL Parameters		
Fabrication parameters and electrochemical characterization		
Platinum loading (mg_{Pt}/cm^2)		0.1 ± 0.01 [2]
Nafion loading (wt. %)		0.3
Active area for CCM 24BC (m^2/g)		33 ± 3 (CV) [2]
Active area for CCM 24BA (m^2/g)		27 ± 5 (CV) [2]
Porosity		0.52
Thickness (μm)		3.0 ± 0.6 (SEM) [2]
Thermal conductivity ($W/(cm \cdot K)$)		0.0027 [183]
Electrical conductivity of carbon black (S/cm)		88.84 [7]
Density of carbon black (g/cm^3)		1.69 [184]
Contact angle (water) in hydrophilic phase		79 °[66]
Contact angle (water) in hydrophobic phase		91 °[185]
Absolute permeability (gas) (m^2)		1.00e-13 [5]
Absolute permeability (liquid) (m^2)		1.00e-19
PSD characterization		
Hydrophilic volume fraction (%)		30 [185]
PSD interconnectivity λ_{PSD}		6.0
Characteristic pore radius (μm)	r_1	0.02
	r_2	0.025
	r_3	0.075
Characteristic pore widths	s_1	0.55
	s_2	0.45
	s_3	1.2
Characteristic pore fraction	$f_{HI,1}$	1.00
	$f_{HI,2}$	0.00
	$f_{HI,3}$	0.00
	$f_{HO,1}$	0.50
	$f_{HO,2}$	0.40
	$f_{HO,3}$	0.10

Lastly, DuPont^{TM} Nafion® (NRE) 211 parameters are presented in Table 4.3. For the simulations with a Gore 5510 membrane all parameters are left the same except for the thickness, the thermal conductivity and equivalent weight which are set to 18 μm, 0.0037 $W/(cm \cdot K)$ [188] and 900, respectively, as shown in Table 4.4.

Table 4.3 – Membrane NRE 211 parameters

PEM	Literature	Value/direction/equation
Water diffusion	[174]	$0.000417\lambda(1.0+161.0exp(-\lambda))exp(-\frac{-2436.0}{T})$, $\lambda > 3.0$
Electro-osmotic drag coefficient	[173]	1.0
Sorption isotherm	[189]	$(1.0+0.2352a_w^2\frac{(T-303.15)}{30.0}(14.22a_w^3-18.92a_w^2+13.41a_w))$, $a_w = RH$
Proton conductivity	[190]	$(-0.000120125\lambda^2+0.01052\lambda-0.020634)exp(751.5412(\frac{1}{303}-\frac{1}{T}))$
Thermal-osmosis	[136]	Cold to hot
Thermal conductivity ($W/(cm \cdot K)$)	[183]	0.0013

Table 4.4 – Parameters for Owejan et al. [1] study

GDL Parameters	MRC 105	TGP-H-060
Porosity [179]	0.72	0.64
Thickness (μm) [179]	215.0	205.5
Thermal conductivity (W/(cm $\cdot$ K)) [1]	0.003	0.014
Tortuosity [179]	1.9	2.81
MPL Parameters		
Thermal conductivity (W/(cm $\cdot$ K)) [180]	0.0005	
CL Parameters		
Thickness (μm)	10	
Catalyst loading (Pt/cm^2)	0.4	
Platinum active area (m^2/g)	70	
Hydrophilic volume fraction (%)	30	
PEM Parameters		
Thickness (μm)	18	
Equivalent weight (EW)	900	
Thermal conductivity (W/(cm $\cdot$ K))	0.0037	

4.2 Conventional Electrode

First, the proposed numerical model is used to reproduce the experimental trends reported in the literature when an MPL is added using the data in Table 4.4. Owejan et al. [1] tested fuel cells with and without an MPL under hot and cold cases under fully humidified conditions. The operating conditions in the hot case are 80°C and 190 kPa back pressure at both anode and cathode. In the cold case, the temperature is reduced to 40°C and the back pressure is 150 kPa.

The input parameters to the model are given in Table 4.4. Other input parameters to the model such as PSD and effective diffusion coefficient are set to be the same as those in the in-house cell because no data were available and in order to provide a fair comparison. No effort was taken to fit the model to

the experimental data.

Electrochemical performance and water balance at 80°C are shown in Figures 4.2 (a) and (b), and 4.3 (a) and (b). The numerical predictions exhibit a similar performance trend as the experimental data. Note that due to the uncertainties associated with CCM properties, a perfect agreement should not be expected. At 80°C, the sensitivity of saturation vapor pressure to temperature is large and any increase in temperature leads to higher vaporization in the electrodes. With a lower thermal conductivity in the GDL, more heat is accumulated in the electrode which leads to complete evaporation of the produced water as shown in Figure 4.3 (a). When the GDL thermal conductivity is higher and the MPL is not included, liquid water starts to accumulate in the electrode and quickly blocks reactant transport as indicated in Figure 4.3 (b). The electrochemical performance is, therefore, substantially reduced due to mass transport losses in the partially saturated electrode. For the cell with MPLs, the MEA is always able to evaporate all liquid water generated in the electrodes.

Figure 4.4 shows the temperature, saturation, oxygen molar fraction and ORR volumetrc current density distributions at the cathode CL for TGP-H-060 at 80°C and 0.9 A/cm^2. With roughly 6°C increase in temperature, the cathode electrode is able to remain less saturated for the cell with the MPL due to higher evaporation. The reduction in saturation allows the reactant to be transported to the CL/PEM side which improves the utilization of the inner catalyst layer. As shown in Figure 4.4 (h), for the cell without the MPL, the reaction is mostly concentrated at the CL/GDL interface due to the blockage of liquid water.

Electrochemical performance and water balance at 40°C are shown in Figures 4.2 (c) and (d), and 4.3 (c) and (d). The electrochemical performance in Figure 4.2 indicates that adding an MPL improves the performance under cold conditions for both GDLs. Figure 4.3 shows that the cells without MPL reach their maximum current densities when the amount of liquid water leaving the cathode boundary is close to the amount of water generated from the ORR. It also shows that, when the current density is higher than 1.0 A/cm^2, the

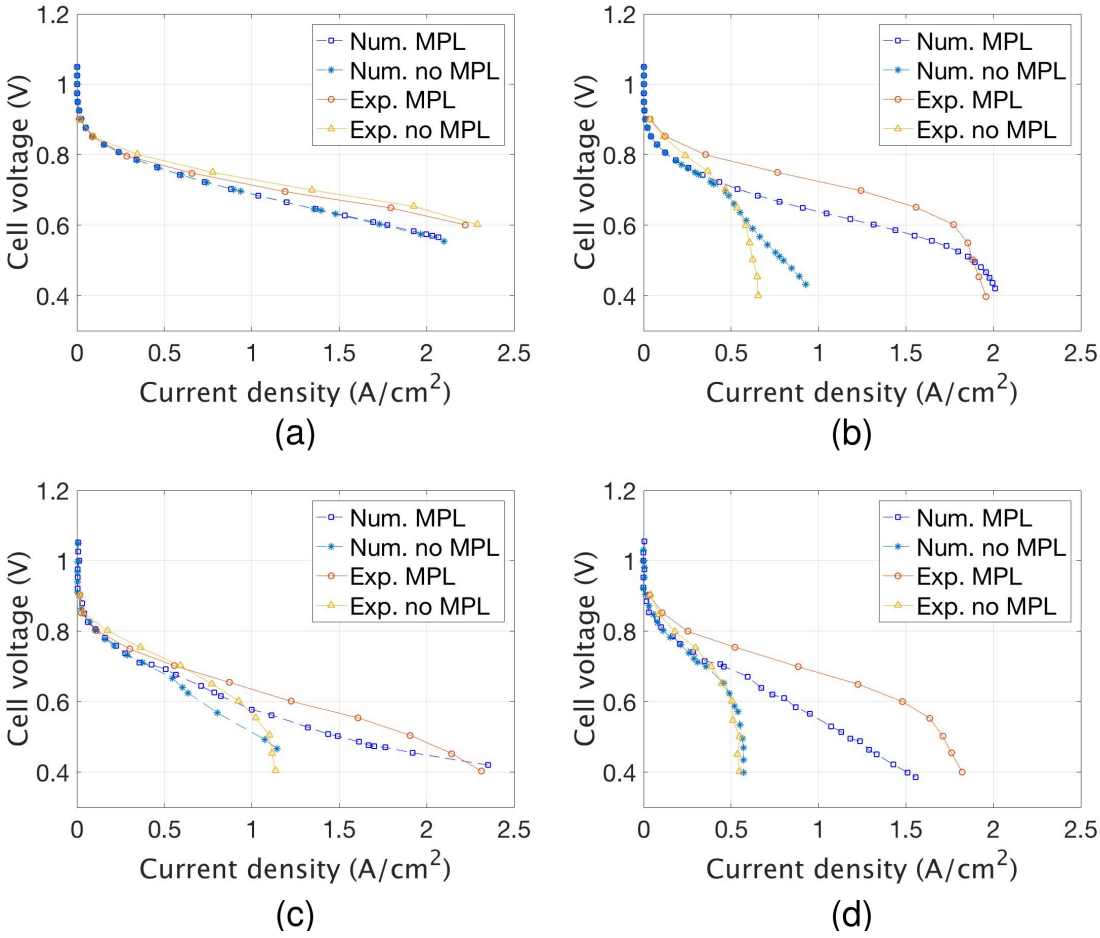

Figure 4.2 – Electrochemical performance under fully humidified condition at 80°C: (a) and (b); and 40°C: (c) and (d); for MRC 105: (a) and (c); and TGP-H-060: (b) and (d); the simulation parameters correspond to the MEA configuration in [1].

amount of liquid water leaving the cathode boundary decreases whereas the water vapor increases with the presence of the MPL.

Overall, the cell with MRC 105 has a better performance with and without MPL than TGP-H-060 at all conditions. This is because MRC 105 has higher porosity, lower tortuosity and lower thermal conductivity which leads to more evaporation in the electrode.

The distributions of temperature, saturation and oxygen molar fraction in the cathode CL are shown in Figure 4.5 for TGP-H-060 at 40°C and 0.59 A/cm^2 for the cell without the MPL and 0.6 A/cm^2 for the cell with the MPL. Water accumulation in the electrode is observed for both cells. However, the water

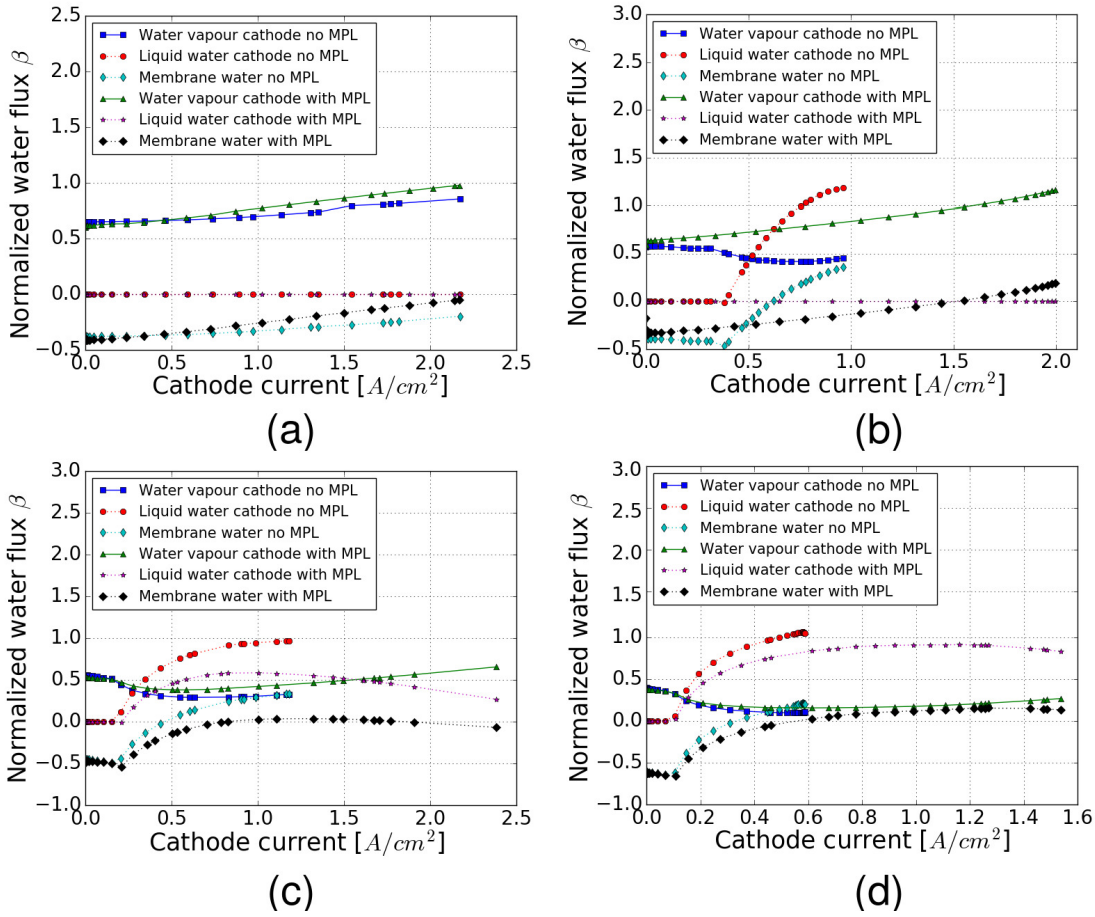

Figure 4.3 – Water balance under fully humidified condition at 80°C: (a) and (b); and 40°C (c) and (d); for MRC 105: (a) and (c); and TGP-H-060: (b) and (d); positive cathode flux is water leaving MEA, positive membrane water flux is from anode to cathode, the simulation parameters correspond to the MEA configuration in [1].

film for the cell without the MPL is closer to the GDL/CL interface and it has a higher saturation as compared to the cell with the MPL. The lower saturation in the cathode CL is due to the increase in temperature, approximately 8°C in this case, which improves the evaporation and reduces the transport resistance. The reason that Figure 4.3(d) shows similar liquid water fluxes at the cathode GDL/channel boundary between the cell with and without the MPL is due to water vapor condensation at the MPL/GDL interface since the GDL/MPL interface is at a colder temperature. As compared to the 80°C case, the cell with the MPL shows a much higher saturation. This is because the temperature effect on saturation pressure is much less at 40°C as compared

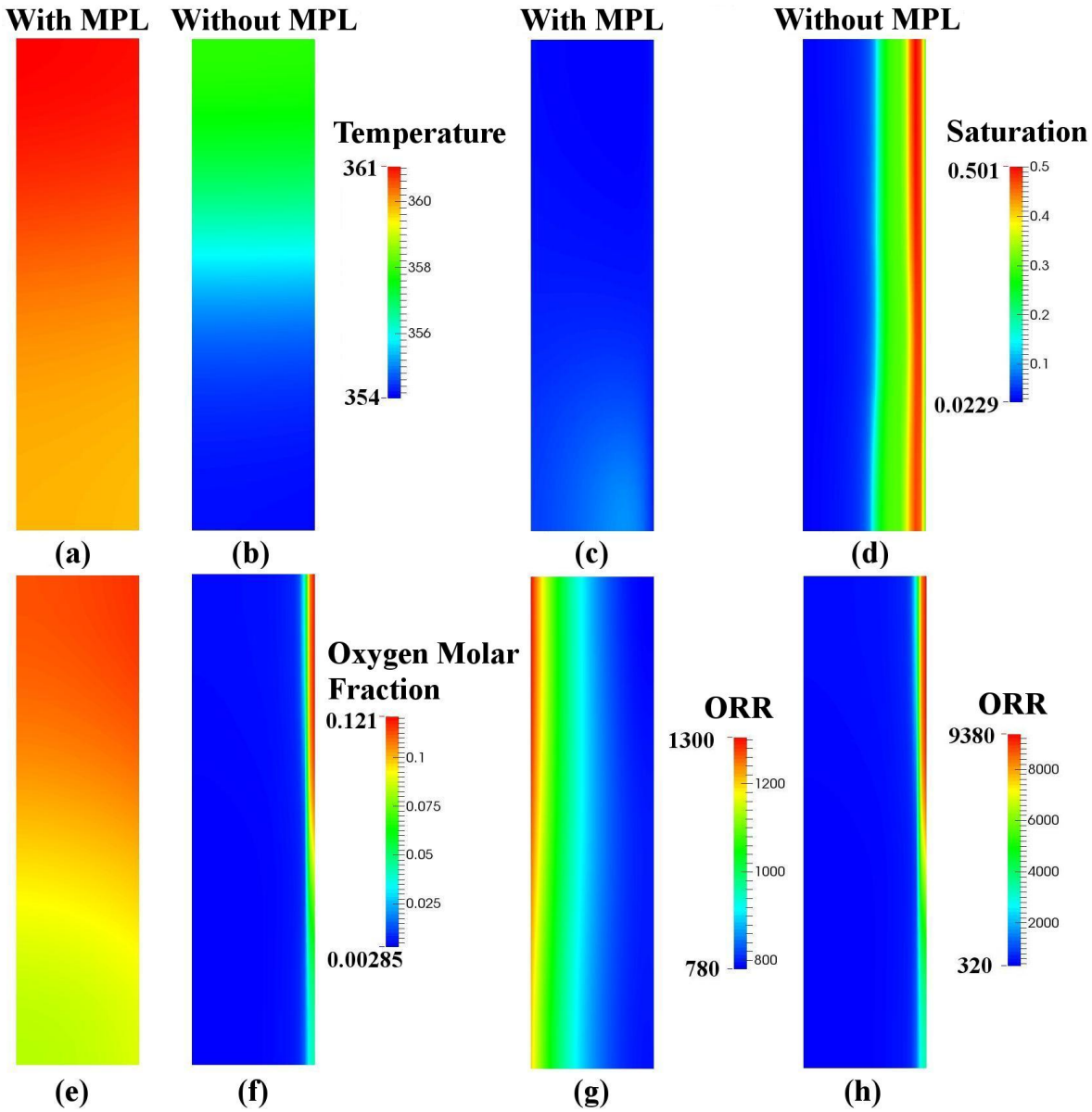

Figure 4.4 – Distributions of temperature (a) and (b), saturation (c) and (d), oxygen molar fraction (e) and (f), and ORR volumetric current density (g) and (h) in the cathode CLs for the cells with and without the MPL, respectively, for TGP-H-060 at 80°C, 100% RH and 0.9 A/cm^2, the simulation parameters correspond to the MEA configuration in [1].

to 80°C.

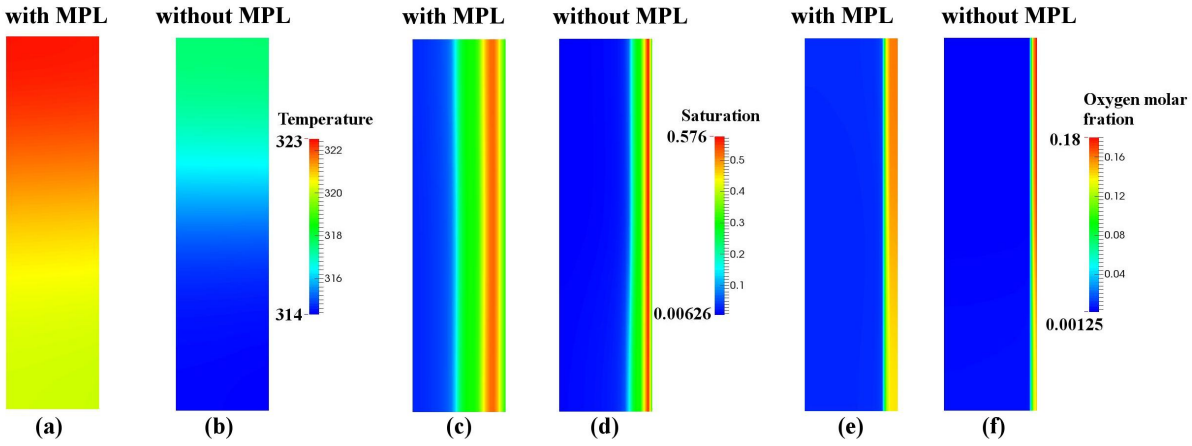

Figure 4.5 – Distributions of temperature (a) and (b), saturation (c) and (d), and oxygen molar fraction (e) and (f) in the cathode CLs for the cells with and without the MPL, respectively, for TGP-H-060 at 40°C, 100% RH and 0.59 A/cm^2 for the cell without the MPL and 0.6 A/cm^2 for the cell with the MPL.

To further understand the effect of the MPL on water management, temperature, saturation, ORR current density and volumetric condensation distributions for the MEA with an MPL are shown in Figure 4.6 at 1.5 A/cm^2. The increased temperature in the cathode CL, to around 60°C, enables the electrode to evaporate most of the produced water as the current density increases from 0.5 A/cm^2 to 1.5 A/cm^2. This minimizes water saturation in the cathode CL and leads to a higher catalyst layer utilization.

4.3 Inkjet Printed Low Loading Electrode

4.3.1 Low Loading Electrode Fabrication and Characterization

A catalyst layer ink is prepared by mixing 37.5 mg of 40% Pt|C catalyst (Alfa Aesar HiSPEC^{TM} 3000) with a 50/50 blend of propylene glycol (PG) and isopropanol (Fisher Scientific). The ink is then placed in a water bath and sonicated for 30 minutes. Next, Nafion ionomer (5wt%, PE1100 Ion Power) is added drop-wise during bath sonication to the ink until a Nafion loading of 30 wt% is obtained. The ink is further sonicated for 15 minutes. Probe sonication

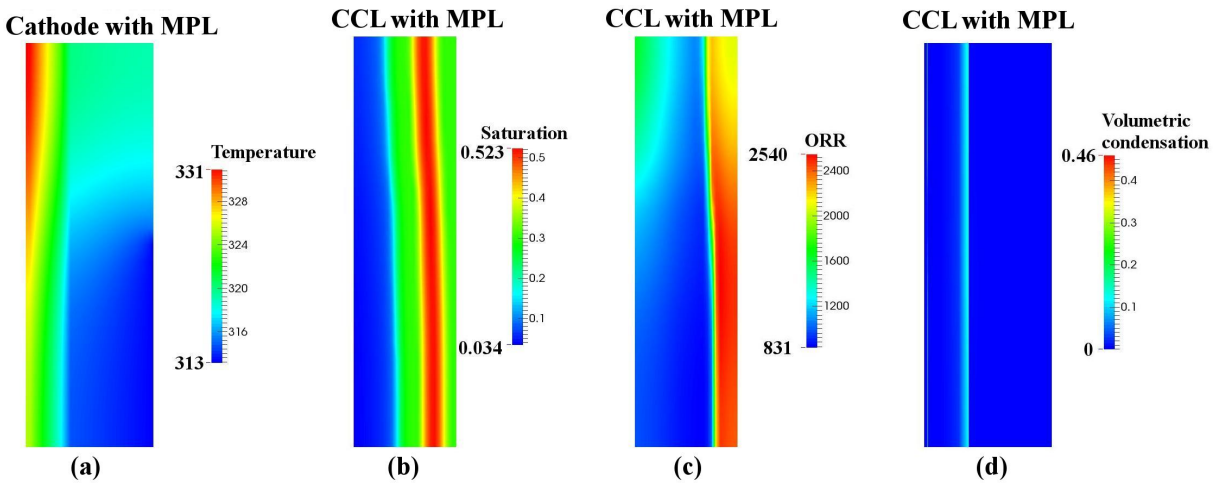

Figure 4.6 – Distributions of temperature (a) in the cathode, saturation (b) in the cathode CL, ORR volumetric current density (c) in the cathode CL, and volumetric condensation in the cathode for the cell with the MPL for TGP-H-060 at 40°C, 100% RH and 1.5 A/cm^2.

is then used at a frequency of 20 kHz for 15 minutes at an amplitude of 20% to further mix the ink. Finally, the ink was bath sonicated for 30 minutes and degassed for 60 minutes.

A commercial piezo-electric printer (Dimatix 2831, Fujifilm Inc) was used to print the catalyst coated membranes (CCMs). The catalyst ink prepared above was deposited over an NRE-211 (Ion Power) membrane until it reached the desired Pt loading, i.e., 0.1 ± 0.01 mg$_{\mathrm{Pt}}$/cm^2.

4.3.2 Membrane Electrode Assembly Testing

All tests were performed on a Scribner 850e test station. A 5 cm^2 fuel cell with parallel channels was assembled with either an SGL 24BA (GDL only) or an SGL 24BC (GDL+MPL). The thickness of the silicon gaskets used for testing was 100 μm (SGL 24BA) and 125μm (SGL 24BC), respectively. The polarization curves were obtained for each MEA by operating the cell at a constant current density in steps of $0.02 A/cm^2$ for one minute. To guarantee the repeatability of the data, three MEAs were tested.

The fuel cells were tested at 80°C, 50% and 90% RH, and 60°C, 90% RH with no back pressure. At 80°C, anode and cathode flow rates of 0.2 SLPM and 0.4 SLPM are used, respectively. At 60°C, constant stoichiometries of 4.0 and

30.0 at the anode and cathode were used in order to minimize the liquid water buildup in the channel. Moreover, in order to make sure the data acquired at 60°C and 90% RH is at steady state, each data point was recorded after a 20 minute hold. To further confirm the cell is operating at steady state, the cell was held constant at two relatively high current densities for two hours. Figure 4.7 provides a 20 minute hold polarization curve and the voltage evolution during a two hour current hold at 0.7 A/cm^2 and 0.9 A/cm^2, respectively. The cell voltage remained relatively uniform during the two hours.

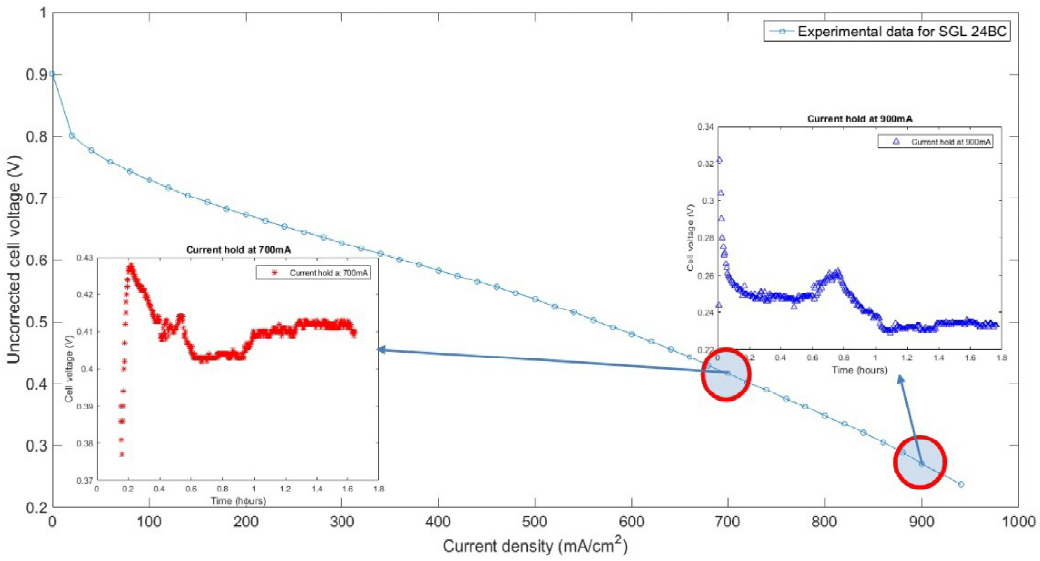

Figure 4.7 – Performance at 60°C and 90% RH with anode and cathode stoichiometry of 4 and 30, respectively (20 minutes hold). The subfigures are at constant current densities for two hours.

4.3.3 Effect of Micro Porous Layer

To examine the role of the MPL on the performance of low loading electrodes fabricated in our laboratory, experiments and simulations are performed concurrently. Figure 4.8 shows reasonable agreement between numerical and experimental results. Corrected polarization curves (see Figure 4.8 (a), (c) and (e)) are used in order to clearly demonstrate the effect of MPL on mass transport and to eliminate the effect of better electrical contact between GDL and CL when an MPL is added, a factor that was not considered in the model. The ohmic losses are shown in Figure 4.8 (b), (d) and (f). The cell ohmic

resistance is obtained experimentally from current interrupt [172] and numerically by calculating the electronic heat loss in GDLs and MPLs and the protonic heat dissipation in the PEM as discussed in [87]. The cells without the MPL experimentally show a higher ohmic resistance and larger data variability whereas after introducing the MPL, the ohmic resistance and data stability improve. This might be because the MPL acts as a transition layer (its pore size is between CL and GDL) which enhances the contact between GDL and CL. The error bars represent the standard deviation of the averaged forward sweep of three different cells.

4.3.3.1 Hot and dry condition

To examine the role of the MPL without the presence of liquid water, a hot/dry condition, i.e., 80 °C and 50% RH, is employed. No significant improvement in performance is observed after introducing the MPL under this condition as shown in Figure 4.8 (a). In fact, at high current densities the corrected cell performance is slightly higher without MPLs both experimentally and numerically, because adding the MPL increases transport resistances.

The experimental data in Figure 4.8 (b) show that without the MPL, the experimental cell resistance experienced great variation and it shows a discrepancy with the numerical prediction. The variation of cell resistance without MPL has been commonly observed in several articles[101, 102, 191]. The reason for the discrepancy might be due to insufficient contact between the GDL and CL which the model does not account for. Adding the MPL reduced the cell resistance and improved data repeatability. This was also observed by Malevich et al. [191] and cannot be studied with the current model. The reasons for the improvement in stability and the discrepancy between experimental and model predicted cell resistances might be due to better interfacial contact between CL/MPL and GDL/MPL as the MPL provides a smoother transition in terms of pore size.

Figure 4.9 (a) shows the water balance in the cell. No major difference is observed in water balance for the cells with and without MPLs and there is no liquid water leaving the GDL/channel boundary. The temperature plot in

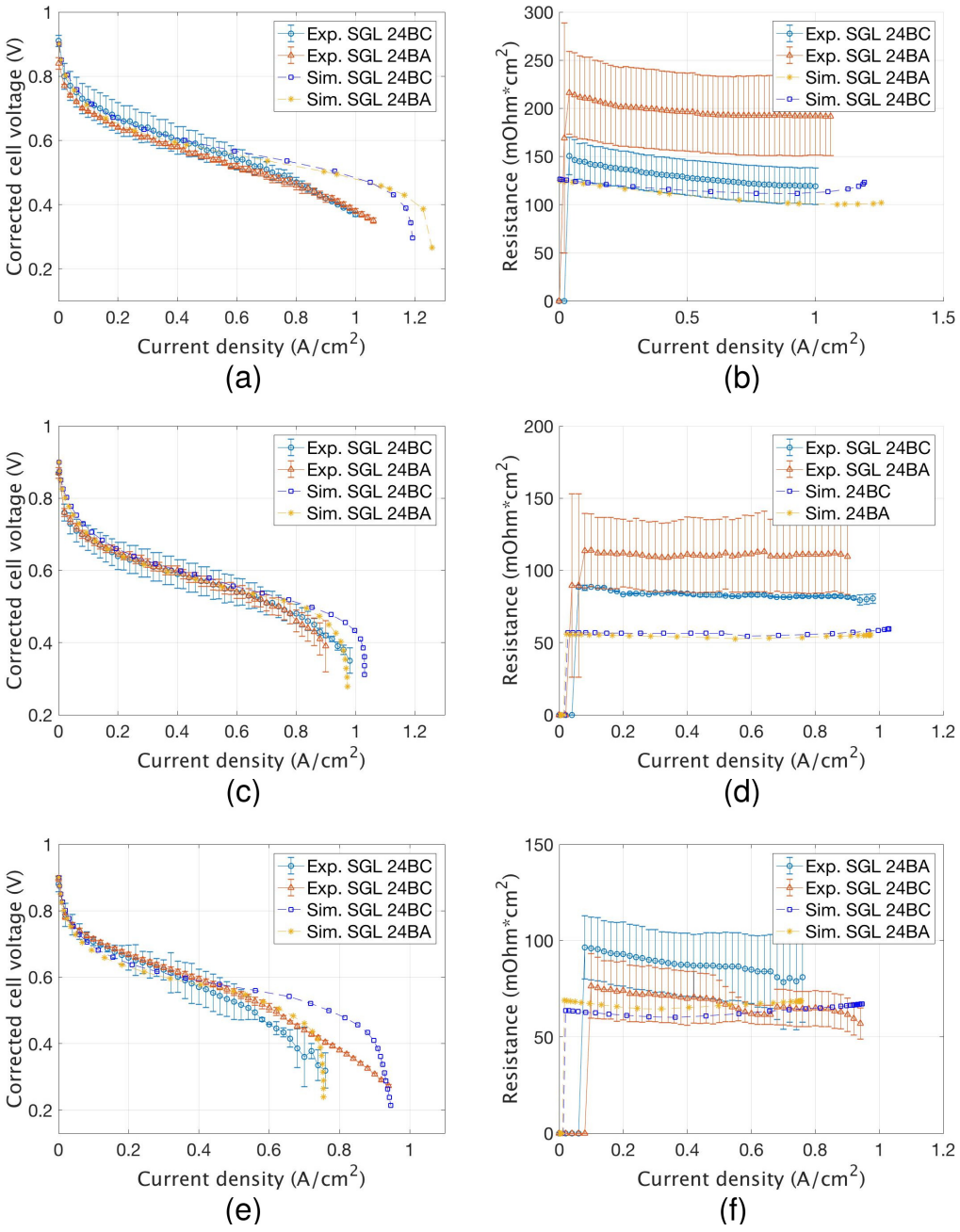

Figure 4.8 – Experimental validation of electrochemical performance and cell resistance at 80°C and 50% RH (a) and (b), at 80°C and 90% RH (c) and (d), and at 60°C and 90% RH (e) and (f) using in-house MEA parameters.

Figure 4.9 (b) shows that the MPL increases the cell temperature.

Our previous work [59] neglected gas convection effects. These have been included in the present model; however, the effects are negligible with over 99% of the oxygen flux due to diffusion.

4.3.3.2 Hot and wet condition

In order to evaluate the role of the MPL at the condition where the phase change effect is apparent and the flow is in the two-phase regime, the cell is operated at 80 °C and 90% RH (hot/wet condition). The electrochemical performance in Figure 4.8 (c) shows that the addition of an MPL results in a mild improvement in cell performance at high current densities both numerically and experimentally. The mild improvement observed at 80°C is expected as the thermal conductivity of SGL 24BA (0.005 W/(cm $\cdot$ K)) lies in between MRC 105 (0.003 W/(cm $\cdot$ K)), which has been shown to be insensitive to the introduction of an MPL, and Toray TGP-H-060 (0.014 W/(cm $\cdot$ K)) which has a strong performance sensitivity to an MPL addition. Further, the inkjet printed electrodes are thinner and have a lower active area which reduces the sensitivity to mass transport losses. The electrode used by Owejan et al. [1] is thicker (10 μm) than the inkjet printed electrode (3 μm). For a thicker electrode, the saturation has a stronger impact on reactant transport because of a longer diffusion path to the reaction site.

As compared to the hot/dry condition, the difference between numerical predictions and experimental data in cell resistances is smaller. This might be because of more hydrated membrane at wet conditions which may reduce contact resistance [192].

The water balance plot in Figure 4.9 (c) shows that adding an MPL under hot/wet condition delays liquid water ejection and forces more water to move from cathode to anode. The above observations can be attributed to the increased temperature in the electrode as shown in Figure 4.9 (d). The predicted temperature difference at 0.9 A/cm^2 is about 2°C higher when an MPL is added, in agreement with the data reported by Burheim et al. [180]. Figure 4.10 shows the distribution of temperature, membrane water content

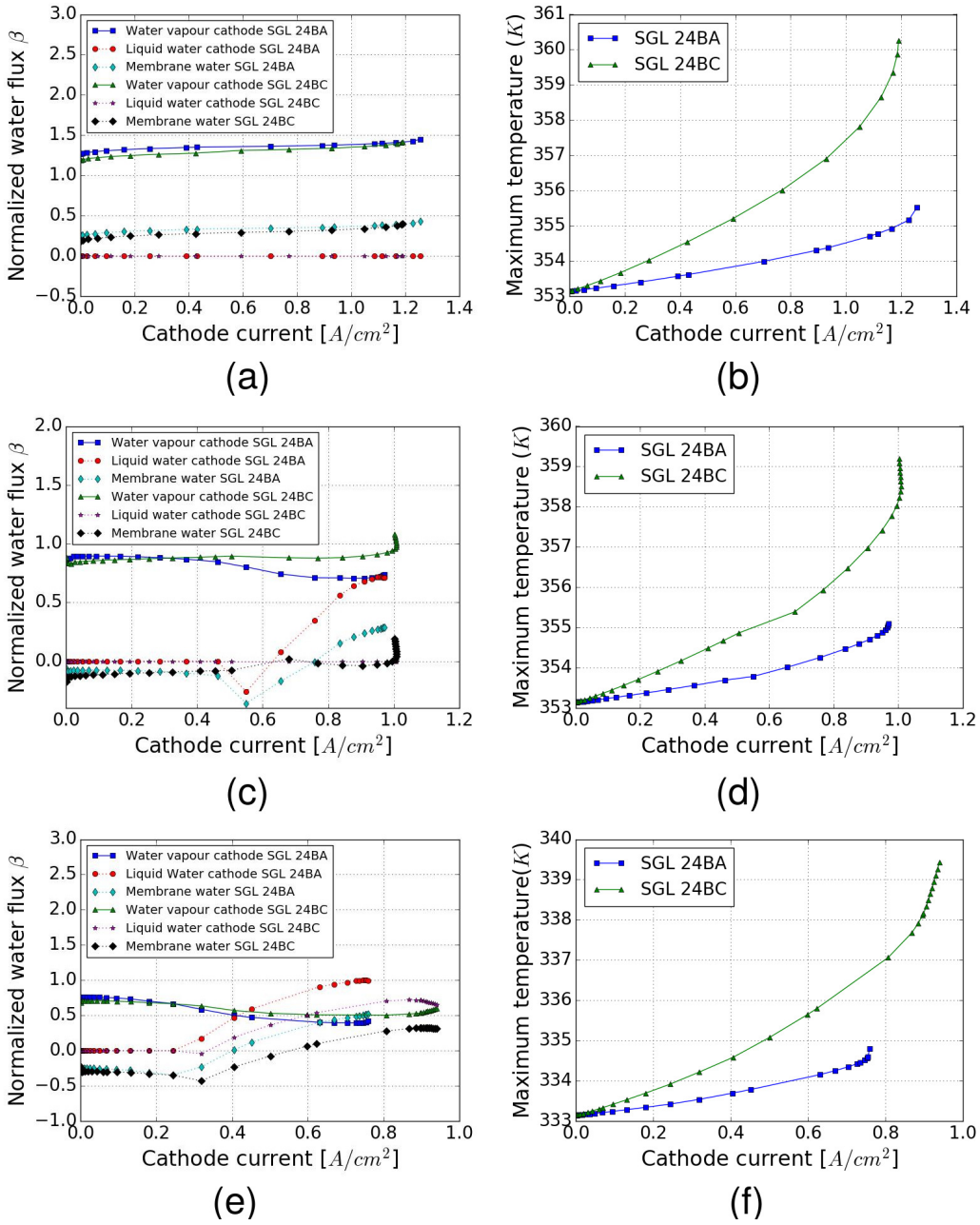

Figure 4.9 – Water balance and maximum cell temperature at 80°C and 50% RH (a) and (b), at 80°C and 90% RH (c) and (d), and at 60°C and 90% RH (e) and (f) for SGL 24BC and SGL 24BA using in-house MEA parameters, positive cathode flux is water leaving MEA, positive membrane water flux is from anode to cathode.

in the CCMs, and water molar fraction as well as saturation in the cathode CL at a current density of 0.9 A/cm^2. The increased temperature results in a different membrane water content distribution as shown in Figure 4.10. In both cells, the ionomer in the cathode CLs is fully hydrated. However, in the anode CLs, the cell with MPLs shows a lower membrane water content due to the increased temperature creating a higher membrane water content gradient leading to a greater water flux from cathode to anode and less water accumulation at the cathode. With the increase in temperature, not only more water moves from cathode to anode, but the cathode electrode is also able to evaporate more water, thereby the water molar fraction is higher in the cell with MPLs than without. With more water being vaporized, the liquid water saturation experienced a substantial decrease after adding MPLs which has also been observed by Deevanhxay et al. [193] with real-time X-ray radiography.

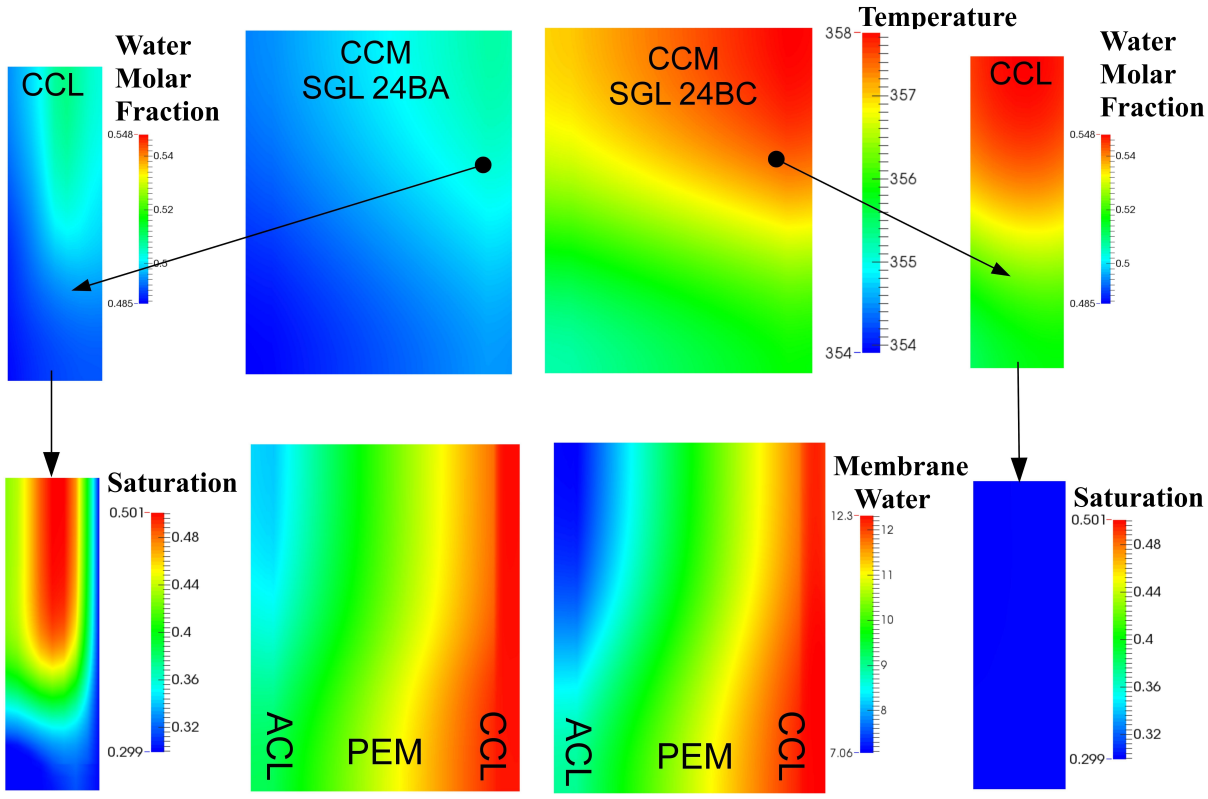

Figure 4.10 – Distributions of CCM temperature and membrane water content, and CCL water molar fraction and saturation for SGL 24BC and SGL 24BA at 80°C, 90% RH and 0.9 A/cm^2

The enhanced back-diffusion seems to contradict the conclusions made by Karan et al. [91] and Atiyeh et al. [101]. However, the enhanced back-diffusion shown in Figure 4.9 (c) is first of all not significant enough to result in anode flooding as reported by Weber et al. [94], and secondly, in Figure 6 (b) reported by Atiyeh et al. [101] showed that adding the MPLs had led to a decrease (roughly 50% change as compared to no MPL) in the amount of water leaving the cathode which indicates the movement of water from the cathode to anode. Lastly, considering the maximum current density reported by Atiyeh et al. [101] is only about 0.7 A/cm^2, the effect of MPL on back-diffusion might be still insignificant under such a low current density.

As shown in Figure 4.9 (c), there is one occasion when a negative liquid water flux is observed. This result is non-physical and it is due to the evaporation in the GDL once the GDL/channel boundary condition changes from no flux to dynamic boundary condition. Typically, the convergence is hard to achieve under this condition, i.e., from single-phase to two-phase regime.

4.3.3.3 Cold and wet condition

In order to study the effect of the MPL in an operating condition where two-phase flow dominates, the conditions studied are at 60°C and 90% RH (cold/wet condition). Figure 4.8 (e) shows a substantial increase in performance after adding the MPL at high current densities. A small discrepancy between model prediction and experimental data is observed at high current density.

Figure 4.8 (f) shows the numerical and experimental cell resistance. As compared to the hot/dry and hot/wet cases, the predicted cell resistance in the cold/wet case shows a better agreement with experimental data. However, the numerical predictions experience an increase in cell resistance at high current densities, whereas the experimental data shows the opposite.

Figure 4.9 (e) and (f) show the water fluxes and the maximum cell temperature, respectively. As compared to the hot/wet case, the reduced operating temperature results in earlier liquid water ejection from the MEA as the vapor saturation pressure decreases with temperature. As explained in the hot/wet

case, inserting an MPL results in a warmer electrode which leads to an increase in water transport from the cathode to anode and a reduction in saturation. Thus, higher oxygen concentration is observed for the cell with an MPL as shown in Figure 4.11.

Owejan et al. [1] hypothesized that the MPL creates an in-plane pathway for gas transport under partially saturated conditions. To examine this effect, the saturation and oxygen molar fraction distributions, and the oxygen molar fraction at GDL/CL and MPL/CL interfaces for the cells with and without MPLs are plotted in Figure 4.12. The figure shows that the MPL is less saturated as compared to the GDL due to its smaller pore size and hydrophobic nature. The line plot of oxygen molar fraction at layer interfaces indicates that having an MPL increases the oxygen concentration under the land area which confirms the hypothesis that the MPL improves the in-plane diffusion.

The gas pressure distributions shown in Figures 4.13 (a) and (b) show that the pressure decreases from GDL/channel boundary to the CL and most of the pressure drop is in the MPL and CL. The reason for the pressure loss is due to condensation. In order to quantify the importance of the convective flow, the ratio of diffusive flux to overall mass flux (diffusion and convection) is shown in Figures 4.13 (c) and (d) for the cathode and in the CL. It can be seen from the figure that the dominant transport mechanism is diffusion. The noise in the data is due to the post-processing which requires taking the derivative of the solution variables, thereby adding extra noise to the data. As compared to the hot/dry case where the diffusion takes up to 99% of the overall mass flux, the ratio goes down to 80% in some regions which indicates that convection is stronger under cold/wet condition. This convective flow slightly enhances the overall mass transport.

4.4 Micro Porous Layer Optimization

In order to evaluate low loading fuel cell performance sensitivity to MPL parameters, a parametric study is carried out for thermal conductivity, thickness, wettability and microstructure properties, i.e., absolute permeability,

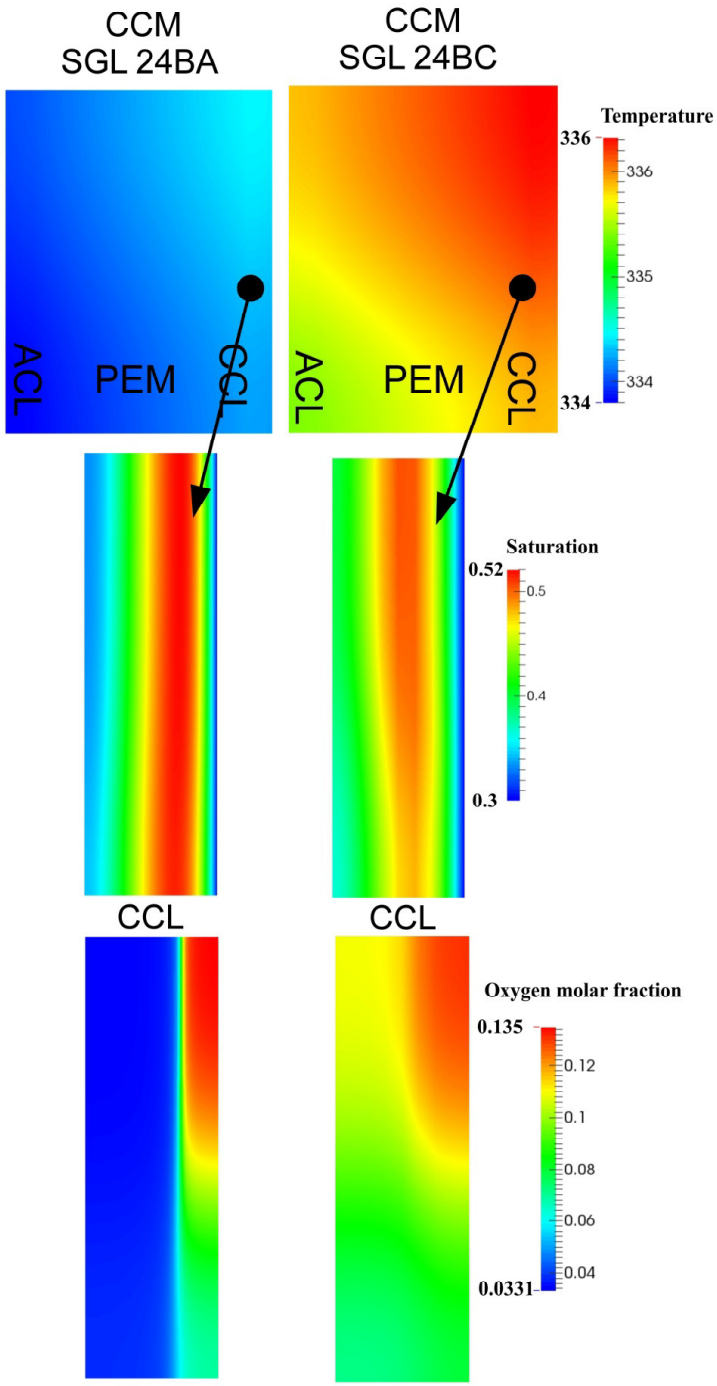

Figure 4.11 – Distributions of temperature in CCMs, and saturation and oxygen molar fraction in CCLs at 60°C, 90% RH and 0.7 A/cm^2 for the cells with and without MPLs.

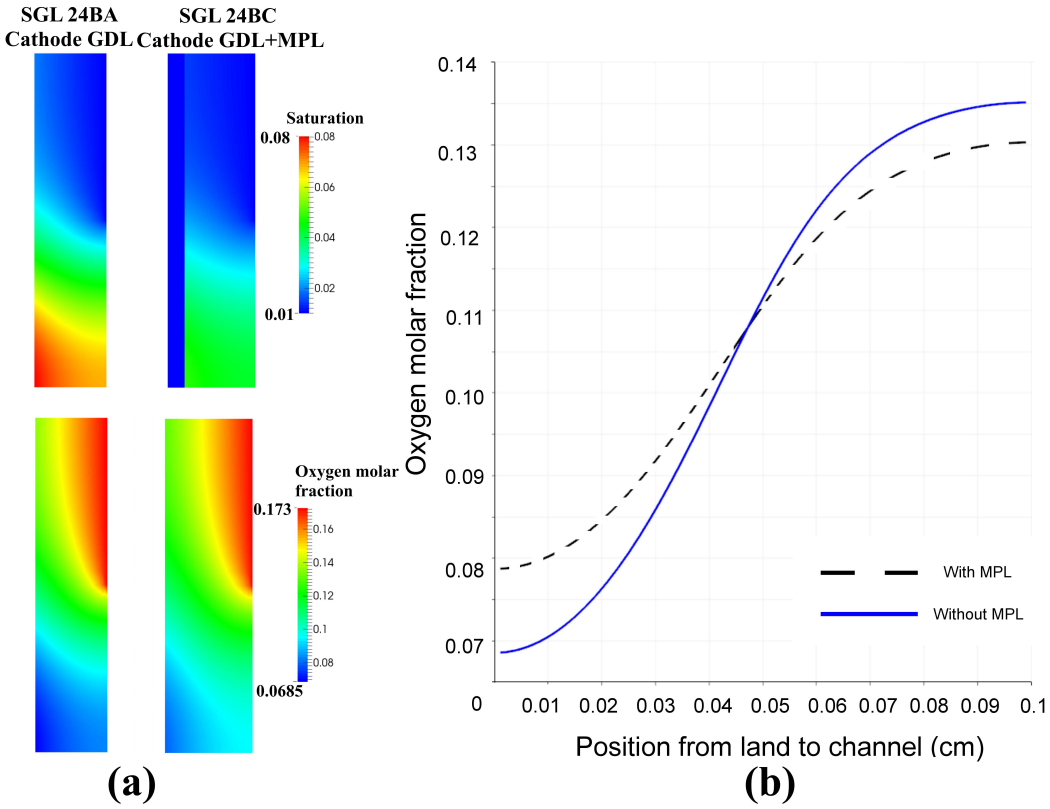

Figure 4.12 – Distributions of saturation and oxygen molar fraction in the cathode without the cathode CL, and the saturation line plot at the GDL/CL and MPL/CL interfaces at 60°C, 90% RH and 0.7 A/cm^2 for the cells with and without MPLs.

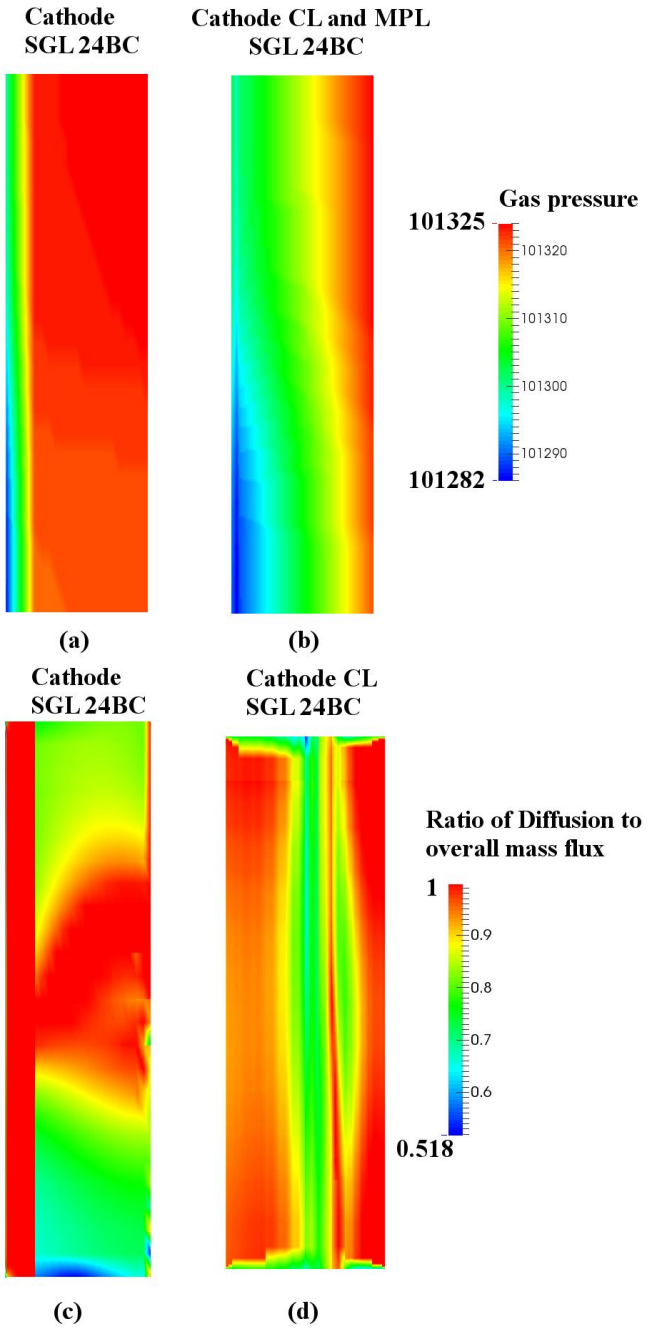

Figure 4.13 – Distributions of total gas pressure (a) in the cathode, (b) in the cathode CL and MPL, and (c) diffusive flux in overall mass flux in the cathode and (d) in the cathode CL for the cell with the MPL at 60°C, 90% RH and 0.7 A/cm^2.

hydrophilic percentage, hydrophobic contact angle and the pore radius. The base line parameters are the ones used in Section 4.3.

4.4.1 Thermal Conductivity

Dry condition - Electrochemical performance of cells with varying MPL thermal conductivity, i.e., base line (0.0008 W/(cm · K)), 0.00008, 0.00035, 0.0005, 0.008, and 0.08 W/(cm · K) are evaluated under hot/dry condition. A parametric study on MPL thermal conductivity showed that the performance is insensitive to in-plane thermal conductivity. Thus, the in-plane thermal conductivity is considered to be constant at 0.0387 W/(cm · K) based on the value reported in [183], although it is likely that MPL is isotropic. Figure 4.14 (a) shows that under hot/dry condition decreasing the MPL thermal conductivity to 0.00008 W/(cm · K) results in a substantial reduction in performance and a reversal in the polarization curve at high current density. The reduced performance is due to membrane dry out. Polarization curve current reversal was also observed experimentally [194] in the case of air-breathing fuel cells. Increasing the MPL thermal conductivity, on the other hand, has no significant effect on performance in the range from baseline to 0.00035 W/(cm · K).

Wet condition - Figure 4.14 (b) and (c) show the electrochemical performance at varying MPL thermal conductivities under hot/wet and cold/wet conditions, respectively. An optimal MPL thermal conductivity is observed in both cases which is about 0.00035 W/(cm · K). An increase in thermal conductivity lowers electrode temperature inhibiting the temperature build-up required to evaporate the water from the electrode. A decrease in thermal conductivity beyond 0.00035 W/(cm · K) however decreases cell performance due to CCM dry out. The maximum temperature in the MEA when the thermal conductivity is 0.00008 W/(cm · K), is 369.0 at its maximum current density under cold/wet condition. An optimal MPL thermal conductivity strikes a balance between a sufficient water evaporation and membrane hydration.

GDL thermal conductivity - Since the thermal conductivity is the key parameter in determining the PEFC performance especially under cold/wet conditions, the effect of GDL thermal conductivity with and without MPLs

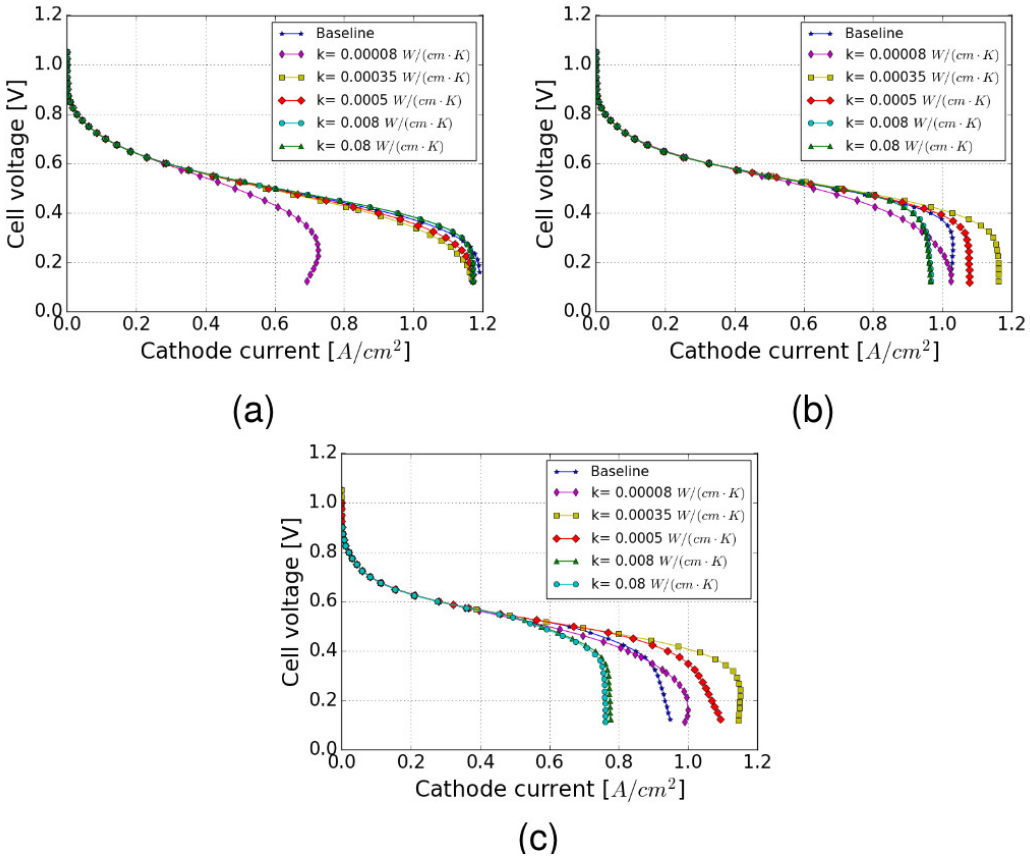

Figure 4.14 – Electrochemical performance at varying MPL thermal conductivities under (a) hot/dry, (b) hot/wet and (c) cold/wet conditions.

has also been evaluated. In the case where the MPL is present, the GDL thermal conductivities being examined are, base line, 0.0003, 0.003, 0.03, 0.3, and 3 W/(cm · K) under cold/wet condition. Figure 4.15 (a) shows the electrochemical performance at varying GDL thermal conductivities. Similar to the MPL thermal conductivity study, an optimal GDL thermal conductivity is also observed. With the GDL thermal conductivity of 0.0003 W/(cm · K), the CCM dries out at high current densities.

Figure 4.15 (b) shows the cell performance with different GDL thermal conductivities for the cells without MPLs. It can be seen from the figure that at a GDL thermal conductivity of 0.0005 W/(cm · K), the best performance is achieved. This means that by tuning the GDL thermal conductivity, a similar performance enhancement can be achieved even without MPLs which highlights the importance of thermal conductivity to cell performance.

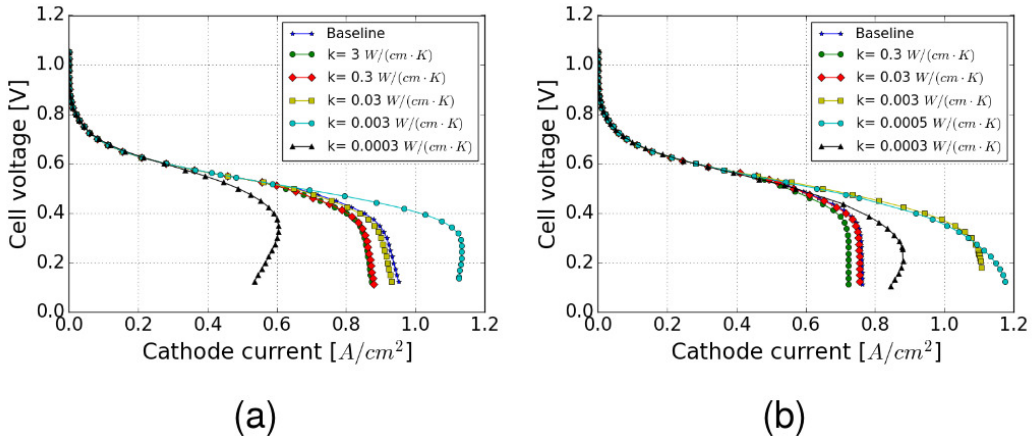

Figure 4.15 – Electrochemical performance at varying GDL thermal conductivities (a) with and (b) without MPLs under cold/wet conditions.

4.4.2 Thickness

Dry condition - Figure 4.16 (a) shows the effect of MPL thickness under hot/dry condition. The improved performance with thinner MPLs shown in Figure 4.16 (a) indicates an MPL is only necessary in this case to enhance the contact between CL and GDL, thereby reducing cell resistance (not included in the model).

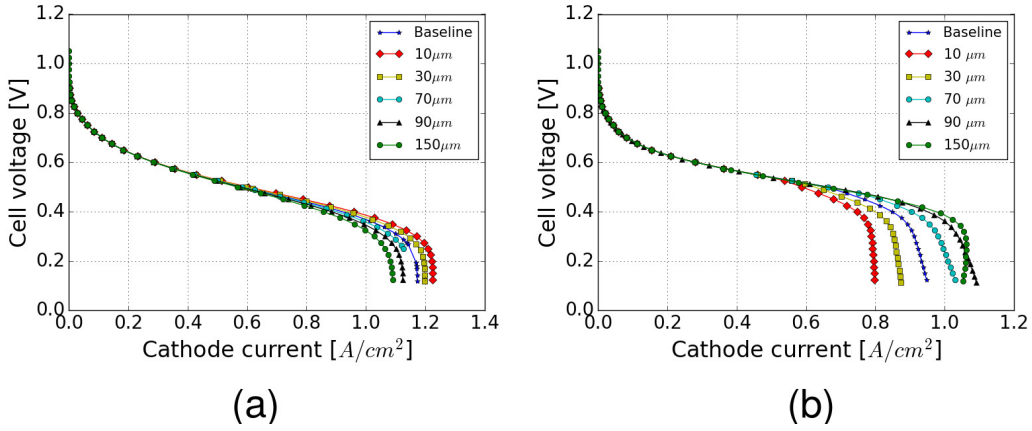

Figure 4.16 – Electrochemical performance at varying MPL thickness under (a) hot/dry and (b) cold/wet conditions.

Wet condition - The effects of MPL thickness on fuel cell performance under cold/wet condition are shown in Figure 4.16 (b). A better performance is achieved with thicker MPL, except in the case of MPL thickness larger than

150 μm. The reverse arc is observed at an MPL thickness of 150 μm at high current densities due to membrane dry out. The results highlight there is a trade-off between MPL thermal conductivity and thickness.

4.4.3 Wettability and Microstructure

By modifying the wettability and microstructure of the MPL, researchers have observed that the MEA performance can be improved [33, 35, 41, 43, 92, 195, 196], especially under wet conditions. A parametric study on MPL wettability and microstructure is, therefore, carried out under cold/wet conditions.

MPL hydrophilic percentage - Figure 4.17 (a) shows the electrochemical performance at varying MPL hydrophilic percentages. An optimum percentage of hydrophilic pores exists from 10% to 20%. The performance at higher MPL hydrophilic percentage is lower due to a higher mass transport loss in the partially saturated MPL. When the hydrophilic percentage is below 10%, the performance decreases.

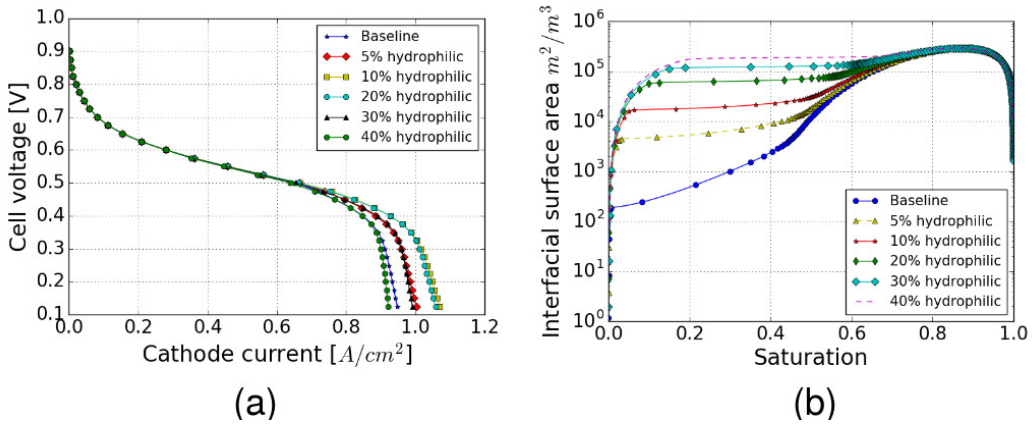

Figure 4.17 – (a) Electrochemical performance at varying MPL hydrophilic percentages and (b) saturation vs. interfacial surface area under cold/wet condition.

With increased hydrophilic percentage, the MPL saturation increases as the hydrophilic pores will be completely filled with liquid water as shown in Figure 4.18. Figure 4.18 shows the saturation distributions in the cathode CL and MPL at 0.9 A/cm^2 at 1%, 20% and 40% MPL hydrophilic percentages. The increased saturation in MPL leads to an increase in liquid-gas interfacial

surface area (see Figure 4.17 (b)). The higher interfacial surface area in the MPL results in a higher MPL water evaporation which reduces liquid water accumulation in the cathode CL (see Figure 4.18) and removes water in vapor phase. When the hydrophilic percentage is higher than 20%, however, the benefit of improving water evaporation starts to decline as the mass transport loss begins to dominate the overall performance due to the increased saturation in MPL.

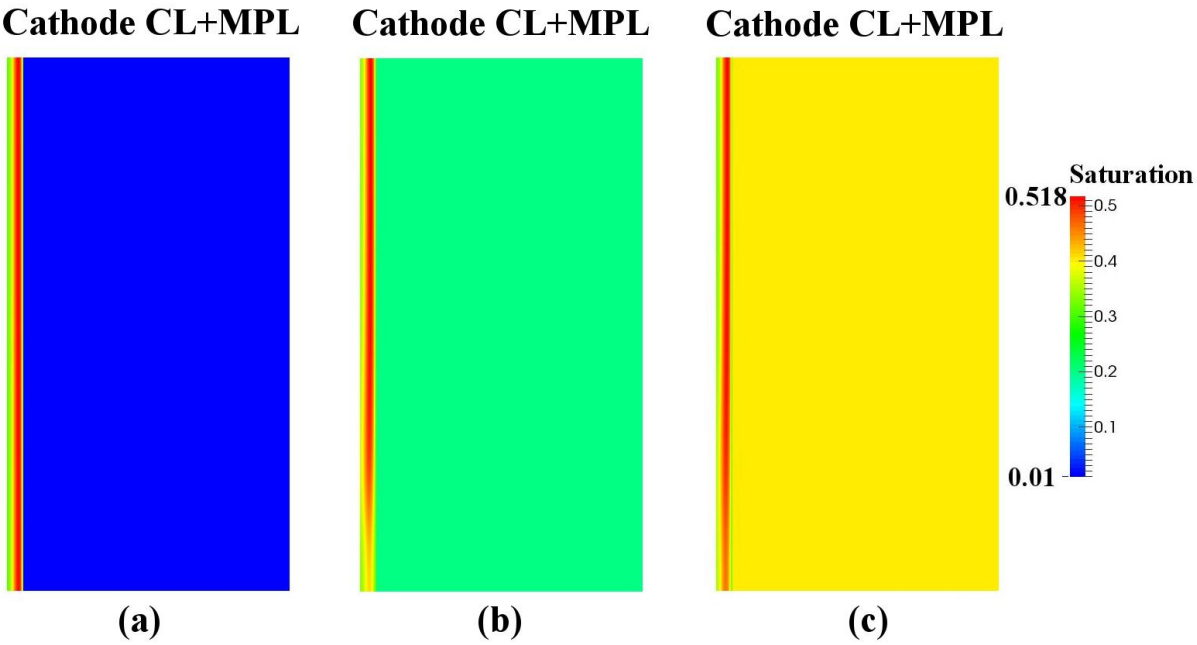

Figure 4.18 – Saturation distributions in the cathode CL and MPL at 0.9 A/cm^2 for (a) 1%, (b) 20% and (c) 40% hydrophilic percentages.

MPL contact angle - Figure 4.19 (a) shows the predicted fuel cell electrochemical performance at varying MPL hydrophobic contact angles. The figure shows that the MPL contact angle has no effect on MEA performance.

MPL PSD - The MEA performance at varying MPL PSDs are shown in Figure 4.19 (b). Varying MPL pore size leads to several changes such as absolute permeability and liquid/gas interfacial surface area, however these appear to have a negligible effect on performance. Based on these results, MPL morphological change should have little effect on performance.

Optimal MPL design - Figure 4.20 provides a unified picture of the optimal

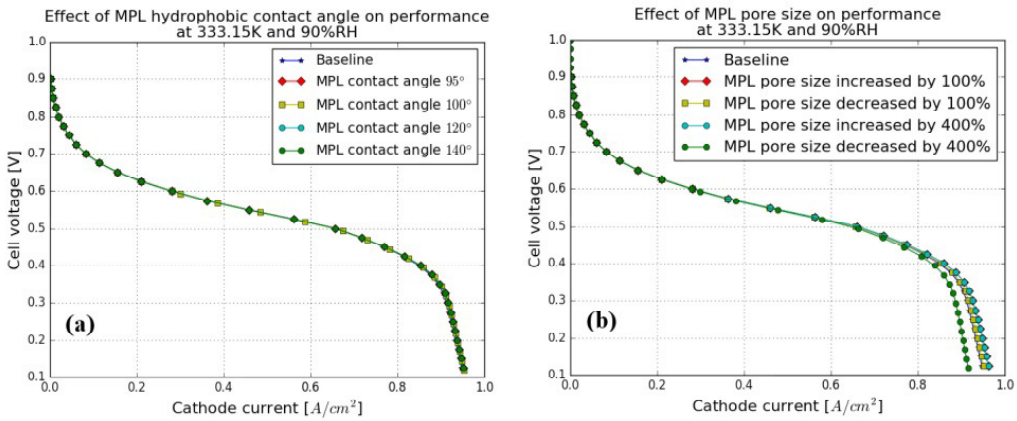

Figure 4.19 – Electrochemical performance at varying MPL (a) hydrophobic contact angles, and (b) PSDs under cold/wet conditions.

MPL design considerations in order to maintain the balance between water and heat management. Under wet conditions, the functions of MPL are: i) vaporizing generated liquid water in the CL to prevent further mass transport losses due to water build-up; ii) enhancing back diffusion; and iii) improving the in-plane diffusive transport. To achieve these three goals, the MPL should have low thermal conductivity, thick and partly hydrophilic.

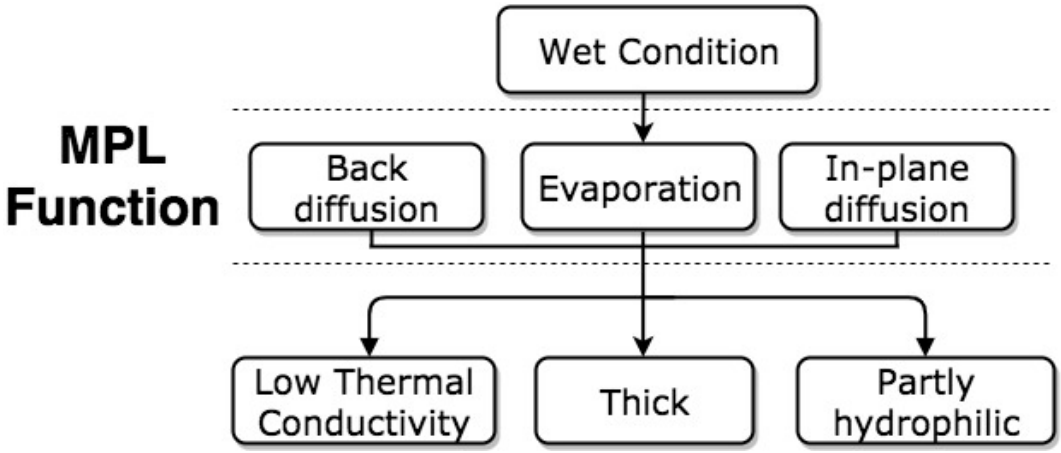

Figure 4.20 – Summary of MPL function and its optimal design.

4.5 Conclusion

A multi-dimensional, non-isothermal and two-phase model developed in Open-FCST [59] is extended to include convection and used to explore the reasons

for the improved fuel cell performance once a micro-porous layer is introduced. The numerical model is validated under varying operating conditions by comparing to experimental data for conventional electrodes in the literature and for low loading electrodes fabricated in our laboratory.

Under hot/dry conditions, adding an MPL has little effect on cell performance. In fact, the reactant transport resistance slightly increased with the presence of the MPL.

Under hot/wet and cold/wet conditions, the MPL acts as heat barrier that warms up the electrode in order to eject more water in the vapor phase and increase back-diffusion from cathode to anode. Under cold/wet conditions, the MPL also increases the in-plane reactant transport. Overall, the reason for the improved fuel cell performance under wet conditions with the presence of the MPL is that the hotter electrode reduces cathode flooding.

Additional benefits of adding a microporous layer observed experimentally include reduced ohmic losses and enhanced cell performance stability. Both of them might be due to the better interfacial contact and stronger mechanical stability. The above observations will be studied in future work.

A parametric study on transport and microstructural MPL parameters under wet conditions revealed that:

1. An optimal MPL thermal conductivity and thickness exist that leads to improved water removal without leading to the CCM dry out.

2. A partly hydrophilic MPL might be advantageous in order to enhance evaporation which can alleviate water accumulation in both MPL and CL.

3. The hydrophobic contact angle and pore size distribution (including absolute permeability) in the MPL have little effect on MEA performance.

Chapter 5

Electrode Architecture Design

New electrode architectures have substantially shown improved platinum utilization as well as fuel cell durability [11, 22, 47, 47–55, 89, 90]. Examples are functionality graded electrodes [47–49], patterned electrodes/PEM [22, 50–55], and nano-structured thin-film (NSTF) electrodes [89, 90]. In this chapter, a new electrode architecture design will be discussed, i.e., electrode coated membrane (ECM).

5.1 Introduction

Reducing the reactant transport losses is important in achieving better performance in PEMFC [55, 114, 131, 197]. For the layers that the reactants transport through, the MPL serves as a transition layer that provides better interfacial contact [83] and improves mass transport by removing water in the vapor phase, especially under wet conditions [103].

Even though the MPL is important to fuel cell performance, very few experimental studies have studied the impact of MPL thickness. Performance enhancement was observed by depositing an MPL directly over a CCM by Park et al. [198]. The MPL thicknesses tested in their experiments were 50 μm and 100 μm which are comparable to the conventional MPL thickness. With inkjet printing technology, fabricating thin MPLs becomes feasible. This enables potential performance advancement for PEMFC by further reducing the reactant transport losses.

Recently, attention has been paid to understand the effect of MPL wettabil-

ity on the in-situ performance. Kitahara et al. [199–202] studied the effect of hydrophilic MPL by replacing PTFE with polyvinyl alcohol (PVA) as the MPL binder. A commercial CCM (Gore PRIMEA) with a Pt loading of 0.4 mg/cm^2 and a CL thickness of 30 μm was used for testing [199]. Improved water retention and cell performance were observed with a hydrophilic MPL coating over a hydrophobic MPL (double MPL) at low RH. Kitahara et al. [200] also studied the effect of hydrophilic coating thickness and PVA/PTFE content in the hydrophilic/hydrophobic MPLs. In their study, the optimal hydrophilic MPL design should have a thickness of 5μm and a PVF and PTFE content of 5 wt% and 10-40 wt%, respectively [199]. Ahn et al. [203] used Nafion ionomer during their carbon ink formulation in order to fabricate MPLs with the hydrophilic polymer. An improvement in the cell performance and lowering of ohmic losses were observed with the presence of a Nafion based MPL on the cathodic side as compared to the PTFE based MPL [203] at low RH. Similarly, Tanuma [204] used a mixture of water, ethanol and Flemion ionomer dispersion to obtain a hydrophilic MPL coating over the GDL substrate. A performance improvement at dry operating condition of 30% RH, 80°C was reported when using the hydrophilic ionomer based MPL [204].

In this work, the proposed numerical model in Chapter 2 is used to analyze the performance of a CCM with a Nafion based carbon ink coated directly over the CL by means of inkjet printing resulting in a novel electrode coated membrane (ECM) architecture. Due to the fabrication method used, a controlled low thickness MPL is achieved. Also, by varying the Nafion content, the effect of MPL hydrophilicity might be modified. The numerical model proposed in this thesis is used to analyze the effect of an ECM on cell performance as well as the transport processes under varying operating conditions. Lastly, in order to achieve optimal ECM design, a parametric study has been performed using the model to find out the optimal ECM parameters.

5.2 Input Parameters

The multi-dimensional, two-phase, non-isothermal model in [103] is used to study the transport processes in a fuel cell equipped with an ECM. Tables 5.1, 5.2, 5.3, 5.5, and 5.6 provide all input parameters. The input parameters for the GDL are summarized in Table 5.1. The values of porosity, thickness, thermal and electrical conductivity in the GDL are obtained from the experiments. The rest of the parameters are based on the values reported in literature.

Table 5.1 – Standard GDL input parameters

GDL Parameters		Value
Porosity		0.8 (measured)
Thickness (μm)		142.0 (measured)
Thermal conductivity (W/(cm $\cdot$ K))		0.003 (measured)
Electrical conductivity, through plane (S/cm)		1.87 (measured)
Electrical conductivity, in plane (S/cm)		272.78 (measured)
Contact angle (water) in hydrophilic phase		70° ([83])
Contact angle (water) in hydrophobic phase		122° ([104])
PSD characterization		
Hydrophilic volume fraction (%)		0.08 ([83])
PSD interconnectivity λ_{PSD}		1.26 ([113])
Absolute permeability (m^2)		1.88×10^{-11} (estimated by PSD model)
Characteristic pore radius (μm)	r_1	14.20 ([163])
	r_2	34.00 ([163])
Characteristic pore widths	s_1	0.35 ([163])
	s_2	1.00 ([163])
Characteristic pore fraction	$f_{HI,1}$	1.00 ([163])
	$f_{HI,2}$	0.00 ([163])
	$f_{HO,1}$	0.31 ([163])
	$f_{HO,2}$	0.69 ([163])

The simulations are carried out with three different MPLs, standard MPL, ECM35 and ECM50. Table 5.2 shows the input parameters for standard MPL.

To fabricate the MPL in the ECM, the carbon ink used was formulated by mixing 37.5 mg of Vulcan XC-72R carbon black with 1:2 ratio of ethylene glycol and isopropanol and 30 wt.% Nafion ionomer (5% wt. LQ-1105, Ion Power). The MPL was then fabricated with 20 printed layers using inkjet printing. The detailed fabrication process can be found in [22]. The difference between ECM35 and ECM50 is the ionomer to carbon ratio (I/C) which is 0.35 and 0.5, respectively.

Input parameters for ECM35 and ECM50 are shown in Table 5.3. The

Table 5.2 – Standard MPL input parameters

MPL Parameters		Value
Porosity		0.7 (measured)
Thickness (μm)		30.0 (measured)
Thermal conductivity (W/(cm $\cdot$ K))		0.0005 ([180])
Electrical conductivity, through plane (S/cm)		6.84 (estimated based on cell resistance)
Electrical conductivity, in plane (S/cm)		6.84 (estimated based on cell resistance)
Contact angle (water) in hydrophilic phase		84° ([66])
Contact angle (water) in hydrophobic phase		110° ([84])
PSD characterization		
Hydrophilic volume fraction (%)		1 (estimated)
PSD interconnectivity λ_{PSD}		0.3 ([119])
Absolute permeability (m^2)		1.39e-13 (estimated by PSD model)
Characteristic pore radius (μm)	r_1	0.072 ([103])
	r_2	0.125 ([103])
	r_3	2.000 ([103])
Characteristic pore widths	s_1	0.35 ([103])
	s_2	0.5 ([103])
	s_3	0.9 ([103])
Characteristic pore fraction	$f_{HI,1}$	0.50 ([103])
	$f_{HI,2}$	0.00 ([103])
	$f_{HI,3}$	0.50 ([103])
	$f_{HO,1}$	0.45 ([103])
	$f_{HO,2}$	0.10 ([103])
	$f_{HO,3}$	0.45 ([103])

hydrophilic percentage for ECM35 and ECM50 are assumed to be 30% and 50%, respectively. The electrical conductivities for all three MPLs are obtained by fitting the experimental cell resistance. The experimental cell resistance is obtained based on the value of the high frequency intercept determined by Electrochemical Impedance Spectroscopy (EIS) at 68° C, 100% RH, and 2.5 bar gauge pressure. It contains electrical resistances for CLs, MPLs and GDLs, and membrane protonic resistance. As the cell resistance was measured with the same CLs, GDLs and membrane, the contributions from them should be constant. Thus, the cell resistance is fitted by varying the MPL electrical conductivity at open circuit voltage (OCV) and the results for three MPLs are shown in Table 5.4.

The PSDs for ECM35 and ECM50 are assumed to be the same as the CL because the same carbon black and inkjet printing fabrication method were used. Different values are used for absolute gas and liquid permeability, and the absolute gas permeability is five order of magnitude higher than absolute liquid permeability. Such difference is attributed to slip flow of gas mixture

at pore walls which enhances gas flow as the pore sizes are close to the mean free path [187].

Table 5.3 – ECM input parameters

Parameters		ECM35	ECM50
Porosity		0.78 (measured)	0.68 (measured)
Thickness (μm)		12.0 (measured)	10.3 (measured)
Hydrophilic percentage (%)		30 (estimated)	50 (estimated)
Electrical conductivity, through-plane (S/cm)		88.84 (estimated)	88.84 (estimated)
Electrical conductivity, in-plane (S/cm)		88.84 (estimated)	88.84 (estimated)
PSD characterization		[103]	
PSD interconnectivity λ_{PSD}		2.5 (estimated)	
Absolute permeability (gas) (m^2)		1.00e-13 (estimated)	
Absolute permeability (liquid) (m^2)		1.00e-18 (estimated)	
Characteristic pore radius (μm)	r_1	0.02	
	r_2	0.025	
	r_3	0.075	
Characteristic pore widths	s_1	0.55	
	s_2	0.45	
	s_3	1.2	
Characteristic pore fraction	$f_{HI,1}$	1.0	
	$f_{HI,2}$	0.0	
	$f_{HI,3}$	0.0	
	$f_{HO,1}$	0.5	
	$f_{HO,2}$	0.4	
	$f_{HO,3}$	0.1	

Table 5.4 – Ohmic resistance fitting.

MPL	Experimental data (m$\Omega \cdot$ cm^2)	Numerical value (m$\Omega \cdot$ cm^2) at OCV
ECM35	54	56
ECM50	58	56
Standard MPL	71	71

All CLs were manufactured using inkjet printing with 10 printed layers and the detailed fabrication process can be found in [2, 22]. Table 5.5 shows the input parameters for CLs. The values of active area were determined by cyclic voltammetry.

The membrane used in all tests is DuPont$^{\text{TM}}$ Nafion® (NRE) 211, and its parameters are shown in Table 5.6. The MEAs were tested on a differential cell with an active area of 45 cm^2 using parallel channels. In order to minimize the channel effect such as oxygen depletion, which the model does not account for, a high flow rate was used, especially at high current densities. The experimental as well as numerical operating conditions are shown in Table 5.7.

Table 5.5 – Standard CLs input parameters

CL Parameters	Value
Fabrication parameters and electrochemical characterization	
Cathodic platinum loading (mg_{Pt}/cm^2)	0.15 (measured)
Anodic platinum loading (mg_{Pt}/cm^2)	0.05 (measured)
Platinum loading on support (%wt.)	0.5 (measured)
Nafion loading (%wt.)	0.285 (measured)
Active area ECM35 (cm^2_{Pt}/cm^3_{CL})	144570 (measured)
Active area ECM50 (cm^2_{Pt}/cm^3_{CL})	140421 (measured)
Active area Standard MEA (cm^2_{Pt}/cm^3_{CL})	114893 (measured)
Porosity	0.695 (measured)
Thickness (μm)	4.7 ± 0.3 (measured)
Thermal conductivity ($W/(cm \cdot K)$)	0.0027 ([183])
Electrical conductivity of carbon black (S/cm)	88.84 ([7])
Density of carbon black (g/cm^3)	1.69 ([184])
PSD characterization (see Table 5.3)	
Hydrophilic volume fraction (%)	30 ([185])
Contact angle (water) in hydrophilic phase	79° ([66])
Contact angle (water) in hydrophobic phase	91° ([185])

It can seen from the table that the RH and inlet pressure changes with the current density. In order to simplify model calculations, the input RH and pressure are held constant in the model. To examine the effect of RH and pressure, a parametric study is performed.

Table 5.6 – Membrane NRE 211 parameters

PEM	Literature	Value/direction/equation
Thickness	[173]	25.4 μm
Water diffusion	[174]	$0.000417\lambda(1.0 + 161.0exp(-\lambda))exp(-\frac{-2436.0}{T})$, $\lambda > 3.0$
Electro-osmotic drag coefficient	[173]	1.0
Sorption isotherm	[189]	$(1.0 + 0.2352a_w^2\frac{(T-303.15)}{30.0}(14.22a_w^3 - 18.92a_w^2 + 13.41a_w))$, $a_w = RH$
Proton conductivity	[190]	$(-0.000120125\lambda^2 + 0.01052\lambda - 0.020634)exp(751.5412(\frac{1}{303} - \frac{1}{T}))$
Thermal-osmosis	[136]	Cold to hot
Thermal conductivity ($W/(cm \cdot K)$)	[183]	0.0013

5.3 Results and Discussions

5.3.1 Comparison to Experimental Data

Experimental results and numerically predicted polarization curves are presented in Figure 5.1. An exact match between the model predictions and experimental data is not expected due to the varying operating conditions in the experiments. The numerical results show similar performance gains for

Table 5.7 – Operating conditions for experiments and model.

Experiments				Model
Current density (A/cm^2)	0.1	1.0	2.1	
Normal condition, temperature (° C)	68	68	68	68
Normal condition, anodic RH (%)	80	80	94	85
Normal condition, cathodic RH (%)	50	70	70	60
Warmup condition, temperature (° C)	40	40	40	40
Warmup condition, anodic RH (%)	100	127	140	100
Warmup condition, cathodic RH (%)	70	50	50	50
Anodic inlet pressure (bar)	1.1	1.9	2.7	2.2
Cathodic inlet pressure (bar)	1.1	1.6	2.3	2.2
Anodic flow rate (slpm)	0.9	2.8	6.0	∞
Cathodic flow rate (slpm)	1.3	6.8	14.3	∞

ECMs under normal condition. Under warmup condition, the model captures the performance drop for different architectures.

Since the operating conditions in the experiments varied, while the simulations operating conditions are kept constant, simulations are performed to study the effect of RH and pressure on cell performance and the results are shown in Figure 5.2 and 5.3. In the simulation, the upper and lower bounds of the RH and pressure are the maximum and minimum values of the experimental operating conditions reported in Table 5.7. Small improvements in performance are observed with higher RHs and pressure, and larger performance sensitivity is observed with pressure as compared to RH, especially under normal conditions. Therefore, using the averaged RH and pressure in the simulation results in a reduced performance.

Overall, one of the reasons for the discrepancy between the experimental data and simulation results is due to the use of the constant operating condition during the simulation. Other reasons include, reactant depletion along the channel, imperfect interfacial contact between GDL/MPL, MPL/CL or CL/PEM, and additional convective transport due to the pressure drop between the channels.

Under normal condition, ECM35 and ECM50 show better performance than standard MPL in both experimental and simulation results. In order to understand the reasons for the improved performance with ECMs, a per-

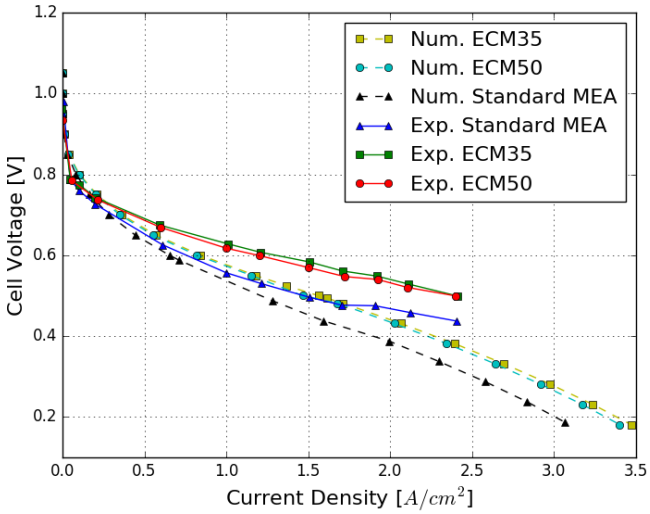

(a)

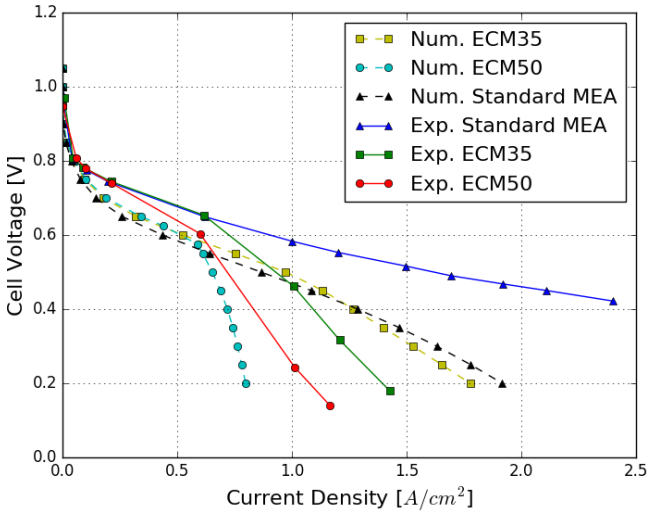

(b)

Figure 5.1 – Polarization curves at (a) normal condition and (b) warmup condition.

formance analysis is conducted by modifying each parameter in the standard MPL, that is different from ECM35, until all parameters are the same as ECM35. The polarization curves are shown in Figure 5.4 and the improvements in cell voltage by modifying parameters in the standard MPL is shown in Figure 5.5 at current densities of 1.5 A/cm^2 and 3.0 A/cm^2, respectively. The first parameter modified in the standard MPL is the value of electrochemically

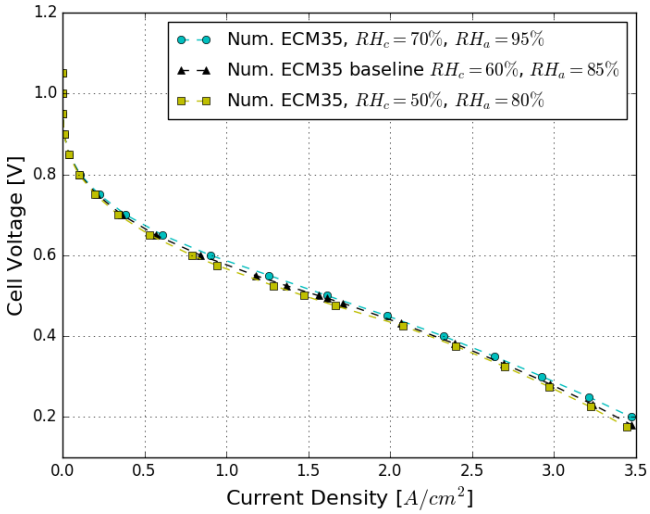

(a)

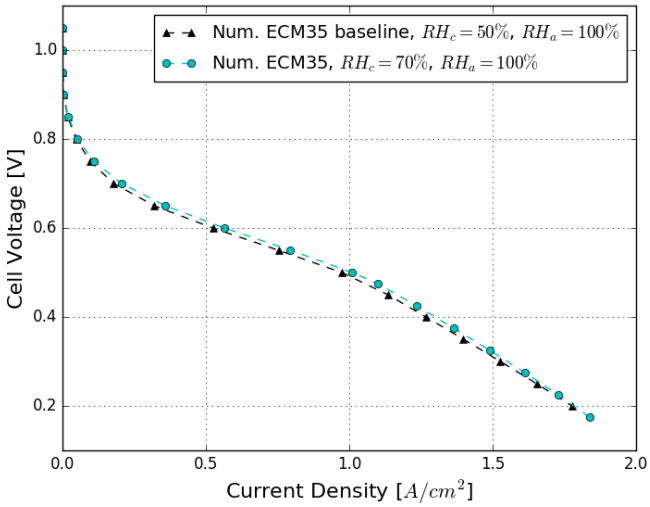

(b)

Figure 5.2 – RH effect on performance at (a) normal condition and (b) warmup condition for ECM35.

active surface area (ECSA) from 114893 cm^2_{Pt}/cm^3_{CL} to 144570 cm^2_{Pt}/cm^3_{CL} which leads to a constant improvement of 18.75 mV in cell voltage. Secondly, the electrical conductivity in the standard MPL is modified to be the same as in ECM35 resulting in 12.5 mV and 37.5 mV cell voltage gain, at 1.5 A/cm^2 and 3.0 A/cm^2, respectively, as compared to the standard MPL of 144570 cm^2_{Pt}/cm^3_{CL} ECSA. Lastly, the thickness of standard MPL has been

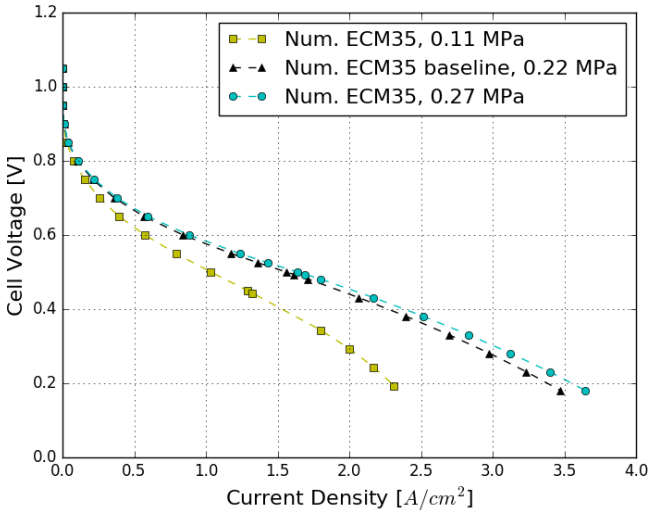

(a)

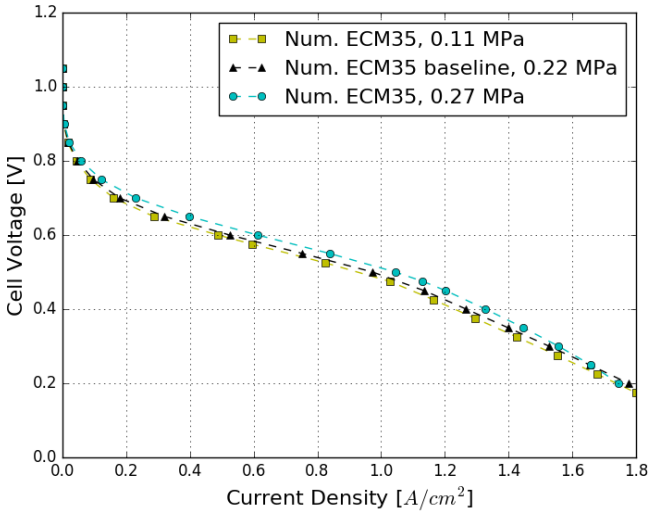

(b)

Figure 5.3 – Pressure effect on performance at (a) normal condition and (b) warmup condition for ECM35.

changed to the value of ECM35 which almost closes the performance gap between standard MPL and ECM35 (see Figure 5.4). The tiny performance gap left in the polarization curve is due to the hydrophilic percentage, where higher hydrophilic percentage in ECM35 leads to slightly better hydrated membrane. Overall, the main contributions for the performance improvements with ECM electrode are improved ohmic transport, and less mass transport losses due to

reduced thickness.

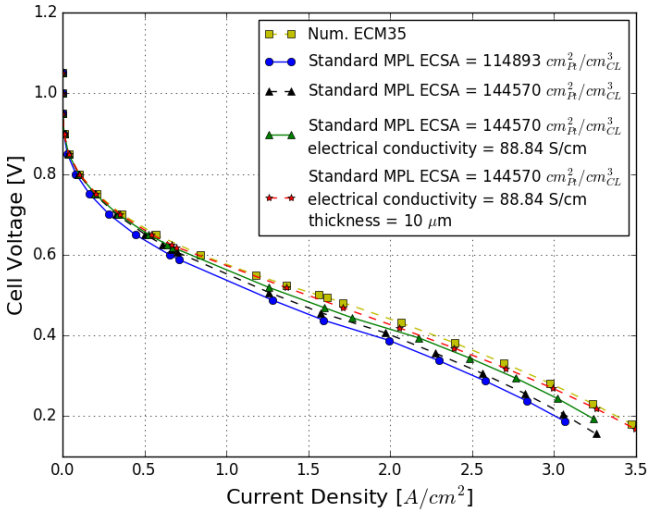

Figure 5.4 – Polarization curves for the effect of each parameter in standard MPL on cell performance as compared to ECM35.

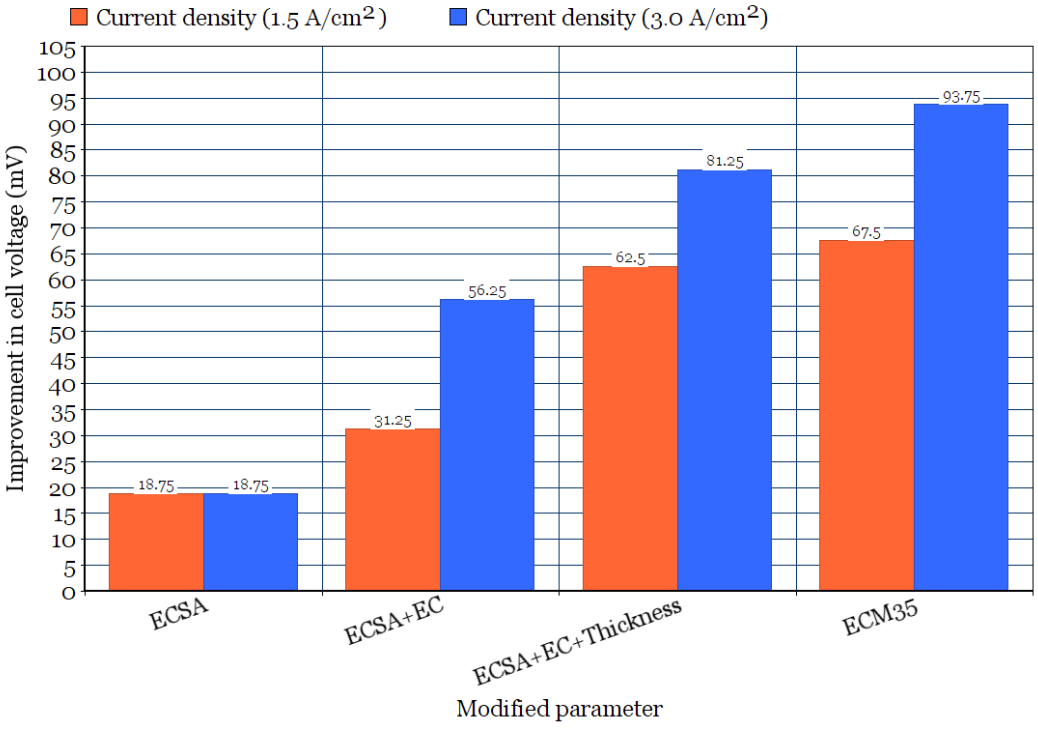

Figure 5.5 – Improvements in cell voltage by modifying parameters in the standard MPL at current densities of 1.5 A/cm^2 and 3.0 A/cm^2, respectively. Note that EC stands for electrical conductivity.

Under the warmup condition, at high current density, the standard MEA shows better performance than ECMs due to improved water rejection. Figure 5.6 shows the saturation distributions in the cathode MPL and CL for three MPLs. Due to higher hydrophilic percentage, the saturation is higher in the MPL for ECMs which leads to more mass transport losses. The increase in saturation in the cathode CL for ECMs is due to lower temperature as shown in 5.7 and lower MPL absolute liquid permeability in ECMs. The former is because the saturation vapor pressure is a function of temperature, as a result, higher temperature in the cathode CL leads to more evaporation. The latter can be explained by the liquid pressure distributions as shown in Figure 5.8. Due to lower absolute liquid permeability in ECMs, higher liquid pressure is required in the cathode CL to move the liquid water from the CL to the MPL, resulting in a gradual decrease in liquid pressure, whereas for standard MPL, less liquid pressure is required which leads to a sharp drop of liquid pressure at the CL/MPL interface.

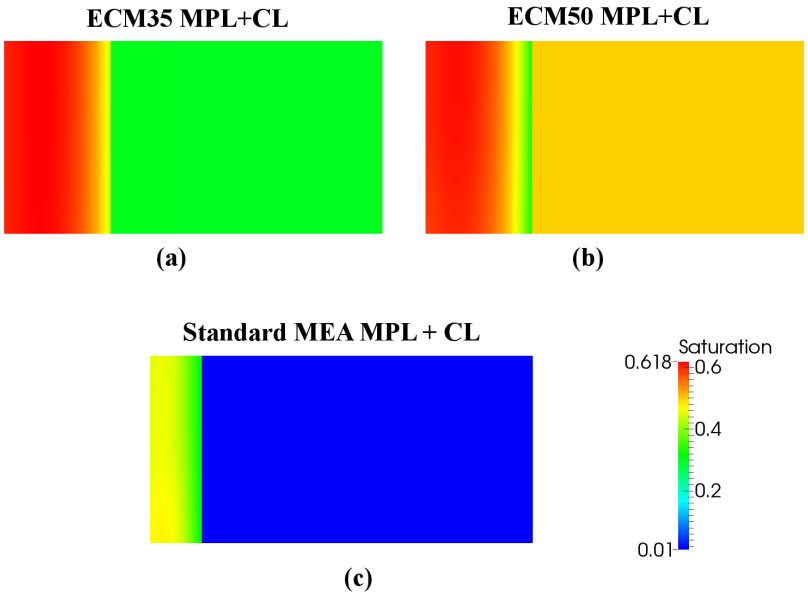

Figure 5.6 – Saturation distributions in the cathode MPL and CL for (a) ECM35, (b) ECM50 and, (c) standard MEA, at 0.7 A/cm^2.

As a result of saturation distributions, more oxygen is observed at high current density for standard MPL as shown in Figure 5.9. Figure 5.9 shows

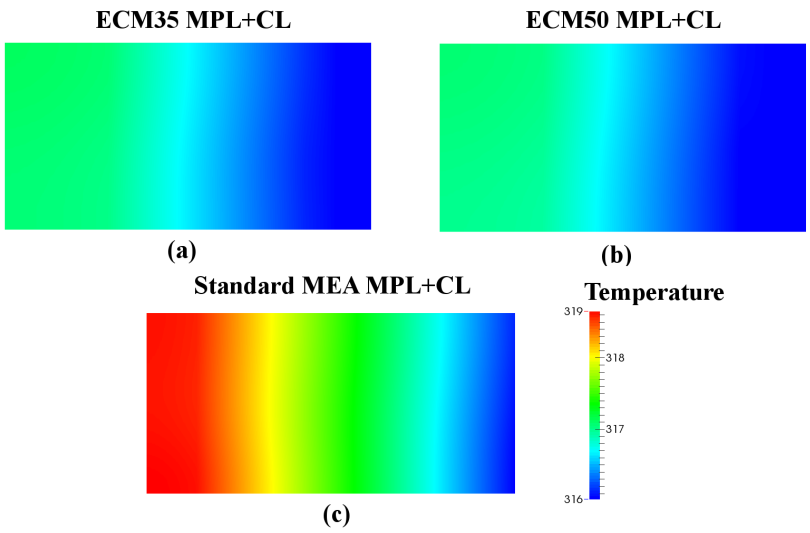

Figure 5.7 – Temperature distributions in the cathode MPL and CL for (a) ECM35, (b) ECM50 and, (c) standard MEA, at 0.7 A/cm^2.

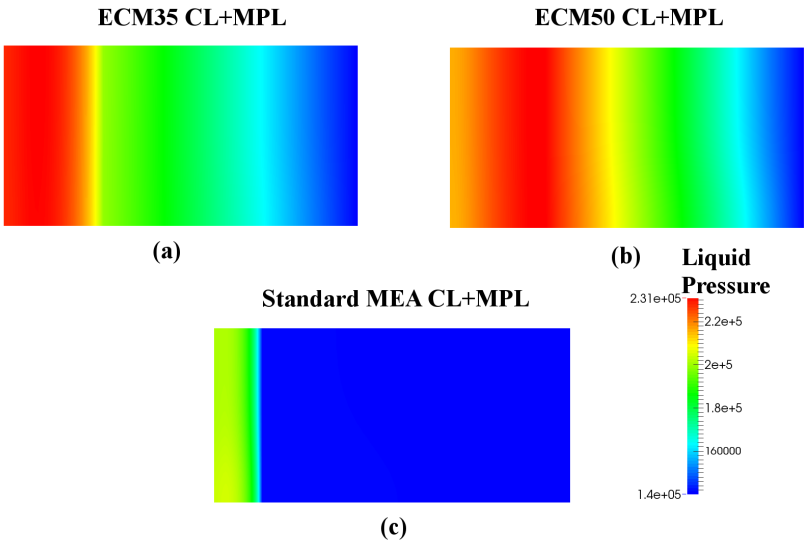

Figure 5.8 – Liquid pressure distributions in the cathode MPL and CL for (a) ECM35, (b) ECM50 and, (c) standard MEA, at 0.7 A/cm^2.

the oxygen molar fraction distributions in the cathode MPL and CL for three MPLs. The least amount of oxygen molar fraction is observed for ECM50.

Figure 5.10 shows the water balance for the three cells. The normalized water flux reported in the figure is defined as,

$$\beta = \frac{2F}{j}\frac{N_{\mathrm{H2O}}}{M_{\mathrm{H2O}}} \tag{5.1}$$

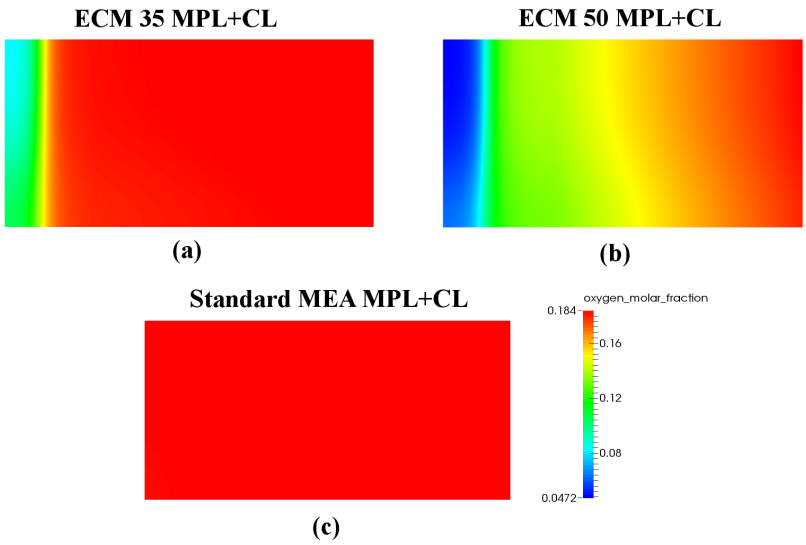

Figure 5.9 – Oxygen molar fraction distributions in the cathode MPL and CL for (a) ECM35, (b) ECM50 and, (c) standard MEA, at 0.7 A/cm^2.

where N_{H2O} is the water flux evaluated at the boundary in g/(cm$^2 \cdot s$), F is Faraday's constant, j is the current density and M_{H2O} is the water molar mass.

Figure 5.10 (a) shows that at high current density, less liquid water is leaving the cathode boundary in the standard MEA as compared to ECM35 at high current density leading to less accumulated water for standard MPL.

Figure 5.10 (b) shows the membrane water transport and water vapor leaving at the cathode boundary. For membrane water transport, since the anode RH is higher than cathode, more water is transported from anode to cathode (negative flux is anode to cathode) resulting in more water vapor leaving at the cathode boundary.

5.3.2 Parametric study ECM35

Since the performance of ECM35 is better than ECM50 under warmup condition and they are almost identical under normal condition, optimizing the layer design of ECM35 offers more potential to achieve higher performance. A parametric study is carried out to examine the effect of ECM35 porosity, thickness, thermal conductivity, electrical conductivity, hydrophilic percentage, and PSD parameters in order to provide guidance in layer design.

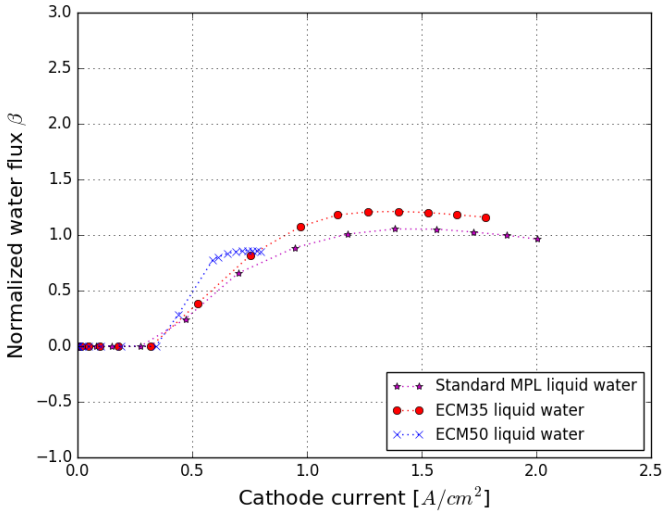

(a)

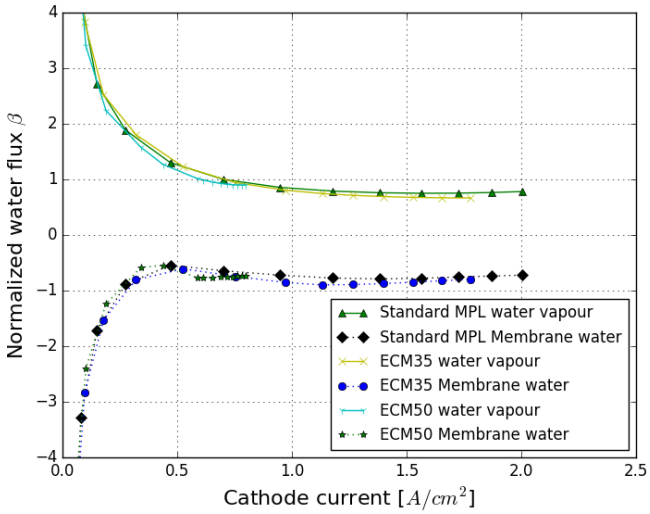

(b)

Figure 5.10 – Water balance: (a) liquid water leaving the cathode boundary, (b) membrane water transport (negative flux is anode to cathode) and water vapor leaving the cathode boundary, for ECM35, ECM50, and standard MPL under warmup condition.

5.3.2.1 Effect of porosity

The effect of porosity on performance under normal and warmup conditions are shown in Figure 5.11. The results show that a decrease in performance is observed when porosity is smaller than 0.78, especially under warmup condi-

tion. Also, when the porosity is higher than 0.78, there is no performance gain in increasing the porosity. It can be concluded from the figure that an optimal porosity, in this case 0.78, exists that results in better performance under both conditions. The optimal porosity will depend on the MPL geometry and properties.

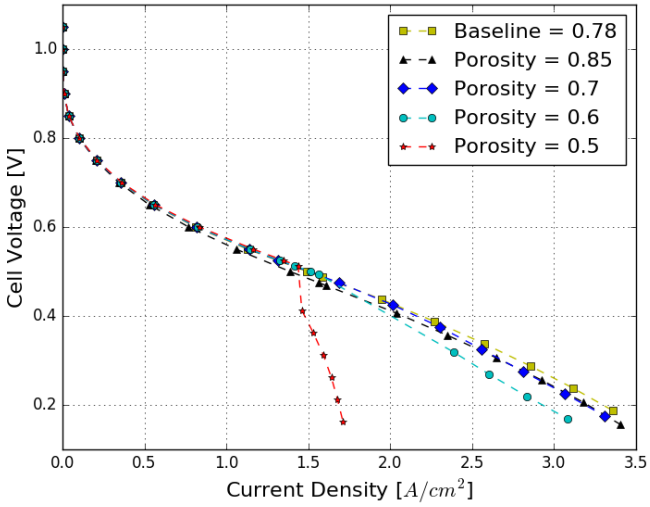

(a)

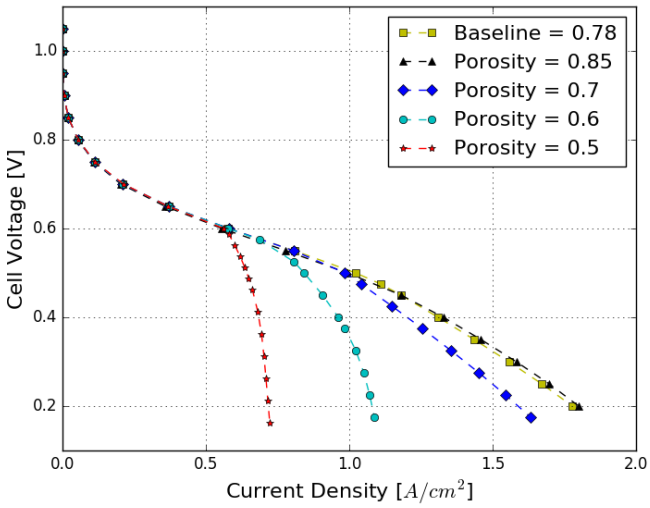

(b)

Figure 5.11 – Polarization curves at (a) normal and (b) warmup conditions for varying porosity.

5.3.2.2 Effect of electrical conductivity

Figure 5.12 shows that the cell performance is insensitive to the MPL electrical conductivity as long as it is higher than 5 S/cm. When the electrical conductivity is smaller than 5 S/cm, reducing the electrical conductivity in the MPL leads to a reduction in cell performance as shown in Figure 5.12.

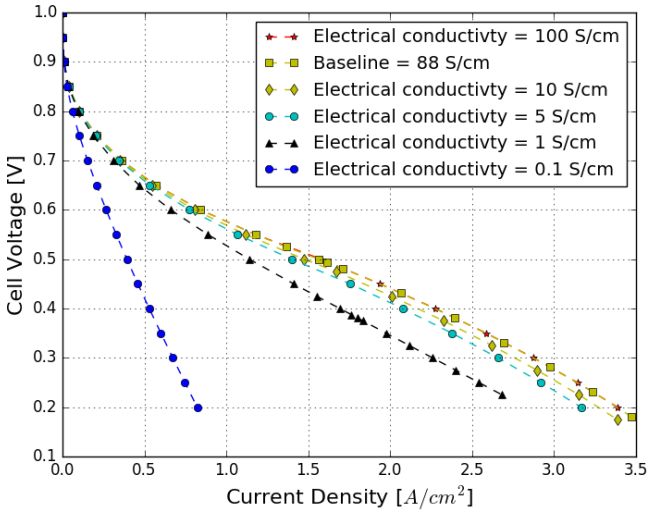

(a)

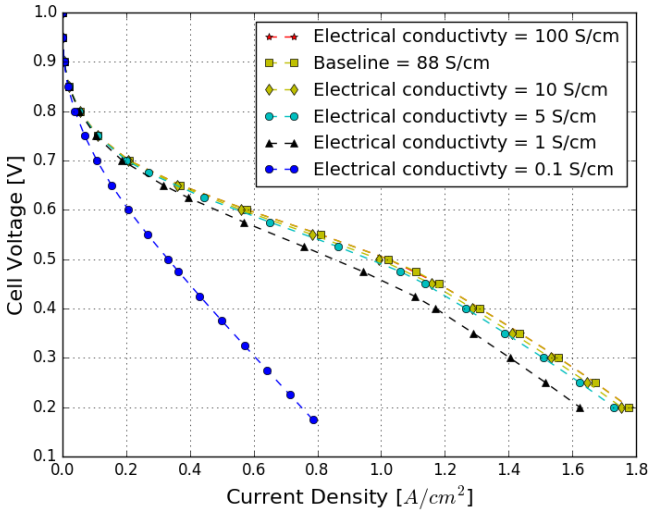

(b)

Figure 5.12 – Polarization curves at (a) normal condition and (b) warmup condition at varying electrical conductivity.

5.3.2.3 Effect of thermal conductivity

The effect of cathode MPL thermal conductivity on cell performance under normal and warmup conditions is shown in Figure 5.13.

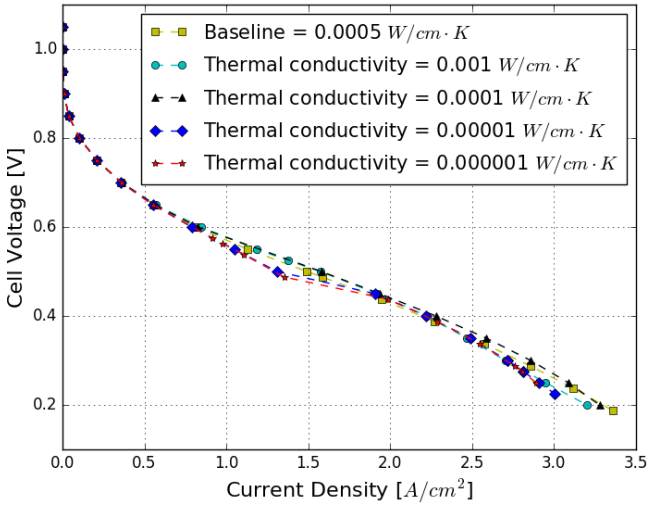

(a)

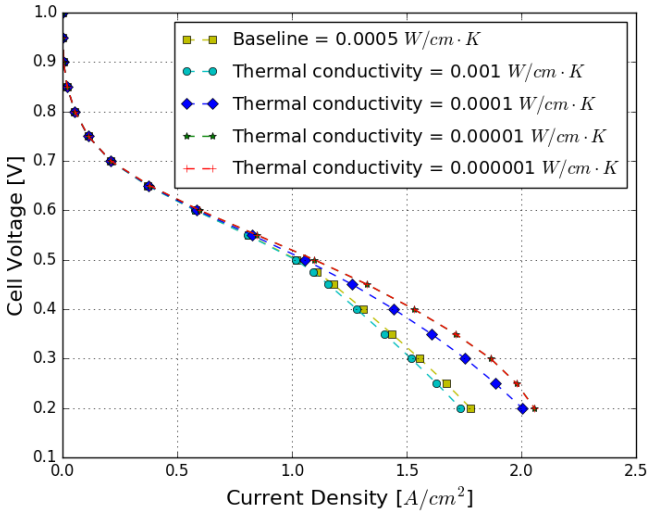

(b)

Figure 5.13 – Polarization curves at (a) normal condition and (b) warmup condition at varying thermal conductivity.

Under normal condition, there is an insignificant impact of thermal conductivity. Under warmup conditions, the figure shows that the best performance is achieved with a low thermal conductivity. This is because higher temperature

leads to more evaporation in the electrode which alleviates the water accumulation as discussed in [103]. A thermal conductivity of 0.0001 W/(cm · K) leads to a performance similar to that of the standard MPL but with a thinner layer. Further improvements in performance are observed at k = 0.00001 W/(cm · K), however, no performance gain is observed for the thermal conductivity below 0.00001 W/(cm · K) (identical performance is observed between k = 0.00001 W/(cm · K) and k = 0.000001 W/(cm · K).

Membrane dryout is not observed either in normal or warmup conditions even with very low thermal conductivity. This is different from the results of the MPL thermal conductivity parametric study in Chapter 4. The reason for the difference is because in this case the anode MPL thermal conductivity is kept constant. Figure 5.14 shows the temperature distributions in the MEA for two different thermal conductivities at 2.0 A/cm^2 under warmup condition. It can seen from the figure that as the cathode MPL thermal conductivity decreases, more temperature is accumulated in the anode, and the change in cathode temperature is small. This indicates that the heat is released from anode due to high thermal conductivity in the anode.

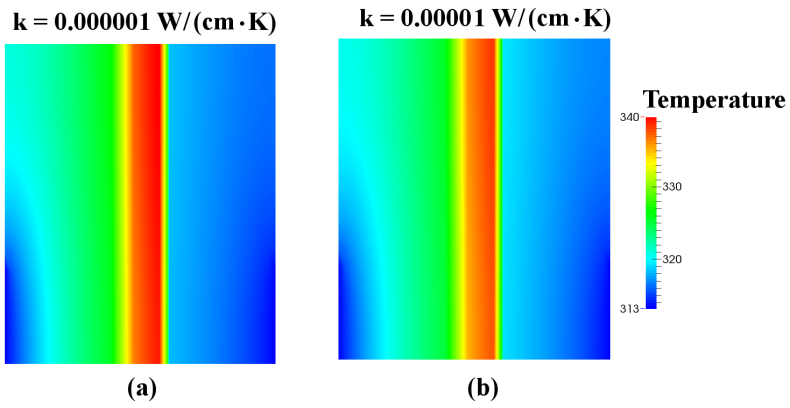

Figure 5.14 – Temperature distributions in the MEA for (a) k = 0.000001 W/(cm·K) and (b) k = 0.00001 W/(cm·K) under warmup condition at 2.0 A/cm^2.

The higher temperature at the anode results in lower membrane water content as shown in Figure 5.15. However, the change in the membrane water content is insignificant as the temperature difference between the two cases is

about 2° C. This indicates that the cell performance is less sensitive to anode hydration as compared to cathode flooding.

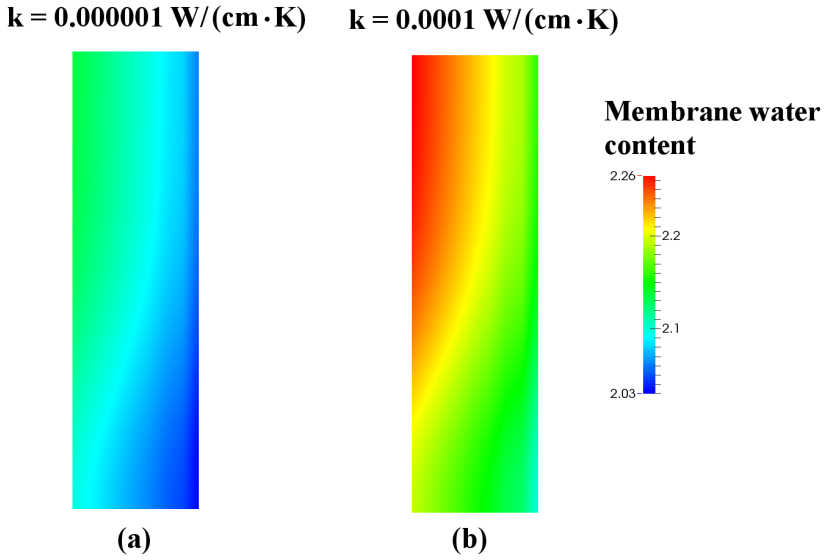

Figure 5.15 – Membrane water content distributions in the anode CL for (a) $k = 0.00001$ W/(cm · K) and (b) $k = 0.0001$ W/(cm · K) under warmup condition at 2.0 A/cm^2.

Similar results are observed under the normal condition as shown in Figure 5.16 and 5.17. The figure shows that as the thermal conductivity is smaller than 0.0001 W/(cm · K), most of the heat is released at the anode, therefore, the increase in temperature is small. Since the cell performance is insensitive to anode hydration as discussed above, the change in membrane water content is insignificant as shown in Figure 5.17.

Reducing the thermal conductivity results in better performance, however, in most materials the electrical conductivity will also decrease with thermal conductivity which might decrease the performance. In designing the optimal ECM, the trade-off between thermal conductivity and electrical conductivity needs to be considered.

5.3.2.4 Effect of thickness

The effect of MPL thickness on performance under normal and warmup conditions is shown in Figure 5.18. The results show that a thinner MPL leads to better performance.

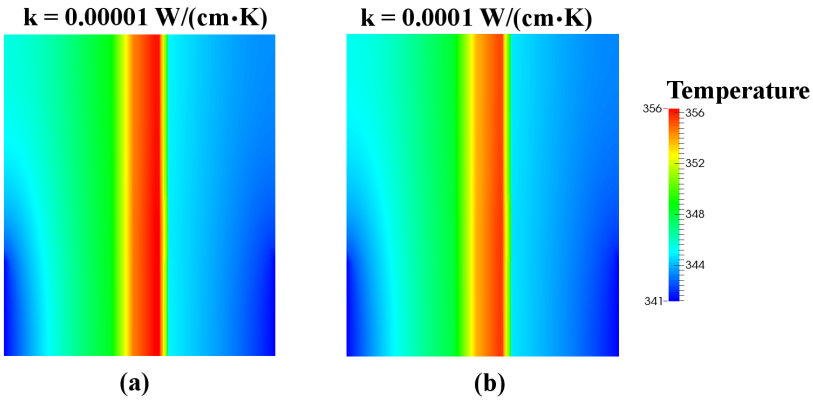

Figure 5.16 – Temperature distributions in the MEA for (a) $k = 0.00001$ W/(cm · K) and (b) $k = 0.0001$ W/(cm · K) under normal condition at 2.0 A/cm^2.

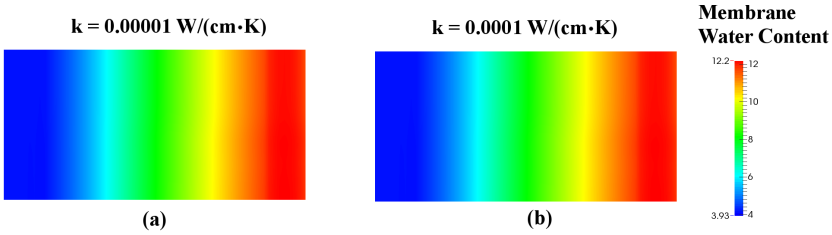

Figure 5.17 – Membrane water content distributions in the CCM for (a) $k = 0.00001$ W/(cm · K) and (b) $k = 0.0001$ W/(cm · K) under normal condition at 2.0 A/cm^2.

The reason for the reduced performance with a thicker CL is due to higher liquid water transport resistance requiring higher liquid pressure to push liquid water through the MPL as shown in Figure 5.19. Unlike the standard MPL, the PSD in the ECM is much smaller and its absolute liquid permeability is about five orders of magnitude lower than the standard MPL. Therefore, increasing the ECM thickness will greatly affect its liquid water transport resistance.

Figure 5.19 shows that liquid water pressure is higher in the cathode CL for the MPL thickness of 20 μm as compared to 1 μm. The higher liquid water pressure results in higher saturation distributions in the cathode CL (see Figure 5.20). Due to the higher saturation, the amount of oxygen is greatly reduced in the cathode CL as shown in Figure 5.21.

Increasing the MPL thickness leads to higher thermal resistance which leads to higher CL evaporation as discussed by Zhou et al. [103]. The temperature

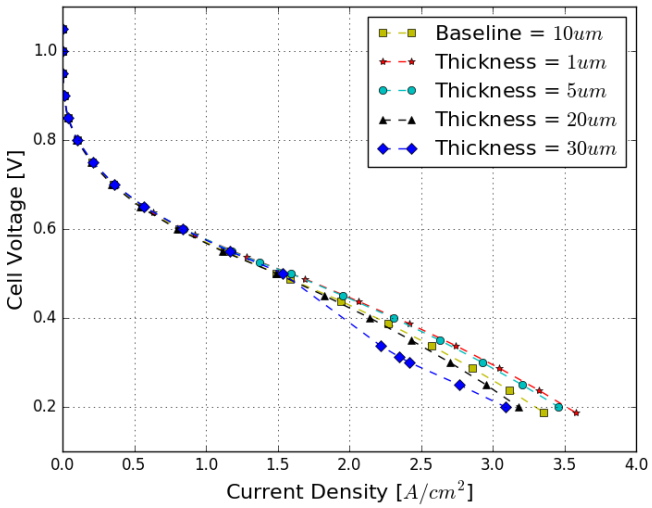

(a)

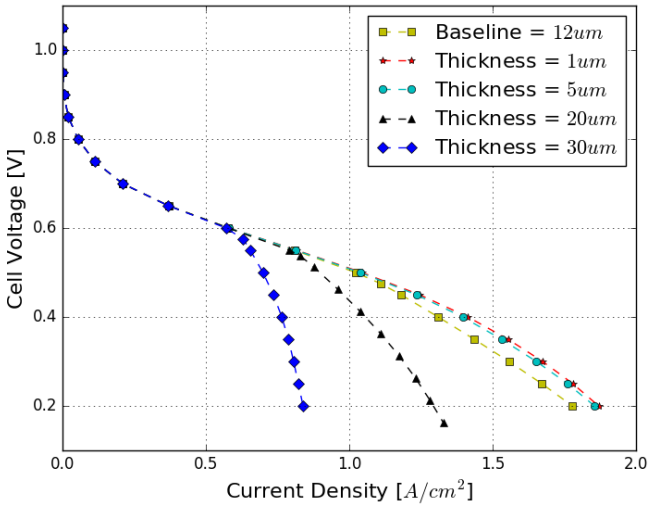

(b)

Figure 5.18 – Polarization curves at (a) normal condition and (b) warmup condition at varying thickness.

distributions in the cathode CL and MPL for 1 μm and 20 μm CL are shown in Figure 5.22. It can be seen from the figure that the temperature has increased by about 1° C with the thicker MPL; however, when operating at 40° C, the effect the temperature on saturation vapor pressure is insignificant. Therefore, the MPL absolute liquid permeability has a greater impact on saturation as compared to the thermal conductivity.

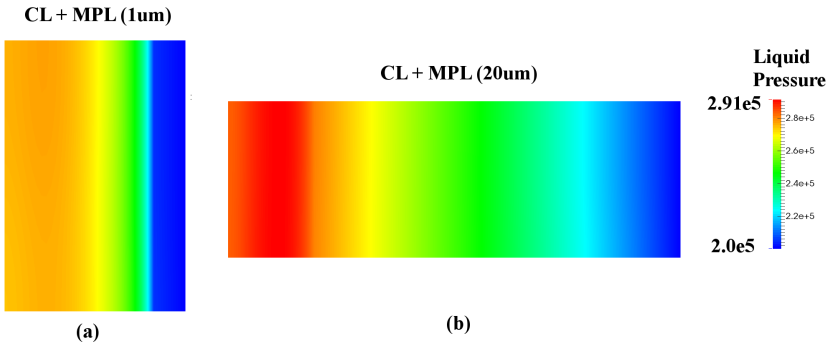

Figure 5.19 – Liquid water pressure distributions in the cathode CL and MPL for (a) 1 μm and (b) 20 μm at 1.0 A/cm^2 under warmup condition.

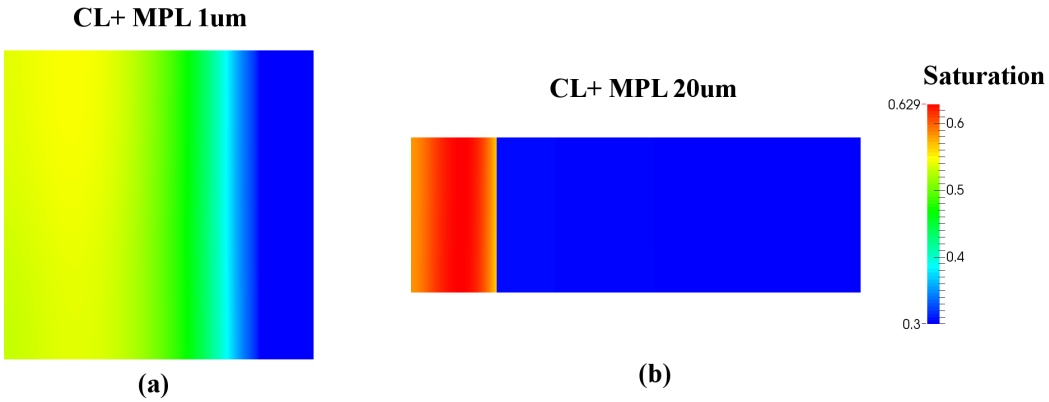

Figure 5.20 – Saturation distributions in the cathode CL and MPL for (a) 1 μm and (b) 20 μm at 1.0 A/cm^2 under warmup condition.

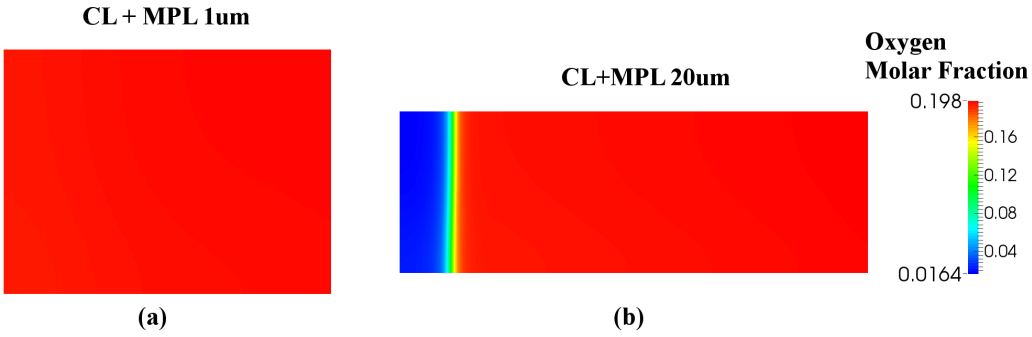

Figure 5.21 – Oxygen molar fraction distributions in the cathode CL and MPL for (a) 1 μm and (b) 20 μm at 1.0 A/cm^2 under warmup condition.

5.3.2.5 Effect of hydrophilicity

The effect of MPL hydrophilicity on cell performance under normal and warmup conditions is shown in Figure 5.23. In the simulation, the global PSD remains

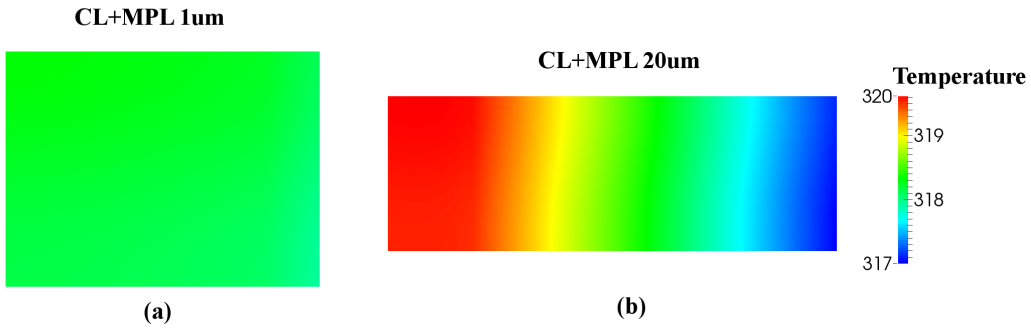

Figure 5.22 – Temperature distributions in the cathode CL and MPL for (a) 1 μm and (b) 20 μm at 1.0 A/cm^2 under warmup condition.

the same, the change of hydrophilic PSD is shown in Figure 5.24 and a uniform distribution of hydrophilic PSD over the global PSD is assumed. The hydrophobic PSD is obtained by subtracting hydrophilic PSD from the global PSD. Figure 5.23 shows that the hydrophilic percentage has little effect on performance under normal conditions.

When the MEA is operating at warmup conditions, the best performance is achieved with 40% hydrophilic percentage. With 80% hydrophilic percentage, the mass transport losses in the MPL greatly reduce performance as the hydrophilic pores are filled by liquid water. In the case of 15% hydrophilic percentage, the reduced performance is due to insufficient evaporation caused by the reduced liquid-gas interfacial surface area as less pores are filled by liquid water which has been discussed in [103].

5.3.2.6 Effect of MPL PSD

The parameters to define the log-normal PSD distribution, i.e., characteristic pore radius r_k and standard deviation s_k, are studied in this section.

Effect of characteristic pore radius $\mathbf{r_k}$ - The cell performance at varying MPL PSDs for different r_k are shown in Figure 5.25 and the MPL PSDs are shown in Figure 5.26. The improvements in performance are observed with the increase in MPL PSD until the MPL PSD is two times larger than the baseline PSD. The increase in performance is greater at warmup conditions as compared to normal conditions.

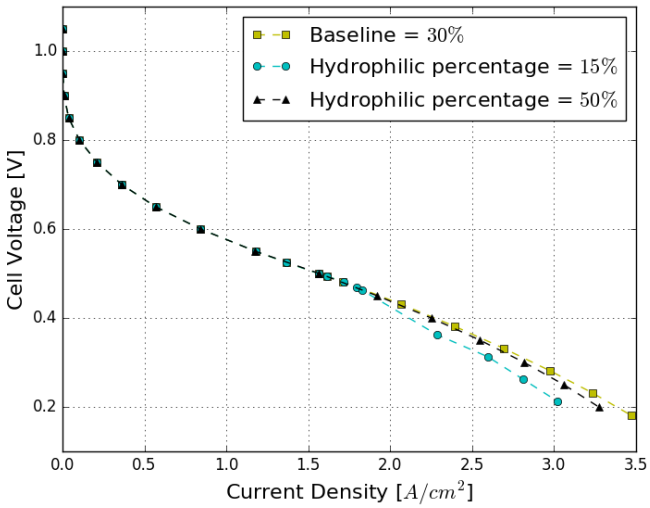

(a)

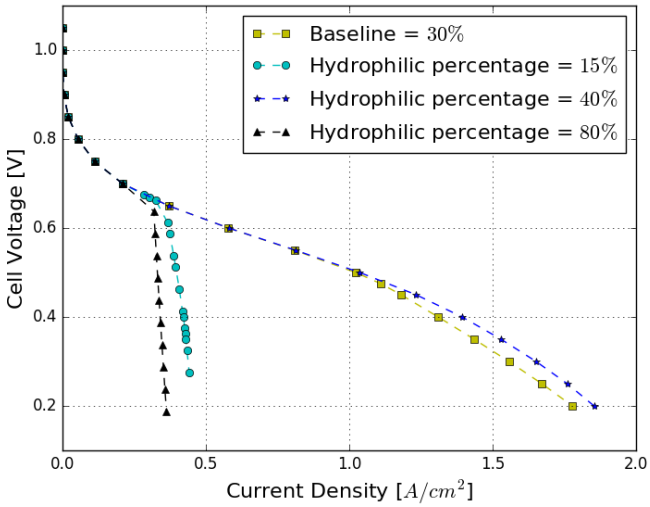

(b)

Figure 5.23 – Polarization curves at (a) normal condition and (b) warmup condition at varying hydrophilic percentage.

The reason for the improved performance is because the bigger MPL PSD results in higher absolute liquid permeability which requires higher liquid pressure for liquid water to travel through the MPL as shown in Figure 5.27. The increase in liquid pressure results in higher saturation in the cathode CL (see Figure 5.28) leading to more mass transport losses.

Effect of PSD standard deviation s_k - Figure 5.29 shows the PSDs at

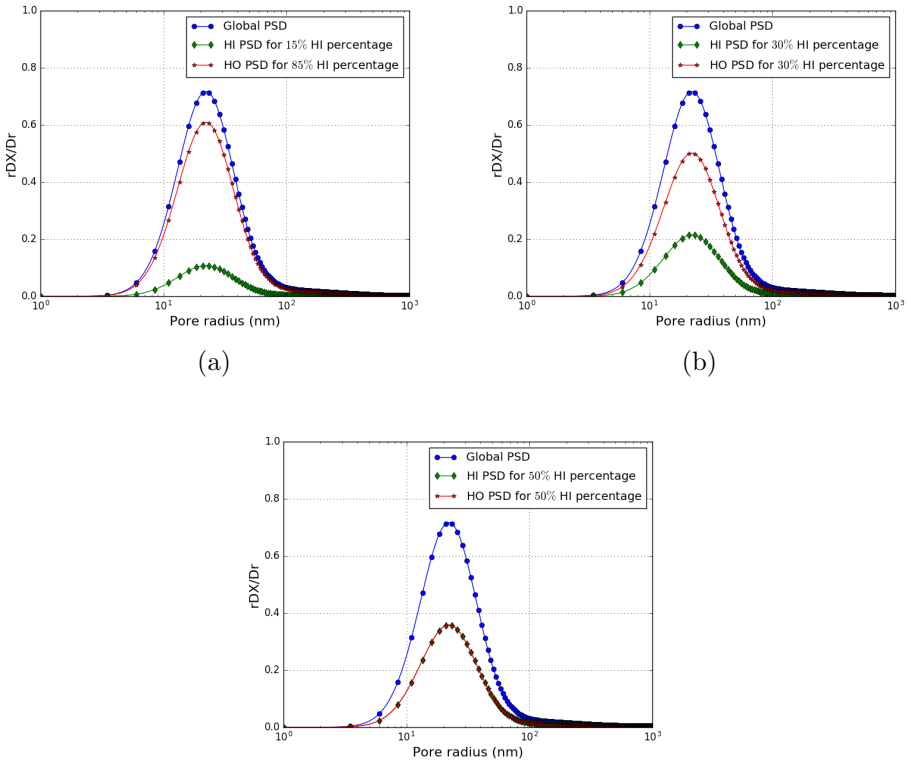

Figure 5.24 – The change in hydrophilic PSD at varying hydrophilic percentage: (a) 15% hydrophilic (HI), (b) 30% and (c) 50%.

varying s_k, and it can be seen from the figure that the PSD is more concentrated in a narrow pore size range with a low s_k, whereas for larger s_k, the PSD is widely spread.

The effect of s_k on cell performance is shown in Figure 5.30. A better performance is observed with a narrower PSD range. This can be explained by capillary pressure vs. saturation curve as shown in Figure 5.31. The figure shows that to reach the same saturation, a higher capillary pressure is required for lower s_k when the saturation is under about 65%. In most of the cases, the saturation in MPL is under 60%; therefore, less saturation is observed in the MPL with lower s_k as shown in Figure 5.32.

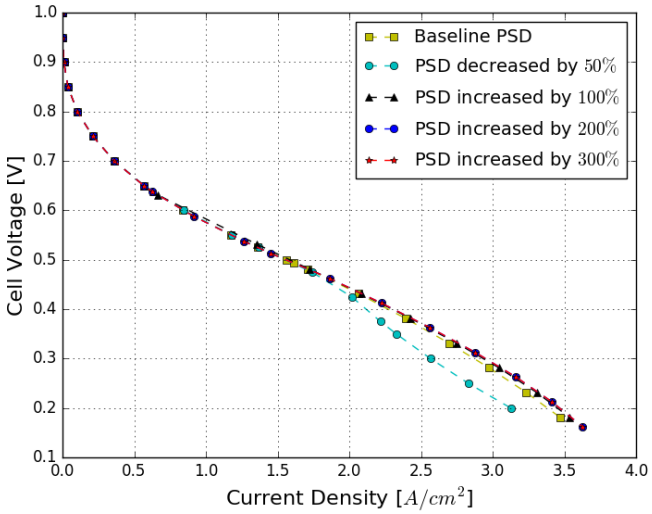

(a)

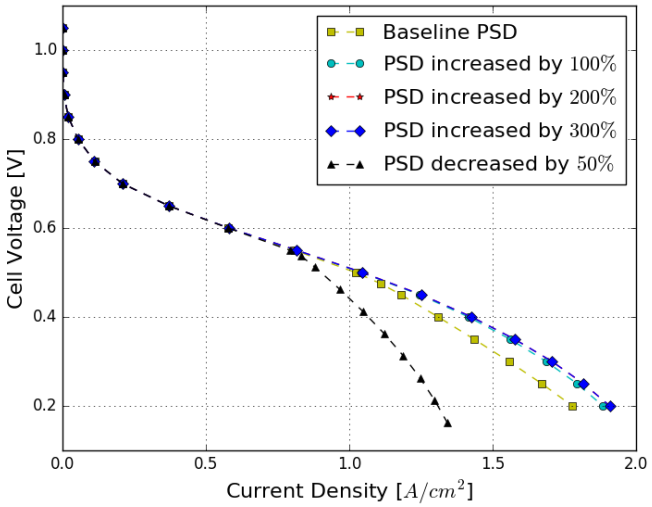

(b)

Figure 5.25 – Polarization curves at (a) normal condition and (b) warmup condition at varying PSD.

5.3.2.7 Optimal ECM35

Based on the parametric studies, an ECM with a porosity 0.78, thickness of 1 μm, thermal conductivity of $k = 0.00001$ W/(cm $\cdot$ K), electrical conductivity of 88 S/cm, 40% hydrophilic percentage, and increased PSD r_k by 200% and $s_k/2$, should offer the best performance. Figure 5.33 shows the performance gain of the improved ECM. No major improvement is observed under normal

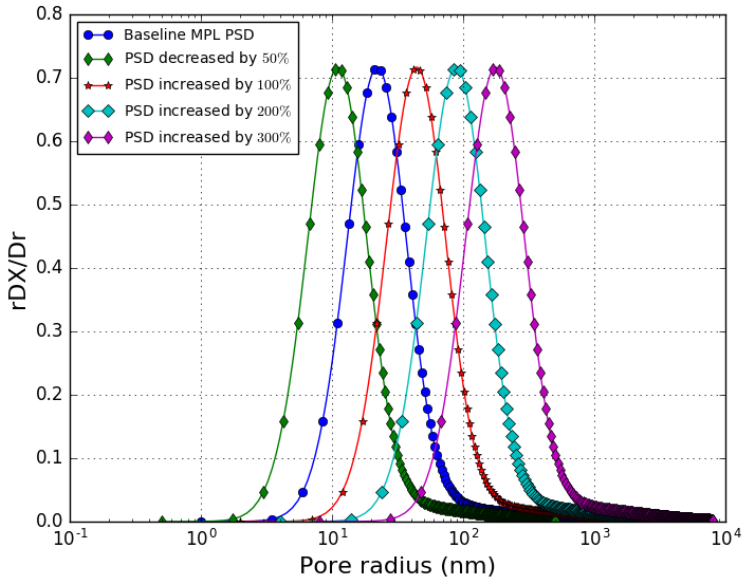

Figure 5.26 – PSDs for varying r_k.

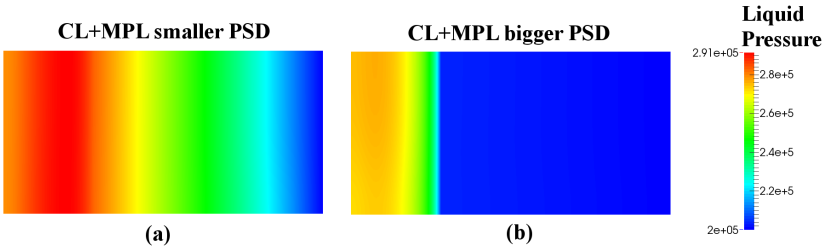

Figure 5.27 – Liquid pressure distributions in the cathode CL and MPL (a) PSD decreased by 50%, (b) PSD increased by 200% under warmup condition at 1 A/cm^2.

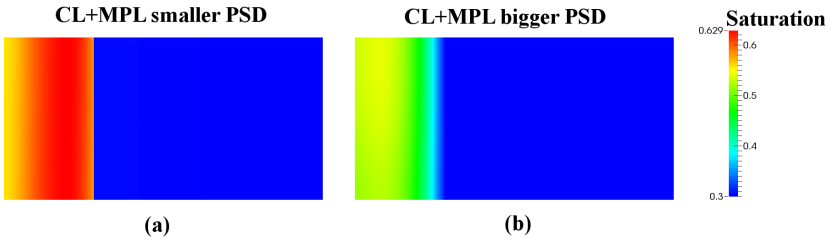

Figure 5.28 – Saturation distributions in the cathode CL and MPL (a) PSD decreased by 50%, (b) PSD increased by 200% under warmup condition at 1 A/cm^2.

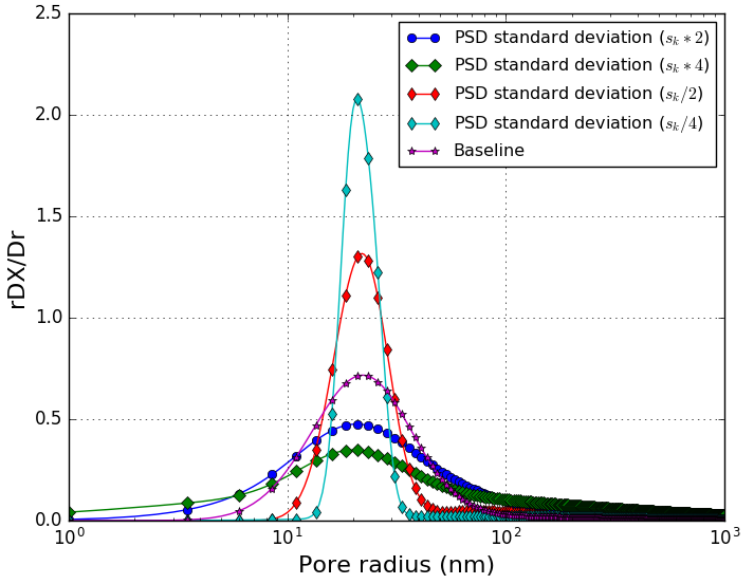

Figure 5.29 – PSDs for varying s_k.

condition; under warmup condition, however, the improved ECM shows better performance as compared to baseline ECM35 and a conventional MPL. The performance gain is about 30% at maximum current density.

5.3.2.8 Performance gain using an optimal MPL

In order to understand the performance gain after using an MPL, the performance of ECMs and standard MPL are compared to the cell without MPLs. Figure 5.34 shows the polarization curves under normal and warmup conditions. The cell without MPLs show better performance as compared to standard MPL and lower performance against ECMs under normal condition. Under warmup condition, performance of ECMs and standard MPL show better performance than the cell without MPLs, except the ECM50.

The reduced performance for the cell without MPLs as compared to ECMs is due to membrane ohmic losses under normal condition. Figure 5.35 shows the CCM membrane water content distributions for the cell without MPLs and ECM35 at 2 A/cm^2. A better hydrated cathode CL is observed for ECM35 as compared to the cell without MPLs. This is due to the higher temperature for ECM35 as shown in Figure 5.36. As a result, the water uptake in the cathode

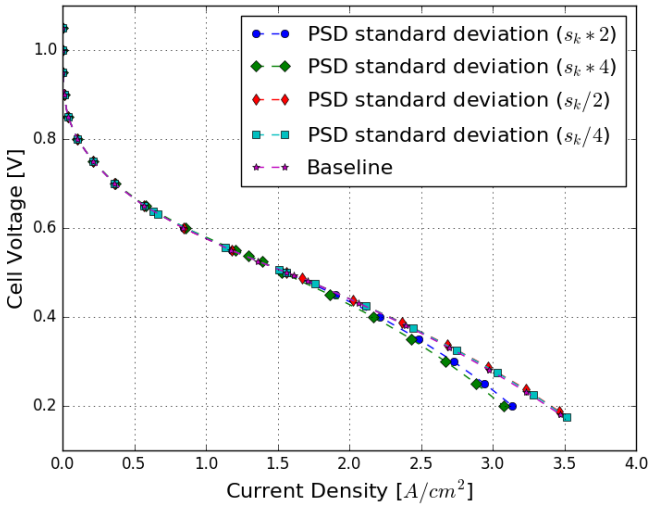

(a)

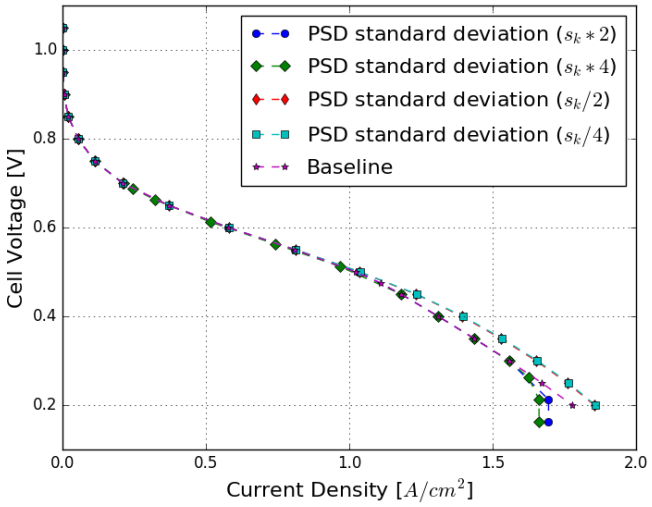

(b)

Figure 5.30 – Polarization curves at (a) normal condition and (b) warmup condition at varying s_k.

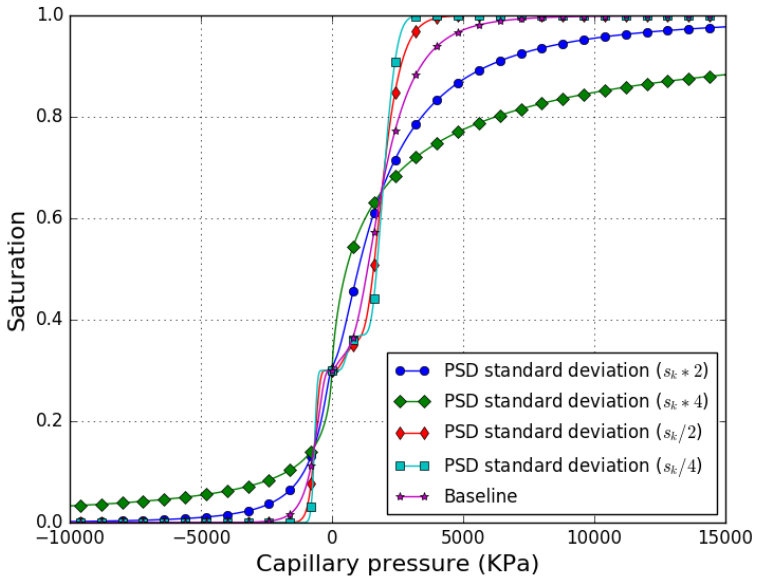

Figure 5.31 – Capillary pressure vs. saturation curves for varying s_k.

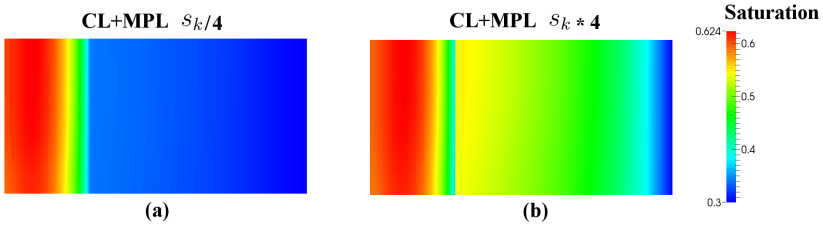

Figure 5.32 – Saturation distributions in the cathode CL and MPL for (a) $s_k/4$ and (b) $s_k * 4$ at 1.5 A/cm^2 under warmup condition.

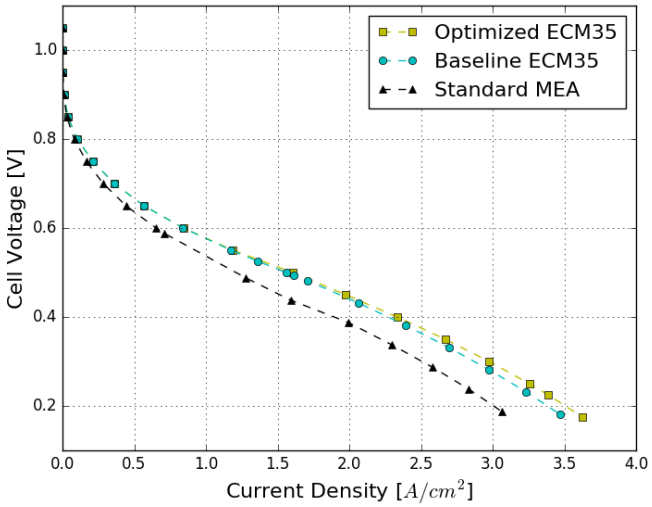

(a)

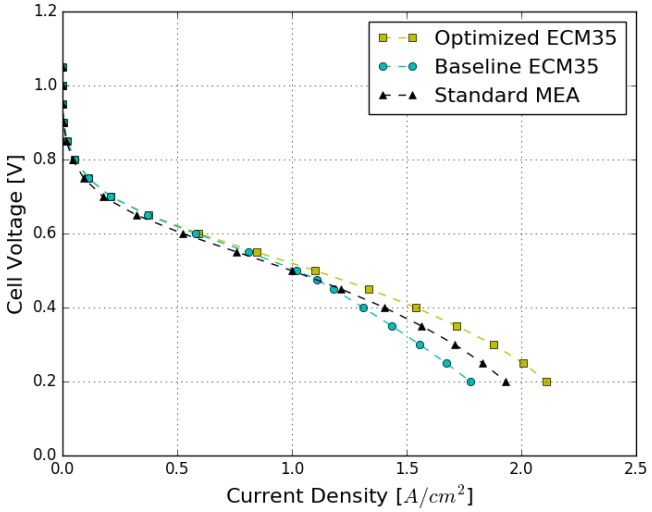

(b)

Figure 5.33 – Optimized ECM35 performance (a) normal condition, and (b) warmup condition.

CL is improved which leads to better proton transport in the cathode CL as shown in Figure 5.37.

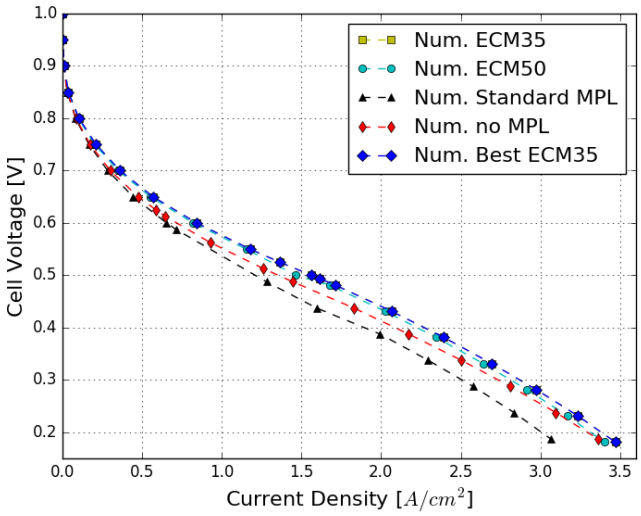

(a)

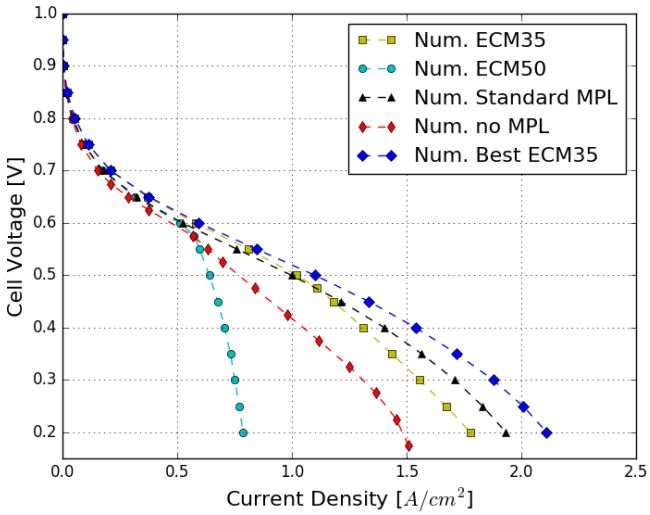

(b)

Figure 5.34 – Polarization curves at (a) normal condition, and (b) warmup condition.

The reasons for the improved performance after adding an MPL under warmup condition are due to better evaporation, enhanced back diffusion and improved in-plane diffusion as discussed in our previous publication [103]. Figure 5.38 shows the temperature and saturation distributions for the cell with-

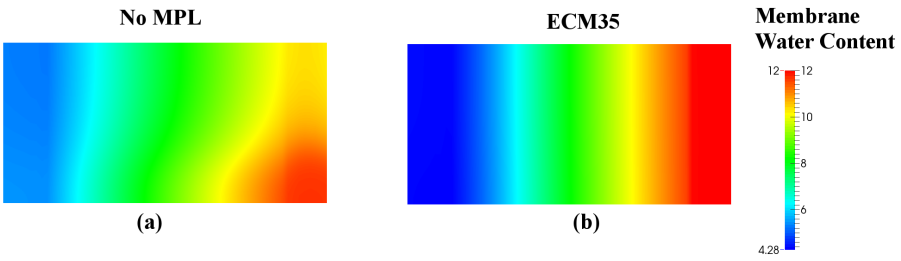

Figure 5.35 – Membrane water content distributions in the CCM (a) no MPL and (b) ECM35 at 2 A/cm^2 under normal condition.

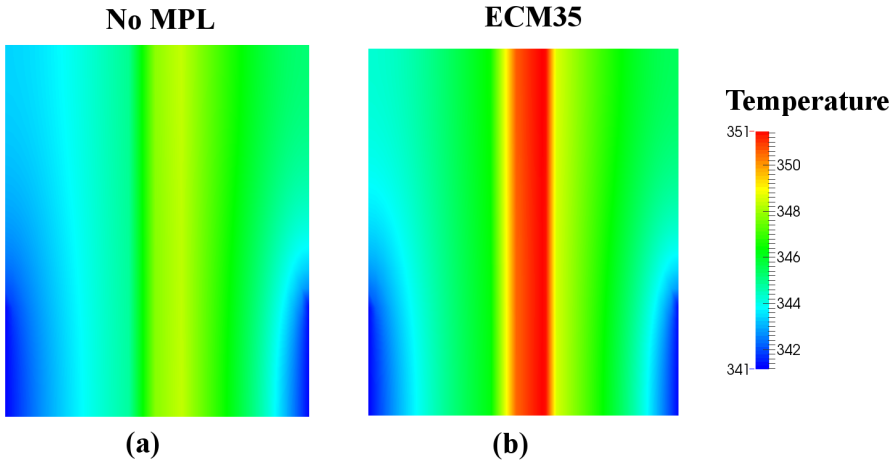

Figure 5.36 – Temperature distributions in the MEA (a) no MPL and (b) ECM35 at 2 A/cm^2 under normal condition.

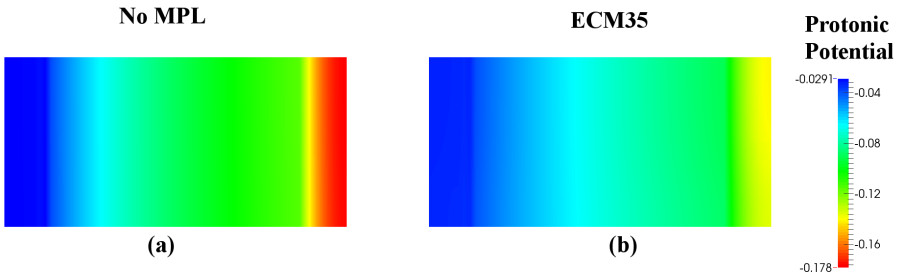

Figure 5.37 – Protonic potential distributions in the CCM (a) no MPL and (b) ECM35 at 2 A/cm^2 under normal condition.

out MPLs at 0.7 A/cm^2. As compared to the temperature distributions in Figure 5.7 and saturation distributions in Figure 5.6 for the cell with MPLs, the temperature is about 2° C lower and saturation is higher for the cell without MPLs. The performance drop of ECM50 as compared to the cell without MPLs is due to higher MPL hydrophilic percentage which increases the mass

transport losses in the MPL.

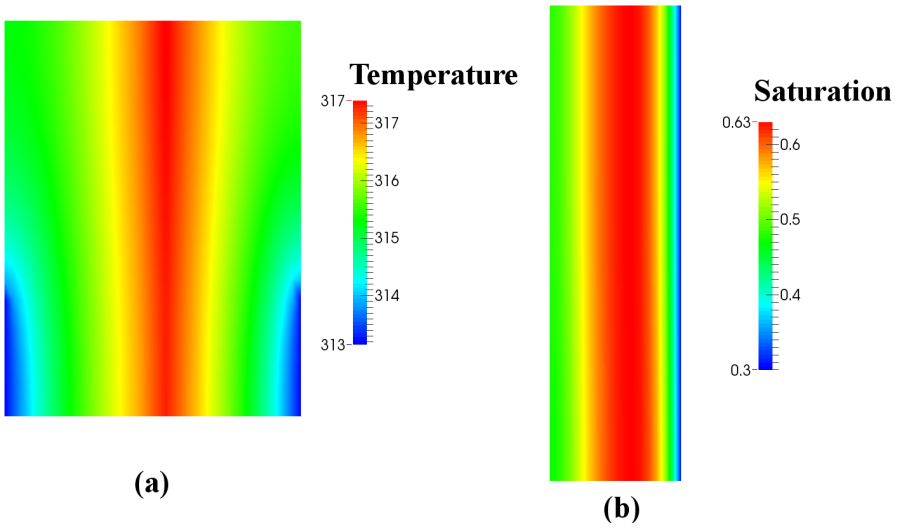

Figure 5.38 – Distributions of (a) temperature in MEA and (b) saturation in the cathode CL for the cell without MPLs at 0.7 A/cm^2.

5.4 Conclusion

A study on a new electrode architecture design that combines CCM and MPL into the same assembly to achieve a much thinner MPL was performed. ECM35 and ECM50 electrodes have demonstrated better performance under normal condition. The reasons for the improved performance for ECM35 and ECM50 under normal condition are higher active area, less ohmic losses, reduced mass transport distance, and better hydrated membrane. The reduced ohmic and mass transport losses, in this case, are the main contributions to the improved performance.

At warmup condition, the conventional MPL shows better performance due to less mass transport losses with reduced water accumulation. The reduced performance under warmup condition for ECMs is due to insufficient evaporation on the electrode, higher saturation in the CL, and higher mass transport losses. The first is due to reduced thickness, however, increasing the thickness of ECM will not improve performance as the absolute liquid permeability has greater impact than the thermal conductivity for ECMs. The second can be

attributed to lower absolute liquid permeability in the MPL for ECMs which requires higher capillary pressure in the CL in order to reject the liquid water. The last is due to the increased hydrophilicity as the hydrophilic pores are filled by liquid water when two-phase flow is present.

No significant improvement is observed by performing a parametric study under normal condition. Under warmup condition, the parametric study for ECM35 suggests,

1. High porosity, in our case about 80%.

2. Electrical conductivity higher than 5 S/cm.

3. A low MPL thermal conductivity ($k = 10^{-5}$ W/(cm $\cdot$ K)), to alleviate cathode water accumulation by evaporation; however, the coupling to the electrical conductivity should also be considered.

4. A thin MPL, lower than 5 μm, to reduce liquid water transport resistance.

5. An intermediate amount of hydrophilic pores of the order of 40% is desired to provide enough interfacial surface area for evaporation and not too high to avoid additional mass transport losses.

6. A large PSD (twice as big as the baseline PSD) and narrow distribution ($s_k/2$) in order to avoid additional liquid water buildup in the cathode CL.

Note that the reason for studying electrical conductivity is because it is coupled with thermal conductivity. Reducing thermal conductivity will benefit the performance; however, the electrical conductivity should not be lower than 5 S/cm to affect the cell performance. With the optimized ECM35, the performance gain under warmup condition is about 20-30% at high current density and the performance is also better than conventional MPL.

Chapter 6

Conclusion and Future Work

6.1 Conclusions

This thesis focused on analyzing the multi-phase flow behavior in PEMFC by developing a mathematical MEA model that accounts for micro-structural details, two-dimensional, non-isothermal effect, and multi-phase transport. The MEA model accounts for gas transport via molecular and Knudsen diffusion, liquid water transport, membrane water transport in ionomer phase by back-diffusion, electro- and thermo-osmosis, and heat generation and transport. Multi-step kinetic models are used to predict anode and cathode electrochemical reactions. Local transport losses at the ionomer interface are accounted for using an ionomer covered catalyst particle model. The two-phase transport related properties are estimated by means of a PSD model and the input PSD is obtained by MIP. The PSD model is validated using the capillary pressure vs. saturation and saturation vs. relative liquid permeability curves based on PSDs from several GDLs.

The MEA model is validated by comparing to experimentally measured electrochemical performance data under various operating conditions. Water accumulation in the catalyst layer and GDL are also compared to neutron and X-ray imaging data and shown to be in agreement. Water fluxes at cathode and anode boundaries and phase change induced flow are analyzed and compared to experimental data.

After the model validation, the proposed multi-dimensional, non-isothermal, two-phase model has been used to study,

1. the effects of GDL and catalyst layer microstructure and wettability on fuel cell performance,

2. the role of the MPL on water and heat management,

3. a new electrode architecture named the electrode coated membrane.

To understand the effect of GDL and catalyst layer microstructure and wettability on fuel cell performance, simulations were performed. Simulation results indicate that when liquid water is present, reactant transport in the catalyst layer is the key factor limiting fuel cell performance. The impact of catalyst layer and GDL hydrophilic volume fraction, hydrophobic contact angle and PSD on performance were studied. Results suggest that when the fuel cell is operating at high relative humidity, GDL parameters have minimal effect on performance and the optimal catalyst layer should have: (a) a large hydrophobic contact angle; (b) a moderate hydrophilic volume fraction, usually 25%, which provides enough liquid-gas interfacial surface area and does not lead to excessive water accumulation, and (c) a large PSD and small pores in the hydrophilic phase.

To study the role of the MPL in improving PEMFC performance, experiments and simulations were carried out at varying operating conditions. Under dry conditions, the MPL is found to have a minimal effect on cell performance, except for improving ohmic transport and performance stability and repeatability. At fully humidified conditions, results show that having an additional MPL increases the temperature in the MEA, thereby enhancing evaporation in the cathode catalyst layer and alleviating cathode water accumulation by forcing more sorbed water to travel from cathode to anode. For the former, the enhanced evaporation is because vapor saturation pressure increases with temperature, and for the latter, as a result of increased temperature, the anode is drier, therefore creating a higher membrane water content gradient from cathode to anode. A mild improvement in performance is also observed due to the improved in-plane diffusion once an MPL is introduced. The improved in-plane diffusion is because of the hydrophobic nature in MPL. Lastly, a parametric

study was performed and the results show that the MPL thermal conductivity is the most critical parameter to improve fuel cell performance, followed by thickness and hydrophilic percentage. Other microstructural parameters appear to have minimal effect. An optimal thermal conductivity, thickness and hydrophilic percentage exist to achieve higher fuel cell performance under fully humidified conditions.

Lastly, the model has been used to analyze the effect of ECM and provide guidance in layer design. The experiments and model predictions have shown that the ECM electrode demonstrates better performance than the conventional MPL under normal condition, whereas under warmup conditions, the conventional MPL shows better performance. Under normal condition, the reasons for the improvements in fuel cell performance for ECMs are the reduced ohmic losses (main contribution) and increased electrochemically active surface area, whereas under warmup condition, the higher performance observed with the conventional MPL is due to better evaporation in the electrode and less mass transport losses through the MPL. In order to achieve a better ECM design, especially at warmup condition, parametric studies were carried out at normal and warmup conditions. Based on the results of parametric studies, at warmup condition, higher performance could be achieved for ECMs than convectional MPL by modifying its properties such as thickness. The results of the parametric study show that the optimal MPL parameters are: (a) high porosity, about 80%; (b) a electrical conductivity higher than 5 S/cm; (c) a low MPL thermal conductivity ($k = 10^{-5}\ W/(cm \cdot K)$) to improve evaporation; (d) MPL thickness of about 5 μm to avoid additional mass transport loss; (e) a moderate amount of hydrophilic PSD to provide enough interfacial surface area for evaporation; and (f) a large PSD in order to avoid additional liquid water buildup in the cathode CL.

In addition to the aforementioned work, during the PhD work, I have also spent four months at Automotive Fuel Cell Cooperation (AFCC) applying the developed model to industrial problems, I have contributed to study patterned electrodes in [2] and to a book chapter [205].

My contributions to the fuel cell scientific community are as follows,

1. developing and validating a novel, open source, non-isothermal two-phase flow model that accounts for micro-structural information (see [59]),

2. illustrating the effects of CL microstructure and wettability on fuel cell performance (see [102]),

3. analyzing the role of the MPL (see [103]),

4. designing a novel electrode architecture, i.e., the electrode coated membrane.

6.2 Scope of Future Work

In the thesis a new electrode architecture was studied that allows for better control of the MPL structure. In recent years, several other electrode architectures have been proposed in the literature in order to improve the catalyst utilization and durability of fuel cells in order to meet the U.S. Department of Energy (DOE) targets of 2020 [22, 47, 47–55, 89, 90]. Water management is of paramount importance to the performance of these electrode architectures, for example, the ultra-thin electrodes developed by 3M, the nano-structured thin-film (NSTF), have shown promising performance operating under dry condition, however, the water management of NSTF is still an issue that needs to be addressed. New electrode architectures that could potentially improve fuel cell performance are: (a) functionality graded electrodes [47–49], (b) patterned electrodes/PEM [22, 50–55], and (c) ultra-thin electrodes [89, 90]. The developed multi-dimensional, non-isothermal, two-phase model can be used to study the change in transport processes after introducing the new electrode architectures, and provide guidance in wettability and microstructural design for these electrodes.

Among the new electrode architectures, patterned electrodes [22, 50–55] have shown great improvements in MEA performance. For example, Koh et al. [54] reported a remarkable performance increase (59% increase in current density under fully humidified condition) with a micropatterned PEM with a width $\times$ gap dimension of 3×5 μm. A similar performance increase was also

observed by Zhou et al. [51] with patterned PEM. The line patterned PEM introduced by Bea et al. [53] showed a maximum 30% increase in current density with 1 μm pattern space, however, with a smaller pattern space of 70 nm, the performance decreases. The above researchers [51, 53, 54] have attributed the improved performance to the increased electrochemical active area and a better reactant transport. However, the physical transport processes in the MEA can not be well studied by the experiments due to the limited resolution. Thereby, the developed two-phase model in this thesis can be used to study the physical transport processes taking place in the above mentioned electrodes. As compared to the experiments, the model also provides good flexibility in simulating varying electrode architectures as well as reducing the overall material cost.

Other applications for the proposed model is to study the MEA component failure which usually happens under cold operations including the rapid start-up and shutdown. Researchers found that the component failure can be subjected to physical damage and electrochemical loss [206–211]. Physical damage involves MPL and catalyst layer cracks and interficial delamination [206, 207, 210, 211], membrane failure (cracks or holes) [208] and GDL fracture [211]. These physical damages, especially the interface delamination which results in interfacial gaps between MEA components, will lead to a significant performance loss. For instance, the study performed by Kim et al. [212] showed that the CL/PEM and CL/MPL interficial delamination had created a significant electronic transport barrier at low humidity.

Among the interface delaminations, the delamination between MPL and catalyst layer interface is of importance as it affects the catalyst utilization, reactant transport and electrical resistance. In particular, the MPL/CL delamination may result not only in a poor electrical contact but also water pooling at the interface which could greatly increase the mass transport resistance. Swamy et al. [213] showed the interface between MPL and catalyst layer could hold a great amount of water in an operating fuel cell. The proposed two-phase model in this thesis can be extended in order to study the effects of CL/MPL delamination, especially water accumulation at the CL/MPL inter-

face by developing a flexible mesh generator and introducing ghost interface cells.

One well-known deficiency of the MEA volume-averaged model is the lack of consideration of discrete water clusters and approximation of the REV in the GDL. This can be solved using pore network models (PNMs) [80, 83] as discussed in the introduction. PNMs are network diagrams that use idealized geometries, i.e., pores and throats, to represent the complex micro-structure of a porous media. PNMs can be used to simulate capillary flow, thermal transport and gas transport in the pore scale. However, solving a fully coupled multi-physics MEA system is still too computationally costly at the moment with pore network models.

Researchers [80, 214] proposed the combination of a pore-level model for the GDL and a volume-averaged model for PEM and catalyst layer to study capillary transport in MEA. The advantages of the coupled model is that the pore network can be used to capture the water transport through the GDLs with inhomogeneous morphology, and the volume-averaged model can be used to model the transport in catalyst layer and MPL and electrochemical reactions with a better computational efficiency. Due to convergence instability however, the joined model in [80] was not able to predict experimental polarization curves. In previous work, a commercial finite element method solver was used and only a weak coupling between programs could be achieved. The model proposed in this thesis is open source and fully customizable, thereby, enabling a closer coupling.

References

[1] Jon P Owejan, Jeanette E Owejan, Wenbin Gu, Thomas A Trabold, Thomas W Tighe, and Mark F Mathias. Water transport mechanisms in pemfc gas diffusion layers. *Journal of The Electrochemical Society*, 157(10):B1456–B1464, 2010.

[2] S. Shukla. PhD thesis, University of Alberta, 2016.

[3] M. Bhaiya, A. Putz, and M. Secanell. Analysis of non-isothermal effects on polymer electrolyte fuel cell electrode assemblies. *Electrochimica Acta*, 147:294–304, 2014.

[4] Pedro Mateo-Villanueva and Marc Secanell. A mixed wettability pore size distribution model for the analysis of water transport in pemfc materials. Master's thesis, University of Alberta, 2013.

[5] Jacob M LaManna, James V Bothe, Feng Yuan Zhang, and Matthew M Mench. Measurement of capillary pressure in fuel cell diffusion media, micro-porous layers, catalyst layers, and interfaces. *Journal of Power Sources*, 271:180–186, 2014.

[6] Z Yu, RN Carter, and J Zhang. Measurements of pore size distribution, porosity, effective oxygen diffusivity, and tortuosity of pem fuel cell electrodes. *Fuel Cells*, 12(4):557–565, 2012.

[7] Marc Secanell, Andreas Putz, Phillip Wardlaw, Valentin Zingan, Madhur Bhaiya, Michael Moore, Jie Zhou, Chad Balen, and Kailyn Domican. Openfcst: An open-source mathematical modelling software for polymer electrolyte fuel cells. *ECS Transactions*, 64(3):655–680, 2014.

[8] Phengxay Deevanhxay, Takashi Sasabe, Shohji Tsushima, and Shuichiro Hirai. In situ diagnostic of liquid water distribution in cathode catalyst layer in an operating pemfc by high-resolution soft x-ray radiography. *Electrochemistry Communications*, 22:33–36, 2012.

[9] J Lee, R Yip, P Antonacci, N Ge, T Kotaka, Y Tabuchi, and A Bazylak. Synchrotron investigation of microporous layer thickness on liquid water distribution in a pem fuel cell. *Journal of the Electrochemical Society*, 162(7):F669–F676, 2015.

[10] IPCC Revised. Ipcc guidelines for national greenhouse gas inventories. *Reference manual*, 3, 1996.

[11] Iryna V Zenyuk, Prodip K Das, and Adam Z Weber. Understanding impacts of catalyst-layer thickness on fuel-cell performance via mathematical modeling. *Journal of the Electrochemical Society*, 163(7):F691–F703, 2016.

[12] K.S. Chen Z.H. Wang, C.Y. Wanga. Two-phase flow and transport in the air cathode of proton exchange membrane fuel cells. *Journal of Power Sources*, 94:40–50, 2001.

[13] Hua Meng and Chao-Yang Wang. Model of two-phase flow and flooding dynamics in polymer electrolyte fuel cells. *Journal of the Electrochemical Society*, 152(9):A1733–A1741, 2005.

[14] D.J. Nelson N.P. Siegel, M.W. Ellis and M.R. von Spakovsky. A two-dimensional computational model of a pemfc with liquid water transport. *Journal of the Electrochemical Society*, 128:173–184, 2004.

[15] Trung Van Nguyen and Mack W Knobbe. A liquid water management strategy for pem fuel cell stacks. *Journal of Power Sources*, 114(1):70–79, 2003.

[16] Hui Li, Yanghua Tang, Zhenwei Wang, Zheng Shi, Shaohong Wu, Datong Song, Jianlu Zhang, Khalid Fatih, Jiujun Zhang, Haijiang Wang, et al. A review of water flooding issues in the proton exchange membrane fuel cell. *Journal of Power Sources*, 178(1):103–117, 2008.

[17] Zhigang Qi and Arthur Kaufman. Improvement of water management by a microporous sublayer for pem fuel cells. *Journal of Power Sources*, 109(1):38–46, 2002.

[18] XL Wang, HM Zhang, JL Zhang, HF Xu, ZQ Tian, J Chen, HX Zhong, YM Liang, and BL Yi. Micro-porous layer with composite carbon black for pem fuel cells. *Electrochimica Acta*, 51(23):4909–4915, 2006.

[19] Jaehyung Park, Ugur Pasaogullari, and Leonard J Bonville. A new ccm/mpl structure for high power density polymer electrolyte fuel cells. *ECS Transactions*, 64(3):353–359, 2014.

[20] Hong Je Cho, Hyunsook Jang, Seokhee Lim, EunAe Cho, Tae-Hoon Lim, In-Hwan Oh, Hyoung-Juhn Kim, and Jong Hyun Jang. Development of a novel decal transfer process for fabrication of high-performance and reliable membrane electrode assemblies for pemfcs. *international journal of hydrogen energy*, 36(19):12465–12473, 2011.

[21] André D Taylor, Edward Y Kim, Virgil P Humes, Jeremy Kizuka, and Levi T Thompson. Inkjet printing of carbon supported platinum 3-d catalyst layers for use in fuel cells. *Journal of Power Sources*, 171(1):101–106, 2007.

[22] Shantanu Shukla, Kailyn Domican, and Marc Secanell. Effect of electrode patterning on pem fuel cell performance using ink-jet printing method. *ECS Transactions*, 64(3):341–352, 2014.

[23] Haolin Tang, Shenlong Wang, Mu Pan, San Ping Jiang, and Yunzhang Ruan. Performance of direct methanol fuel cells prepared by hot-pressed mea and catalyst-coated membrane (ccm). *Electrochimica Acta*, 52(11):3714–3718, 2007.

[24] Mark K Debe, Richard J Poirier, Michael K Wackerfuss, and Raymond J Ziegler. Membrane electrode assembly, 1999. US Patent 5,879,828.

[25] In-Su Park, Wen Li, and Arumugam Manthiram. Fabrication of catalyst-coated membrane-electrode assemblies by doctor blade method and their performance in fuel cells. *Journal of Power Sources*, 195(20):7078–7082, 2010.

[26] A Lindermeir, G Rosenthal, U Kunz, and U Hoffmann. On the question of mea preparation for dmfcs. *Journal of Power Sources*, 129(2):180–187, 2004.

[27] Haolin Tang, Xiaoen Wang, Mu Pan, and Fang Wang. Fabrication and characterization of improved pfsa/eptfe composite polymer electrolyte membranes. *Journal of Membrane Science*, 306(1-2):298–306, 2007.

[28] Jin Hyun Nam and Massoud Kaviany. Effective diffusivity and water-saturation distribution in single-and two-layer pemfc diffusion medium. *International Journal of Heat and Mass Transfer*, 46(24):4595–4611, 2003.

[29] Chaozhong Qin, Dirk Rensink, Stephan Fell, and S Majid Hassanizadeh. Two-phase flow modeling for the cathode side of a polymer electrolyte fuel cell. *Journal of power sources*, 197:136–144, 2012.

[30] Michael Eikerling. Water management in cathode catalyst layers of pem fuel cells a structure-based model. *Journal of the Electrochemical Society*, 153(3):E58–E70, 2006.

[31] Adam Z Weber, Robert M Darling, and John Newman. Modeling two-phase behavior in pefcs. *Journal of the Electrochemical Society*, 151(10):A1715–A1727, 2004.

[32] Yun Wang, Suman Basu, and Chao-Yang Wang. Modeling two-phase flow in pem fuel cell channels. *Journal of Power Sources*, 179(2):603–617, 2008.

[33] Anthony Thomas, Gaël Maranzana, Sophie Didierjean, Jérôme Dillet, and Olivier Lottin. Thermal and water transfer in pemfcs: Investigating the role of the microporous layer. *International Journal of Hydrogen Energy*, 39(6):2649–2658, 2014.

[34] Satish G Kandlikar and Zijie Lu. Thermal management issues in a pemfc stack–a brief review of current status. *Applied Thermal Engineering*, 29(7):1276–1280, 2009.

[35] R Alink, J Haussmann, H Markötter, M Schwager, I Manke, and D Gerteisen. The influence of porous transport layer modifications on the water management in polymer electrolyte membrane fuel cells. *Journal of Power Sources*, 233:358–368, 2013.

[36] D Gerteisen, T Heilmann, and C Ziegler. Enhancing liquid water transport by laser perforation of a gdl in a pem fuel cell. *Journal of Power Sources*, 177(2):348–354, 2008.

[37] MP Manahan, MC Hatzell, EC Kumbur, and MM Mench. Laser perforated fuel cell diffusion media. part i: Related changes in performance and water content. *Journal of Power Sources*, 196(13):5573–5582, 2011.

[38] Jeff T Gostick, Marios A Ioannidis, Michael W Fowler, and Mark D Pritzker. On the role of the microporous layer in pemfc operation. *Electrochemistry Communications*, 11(3):576–579, 2009.

[39] Ruediger Schweiss, Marcus Steeb, and Peter M Wilde. Mitigation of water management in pem fuel cell cathodes by hydrophilic wicking microporous layers. *Fuel Cells*, 10(6):1176–1180, 2010.

[40] Rangachary Mukundan, John Davey, Joseph D Fairweather, Dusan Spernjak, Jacob S Spendelow, Daniel S Hussey, David Jacobson, Peter Wilde, Ruediger Schweiss, and Rodney L Borup. Effect of hydrophilic treatment of microporous layer on fuel cell performance. *ECS Transactions*, 33(1):1109–1114, 2010.

[41] Rangachary Mukundan, John Davey, Joseph D Fairweather, Dusan Spernjak, Jacob S Spendelow, Daniel S Hussey, David Jacobson, Peter Wilde, Ruediger Schweiss, and Rodney L Borup. Effect of hydrophilic treatment of microporous layer on fuel cell performance. *ECS Transactions*, 33(1):1109–1114, 2010.

[42] Sehkyu Park and Branko N Popov. Effect of hydrophobicity and pore geometry in cathode gdl on pem fuel cell performance. *Electrochimica Acta*, 54(12):3473–3479, 2009.

[43] Gu-Gon Park, Young-Jun Sohn, Tae-Hyun Yang, Young-Gi Yoon, Won-Yong Lee, and Chang-Soo Kim. Effect of ptfe contents in the gas diffusion media on the performance of pemfc. *Journal of Power Sources*, 131(1):182–187, 2004.

[44] S Litster and G McLean. Pem fuel cell electrodes. *Journal of Power Sources*, 130(1):61–76, 2004.

[45] FE Hizir, SO Ural, EC Kumbur, and MM Mench. Characterization of interfacial morphology in polymer electrolyte fuel cells: Micro-porous layer and catalyst layer surfaces. *Journal of Power Sources*, 195(11):3463–3471, 2010.

[46] Jin Hyun Nam, Kyu-Jin Lee, Gi-Suk Hwang, Charn-Jung Kim, and Massoud Kaviany. Microporous layer for water morphology control in pemfc. *International Journal of Heat and Mass Transfer*, 52(11):2779–2791, 2009.

[47] Zhong Xie, Titichai Navessin, Ken Shi, Robert Chow, Qianpu Wang, Datong Song, Bernhard Andreaus, Michael Eikerling, Zhongsheng Liu, and Steven Holdcroft. Functionally graded cathode catalyst layers for polymer electrolyte fuel cells ii. experimental study of the effect of nafion distribution. *Journal of the Electrochemical Society*, 152(6):A1171–A1179, 2005.

[48] Firat C Cetinbas, Suresh G Advani, and Ajay K Prasad. Investigation of a polymer electrolyte membrane fuel cell catalyst layer with bidirectionally-graded composition. *Journal of Power Sources*, 270:594–602, 2014.

[49] Kun-Ho Kim, Kwan-Young Lee, Hyoung-Juhn Kim, EunAe Cho, Sang-Yeop Lee, Tae-Hoon Lim, Sung Pil Yoon, In Chul Hwang, and Jong Hyun Jang. The effects of nafion® ionomer content in pemfc meas prepared by a catalyst-coated membrane (ccm) spraying method. *international journal of hydrogen energy*, 35(5):2119–2126, 2010.

[50] MD Gasda, GA Eisman, and D Gall. Nanorod pem fuel cell cathodes with controlled porosity. *Journal of the Electrochemical Society*, 157(3):B437–B440, 2010.

[51] Zhilian Zhou, Raymond N Dominey, Jason P Rolland, Benjamin W Maynor, Ashish A Pandya, and Joseph M DeSimone. Molded, high surface area polymer electrolyte membranes from cured liquid precursors. *Journal of the American Chemical Society*, 128(39):12963–12972, 2006.

[52] Masato Aizawa, Hisaaki Gyoten, Abdu Salah, and Xinbing Liu. Pillar structured membranes for suppressing cathodic concentration overvoltage in pemfcs at elevated temperature/low relative humidity. *Journal of The Electrochemical Society*, 157(12):B1844–B1851, 2010.

[53] Jin Woo Bae, Yong-Hun Cho, Yung-Eun Sung, Kyusoon Shin, and Jae Young Jho. Performance enhancement of polymer electrolyte membrane fuel cell by employing line-patterned nafion membrane. *Journal of Industrial and Engineering Chemistry*, 18(3):876–879, 2012.

[54] Jong Kwan Koh, Yukwon Jeon, Yong Il Cho, Jong Hak Kim, and Yong-Gun Shul. A facile preparation method of surface patterned polymer

electrolyte membranes for fuel cell applications. *Journal of Materials Chemistry A*, 2(23):8652–8659, 2014.

[55] Ashvini B Deshmukh, Vinayak S Kale, Vishal M Dhavale, K Sreekumar, K Vijayamohanan, and Manjusha V Shelke. Direct transfer of micro-molded electrodes for enhanced mass transport and water management in pemfc. *Electrochemistry Communications*, 12(11):1638–1641, 2010.

[56] Hua Meng. A two-phase non-isothermal mixed-domain PEM fuel cell model and its application to two-dimensional simulations. *Journal of Power Sources*, 168(1):218–228, 2007.

[57] Robert M. Darling Adam Z. Weber and John Newmana. Modeling two-phase behavior in pefcs. *Journal of The Electrochemical Society*, 151(10):A1715–A1727, 2004.

[58] Vincenzo Mulone and Kunal Karan. Analysis of capillary flow driven model for water transport in pefc cathode catalyst layer: Consideration of mixed wettability and pore size distribution. *International Journal of Hydrogen Energy*, 38(1):558–569, 2013.

[59] J Zhou, A Putz, and M Secanell. A mixed wettability pore size distribution based mathematical model for analyzing two-phase flow in porous electrodes i. mathematical model. *Journal of The Electrochemical Society*, 164(6):F530–F539, 2017.

[60] Jeff T Gostick, Marios A Ioannidis, Michael W Fowler, and Mark D Pritzker. Pore network modeling of fibrous gas diffusion layers for polymer electrolyte membrane fuel cells. *Journal of Power Sources*, 173(1):277–290, 2007.

[61] Puneet K Sinha and Chao-Yang Wang. Pore-network modeling of liquid water transport in gas diffusion layer of a polymer electrolyte fuel cell. *Electrochimica Acta*, 52(28):7936–7945, 2007.

[62] M. Sabharwal, L. M. Pant, A. Putz, D. Susac, J. Jankovic, and M. Secanell. Analysis of catalyst layer microstructures: From imaging to performance. *Fuel Cells*, 10(1002):201600008, 2016.

[63] J Hinebaugh, J Gostick, and A Bazylak. Stochastic modeling of polymer electrolyte membrane fuel cell gas diffusion layers–part 2: A comprehen-

sive substrate model with pore size distribution and heterogeneity effects. *International Journal of Hydrogen Energy*, 2017.

[64] R Singh, AR Akhgar, PC Sui, KJ Lange, and N Djilali. Dual-beam fib/sem characterization, statistical reconstruction, and pore scale modeling of a pemfc catalyst layer. *Journal of The Electrochemical Society*, 161(4):F415–F424, 2014.

[65] M. Rebai and M. Prat. Scale effect and two-phase flow in a thin hydrophobic porous layer. Application to water transport in gas diffusion layers of proton exchange membrane fuel cells. *Journal of Power Sources*, 192(2):534–543, 2009.

[66] Tatyana Soboleva, Kourosh Malek, Zhong Xie, Titichai Navessin, and Steven Holdcroft. Pemfc catalyst layers: the role of micropores and mesopores on water sorption and fuel cell activity. *ACS applied materials & interfaces*, 3(6):1827–1837, 2011.

[67] Simon Thiele, Roland Zengerle, and Christoph Ziegler. Nano-morphology of a polymer electrolyte fuel cell catalyst layer—Imaging, reconstruction and analysis. *Nano Research*, 4(9):849–860, 2011.

[68] S. Litster, W. K. Epting, E. A.Wargo, S. R. Kalidindi, and E. C. Kumbur. Morphological analyses of polymer electrolyte fuel cell electrodes with nano-scale computed tomography imaging. *Fuel Cells*, 13(5):935–945, 2013.

[69] Jeff T. Gostick, Marios A. Ioannidis, Mark D. Pritzker, and Michael W. Fowler. Impact of liquid water on reactant mass transfer in pem fuel cell electrodes. *Journal of The Electrochemical Society*, 157(4):B563–B571, 2010.

[70] Wensheng He, Jung S Yi, and Trung Van Nguyen. Two-phase flow model of the cathode of pem fuel cells using interdigitated flow fields. *AIChE Journal*, 46(10):2053–2064, 2000.

[71] Dilip Natarajan and Trung Van Nguyen. Three-dimensional effects of liquid water flooding in the cathode of a PEM fuel cell. *Journal of Power Sources*, 115(1):66–80, 2003.

[72] Hua Meng. A three-dimensional pem fuel cell model with consistent treatment of water transport in mea. *Journal of Power Sources*, 162(1):426–435, 2006.

[73] Hua Meng. Numerical investigation of transient responses of a pem fuel cell using a two-phase non-isothermal mixed-domain model. *Journal of Power Sources*, 171(2):738–746, 2007.

[74] U. Pasaogullari and C. Y. Wang. Two-phase transport and the role of micro-porous layer in polymer electrolyte fuel cells. *ELECTROCHIMICA ACTA.*, 49(25):4359–4369, 2004.

[75] Z. H. Wang, C. Y. Wang, and K. S. Chen. Two-phase flow and transport in the air cathode of proton exchange membrane fuel cells. *JOURNAL OF POWER SOURCES*, 94(1):40–50, 2001.

[76] T. Kotaka, Y. Tabuchi, U. Pasaogullari, and C. Y. Wang. Impact of interfacial water transport in pemfcs on cell performance. *Electrochimica Acta*, 146(1):618–629, 2014.

[77] Vladimir Gurau, Robert V Edwards, J Adin Mann, and Tom A Zawodzinski. A look at the multiphase mixture model for pem fuel cell simulations. *Electrochemical and Solid-State Letters*, 11(8):B132–B135, 2008.

[78] Adam Z Weber and John Newman. Coupled thermal and water management in polymer electrolyte fuel cells. *Journal of the Electrochemical Society*, 153(12):A2205–A2214, 2006.

[79] Torsten Berning, DM Lu, and N Djilali. Three-dimensional computational analysis of transport phenomena in a pem fuel cell. *Journal of power sources*, 106(1-2):284–294, 2002.

[80] Iryna V Zenyuk, Ezequiel Medici, Jeffrey Allen, and Adam Z Weber. Coupling continuum and pore-network models for polymer-electrolyte fuel cells. *International Journal of Hydrogen Energy*, 40(46):16831–16845.

[81] Liang Hao and Ping Cheng. Lattice boltzmann simulations of water transport in gas diffusion layer of a polymer electrolyte membrane fuel cell. *Journal of Power Sources*, 195(12):3870–3881, 2010.

[82] Kwang Nam Kim, Jung Ho Kang, Sang Gun Lee, Jin Hyun Nam, and Charn-Jung Kim. Lattice boltzmann simulation of liquid water transport in microporous and gas diffusion layers of polymer electrolyte membrane fuel cells. *Journal of Power Sources*, 278:703–717, 2015.

[83] Jeff T Gostick, Marios A Ioannidis, Michael W Fowler, and Mark D Pritzker. Wettability and capillary behavior of fibrous gas diffusion media for polymer electrolyte membrane fuel cells. *Journal of Power Sources*, 194(1):433–444, 2009.

[84] Adam Z Weber. Improved modeling and understanding of diffusion-media wettability on polymer-electrolyte-fuel-cell performance. *Journal of Power Sources*, 195(16):5292–5304, 2010.

[85] Jeffrey T Gostick, Michael W Fowler, Marios A Ioannidis, Mark D Pritzker, Yu M Volfkovich, and A Sakars. Capillary pressure and hydrophilic porosity in gas diffusion layers for polymer electrolyte fuel cells. *Journal of Power Sources*, 156(2):375–387, 2006.

[86] Michael J Martínez, Sirivatch Shimpalee, JW Van Zee, and AV Sakars. Assessing methods and data for pore-size distribution of pemfc gas-diffusion media. *Journal of the Electrochemical Society*, 156(5):B558–B564, 2009.

[87] Marc Secanell, Andreas Putz, Shantanu Shukla, Phillip Wardlaw, Madhur Bhaiya, Lalit M Pant, and Mayank Sabharwal. Mathematical modelling and experimental analysis of thin, low-loading fuel cell electrodes. *ECS Transactions*, 69(17):157–187, 2015.

[88] Datong Song, Qianpu Wang, Zhongsheng Liu, Titichai Navessin, Michael Eikerling, and Steven Holdcroft. Numerical optimization study of the catalyst layer of pem fuel cell cathode. *Journal of Power Sources*, 126(1):104–111, 2004.

[89] Mark K Debe. Nanostructured thin film electrocatalysts for pem fuel cells-a tutorial on the fundamental characteristics and practical properties of nstf catalysts. *Ecs Transactions*, 45(2):47–68, 2012.

[90] Mark K Debe. Electrocatalyst approaches and challenges for automotive fuel cells. *Nature*, 486(7401):43–51, 2012.

[91] Kunal Karan, Hasan Atiyeh, Aaron Phoenix, Ela Halliop, Jon Pharoah, and Brant Peppley. An experimental investigation of water transport in pemfcs the role of microporous layers. *Electrochemical and solid-state letters*, 10(2):B34–B38, 2007.

[92] Paola Gallo Stampino, Cinzia Cristiani, Giovanni Dotelli, Luca Omati, Luca Zampori, Renato Pelosato, and Manfredo Guilizzoni. Effect of different substrates, inks composition and rheology on coating deposition of microporous layer (mpl) for pem-fcs. *Catalysis Today*, 147:S30–S35, 2009.

[93] T Tanuma and S Kinoshita. Impact of cathode fabrication on fuel cell performance. *Journal of The Electrochemical Society*, 161(1):F94–F98, 2014.

[94] AZ Weber and J Newman. Effects of microporous layers in polymer electrolyte fuel cells. *Journal of the Electrochemical Society*, 152(4):A677–A688, 2005.

[95] Morteza Baghalha, M. Eikerling, and J. Stumper. The effect of mpl permeability on water fluxes in pem fuel cells: A lumped approach. *ECS Transactions*, 33:1529–1544, 2010.

[96] D. Spernjak, A. K. Prasad, and S. G. Advani. Experimental investigation of liquid water formation and transport in a transparent single-serpentine pem fuel cell. *JOURNAL OF POWER SOURCES*, 170(2):334–344, 2007.

[97] Guangyu Lin and Trung Van Nguyen. Effect of thickness and hydrophobic polymer content of the gas diffusion layer on electrode flooding level in a pemfc. *Journal of the Electrochemical Society*, 152(10):A1942–A1948, 2005.

[98] J. H. Nam, K. J. Lee, G. S. Hwang, C. J. Kim, and M. Kaviany. Microporous layer for water morphology control in pemfc. *INTERNATIONAL JOURNAL OF HEAT AND MASS TRANSFER*, 52(11):2779–2791, 2009.

[99] Ugur Pasaogullari, Chao-Yang Wang, and Ken S Chen. Two-phase transport in polymer electrolyte fuel cells with bilayer cathode gas diffusion

media. *Journal of The Electrochemical Society*, 152(8):A1574–A1582, 2005.

[100] AZ Weber and MA Hickner. Modeling and high-resolution-imaging studies of water-content profiles in a polymer-electrolyte-fuel-cell membrane-electrode assembly. *Electrochimica Acta*, 53(26):7668–7674, 2008.

[101] Hasan K Atiyeh, Kunal Karan, Brant Peppley, Aaron Phoenix, Ela Halliop, and Jon Pharoah. Experimental investigation of the role of a microporous layer on the water transport and performance of a pem fuel cell. *Journal of The Electrochemical Society*, 170(1):111–121, 2007.

[102] J Zhou, D Stanier, A Putz, and M Secanell. A mixed wettability pore size distribution based mathematical model for analyzing two-phase flow in porous electrodes ii. model validation and analysis of micro-structural parameters. *Journal of The Electrochemical Society*, 164(6):F540–F556, 2017.

[103] J. Zhou, S. Shukla, A. Putz, and M. Secanell. Analysis of the role of the microporous layer in improving polymer electrolyte fuel cell performance. *Electrochimica Acta*, 268C:366–382, 2018.

[104] Jeffrey T Gostick, Michael W Fowler, Marios A Ioannidis, Mark D Pritzker, Yu M Volfkovich, and A Sakars. Capillary pressure and hydrophilic porosity in gas diffusion layers for polymer electrolyte fuel cells. *Journal of Power Sources*, 156(2):375–387, 2006.

[105] Jian Xie, Karren L More, Thomas A Zawodzinski, and Wayne H Smith. Porosimetry of meas made by "thin film decal" method and its effect on performance of pefcs. *Journal of the Electrochemical Society*, 151(11):A1841–A1846, 2004.

[106] Swagatam Das, Ajith Abraham, and Amit Konar. Particle swarm optimization and differential evolution algorithms: technical analysis, applications and hybridization perspectives. *Advances of computational intelligence in industrial systems*, pages 1–38, 2008.

[107] Bruce R Munson, Theodore H Okiishi, Alric P Rothmayer, and Wade W Huebsch. *Fundamentals of fluid mechanics*. John Wiley & Sons, 2014.

[108] Joseph D Fairweather, Perry Cheung, and Daniel T Schwartz. The effects of wetproofing on the capillary properties of proton exchange membrane fuel cell gas diffusion layers. *Journal of Power Sources*, 195(3):787–793, 2010.

[109] IS Hussaini and CY Wang. Measurement of relative permeability of fuel cell diffusion media. *Journal of Power Sources*, 195(12):3830–3840, 2010.

[110] Gang Luo, Yan Ji, Chao-Yang Wang, and Puneet K Sinha. Modeling liquid water transport in gas diffusion layers by topologically equivalent pore network. *Electrochimica Acta*, 55(19):5332–5341, 2010.

[111] Tetsuya Koido, Toru Furusawa, and Koji Moriyama. An approach to modeling two-phase transport in the gas diffusion layer of a proton exchange membrane fuel cell. *Journal of Power Sources*, 175(1):127–136, 2008.

[112] Prafful Mangal, Mark Dumontier, Nicholas Carrigy, and Marc Secanell. Measurements of permeability and effective in-plane gas diffusivity of gas diffusion media under compression. *ECS Transactions*, 64(3):487–499, 2014.

[113] Nicholas B Carrigy, Lalit M Pant, Sushanta Mitra, and Marc Secanell. Knudsen diffusivity and permeability of pemfc microporous coated gas diffusion layers for different polytetrafluoroethylene loadings. *Journal of The Electrochemical Society*, 160(2):F81–F89, 2013.

[114] Prafful Mangal, Lalit M Pant, Nicholas Carrigy, Mark Dumontier, Valentin Zingan, Sushanta Mitra, and Marc Secanell. Experimental study of mass transport in PEMFCs: through plane permeability and molecular diffusivity in GDLs. *Electrochimica Acta*, 167:160–171, 2015.

[115] Jeff T Gostick, Michael W Fowler, Mark D Pritzker, Marios A Ioannidis, and Leya M Behra. In-plane and through-plane gas permeability of carbon fiber electrode backing layers. *Journal of Power Sources*, 162(1):228–238, 2006.

[116] M. V. Williams, E. Begg, L. Bonville, H.R.Kunz, and J.M. Fenton. Characterization of gas diffusion layers for PEMFC. *Journal of the Electrochemical Society*, 151(8):A1173–A1180, 2004.

[117] J. Ihonen, M. Mikkola, and G. Lindbergh. Flooding of gas diffusion backing in PEFCs: Physical and electrochemical characterization. *Journal of the Electrochemical Society*, 151(8):A1152–A1161, 2004.

[118] M Prasanna, HY Ha, EA Cho, S-A Hong, and I-H Oh. Influence of cathode gas diffusion media on the performance of the pemfcs. *Journal of Power Sources*, 131(1):147–154, 2004.

[119] L. M. Pant, S. K. Mitra, and M. Secanell. Absolute permeability and knudsen diffusivity measurements in pemfc gas diffusion layers and micro porous layers. *Journal of Power Sources*, 206(0):153 – 160, 2012.

[120] Vladimir Gurau, Michael J Bluemle, Emory S De Castro, Yu-Min Tsou, Thomas A Zawodzinski Jr, and J Adin Mann Jr. Characterization of transport properties in gas diffusion layers for proton exchange membrane fuel cells: 2. Absolute permeability. *Journal of Power Sources*, 165(2):793–802, 2007.

[121] H Dohle, R Jung, N Kimiaie, J Mergel, and M Müller. Interaction between the diffusion layer and the flow field of polymer electrolyte fuel cellsexperiments and simulation studies. *Journal of Power Sources*, 124(2):371–384, 2003.

[122] Pablo A. García-Salaberri, Jeff T. Gostick, Gisuk Hwang, Adam Z. Weber, and Marcos Vera. Effective diffusivity in partially-saturated carbon-fi ber gas diffusion layers: Effect of local saturation and application to macroscopic continuum models. *Journal of Power Sources*, 296:440–453, 2015.

[123] HM Yu, C Ziegler, M Oszcipok, M Zobel, and C Hebling. Hydrophilicity and hydrophobicity study of catalyst layers in proton exchange membrane fuel cells. *Electrochimica Acta*, 51(7):1199–1207, 2006.

[124] TA Zawodzinski, Shimshon Gottesfeld, S Shoichet, and TJ McCarthy. The contact angle between water and the surface of perfluorosulphonic acid membranes. *Journal of applied electrochemistry*, 23(1):86–88, 1993.

[125] CH Bosanquet. Lv. on the flow of liquids into capillary tubes. *The London, Edinburgh, and Dublin Philosophical Magazine and Journal of Science*, 45(267):525–531, 1923.

[126] M. Eikerling and A. A. Kornyshev. Modelling the performance of the cathode catalyst layer of polymer electrolyte fuel cells. *Journal of Electroanalytical Chemistry*, 453(1):89–106, 1998.

[127] M. Secanell. Computational modeling and optimization of proton exchange membrane fuel cells. *PhD thesis*, University of Victoria, 2007.

[128] Peter Dobson. Investigation of the polymer electrolyte membrane fuel cell catalyst layer microstructure. 2011.

[129] Michael Moore. Investigation of the double-trap intrinsic kinetic equation for the oxygen reduction reaction and its implementation into a membrane electrode assembly model. 2012.

[130] Madhur Bhaiya, Andreas Putz, and Marc Secanell. A comprehensive single-phase, non-isothermal mathematical mea model and analysis of non-isothermal effects. *ECS Transactions*, 64(3):567–579, 2014.

[131] M. Moore, P. Wardlaw, P. Dobson, J.J. Boisvert, A. Putz, R.J. Spiteri, and M. Secanell. Understanding the effect of kinetic and mass transport processes in cathode agglomerates. *Journal of the Electrochemical Society*, 161(8):E3125–E3137, 2014.

[132] Jia X. Wang, Thomas E. Springe, and Radoslav R. Adzic. Dual-pathway kinetic equation for the hydrogen oxidation reaction on pt electrodes. *Joural of the Electrochemical Society*, 153(9):A1732–A1740, 2006.

[133] F.M. White. *Viscous fluid flow*. McGraw-Hill, 2nd edition, 1991.

[134] Sydney Chapman and Thomas George Cowling. *The mathematical theory of non-uniform gases: an account of the kinetic theory of viscosity, thermal conduction and diffusion in gases*. Cambridge university press, 1970.

[135] M. Bhaiya. An open-source two-phase non-isothermal mathematical model of a polymer electrolyte membrane fuel cell. *University of Alberta*, Master thesis, 2014.

[136] Soowhan Kim and MM Mench. Investigation of temperature-driven water transport in polymer electrolyte fuel cell: Thermo-osmosis in membranes. *Journal of Membrane Science*, 328(1):113–120, 2009.

[137] J. P. Villaluenga, B. Seoane, V. M. Barragan, and C. Ruiz-Bauza. Thermo-osmosis of mixtures of water and methanol through a nafion membrane. *Journal of Membrane Science*, 274(1):116–122, 2006.

[138] James T Hinatsu, Minoru Mizuhata, and Hiroyasu Takenaka. Water uptake of perfluorosulfonic acid membranes from liquid water and water vapor. *Journal of the Electrochemical Society*, 141(6):1493–1498, 1994.

[139] Ahmet Kusoglu and Adam Z. Weber. New Insights into Perfluorinated Sulfonic-Acid Ionomers. *Chemical Reviews*, 117(3):987–1104, 2017.

[140] Allen J. Bard and Larry R. Faulkner. *Electrochemical methods: fundamentals and applications*. John Wiley & Sons, Inc., second edition, 2001.

[141] C.O. Popiel and J. Wojtkowiak. Simple formulas for thermophysical properties of liquid water for heat transfer calculations (from 0 ℃to 150 ℃). *Heat Transfer Engineering*, 19(3):87–101, 1998.

[142] DA Noren and MA Hoffman. Clarifying the butler–volmer equation and related approximations for calculating activation losses in solid oxide fuel cell models. *Journal of Power Sources*, 152:175–181, 2005.

[143] Shengli Chen and Anthony Kucernak. Electrocatalysis under conditions of high mass transport: investigation of hydrogen oxidation on single submicron Pt particles supported on carbon. *The Journal of Physical Chemistry B*, 108(37):13984–13994, 2004.

[144] HA Gasteiger, JE Panels, and SG Yan. Dependence of PEM fuel cell performance on catalyst loading. *Journal of Power Sources*, 127(1):162–171, 2004.

[145] A Damjanovic and V Brusic. Electrode kinetics of oxygen reduction on oxide-free platinum electrodes. *Electrochimica Acta*, 12(6):615–628, 1967.

[146] Marta Paucirova, DM Drazic, and A Damjanovic. The effect of surface coverage by adsorbed oxygen on the kinetics of oxygen reduction at oxide free platinum. *Electrochimica Acta*, 18(12):945–951, 1973.

[147] Matthew Markiewicz, Christopher Zalitis, and Anthony Kucernak. Performance measurements and modelling of the ORR on fuel cell

electrocatalysts–the modified double trap model. *Electrochimica Acta*, 179:126–136, 2015.

[148] Jia X Wang, Thomas E Springer, and Radoslav R Adzic. Dual-pathway kinetic equation for the hydrogen oxidation reaction on Pt electrodes. *Journal of the Electrochemical Society*, 153(9):A1732–A1740, 2006.

[149] Jia X Wang, Junliang Zhang, and Radoslav R Adzic. Double-trap kinetic equation for the oxygen reduction reaction on Pt (111) in acidic media. *The Journal of Physical Chemistry A*, 111(49):12702–12710, 2007.

[150] William K. Epting, Jeff Gelb, and Shawn Litster. Resolving the Three-Dimensional Microstructure of Polymer Electrolyte Fuel Cell Electrodes using Nanometer-Scale X-ray Computed Tomography. *Advanced Functional Materials*, 22(3):555–560, 2012.

[151] Daisuke Tashima, Hiromu Yoshitama, Masahisa Otsubo, Seiji Maeno, and Yoshinobu Nagasawa. Evaluation of electric double layer capacitor using Ketjen black as conductive nanofiller . *Electrochimica Acta*, 56(24):8941–8946, 2011.

[152] Dustin Banham, Fangxia Feng, Tobias Fürstenhaupt, Katie Pei, Siyu Ye, and Viola Birss. Effect of Pt-loaded carbon support nanostructure on oxygen reduction catalysis . *Journal of Power Sources*, 196(13):5438–5445, 2011.

[153] Philip Wardlaw. Modelling of pemfc catalyst layer mass transport and electro-chemical reactions using multi-scale simulations. Master's thesis, 2014.

[154] T. Suzuki, K. Kudo, and Y. Morimoto. Model for investigation of oxygen transport limitation in a polymer electrolyte fuel cell. *Journal of Power Sources*, 222(15):379–389, January 2013.

[155] P.J. Culligan and D.A. Barry. Scaling immiscible flow in porous media. Technical report, Research Report ED 1207 PC, Centre for Water Research, University of Western Australia, Perth, Australia, 1996.

[156] K. Jiao and X. Li. Water transport in polymer electrolyte membrane fuel cells. *Progress in Energy and Combustion Science*, 37(3):221–291, 2011.

[157] S. Litster and N. Djilali. *Transport phenomena in fuel cells*, chapter 5. WIT Press, Ashurst, U.K., 1st edition, 2006.

[158] Guangli He, Pingwen Ming, Zongchang Zhao, Abuliti Abudula, and Yu Xiao. A two-fluid model for two-phase flow in pemfcs. *Journal of Power Sources*, 163(2):864–873, 2007.

[159] David G Luenberger. *Optimization by vector space methods*. John Wiley & Sons, 1997.

[160] W. Bangerth, D. Davydov, T. Heister, L. Heltai, G. Kanschat, M. Kronbichler, M. Maier, B. Turcksin, and D. Wells. The deal.ii library, version 8.4. *Journal of Numerical Mathematics*, 24, 2016.

[161] P. R. Amestoy, A. Guermouche, J. Y. LExcellent, and S. p. Pralet. Hybrid scheduling for the parallel solution of linear systems. *Parallel Computing -Amsterdam-*, 32(2):136–156, 2006.

[162] De SR Gago, DW Kelly, OC Zienkiewicz, I Babuska, et al. A posteriori error analysis and adaptive processes in the finite element method: Part ii—adaptive mesh refinement. *International Journal for Numerical Methods in Engineering*, 19(11):1621–1656, 1983.

[163] J Zhou, A Putz, and M Secanell. A mixed wettability pore size distribution based mathematical model for analyzing two-phase flow in porous electrodes i. mathematical model. *Journal of The Electrochemical Society*, 164(6):F530–F539, 2017.

[164] Takashi Sasabe, Shohji Tsushima, and Shuichiro Hirai. In-situ visualization of liquid water in an operating pemfc by soft x-ray radiography. *International Journal of Hydrogen Energy*, 35(20):11119–11128, 2010.

[165] AZ Weber and MA Hickner. Modeling and high-resolution-imaging studies of water-content profiles in a polymer-electrolyte-fuel-cell membrane-electrode assembly. *Electrochimica Acta*, 53(26):7668–7674, 2008.

[166] H. K. Atiyeh, K. Karan, B. Peppley, A. Phoenix, E. Halliop, and J. Pharoah. Experimental investigation of the role of a microporous layer on the water transport and performance of a pem fuel cell. *Journal of Power Sources*, 170(1):111–121, 2007.

[167] Un Ho Jung, Ki Tae Park, Eun Hee Park, and Sung Hyun Kim. Improvement of low-humidity performance of pemfc by addition of hydrophilic sio 2 particles to catalyst layer. *Journal of power sources*, 159(1):529–532, 2006.

[168] Zhili Miao, Hongmei Yu, Wei Song, Dan Zhao, Lixing Hao, Baolian Yi, and Zhigang Shao. Effect of hydrophilic sio 2 additive in cathode catalyst layers on proton exchange membrane fuel cells. *Electrochemistry Communications*, 11(4):787–790, 2009.

[169] Jia X. Wang, Thomas E. Springer, and Radoslav R. Adzic. Dual-pathway kinetic equation for the hydrogen oxidation reaction on pt electrodes. *Journal of The Electrochemical Society*, 153(9):A1732–A1740, 2006.

[170] S. Shukla, D. Stanier, M. S. Saha, J. Stumper, and M. Secanell. Analysis of inkjet printed pefc electrodes with varying platinum loading. *Journal of the Electrochemical Society*, 163(7):F677–F687, 2016.

[171] Iryna V. Zenyuk, Adrien Lamibrac, Jens Joachim Eller, Dilworth Y. Parkinson, Federica Marone, Felix N Büchi, and Adam Z Weber. Investigating evaporation in gas diffusion layers for fuel cells with x-ray computed tomography. *The Journal of Physical Chemistry C*, 2016.

[172] KR Cooper and M Smith. Electrical test methods for on-line fuel cell ohmic resistance measurement. *Journal of Power Sources*, 160(2):1088–1095, 2006.

[173] Adachi Makoto, Titichai Navessin, Zhong Xie, Frisken Barbara, and Steven Holdcroft. Correlation of in situ and ex situ measurements of water permeation through nafion nre211 proton exchange membranes. *Journal of The Electrochemical Society*, 156(6):B782–B790, 2009.

[174] Motupally Sathya, Becker Aaron J., and Weidner John W. Diffusion of water in nafion 115 membranes. *Joural of The Electrochemical Society*, 147(9):3171–3177, 2000.

[175] Thomas F. Fuller. *Solid-Polymer-Electrolyte Fuel Cells*. PhD thesis, 1992.

[176] Trung V. Nguyen and Ralph E. White. A water and heat management model for proton-exchange-membrane fuel cells. *Joural of the Electrochemical Society*, 140:2178, 1993.

[177] Qiangu Yan, H Toghiani, and Heath Causey. Steady state and dynamic performance of proton exchange membrane fuel cells (pemfcs) under various operating conditions and load changes. *Journal of Power Sources*, 161(1):492–502, 2006.

[178] Nada Zamel, Efim Litovsky, Saher Shakhshir, Xianguo Li, and Jacob Kleiman. Measurement of in-plane thermal conductivity of carbon paper diffusion media in the temperature range of- 20 c to+ 120 c. *Applied energy*, 88(9):3042–3050, 2011.

[179] Iryna V. Zenyuk, Dilworth Y. Parkinson, Liam G. Connolly, and Adam Z. Weber. Gas-diffusion-layer structural properties under compression via x-ray tomography. *Journal of Power Sources*, 328:364–376, 2016.

[180] O. S. Burheim, H. Su, S. Pasupathi, J. G. Pharoah, and B. G. Pollet. Thermal conductivity and temperature profiles of the micro porous layers used for the polymer electrolyte membrane fuel cell. *International Journal of Hydrogen Energy*, 38(20):8437–8447, 2013.

[181] EA Wargo, T Kotaka, Y Tabuchi, and EC Kumbur. Comparison of focused ion beam versus nano-scale x-ray computed tomography for resolving 3-d microstructures of porous fuel cell materials. *Journal of Power Sources*, 241:608–618, 2013.

[182] A. El-kharouf, T. J. Mason, D. J. Brett, and B. G. Pollet. Ex-situ characterisation of gas diffusion layers for proton exchange membrane fuel cells. *JOURNAL OF POWER SOURCES*, 218(1):393–404, 2012.

[183] M. Khandelwal and M. M. Mench. Direct measurement of through-plane thermal conductivity and contact resistance in fuel cell materials. *Journal of Power Sources*, 161(2):1106–1115, 2006.

[184] S Shukla, D Stanier, MS Saha, J Stumper, and M Secanell. Analysis of inkjet printed pefc electrodes with varying platinum loading. *Journal of The Electrochemical Society*, 163(7):F677–F687, 2016.

[185] Ahmet Kusoglu, Anthony Kwong, Kyle T. Clark, Haluna P. Gunterman, and Adam Z. Weber. Water uptake of fuel-cell catalyst layers. *Journal of The Electrochemical Society*, 159(9):F530–F535, 2012.

[186] Jon P. Owejan, Jeanette E. Owejan, and Wenbin Gua. Impact of platinum loading and catalyst layer structure on pemfc performance. *Journal of The Electrochemical Society*, 160(8):F824–F833, 2013.

[187] W Tanikawa and T Shimamoto. Klinkenberg effect for gas permeability and its comparison to water permeability for porous sedimentary rocks. *Hydrology and Earth System Sciences Discussions*, 3(4):1315–1338, 2006.

[188] Soowhan Kim and MM Mench. Investigation of temperature-driven water transport in polymer electrolyte fuel cell: phase-change-induced flow. *Journal of The Electrochemical Society*, 156(3):B353–B362, 2009.

[189] Y. Liu, M.W. Murphy, D.R. Baker, W. Gu, C. Ji, J. Jorne, and H.A. Gasteiger. Proton conduction and oxygen reduction kinetics in PEM fuel cell cathodes: effects of ionomer-to-carbon ratio and relative humidity. *Journal of the Electrochemical Society*, 156(8):B970–B980, 2009.

[190] T Bekkedahl. In-plane conductivity testing procedures & results. In *DOE High Temperature Membrane Working Group Meeting, Arlington, VA*, 2007.

[191] Dzmitry Malevich, Ela Halliop, Brant A. Peppley, Jon G. Pharoah, and Kunal Karan. Investigation of charge-transfer and mass-transport resistances in pemfcs with microporous layer using electrochemical impedance spectroscopy. *Journal of The Electrochemical Society*, 156(2):B216–B224, 2009.

[192] Y. Zhou, G. Lin, A. J. Shih, and S. J. Hu. Assembly pressure and membrane swelling in pem fuel cells. *Journal of Power Sources*, 192(2):544–551, 2009.

[193] P. Deevanhxay, T. Sasabe, S. Tsushima, and S. Hirai. Effect of liquid water distribution in gas diffusion media with and without microporous layer on pem fuel cell performance. *Electrochemistry Communications*, 34(1):239–241, 2013.

[194] Tibor Fabian, Jonathan D Posner, Ryan OHayre, Suk-Won Cha, John K Eaton, Fritz B Prinz, and Juan G Santiago. The role of ambient conditions on the performance of a planar, air-breathing hydrogen pem fuel cell. *Journal of Power Sources*, 161(1):168–182, 2006.

[195] S. Park, J. W. Lee, and B. N. Popov. Effect of ptfe content in microporous layer on water management in pem fuel cells. *Journal of Power Sources*, 177(2):457–463, 2008.

[196] H. Sadeghifar, N. Djilali, and M. Bahrami. Effect of polytetrafluoroethylene (ptfe) and micro porous layer (mpl) on thermal conductivity of fuel cell gas diffusion layers: Modeling and experiments. *Journal of Power Sources*, 248(1):632–641, 2014.

[197] A. Weber and A. Kusoglu. Unexplained transport resistances for low-loaded fuel-cell catalyst layers. *JOURNAL OF MATERIALS CHEMISTRY. A*, 2(41):17207–17211, 2014.

[198] Jaehyung Park, Ugur Pasaogullari, and Leonard J Bonville. Characterization studies of a new mea structure for polymer electrolyte fuel cells. *ECS Transactions*, 69(17):1355–1362, 2015.

[199] T Kitahara, H Nakajima, and K Mori. Hydrophilic and hydrophobic double microporous layer coated gas diffusion layer for enhancing performance of polymer electrolyte fuel cells under no-humidification at the cathode. *Journal of Power Sources*, 199:29–36, 2012.

[200] T Kitahara, H Nakajima, and M Morishita. Water vapor exchange system using a hydrophilic microporous layer coated gas diffusion layer to enhance performance of polymer electrolyte fuel cells without cathode humidification. *Journal of Power Sources*, 214:100–106, 2012.

[201] T Kitahara, H Nakajima, M Inamoto, and M Morishita. Novel hydrophilic and hydrophobic double microporous layer coated gas diffusion layer to enhance performance of polymer electrolyte fuel cells under both low and high humidity. *Journal of Power Sources*, 234:129–138, 2013.

[202] T Kitahara, H Nakajima, M Inamoto, and K Shinto. Triple microporous layer coated gas diffusion layer for performance enhancement of polymer electrolyte fuel cells under both low and high humidity conditions. *Journal of Power Sources*, 248:1256–1263, 2014.

[203] M Ahn, Y Cho, Y Cho, J Kim, N Jung, and Y Sung. Influence of hydrophilicity in micro-porous layer for polymer electrolyte membrane fuel cells. *Electrochimica Acta*, 56(5):2450–2457, 2011.

[204] T Tanuma and S Kinoshita. Impact of cathode fabrication on fuel cell performance. *Journal of The Electrochemical Society*, 161(1):F94–F98, 2014.

[205] M. Secanell, A. Jarauta, A. Kosakian, M. Sabharwal, and J. Zhou. *PEM Fuel Cells, Modeling, In: Meyers R. (eds) Encyclopedia of Sustainability Science and Technology*. Springer, 2017.

[206] Qiangu Yan, Hossein Toghiani, Young-Whan Lee, Kaiwen Liang, and Heath Causey. Effect of sub-freezing temperatures on a pem fuel cell performance, startup and fuel cell components. *Journal of Power Sources*, 160(2):1242–1250, 2006.

[207] H Markötter, J Haussmann, R Alink, C Tötzke, T Arlt, M Klages, Heinrich Riesemeier, J Scholta, D Gerteisen, J Banhart, et al. Influence of cracks in the microporous layer on the water distribution in a pem fuel cell investigated by synchrotron radiography. *Electrochemistry Communications*, 34:22–24, 2013.

[208] S Kim and MM Mench. Physical degradation of membrane electrode assemblies undergoing freeze/thaw cycling: Micro-structure effects. *Journal of Power Sources*, 174(1):206–220, 2007.

[209] Junbo Hou, Hongmei Yu, Shengsheng Zhang, Shucheng Sun, Hongwei Wang, Baolian Yi, and Pingwen Ming. Analysis of pemfc freeze degradation at- 20 c after gas purging. *Journal of Power Sources*, 162(1):513–520, 2006.

[210] Qunhui Guo and Zhigang Qi. Effect of freeze-thaw cycles on the properties and performance of membrane-electrode assemblies. *Journal of Power Sources*, 160(2):1269–1274, 2006.

[211] Soowhan Kim, Byung Ki Ahn, and MM Mench. Physical degradation of membrane electrode assemblies undergoing freeze/thaw cycling: Diffusion media effects. *Journal of Power Sources*, 179(1):140–146, 2008.

[212] Soowhan Kim, Manish Khandelwal, Charles Chacko, and MM Mench. Investigation of the impact of interfacial delamination on polymer electrolyte fuel cell performance. *Journal of the Electrochemical Society*, 156(1):B99–B108, 2009.

[213] Tushar Swamy, EC Kumbur, and MM Mench. Characterization of interfacial structure in pefcs: water storage and contact resistance model. *Journal of The Electrochemical Society*, 157(1):B77–B85, 2010.

[214] EF Medici, IV Zenyuk, DY Parkinson, AZ Weber, and JS Allen. Understanding water transport in polymer electrolyte fuel cells using coupled continuum and pore-network models. *Fuel Cells*, 16(6):725–733, 2016.

Appendix A

Appendix

A.1 Relative Liquid Permeability

For hydrophilic and hydrophobic pores, integration of equation (2.18) leads to [4]:

$$k_{L,\mathrm{HI}} = \frac{F_{\mathrm{HI}}}{16}\left[\frac{\varepsilon_o S}{\lambda_{\mathrm{PSD}}}\right]^2 \sum_k \exp\left(-2\, s_{\mathrm{HI},k}^2\right) r_{\mathrm{HI},k}^2 f_{\mathrm{HI},k} \left[\mathrm{erf}\left(\frac{\ln\left(r_{c,\mathrm{HI}}\right) - \ln\left(r_{\mathrm{HI},k}\right)}{s_{\mathrm{HI},k}\sqrt{2}} - s_{\mathrm{HI},k}\sqrt{2}\right) + 1\right] \tag{A.1}$$

$$k_{L,HO} = \frac{F_{HO}}{16}\left[\frac{\varepsilon_o S}{\lambda_{\mathrm{PSD}}}\right]^2 \sum_k \exp\left(-2\, s_{\mathrm{HO},k}^2\right) r_{\mathrm{HO},k}^2 f_{\mathrm{HO},k} \left[-\mathrm{erf}\left(\frac{\ln\left(r_{c,\mathrm{HO}}\right) - \ln\left(r_{\mathrm{HO},k}\right)}{s_{\mathrm{HO},k}\sqrt{2}} - s_{\mathrm{HO},k}\sqrt{2}\right) + 1\right] \tag{A.2}$$

A.2 Relative gas permeability

For hydrophilic and hydrophobic pores, using the log-normal pore size distribution equation in equation (8) in reference [59], the integrated forms of $k_{g,\mathrm{HI}}$ and $k_{g,\mathrm{HO}}$ [4] in equation (2.19) are:

$$k_{g,\mathrm{HI}} = \frac{F_{\mathrm{HI}}}{16 k_{\mathrm{sat}}}\left[\frac{\varepsilon_o (1-S)}{\lambda_{\mathrm{PSD}}}\right]^2 \sum_k \exp\left(-2\, s_{\mathrm{HI},k}^2\right) r_{\mathrm{HI},k}^2 f_{\mathrm{HI},k} \left[-\mathrm{erf}\left(\frac{\ln\left(r_{c,\mathrm{HI}}\right) - \ln\left(r_{\mathrm{HI},k}\right)}{s_{\mathrm{HI},k}\sqrt{2}} - s_{\mathrm{HI},k}\sqrt{2}\right) + 1\right] \tag{A.3}$$

$$k_{g,HO} = \frac{F_{HO}}{16 k_{\mathrm{sat}}}\left[\frac{\varepsilon_o (1-S)}{\lambda_{\mathrm{PSD}}}\right]^2 \sum_k \exp\left(-2\, s_{\mathrm{HO},k}^2\right) r_{\mathrm{HO},k}^2 f_{\mathrm{HO},k} \tag{A.4}$$

$$\left[\operatorname{erf}\left(\frac{\ln\left(r_{c,\mathrm{HO}}\right)-\ln\left(r_{\mathrm{HO},k}\right)}{s_{\mathrm{HO},k}\sqrt{2}}-s_{\mathrm{HO},k}\sqrt{2}\right)+1\right]$$

A.3 Interfacial surface area

For hydrophilic and hydrophobic pores, integration of equation (2.22) results in [4]:

$$\frac{a(r)_{\mathrm{HI}}}{V_T}=F_{\mathrm{HI}}\sum_k\frac{f_{k,\mathrm{HI}}\exp\left(\frac{s_{k,\mathrm{HI}}^2}{2}\right)}{8\,r_{k,\mathrm{HI}}}\left[1+\operatorname{erf}\left(\frac{\ln(r_{cr})-\ln(r_{k,\mathrm{HI}})}{s_{k,\mathrm{HI}}\sqrt{2}}+\frac{s_{k,\mathrm{HI}}\sqrt{2}}{2}\right)\right] \tag{A.5}$$

$$\frac{a(r)_{\mathrm{HO}}}{V_T}=F_{\mathrm{HO}}\sum_k\frac{f_{k,\mathrm{HO}}\exp\left(\frac{s_{k,\mathrm{HO}}^2}{2}\right)}{8\,r_{k,\mathrm{HO}}}\left[1-\operatorname{erf}\left(\frac{\ln(r_{cr})-\ln(r_{k,\mathrm{HO}})}{s_{k,\mathrm{HO}}\sqrt{2}}+\frac{s_{k,\mathrm{HO}}\sqrt{2}}{2}\right)\right] \tag{A.6}$$

A.4 Average Knudsen radius

Integration of equation (2.24) over the pore sizes results in the average Knudsen radius for the PSD model for the hydrophilic network, i.e. [4]:

$$\int_{r_{c,\mathrm{HI}}}^{\infty}\frac{1}{V_T}\frac{dV_{\mathrm{HI}}(r)}{dr}dr=F_{\mathrm{HI}}\sum_k\frac{f_{\mathrm{HI},r,k}}{2}\left[1-\operatorname{erf}\left(\frac{\ln(r_{c,\mathrm{HI}})-\ln(r_{\mathrm{HI},k})}{s_{\mathrm{HI},k}\sqrt{2}}\right)\right] \tag{A.7}$$

$$\int_{r_{c,\mathrm{HI}}}^{\infty}\frac{1}{V_T}\frac{da_{\mathrm{wall,HI}}(r)}{dr}dr=\sum_k\frac{F_{\mathrm{HI}}\,f_{k,\mathrm{HI}}}{r_{k,\mathrm{HI}}}\exp\left(\frac{s_{k,\mathrm{HI}}^2}{2}\right)\left[1-\operatorname{erf}\left(\frac{\ln(r_{c,\mathrm{HI}})-\ln(r_{k,\mathrm{HI}})}{s_{k,\mathrm{HI}}\sqrt{2}}+\frac{s_{k,\mathrm{HI}}}{\sqrt{2}}\right)\right] \tag{A.8}$$

and for the hydrophobic network we obtain:

$$\int_0^{r_{c,\mathrm{HO}}} \frac{1}{V_T}\frac{dV_{\mathrm{HO}}(r)}{dr}dr = F_{\mathrm{HO}}\sum_k \frac{f_{\mathrm{HO},k}}{2}\left[1+\mathrm{erf}\left(\frac{\ln(r_{c,\mathrm{HO}})-\ln(r_{\mathrm{HO},k})}{s_{\mathrm{HO},k}\sqrt{2}}\right)\right] \tag{A.9}$$

$$\int_0^{r_{c,\mathrm{HO}}} \frac{1}{V_T}\frac{da_{\mathrm{wall,HO}}(r)}{dr}dr = \sum_k \frac{F_{\mathrm{HO}}\, f_{k,\mathrm{HO}}}{r_{k,\mathrm{HO}}}\exp\left(\frac{s_{k,\mathrm{HO}}^2}{2}\right) \left[1+\mathrm{erf}\left(\frac{\ln(r_{c,\mathrm{HO}})-\ln(r_{k,\mathrm{HO}})}{s_{k,\mathrm{HO}}\sqrt{2}}+\frac{s_{k,\mathrm{HO}}}{\sqrt{2}}\right)\right] \tag{A.10}$$